Understanding confinement effects and nano structuring in heterogeneous catalysis

Slot, T.K.

Publication date
2021

Document Version
Final published version

Understanding confinement effects and nanostructuring in heterogeneous catalysis

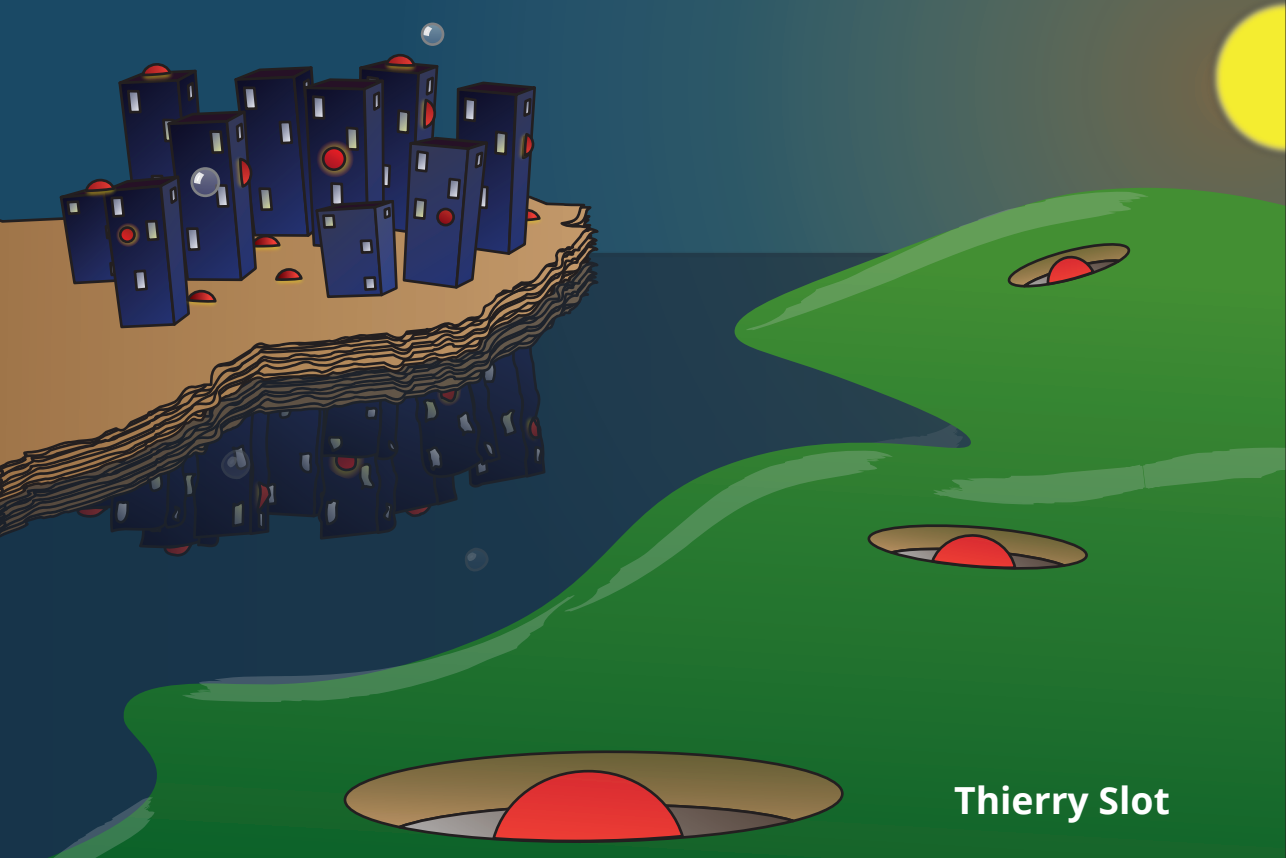

Thierry Slot

Understanding confinement effects and nano structuring in heterogeneous catalysis

Understanding confinement effects and nano structuring in heterogeneous catalysis

ACADEMISCH PROEFSCHRIFT

ter verkrijging van de graad van doctor

aan de Universiteit van Amsterdam

op gezag van Rector Magnificus

prof. dr. ir. K.I.J. Maex

ten overstaan van een door het College voor Promoties ingestelde

commissie, in het openbaar te verdedigen

op maandag 12 april 2021, te 14.00 uur

door

Thierry Kilian Slot

geboren te Alkmaar

Promotiecommissie

Promotores:	prof. dr. G. Rothenberg	Universiteit van Amsterdam
	dr. N. R. Shiju	Universiteit van Amsterdam
Overige leden:	prof. dr. P. E. de Jongh	Universiteit Utrecht
	Prof. dr. L. Bonneviot	École Normale Supérieure de Lyon
	Prof. dr. H. Xu	Fudan University, China
	Prof. dr. E. J. Meijer	Universiteit van Amsterdam
	Dr. H. Zhang	Universiteit van Amsterdam
	Dr. F. Mutti	Universiteit van Amsterdam

Faculteit der Natuurwetenschappen, Wiskunde en Informatica

The research presented in this dissertation was carried out at the Van 't Hoff Institute for Molecular Sciences of the University of Amsterdam, and is part of the Sustainable Chemistry Research Priority Area. The work was financially supported by the Netherlands Organisation for Scientific Research (NWO) TOP-PUNT project *Catalysis in Confined Spaces* [718.015.004].

Cover illustration: The cover illustration was inspired by SEM and TEM data of two catalysts, each representing a part of this thesis: The catalyst on the right symbolizes our synthetic approach for controlling confinement at surfaces (Chapter 3), and on the left, the work on MXenes (Chapters 4-6) is symbolized by a small city on a 'MXene' cliff. The buildings represent the surface-grown TiO_2 crystals. The back cover features the bubble counter (Chapter 2) which was used for a large portion of the kinetic measurements in Chapters 2, 3, 5 and 6.

Cover design: Thierry Slot

Printing: Ridderprint

ISBN: 978-94-6416-483-1

An electronic version of this dissertation is available at

http://dare.uva.nl/

To my parents,

Contents

1

Introduction

1

Confinement became the word of the year 2020, but unfortunately not for the reasons I had hoped. The COVID-19 pandemic changed many aspects of our daily lives. It will have far-reaching economic consequences and influence the chemical industry for many years to come. Whereas we used to rely on big networks of global chemical producers to provide continuity in chemical supply, it became apparent that this does not sustain in times of crisis. This realization accelerated a shift towards de-globalisation, with the goal of making markets less vulnerable to supply chain disruptions. This requires to source chemicals locally, making it ever so important to create processes that can adapt well to changes in feedstocks quality/composition. Such a transition also requires the development of adaptable catalysts, for which we can take inspiration from nature, and maybe even from the virus that started this shift in the first place: enzymes, nature's catalysts.

Enzymes are the workhorses that make life possible. They generally show a superb reactivity and selectivity, and are roughly 20–100 nm in size. An enzyme's protein chain cradles the reactant molecule at its active centre, which stabilizes the transition state by creating a well-defined confined space in which the reaction occurs.[1] This confined space is key to its efficiency. Enzymes employ a two-step strategy to destabilize their target substrates: First, the substrate is lured in with a strong interaction, after which the molecule is locally destabilized, resulting in a transition state. Here, the substrate is forced to take on a high-energy/low entropy configuration, effectively lowering the activation energy and accelerating the reaction. The protein chain helps in blocking alternative reaction pathways by restricting the access to the transition state.[2–4] The confinement is essential for the high efficiency of the enzymes. There are almost no examples where one can simply take the active centre from an enzyme and have it perform just as well without the protein environment.[5] Despite their excellent performance in biological systems, enzymes have a narrow window of application: They easily degrade or denature when exposed to heat, a different pH or strong concentrations of reactants.

Unlike enzymes, heterogeneous catalysts are typically very robust, operating well in a wide range of operating conditions. However, design of heterogeneous catalysts focuses mostly on the reactive centre, largely ignoring the complex coordination sphere that is available in an enzyme.[6,7] In essence, a good catalyst needs to leverage the advantages of both *chemistry* and *physics* to catalyse the reaction it was designed for. Physics "sets the stage" for the reaction by taking care of all processes around the active site: reactant diffusion, sorption, heat management, availability of active sites (surface area), and shape-selectivity (porosity). Chemistry is responsible for the catalytic transformation, determining the catalysts' activity and selectivity by electronic and often steric interactions/effects. However, the question of how confinement influences the reaction remains largely unanswered.

In this thesis, we study how confinement influences chemical reactions at a surface. We approach this from two angles, corresponding to the two parts in this thesis. In the first part, we study the role of confinement in heterogeneous catalysis. We will investigate the current definitions and understanding of confinement and analyse their origin. Then, we set up an experimental approach to isolate and study confinement effects by gradually restricting access to the active site. The second part of the thesis focuses on confinement in two-dimensional materials and how nano-structuring influences catalysis. We studied $Ti_3C_2T_x$ MXenes, a novel material whose surface can easily be modified into different structures. Nano-structuring alters the space around the active site and influences catalytic activity and selectivity.

1.1 Confinement in catalysis: what is confinement?

The purest definition of confinement has to be from a statistical-mechanics point of view: a reduction of degrees of freedom of the reactant in the transition state. However, in practice this is impossible to achieve without simultaneously influencing the reactant and/or active site electronically. This makes it very difficult to distinguish the effects of *statistical* confinement from other effects (electronic / cooperative effects). The catalysis community uses a broad definition of confinement, which describes materials such as cages, zeolites, carbon nano tubes, MOFs, COFs, nano reactors, and reactions between surfaces as confined spaces. Here, confinement is defined as a (partially) closed reaction space, a so-called *"molecular flask"* where the active site is located and the reaction takes place.[8,9] This space can be several angstroms in size, up to several tens of nanometres. Some examples of confining geometries are illustrated in Figure 1.1.

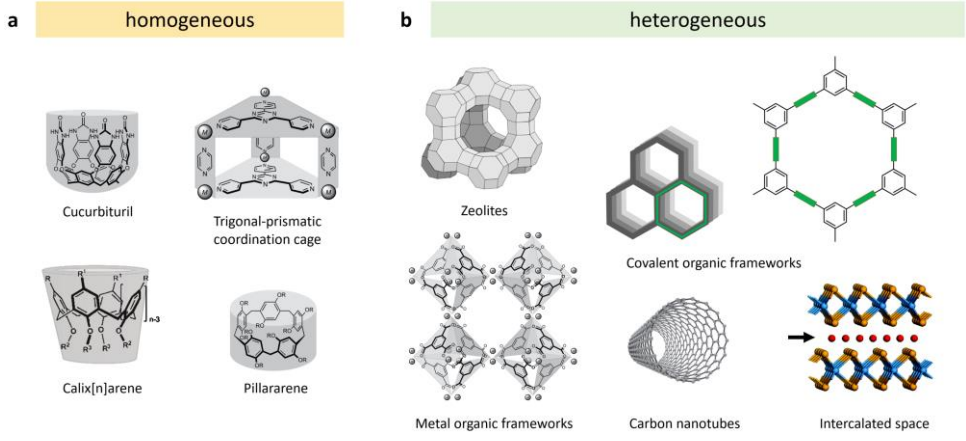

Figure 1.1. Examples of confined spaces in (**a**) homogeneous, and (**b**) heterogeneous catalysis. (partially reproduced from Klajn *et al.*)[10]

1.2 Quantum confinement

We can distinguish two kinds of confinement: (1) "molecular flask" confinement of the active site, where the catalyst is encapsulated in a space, separated from the bulk of the reactant, and (2) quantum confinement, which is only relevant at very small distances for small molecules (<5 nm). Both effects can influence the reaction rate, but by different mechanisms.

Quantum confinement is a direct result from the particle-wave duality at a (sub) nanometre scale. It appears when a particles' wavefunction is constrained within a potential well of a similar size as its De Broglie wavelength (λ_B, see Eq. 1.1). Energy levels get quantized, and start spreading out compared to the bulk material. A classical illustration of this effect can be seen in CdSe quantum dots, where the size of the CdSe crystal influences the bandgap (E_{bg}) between the valence and conduction bands, which can be directly observed as a corresponding change of colours in fluorescence (Figure 1.2).[11]

$$p = \hbar k = \frac{h}{\lambda_B} \quad , \quad E = \frac{p^2}{2m} \approx \frac{3}{2} k_B T \quad \rightarrow \quad \lambda_B = \frac{h}{\sqrt{3 m k_B T}} \approx 6.2 \text{ nm (at 300K)} \tag{1.1}$$

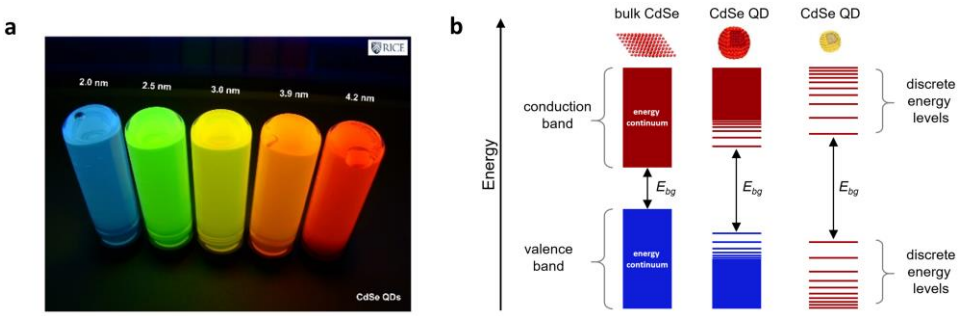

Figure 1.2. (**a**) Cadmium selenide quantum dots and (**b**) quantum confinement leading to increased energy separation.[12]

Electrons are the basis of chemistry: they are the glue that hold the atoms together within a molecule and they initiate the making and breaking of bonds. At what size can we expect electrons to experience confinement effects? We can estimate this from a back-of-the-envelope calculation, modelling an electron in an ideal gas in an infinite-potential well. Using Eq. 1.1 we obtain a De Broglie wavelength of roughly 6–7 nm, illustrating that confinement effects should be expected at the size range relevant for catalysis. This quantum confinement effect is indeed present in metal nanoparticles below 5 nm, and is one of the effects improving activity at smaller particle size. Mesoporous structures can also contribute quantum confinement this way. Similar to the idealized single-electron example, the reactant in a mesoporous structure can be confined in a 3-dimensional space (pore), which similarly induces separation/ quantization of the (molecular) energy levels. However, it is important to realize that

because molecules are much larger than a single electron, their De Broglie wavelengths are much shorter. This means that quantum confinement effects will only be relevant at very small distances, thereby limiting these influences to smaller molecules such as O_2, H_2, H_2O, CO_2, CO, BH_3.

This emphasizes the importance of the distinction between the two kinds of confinement. It is clear how quantum confinement can alter catalytic reactions by changing the electronic structure of a catalytic nanoparticle, potentially influencing adsorption, reaction and desorption steps.[13] However, how confinement works over larger distances is still unclear.

1.3 Principles of confinement in chemistry

Confinement is guided by several principles that are closely related to how enzymes achieve such high turnover frequencies and excellent selectivities. The structure around the active site, also called the secondary coordination sphere, is vital for this. Confinement in nano-spaces or "molecular flasks" improves reaction rates, for reactions with and without catalyst.[8] The confined environment mostly changes geometrical constraints, and sorption parameters, resulting in a change to the potential energy surface (PES) which directly influences the reaction conversion and selectivity.

When investigating the mechanisms of action, most confinement catalysts use one or more of the following strategies: increasing the local concentration of reactants (or catalysts), pre-organisation of reactants (and catalysts) or stabilizing the transition state under confinement.[10] Our hypothesis is that all these effects can be captured in a reaction coordinate diagram (Figure 1.3). They act through either: (1) increasing local concentration (e.g. through binding), (2) stabilizing (lowering) the transition state, or (3) reducing degrees of freedom from the potential-energy landscape (pre-organisation and pathway blocking) when it reaches the transition state. This approach allows for a more abstract description in terms of entropy and enthalpy and a convenient integration with Arrhenius relations and transition state theory.

The increased local concentration is merely a statistical effect. The more molecules you have close by, the larger the likelihood some of them will pass through a reaction pathway. This explains the enhanced reactivity due to over-solubility of reactants in the nano-confined spaces.[14–20]

Pre-organization rules out many structural conformations that could lead to unwanted side products. The energy of the transition state barrier is the most important factor influencing the reaction chemistry. It is directly related to the Gibbs free energy of the reaction which contains both entropy and enthalpy terms (Figure 1.3). If the reactive

centre does not change, we expect pre-organisation (and also confinement) to influence only the entropy part of this equation.

1.4 Measuring confinement

Quantifying confinement effects is already a formidable challenge, let alone *in-situ* observations. Most effects are quantified as difference or ratio of reaction rates in a confinement situation *vs.* non-confined. This however does not allow us to make any comparisons between different catalyst systems. Another approach is using spectroscopic techniques (analogous to quantum dot fluorescence) to monitor HOMO/LUMO energy levels of reactants experiencing confinement, but generally this only gives information on the majority of the reactant molecules, which do not experience any confinement. *In-situ* spectroscopic techniques might give insights on dynamics. Even then, the intermediates are generally very short-lived and are difficult to observe, even in carefully tailored model systems. In almost all real-world (i.e. non-model) catalytic systems, this approach is not feasible. However, one *can* relate the confinement principles with a reaction-coordinate diagram (Figure 1.3). This allows us to relate changes in the energy levels due to confinement with experimental data on reaction kinetics by using Eyring or Arrhenius relations.

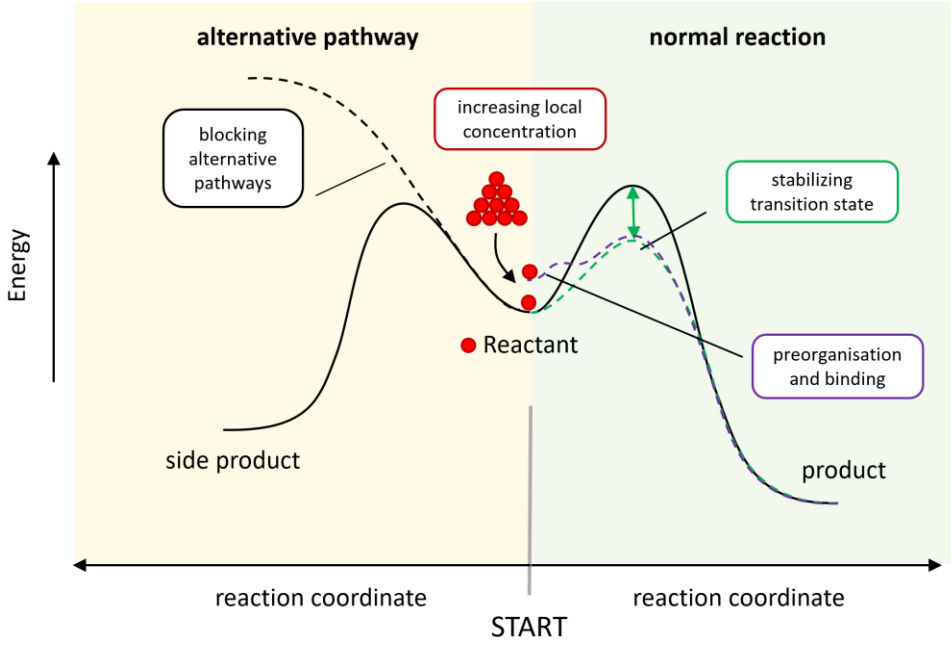

Figure 1.3. Reaction coordinate diagram showing the various effects of confinement: increasing local concentration, stabilizing transition state, and pre-organisation.

In a reaction diagram, the height of the transition state barrier is defined in Gibbs free energy ($\Delta G^{\ddagger} = \Delta H^{\ddagger} - T\Delta S^{\ddagger}$), which consist of an enthalpy and entropy term. This allows for a description in terms of entropy and enthalpy changes, and conveniently integrates with Arrhenius relations and transition state theory. Increasing local concentration (e.g. through adsorption) does not influence the energy levels, but just increases the rate of the reaction by increasing number of molecules starting on the reaction pathway. Reducing degrees of freedom from the potential-energy landscape (pre-organisation) influences the entropy term of $\Delta G^{\ddagger}$. Stabilizing the transition state (lowering the energy level) influences the enthalpy term of $\Delta G^{\ddagger}$. From this perspective we expect confinement effects to mainly have an influence on the entropy term.

The big advantage of relating the confinement principles with a reaction barrier model, is that it can be analysed using the empirical Arrhenius equation (Eq. 1.3) or the Eyring equation (Eq. 1.4). The Eyring equation follows from transition state theory for which Eyring, Polanyi and Evans laid the foundation. This provides a way to calculate rate constants for reactions based on first principles. One of the key ideas introduced by Eyring, Polanyi and Evans was the notion that activated complexes are in quasi-equilibrium with the reactants (Eq. 1.2). Once the reactant crosses the transition state barrier it would not cross back.

$$\mathrm{A} + \mathrm{B} \leftrightarrow [\mathrm{AB}]^{\ddagger} \rightarrow \mathrm{P} \tag{1.2}$$

Transition state theory assumes three things: (a) the reactants are in quasi-equilibrium with the transition state, (b) the energy distribution of the reactants follow the Boltzmann distribution, and (c) the activated complex only crosses the transition state once.[21] The transition state is in a shallow potential well with a very low vibrational frequency, much lower than the reactants/products. The motion leading to the product is assumed to be a specific vibration with frequency ν. This results in the Eyring-Polanyi Evans equation (Eq. 1.4) which can be linearized accordingly (Eq. 1.5).

$$k = A \cdot e^{\frac{-E_a}{RT}} \tag{1.3}$$

$$k = \frac{\kappa k_B T}{h} \cdot e^{\frac{-\Delta G^{\ddagger}}{RT}} = \frac{\kappa k_B T}{h} \cdot e^{\frac{-\Delta S^{\ddagger}}{R}} \cdot e^{\frac{-\Delta H^{\ddagger}}{RT}} \cdot \left(c^{\ominus}\right)^{1-m} \tag{1.4}$$

$$\ln\left(\frac{k}{T}\right) = \frac{-\Delta H^{\ddagger}}{R}\frac{1}{T} + \ln\frac{\kappa k_B}{h} + \frac{-\Delta S^{\ddagger}}{R} \tag{1.5}$$

Here, k is the reaction rate, κ is the transmission coefficient, k_B is the Boltzmann constant, T is temperature, h is the Planck constant, R is the gas constant, $\Delta S^{\ddagger}$ is the activation entropy, $\Delta H^{\ddagger}$ is the activation enthalpy, $c^{\ominus}$ is the is the standard concentration (1 mol L^{-1}) and m is the molecularity of the reaction.

The Eyring equation takes a similar exponential form as the Arrhenius equation. It is tempting to equate the enthalpy of activation with Arrhenius's activation energy, however, they are not identical. The activation energy $E_a = \Delta H^{\ddagger} + (1 - \Delta n^{\ddagger})RT$, where $\Delta n^{\ddagger}$ is the change in the number of molecules on forming the transition state.[22] However, when E_a is much larger than RT (which is in most cases) they are comparable. When we compare the Arrhenius equation (Eq. 1.3) to the Eyring equation (Eq. 1.4) we notice that enthalpy is represented in the exponential term and entropy is represented in the pre-exponential factor.

Understanding and predicting the entropy of confined molecules is a challenge, but there is some evidence from studies in zeolites that confinement, entropy and the Arrhenius pre-exponential factor are related.[23,24] In one example, the enthalpy and entropy changes upon confinement were mainly caused by Van der Waals forces in small pores.[25,26] Also, acidity in zeolites (hydronium formation by Brønsted acid sites) can be influenced by confinement.[27] At low water concentrations the Gibbs free energy is dominated by enthalpy, while at higher concentrations it is dominated by entropy. Entropy increases linearly with water concentration. Dauenhauer *et al.* used aluminosilicate zeolite frameworks with different pore sizes and cavity structures to examine this phenomenon. They showed that entropy of adsorption is a linear combination of rotational and translational entropy. Adsorption entropy can be predicted using only occupiable volume.[23]

Arrhenius and/or Eyring analysis are useful tools for studying the contributions from entropy and enthalpy in chemical reactions. This way we can study confinement effects indirectly, through the reaction kinetics at different temperatures. Also, this is an approach that can be applied to most reactions and does not require any difficult (*in-situ*) spectroscopic techniques. However, this type of kinetic analysis requires us to obtain very accurate reaction-rate data at many different temperatures. In Chapter 2 we have devised a novel method to monitor gas reactions in real-time and obtain accurate rate measurements at different temperatures. This way, we were able to obtain Arrhenius plots with over 300 data points, where each data point represents 10 – 40 measurements. We used ammonia borane hydrolysis as a benchmark reaction, because of its small size and high selectivity for hydrogen generation.

Conditions for using Arrhenius' approach in heterogeneous catalysis

There are a few constraints on using the Arrhenius equation. The number of active sites and the type of active sites must remain the same throughout the experiment (also at different temperatures). Furthermore, there must be one rate-determining step. The Langmuir Hinshelwood mechanism involves a minimum of three elemental steps: adsorption, reaction and desorption. The energy transition can be seen as the sum of the individual elementary-step energies. To isolate the activation energy of the chemical transformation there must be one rate-determining step. This allows

adsorbed reactants to pool at the base of the transition state barrier, where the reaction rate is determined solely by the number of molecules crossing the barrier. When the reaction is performed at different temperatures, this rate-determining step should remain the same. If it changes, it could show up in the Arrhenius plot as a change in activation energy.

Single-atom

The bottom limit for quantum confinement would be the single atom. Because sometimes the best catalytically active elements are precious and are of limited supply, there has been a growing effort to produce single-atom catalysts which offer a 100% atom efficiency.[28–32] Yet at these sizes, any confining action also changes the electronic levels of the atoms/molecules, opening up new reactive pathways. For example, in Pt/CeO_2, the Pt can dynamically inject electrons in the Ce 4f levels, enabling new catalytic pathways towards CO oxidation.[33] Pérez-Ramírez *et al.* showed how surface nano-structuring improves the stability and performance of platinum single-atom catalysts in vinyl chloride production.[34]

In alloys, single atom sites are even more interesting. Wavefunction mixing results in an electronic structure that resembles that of a *free metal atom*, so adsorbates bind to it like they do in molecular metal complexes.[35] This is a nice way of heterogenizing the reactive power of homogeneous metal catalysts.

1.5 "Molecular flasks" in catalysis

How does physical confinement (or a "molecular flask") influence a reaction? Many confinement effects were observed in confined-space systems during the last two decades. The following brief summary collects the most important examples of confinement in homogeneous and heterogeneous catalysis.

Homogeneous catalysis

Homogeneous catalysis has a unique position in the study of confinement, because the catalytic sites are well-defined and well distributed in a solution. Changing the ligands surrounding a metal centre directly influences the potential energy surface through both electronic- (influencing binding strength) and steric effects (shielding certain approach pathways). Encapsulation of such a catalyst inside another molecule imposes so-called second coordination sphere effects on the catalysts.[7] There are many examples of such systems: cyclodextrins,[36–39] calix[n]arenes,[40–46] cucurbit[n]urils,[47–51] and self-assembled cages.[52–57] These systems offer a hydrophobic pocket with different rim structures. These containers mostly affect *selectivity* of the catalysts. The selectivity is influenced by the size of the cavity, which has a preference for a substrate of particular size. Cages can form additional

interactions with the catalyst at the core, which can stabilize the transition state of the encapsulated catalyst, improving activity and selectivity.[58–62]

Heterogeneous catalysis

Zeolites

Zeolites are crystalline microporous (alumino)silicates that form well-defined pores of the size of a reactant molecule (0.2-1.2 nm). Their general formula is $M_X(AlO_2)_X(SiO_2)_Y$ where M are cations that balance the formal negative charge on the aluminium atoms.[63] Zeolites are highly tuneable, stable, and have a strictly controlled pore size, finding many applications in industrial processes including catalysis, separation and ion exchange.[64] Corma *et al.* were among the first to study confinement in zeolites. They showed that confinement of a reactant in zeolites will result in an increase of its molecular orbital energies.[65] The highest occupied molecular orbital (HOMO) is more susceptible to these effects than the lowest unoccupied molecular orbital (LUMO), decreasing the frontier molecular orbital band gap. Additionally, this type of confinement can also influence aromaticity of reactants, as was shown for anthracene.[66] Zeolites often contain acidic sites such as Lewis and Brønsted acidic sites. These acid sites often play a big part in the catalytic cycle of reactions like isomerisation, cracking, alkylation, and hydrolysis.[67–70] Different acid strengths can be observed in different sections of a zeolite. For example, a study of super-acidic MOR showed that its 8-MR side pockets possessed super-acidity caused by the strong pore confinement effect in that region of the zeolite.[71]

Confining guests (molecules, clusters or particles) inside a nano-porous host such as a zeolite is one of the most widely used post-synthetic modification strategies for porous materials, often yielding highly active and stable heterogeneous catalysts.[72–87] Counter-intuitively, this does not lead to decreased reaction rates. On the contrary, often authors report great boosts in activity or selectivity when a reactant can be confined in one way or another.[88–92] The improvement of catalytic performance is generally attributed to over-solubility of the reactants in the nano-confined spaces.[14,15]

Zeolites also indirectly influence selectivity and reactivity through effects such as shape-selection, pre-organisation and polarity. One of the best illustrations of shape-selection is selective isomerisation of xylene by ZSM-5.[64,93] Access to the catalyst was restricted by a partial blocking of the pore openings of the zeolite, favouring diffusion of para-xylene over meta- and ortho xylene. An example of pre-organisation is the aromatization of n-hexane, where zeolites impregnated with metals form large amounts of benzene.[94,95] This high benzene selectivity was the result of pre-organisation of the n-hexane by the zeolite pore, facilitating cyclization into benzene. The polarity of the zeolite's surface can be tuned by changing the Si/Al ratio. Polarity

can influence the local concentration of reactants through increased adsorption or desorption.[96–99] One nice example is olefin oxidation where lowering the zeolite polarity increased epoxide selectivity from 26% to 96%.[100]

Metal-organic frameworks (MOFs)

MOFs are composed using two major components: a metal ion or cluster and organic linker molecules. This makes it possible to obtain topologies with very well-defined unit-cell structure. They exhibit attractive features such as a crystalline nature, permanent porosity, a high surface area, large pore volume, low density while still offering relative flexible structures.[101,102] MOFs are more variable than zeolites because of the versatile coordination chemistry combined with a large choice of polytopic linkers and terminating ligands.[103] In most cases their confining effects are driven by the size of the (often chiral) cavities. Polymerization reactions such as acetylene or divinyl benzene polymerization show a strong preference for trans polymerization over cross-linked products in the presence of MOF frameworks.[104–106] Here, the size of the channels and the flexibility of the framework are the key to the high selectivity.[106] Metal nanoclusters (Pt, Au, Pd, PdCo bimetallics, and Ru) have also been encapsulated successfully in MOFs, although complete encapsulation of nanoparticles still remains a challenge.[72,73,107–111] MOFs also show great potential to functionalize linkers with a variety of groups such as amine or lanthanide groups for Brønsted-basic or Lewis-acid catalysis, respectively.[112,113] The effect of cavity wall modification on the performance of a catalyst enables in-depth studies on the effect of the side-walls in MOF catalysis.[114] These mainly influence the enthalpy of the reaction. Overall, the effects of confinement on MOF selectivity stems from their cavity size, enabling reactant molecules to react head-on in the interconnected pore network. Side-wall effects seem to primarily stabilize the transition state.

Covalent-organic frameworks (COFs)

COFs are related to MOFs and are constructed by covalent bonds, rather than coordination chemistry. This results in crystalline porous polymers with excellent thermal stability, where the geometry can be tuned by the directionality of the covalent bonds used.[115–121] Shustova *et al.* studied confinement by probing the electronic structure of confined chromophores.[122] Their hypothesis is that a confined space could potentially affect the emission profile of the guest molecule. They used several scaffolds to confine a variety of chromophores. They found that keeping the scaffold constant and varying the guest molecule did not change the emission maximum, whereas varying the pore size by using different scaffolds *did* lead to a bathochromic shift in the emission profile of the guest molecule. This is an interesting finding, because the chromophores generally do not interact with the framework and are able to move freely. This study might be the closest we can get to estimate the electronic

effects of confining reactants in MOF/COF structures. A similar bathochromic shift was observed when the chromophore was reaction-generated inside the framework.[123,124]

1.6 Surface nano-structuring: two-dimensional confined spaces

Two dimensional materials carry two types of confinement: interlayer confinement and surface confinement (Figure 1.4).[125] Interlayer confinement is about confining the reactants in the interlayer space of a layered materials, such as MXene,[126,127] layered double hydroxides,[128,129] silicates,[130,131] graphite,[132,133] and MoS_2[134,135] (Figure 1.4**a**). Catalysis under 2D materials is a field pioneered by Bao and Fu.[136] The confinement originates from intercalation of active sites between a one-atom thick 'Van der Waals' material and the underlying substrate (metal or silicon nitride).[137–139] The top layer is semipermeable, allowing reactants to pass. Both the particles in the active site as well as reactants are stabilized by the covering layer.[140] In one example, gold nanoparticles confined between LDA layers showed a 10-fold higher catalytic activity for C–H bond oxidation compared to Au on LDH.[141]

One disadvantage of interlayer confinement is that the confining action itself restricts access to the confined space. This makes it difficult to get a substrate molecule to voluntarily go into these spaces. Surface confinement attempts to solve this by utilizing surface functional groups to adsorb reactants, thus "confining" them to the surface (Figure 4**b**).[34,142–144] Nano-structuring of a catalyst's surface can be viewed as an intermediate form of confinement, between a non-functionalized surface and full confinement like for example a zeolite or porous carbon. These features form confined spaces around active sites, while still allowing for access of reactants (Figure 1.4**c**). This is the approach we chose in this work to study the effect of confinement on $Pt/\gamma Al_2O_3$ catalysts. Yamauchi *et al.* synthesized nano-reactors of about 8-10 nm on the surface of MXene, using a soft-template self-assembly method.[145] Another example is to selectively embed Pt nanoparticles in nano-pores of a carbon support, aiming to improve the metal utilization degree and stability.[146]

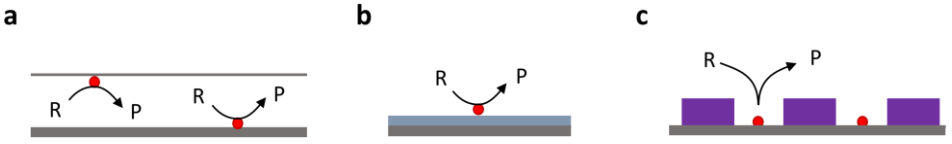

Figure 1.4. Schematic diagram with examples of (**a**) interlayer-space confinement, (**b**) surface confinement (e.g. functional groups stimulating adsorption), and (**c**) surface confinement due to post-synthetic surface modification. R = reactant, P = product.

Overall, these catalysts improve activity or selectivity by using the structuring properties to their advantage. In most cases, this leads to an electronic interplay with the active site, changing energy levels and modifying the activation energy.[26] Some

structures seem to play a purely geometric role, for example controlling the selectivity by restricting access of reactants at a distance from the active site, whereas other structures mainly influence activity by lowering the activation barrier. One of the more counter-intuitive features of these confinement catalysts is that they are more active when the access to the active site is restricted. Several reactants over-concentrate in the nano-cavities, explaining the increased reaction rate.[14–20,91]

A role for novel two-dimensional materials

Post-synthetic modification has been a popular technique for transforming the structure of the parent material to suit the properties of the application. There are many ways to apply structure to the surface of a heterogeneous catalyst. This can be as simple as a controlled distribution of active sites, delamination, or etching, but also by creating larger structures such as amorphous or crystalline layers, porosity and even cages.[147–149] Such modifications influence chemistry of the active site through steric and/or electronic effects, thereby parameters such as catalyst activity and selectivity, adsorption and diffusion.

1.7 Scope of this thesis

In this thesis we studied different types of confinement of active species and the effect this had on catalytic performance. In Chapter 2, we report a method to produce Pt particles with varying amounts of confined space around the particle. To measure the confinement effects, we developed a novel method and device (“bubble counter”) to monitor gas-producing reactions. This allowed us to study kinetics of a reaction such as ammonia borane hydrolysis in great detail giving highly detailed Arrhenius plots with hundreds of data points. This also allowed us to study confinement effects using the Arrhenius or Eyring relations. We then applied this method to measure confinement effects around spatially confined Pt nanoparticles (Chapter 3). We developed a new synthetic process to create free spaces around the Pt particles using a thiol-templating strategy followed by a phosphonic acid coating and subsequent removal of the thiol template.

In the second part of this thesis, we report the studies with MXenes and MAX phase materials. MXene is a novel two-dimensional material with both ceramic and metallic properties. It is conductive, yet its outer surface is sensitive to oxidation and easily forms metal-oxide nanostructures depending on the method of oxidation.[148–153] MXene materials are prepared by extracting the 'A' layers from so-called MAX phases, a material with formula $M_{n+1}AX_n$, (MAX) where M is an early transition metal, A is an A-group element, and X is either carbon or nitrogen.[154–156] We explored novel MAX phase materials and MXenes as heterogeneous catalysts. Up to now, only a handful thermo-catalytic applications of MXenes in heterogeneous catalysis are known.[155,157,158]

In Chapter 4, we show that etching and delamination of MAX phase material creates a partially opened multilayer MXene surface with many acid functionalities. We applied this material to the acid-catalysed styrene oxide ring opening reaction. Post-synthetic modification of the MXene changed the nature of these acid sites. The resulting nanostructuring of the MXene surface improved the selectivity of the reaction, effectively changing the type of surface acidic sites to control the reaction's activity and selectivity.

We then explored the use of MXenes as supports for catalytic metal nanoparticles. We found that MXene materials have a big influence on the supported particles, allowing us to "tune" metal-catalysed heterogeneous reactions by changing the support. We used the oxidation sensitivity of MXene to create new materials that boost the activity of Pt nanoparticles through an electronic interaction with the material (Chapter 5).

During the studies of MXene, we found that fluorine etching is largely responsible for their oxidation sensitivity. Therefore, we also investigated a fluorine-free method (alkaline etching) to delaminate $Ti_3(Al_{0.8}Sn_{0.2})C_2$ MAX phases. Our method of partial delamination created very active Ru catalysts in the hydrolysis of ammonia borane and the reduction of 4-nitroaniline using ammonia borane as reductant (Chapter 6). We found the Ru particles to be especially well dispersed on the MXene surfaces. An electronic interaction of the Ru with the support was observed, likely caused by remaining Sn that was not removed by the etching process.

1.8 References

[1] B. Maity, K. Fujita, T. Ueno, *Curr. Opin. Chem. Biol.* **2015**, *25*, 88–97.

[2] N. Wu, Y. Mo, J. Gao, E. F. Pai, *Proc. Natl. Acad. Sci.* **2000**, *97*, 2017–2022.

[3] S. Lüdtke, P. Neumann, K. M. Erixon, F. Leeper, R. Kluger, R. Ficner, K. Tittmann, *Nat. Chem.* **2013**, *5*, 762–767.

[4] M. Fujihashi, T. Ishida, S. Kuroda, L. P. Kotra, E. F. Pai, K. Miki, *J. Am. Chem. Soc.* **2013**, *135*, 17432–17443.

[5] M. J. Wiester, P. A. Ulmann, C. A. Mirkin, *Angew. Chem. Int. Ed.* **2011**, *50*, 114–137.

[6] G. Giannakakis, M. Flytzani-Stephanopoulos, E. C. H. Sykes, *Acc. Chem. Res.* **2019**, *52*, 237–247.

[7] V. Mouarrawis, R. Plessius, J. I. van der Vlugt, J. N. H. Reek, *Front. Chem.* **2018**, *6*, DOI 10.3389/fchem.2018.00623.

[8] M. Yoshizawa, J. K. Klosterman, M. Fujita, *Angew. Chem. Int. Ed.* **2009**, *48*, 3418–3438.

[9] Y. Inokuma, M. Kawano, M. Fujita, *Nat. Chem.* **2011**, *3*, 349–358.

[10] A. B. Grommet, M. Feller, R. Klajn, *Nat. Nanotechnol.* **2020**, *15*, 256–271.

[11] D. Bera, L. Qian, T.-K. Tseng, P. H. Holloway, *Materials* **2010**, *3*, 2260–2345.

[12] "Quantum Dots: The Basics," can be found under https://www.findlight.net/blog/2018/08/02/quantum-dots-basics/, **2018**.

[13] L.-C. Chen, Y.-K. Xiao, N.-J. Ke, C.-Y. Shih, T.-F. Yeh, Y.-L. Lee, H. Teng, *J. Mater. Chem. A* **2018**, *6*, 18216–18224.

[14] L. N. Ho, Y. Schuurman, D. Farrusseng, B. Coasne, *J. Phys. Chem. C* **2015**, *119*, 21547–21554.

[15] C.-C. Liu, C.-Y. Mou, S. S.-F. Yu, S. I. Chan, *Energy Environ. Sci.* **2016**, *9*, 1361–1374.

[16] L. N. Ho, S. Clauzier, Y. Schuurman, D. Farrusseng, B. Coasne, *J. Phys. Chem. Lett.* **2013**, *4*, 2274–2278.

[17] N. L. Ho, J. Perez-Pellitero, F. Porcheron, R. J.-M. Pellenq, *J. Phys. Chem. C* **2012**, *116*, 3600–3607.

[18] A. Luzar, D. Bratko, *J. Phys. Chem. B* **2005**, *109*, 22545–22552.

[19] S. Miachon, V. V. Syakaev, A. Rakhmatullin, M. Pera-Titus, S. Caldarelli, J.-A. Dalmon, *ChemPhysChem* **2008**, *9*, 78–82.

[20] D. Bratko, A. Luzar, *Langmuir* **2008**, *24*, 1247–1253.

[21] J. F. Perez-Benito, *J. Chem. Educ.* **2017**, *94*, 1238–1246.

[22] J. I. Steinfeld, J. S. Francisco, W. L. Hase, W. L. Hase, *Chemical Kinetics and Dynamics*, Prentice Hall, **1999**.

[23] P. J. Dauenhauer, O. A. Abdelrahman, *ACS Cent. Sci.* **2018**, *4*, 1235–1243.

[24] A. Janda, B. Vlaisavljevich, L.-C. Lin, B. Smit, A. T. Bell, *J. Am. Chem. Soc.* **2016**, *138*, 4739–4756.

[25] M. Maestri, E. Iglesia, *Phys. Chem. Chem. Phys.* **2018**, *20*, 15725–15735.

[26] L. Annamalai, Y. Liu, S. Ezenwa, Y. Dang, S. L. Suib, P. Deshlahra, *ACS Catal.* **2018**, *8*, 7051–7067.

[27] E. Grifoni, G. Piccini, J. Lercher, V.-A. Glezakou, R. Rousseau, M. Parrinello, *Confinement Effects and Acid Strength in Zeolites*, In Review, **2020**.

[28] Y. Cheng, J. Dai, Y. Song, Yumin. Zhang, *Nanoscale* **2019**, *11*, 18132–18141.

[29] B. Huang, N. Li, W.-J. Ong, Naigen. Zhou, *J. Mater. Chem. Mater. Energy Sustain.* **2019**, 7, 27620–27631.

[30] V. Ramalingam, P. Varadhan, H.-C. Fu, H. Kim, D. Zhang, S. Chen, L. Song, D. Ma, Y. Wang, H. N. Alshareef, J.-H. He, *Adv. Mater.* **2019**, *31*, 1903841.

[31] J. Zhang, Y. Zhao, X. Guo, C. Chen, C.-L. Dong, R.-S. Liu, C.-P. Han, Y. Li, Y. Gogotsi, G. Wang, *Nat. Catal.* **2018**, *1*, 985–992.

[32] C. Zhang, J. Sha, H. Fei, M. Liu, S. Yazdi, J. Zhang, Q. Zhong, X. Zou, N. Zhao, H. Yu, Z. Jiang, E. Ringe, B. I. Yakobson, J. Dong, D. Chen, J. M. Tour, *ACS Nano* **2017**, *11*, 6930–6941.

[33] N. Daelman, M. Capdevila-Cortada, N. López, *Nat. Mater.* **2019**, *18*, 1215–1221.

[34] S. K. Kaiser, E. Fako, G. Manzocchi, F. Krumeich, R. Hauert, A. H. Clark, O. V. Safonova, N. López, J. Pérez-Ramírez, *Nat. Catal.* **2020**, *3*, 376–385.

[35] M. T. Greiner, T. E. Jones, S. Beeg, L. Zwiener, M. Scherzer, F. Girgsdies, S. Piccinin, M. Armbrüster, A. Knop-Gericke, R. Schlögl, *Nat. Chem.* **2018**, *10*, 1008–1015.

[36] R. Breslow, P. Campbell, *J. Am. Chem. Soc.* **1969**, *91*, 3085–3085.

[37] R. Breslow, L. E. Overman, *J. Am. Chem. Soc.* **1970**, *92*, 1075–1077.

[38] M. Jouffroy, R. Gramage-Doria, D. Armspach, D. Sémeril, W. Oberhauser, D. Matt, L. Toupet, *Angew. Chem. Int. Ed.* **2014**, *53*, 3937–3940.

[39] M. Guitet, P. Zhang, F. Marcelo, C. Tugny, J. Jiménez-Barbero, O. Buriez, C. Amatore, V. Mouriès-Mansuy, J.-P. Goddard, L. Fensterbank, Y. Zhang, S. Roland, M. Ménand, M. Sollogoub, *Angew. Chem.* **2013**, *125*, 7354–7359.

[40] Z.-Y. Li, Y. Chen, C.-Q. Zheng, Y. Yin, L. Wang, X.-Q. Sun, *Tetrahedron* **2017**, *73*, 78–85.

[41] S.-Y. Li, Y.-W. Xu, J.-M. Liu, C.-Y. Su, *Int. J. Mol. Sci.* **2011**, *12*, 429–455.

[42] A. L. Maksimov, T. S. Buchneva, E. A. Karakhanov, *J. Mol. Catal. Chem.* **2004**, *217*, 59–67.

[43] L. Monnereau, D. Sémeril, D. Matt, C. Gourlaouen, *Eur. J. Inorg. Chem.* **2017**, *2017*, 581–586.

[44] L. Monnereau, D. Sémeril, D. Matt, *Adv. Synth. Catal.* **2013**, *355*, 1351–1360.

[45] L. Monnereau, D. Sémeril, D. Matt, L. Toupet, *Chem. – Eur. J.* **2010**, *16*, 9237–9247.

[46] E. Demircan, S. Eymur, A. S. Demir, *Tetrahedron Asymmetry* **2014**, *25*, 443–448.

[47] L. Zheng, S. Sonzini, M. Ambarwati, E. Rosta, O. A. Scherman, A. Herrmann, *Angew. Chem. Int. Ed.* **2015**, *54*, 13007–13011.

[48] H. Cong, Z. Tao, S.-F. Xue, Q.-J. Zhu, *Curr. Org. Chem.* **2011**, *15*, 86–95.

[49] S. M. de Lima, J. A. Gómez, V. P. Barros, G. de S. Vertuan, M. das D. Assis, C. F. de O. Graeff, G. J.-F. Demets, *Polyhedron* **2010**, *29*, 3008–3013.

[50] B. C. Pemberton, R. Raghunathan, S. Volla, J. Sivaguru, *Chem. – Eur. J.* **2012**, *18*, 12178–12190.

[51] A. L. Koner, C. Márquez, M. H. Dickman, W. M. Nau, *Angew. Chem. Int. Ed.* **2011**, *50*, 545–548.

[52] M. Yoshizawa, M. Tamura, M. Fujita, *Science* **2006**, *312*, 251–254.

[53] T. Heinz, D. M. Rudkevich, J. Rebek, *Nature* **1998**, *394*, 764–766.

[54] M. Fujita, J. Yazaki, K. Ogura, *J. Am. Chem. Soc.* **1990**, *112*, 5645–5647.

[55] C. L. D. Gibb, B. C. Gibb, *J. Am. Chem. Soc.* **2004**, *126*, 11408–11409.

[56] T. Gadzikwa, R. Bellini, H. L. Dekker, J. N. H. Reek, *J. Am. Chem. Soc.* **2012**, *134*, 2860–2863.

[57] Q.-Q. Wang, S. Gonell, S. H. A. M. Leenders, M. Dürr, I. Ivanović-Burmazović, J. N. H. Reek, *Nat. Chem.* **2016**, *8*, 225–230.

[58] M. D. Pluth, R. G. Bergman, K. N. Raymond, *J. Am. Chem. Soc.* **2008**, *130*, 11423–11429.

[59] S. H. A. M. Leenders, R. Gramage-Doria, B. de Bruin, J. N. H. Reek, *Chem. Soc. Rev.* **2015**, *44*, 433–448.

[60] M. D. Pluth, R. G. Bergman, K. N. Raymond, *Science* **2007**, *316*, 85–88.

[61] H. Amouri, C. Desmarets, J. Moussa, *Chem. Rev.* **2012**, *112*, 2015–2041.

[62] D. M. Vriezema, M. Comellas Aragonès, J. A. A. W. Elemans, J. J. L. M. Cornelissen, A. E. Rowan, R. J. M. Nolte, *Chem. Rev.* **2005**, *105*, 1445–1490.

[63] C. S. Cundy, P. A. Cox, *Chem. Rev.* **2003**, *103*, 663–702.

[64] G. Rothenberg, *Catalysis: Concepts and Green Applications*, Wiley-VCH, **2017**.

[65] E. L. Clennan, in *Adv. Phys. Org. Chem.* (Ed.: J.P. Richard), Academic Press, **2007**, pp. 225–269.

[66] F. Márquez, H. García, E. Palomares, L. Fernández, A. Corma, *J. Am. Chem. Soc.* **2000**, *122*, 6520–6521.

[67] G. Busca, *Chem. Rev.* **2007**, *107*, 5366–5410.

[68] E. G. Derouane, J. C. Védrine, R. R. Pinto, P. M. Borges, L. Costa, M. A. N. D. A. Lemos, F. Lemos, F. R. Ribeiro, *Catal. Rev.* **2013**, *55*, 454–515.

[69] H. Hattori, Y. Ono, *Solid Acid Catalysis: From Fundamentals to Applications*, CRC Press, **2015**.

[70] J. Weitkamp, *Solid State Ion.* **2000**, *131*, 175–188.

[71] W. Chen, X. Yi, L. Huang, W. Liu, G. Li, D. Acharya, X. Sun, A. Zheng, *Catal. Sci. Technol.* **2019**, *9*, 5045–5057.

[72] T. Wang, L. Gao, J. Hou, S. J. A. Herou, J. T. Griffiths, W. Li, J. Dong, S. Gao, M.-M. Titirici, R. V. Kumar, A. K. Cheetham, X. Bao, Q. Fu, S. K. Smoukov, *Nat. Commun.* **2019**, *10*, 1340.

[73] B. An, J. Zhang, K. Cheng, P. Ji, C. Wang, W. Lin, *J. Am. Chem. Soc.* **2017**, *139*, 3834–3840.

[74] T. Wang, H.-K. Kim, Y. Liu, W. Li, J. T. Griffiths, Y. Wu, S. Laha, K. D. Fong, F. Podjaski, C. Yun, R. V. Kumar, B. V. Lotsch, A. K. Cheetham, S. K. Smoukov, *J. Am. Chem. Soc.* **2018**, *140*, 6130–6136.

[75] L. Chen, R. Luque, Y. Li, *Chem. Soc. Rev.* **2017**, *46*, 4614–4630.

[76] A. Corma, H. García, F. X. Llabrés i Xamena, *Chem. Rev.* **2010**, *110*, 4606–4655.

[77] T. Wang, M. Farajollahi, S. Henke, T. Zhu, S. R. Bajpe, S. Sun, J. S. Barnard, J. S. Lee, J. D. W. Madden, A. K. Cheetham, S. K. Smoukov, *Mater. Horiz.* **2017**, *4*, 64–71.

[78] M. D. Allendorf, M. E. Foster, F. Léonard, V. Stavila, P. L. Feng, F. P. Doty, K. Leong, E. Y. Ma, S. R. Johnston, A. A. Talin, *J. Phys. Chem. Lett.* **2015**, *6*, 1182–1195.

[79] K. Moller, T. Bein, *Chem. Mater.* **1998**, *10*, 2950–2963.

[80] J. Lee, O. K. Farha, J. Roberts, K. A. Scheidt, S. T. Nguyen, J. T. Hupp, *Chem. Soc. Rev.* **2009**, *38*, 1450–1459.

[81] J. Juan-Alcañiz, J. Gascon, F. Kapteijn, *J. Mater. Chem.* **2012**, *22*, 10102–10118.

[82] M. Meilikhov, K. Yusenko, D. Esken, S. Turner, G. Van Tendeloo, R. A. Fischer, *Eur. J. Inorg. Chem.* **2010**, *2010*, 3701–3714.

[83] Y. Yang, J.-S. Chen, J.-Y. Liu, G.-J. Zhao, L. Liu, K.-L. Han, T. R. Cook, P. J. Stang, *J. Phys. Chem. Lett.* **2015**, *6*, 1942–1947.

[84] G. D. Stucky, J. E. M. Dougall, *Science* **1990**, *247*, 669–678.

[85] M. Fujita, D. Oguro, M. Miyazawa, H. Oka, K. Yamaguchi, K. Ogura, *Nature* **1995**, *378*, 469–471.

[86] A. Corma, H. Garcia, *Eur. J. Inorg. Chem.* **2004**, *2004*, 1143–1164.

[87] X. Pan, X. Bao, *Acc. Chem. Res.* **2011**, *44*, 553–562.

[88] D. Liu, G. Zhang, Q. Ji, Y. Zhang, Jinghong. Li, *ACS Appl. Mater. Interfaces* **2019**, *11*, 25758–25765.

[89] X. Chen, Z.-Z. Lin, M. Ju, L.-X. Guo, *Appl. Surf. Sci.* **2019**, *479*, 685–692.

[90] E. W. Elliott, R. D. Glover, J. E. Hutchison, *ACS Nano* **2015**, *9*, 3050–3059.

[91] C.-C. Liu, R. Ramu, S. I. Chan, C.-Y. Mou, S. S.-F. Yu, *Catal. Sci. Technol.* **2016**, *6*, 7623–7630.

[92] Á. Szécsényi, E. Khramenkova, I. Yu. Chernyshov, G. Li, J. Gascon, E. A. Pidko, *ACS Catal.* **2019**, *9*, 9276–9284.

[93] W. W. Kaeding, C. Chu, L. B. Young, B. Weinstein, S. A. Butter, *J. Catal.* **1981**, *67*, 159–174.

[94] J. Kanai, N. Kawata, *Appl. Catal.* **1989**, *55*, 115–122.

[95] E. G. Derouane, D. J. Vanderveken, *Appl. Catal.* **1988**, *45*, L15–L22.

[96] H. Ogawa, T. Koh, K. Taya, T. Chihara, *J. Catal.* **1994**, *148*, 493–500.

[97] R. Gounder, M. E. Davis, *AIChE J.* **2013**, *59*, 3349–3358.

[98] M. J. Climent, A. Corma, A. Velty, M. Susarte, *J. Catal.* **2000**, *196*, 345–351.

[99] J. Weitkamp, L. Puppe, *Catalysis and Zeolites: Fundamentals and Applications*, Springer Science & Business Media, **2013**.

[100] A. Corma, *J. Catal.* **2003**, *216*, 298–312.

[101] A. Kirchon, L. Feng, H. F. Drake, E. A. Joseph, H.-C. Zhou, *Chem. Soc. Rev.* **2018**, *47*, 8611–8638.

[102] T. Ghanbari, F. Abnisa, W. M. A. Wan Daud, *Sci. Total Environ.* **2020**, *707*, 135090.

[103] R. Banerjee, A. Phan, B. Wang, C. Knobler, H. Furukawa, M. O'Keeffe, O. M. Yaghi, *Science* **2008**, *319*, 939–943.

[104] R. Matsuda, R. Kitaura, S. Kitagawa, Y. Kubota, R. V. Belosludov, T. C. Kobayashi, H. Sakamoto, T. Chiba, M. Takata, Y. Kawazoe, Y. Mita, *Nature* **2005**, *436*, 238–241.

[105] T. Uemura, R. Kitaura, Y. Ohta, M. Nagaoka, S. Kitagawa, *Angew. Chem. Int. Ed.* **2006**, *45*, 4112–4116.

[106] T. Uemura, D. Hiramatsu, Y. Kubota, M. Takata, S. Kitagawa, *Angew. Chem. Int. Ed.* **2007**, *46*, 4987–4990.

[107] S. Opelt, V. Krug, J. Sonntag, M. Hunger, E. Klemm, *Microporous Mesoporous Mater.* **2012**, *147*, 327–333.

[108] S. Opelt, S. Türk, E. Dietzsch, A. Henschel, S. Kaskel, E. Klemm, *Catal. Commun.* **2008**, *9*, 1286–1290.

[109] Z. Guo, C. Xiao, R. V. Maligal-Ganesh, L. Zhou, T. W. Goh, X. Li, D. Tesfagaber, A. Thiel, W. Huang, *ACS Catal.* **2014**, *4*, 1340–1348.

[110] S. Choi, M. Oh, *Angew. Chem.* **2019**, *131*, 876–881.

[111] Y.-Z. Chen, Q. Xu, S.-H. Yu, H.-L. Jiang, *Small* **2015**, *11*, 71–76.

[112] P. Wu, J. Wang, Y. Li, C. He, Z. Xie, C. Duan, *Adv. Funct. Mater.* **2011**, *21*, 2788–2794.

[113] M. Hartmann, M. Fischer, *Microporous Mesoporous Mater.* **2012**, *164*, 38–43.

[114] F. Vermoortele, M. Vandichel, B. Van de Voorde, R. Ameloot, M. Waroquier, V. Van Speybroeck, D. E. De Vos, *Angew. Chem. Int. Ed.* **2012**, *51*, 4887–4890.

[115] Q. Fang, S. Gu, J. Zheng, Z. Zhuang, S. Qiu, Y. Yan, *Angew. Chem. Int. Ed.* **2014**, *53*, 2878–2882.

[116] P. J. Waller, F. Gándara, O. M. Yaghi, *Acc. Chem. Res.* **2015**, *48*, 3053–3063.

[117] X. Han, Q. Xia, J. Huang, Y. Liu, C. Tan, Y. Cui, *J. Am. Chem. Soc.* **2017**, *139*, 8693–8697.

[118] F. Yu, D. Poole, S. Mathew, N. Yan, J. Hessels, N. Orth, I. Ivanović-Burmazović, J. N. H. Reek, *Angew. Chem. Int. Ed.* **2018**, *57*, 11247–11251.

[119] H. M. El-Kaderi, J. R. Hunt, J. L. Mendoza-Cortés, A. P. Côté, R. E. Taylor, M. O'Keeffe, O. M. Yaghi, *Science* **2007**, *316*, 268–272.

[120] A. P. Côté, A. I. Benin, N. W. Ockwig, M. O'Keeffe, A. J. Matzger, O. M. Yaghi, *Science* **2005**, *310*, 1166–1170.

[121] C. S. Diercks, O. M. Yaghi, *Science* **2017**, *355*, DOI 10.1126/science.aal1585.

[122] E. A. Dolgopolova, A. A. Berseneva, M. S. Faillace, O. A. Ejegbavwo, G. A. Leith, S. W. Choi, H. N. Gregory, A. M. Rice, M. D. Smith, M. Chruszcz, S. Garashchuk, K. Mythreye, N. B. Shustova, *J. Am. Chem. Soc.* **2020**, *142*, 4769–4783.

[123] J. M. Lerestif, J. Perrocheau, F. Tonnard, J. P. Bazureau, J. Hamelin, *Tetrahedron* **1995**, *51*, 6757–6774.

[124] A. Baldridge, J. Kowalik, L. M. Tolbert, *Synthesis* **2010**, *2010*, 2424–2436.

[125] Z. Li, X. Zhang, H. Cheng, J. Liu, M. Shao, M. Wei, D. G. Evans, H. Zhang, X. Duan, *Adv. Energy Mater.* **2020**, *10*, 1900486.

[126] M. Naguib, V. N. Mochalin, M. W. Barsoum, Y. Gogotsi, *Adv. Mater.* **2014**, *26*, 992–1005.

[127] B. Anasori, M. R. Lukatskaya, Y. Gogotsi, *Nat. Rev. Mater.* **2017**, *2*, 1–17.

[128] M. Shao, R. Zhang, Z. Li, M. Wei, D. G. Evans, X. Duan, *Chem. Commun.* **2015**, *51*, 15880–15893.

[129] Z. Li, H. Duan, M. Shao, J. Li, D. O'Hare, M. Wei, Z. L. Wang, *Chem* **2018**, *4*, 2168–2179.

[130] H. P. Eugster, *Science* **1967**, *157*, 1177–1180.

[131] E. Manias, A. Touny, L. Wu, K. Strawhecker, B. Lu, T. C. Chung, *Chem. Mater.* **2001**, *13*, 3516–3523.

[132] M. J. Allen, V. C. Tung, R. B. Kaner, *Chem. Rev.* **2010**, *110*, 132–145.

[133] Y. Zhang, L. Zhang, C. Zhou, *Acc. Chem. Res.* **2013**, *46*, 2329–2339.

[134] M. Chhowalla, H. S. Shin, G. Eda, L.-J. Li, K. P. Loh, H. Zhang, *Nat. Chem.* **2013**, *5*, 263–275.

[135] C. Backes, N. C. Berner, X. Chen, P. Lafargue, P. LaPlace, M. Freeley, G. S. Duesberg, J. N. Coleman, A. R. McDonald, *Angew. Chem. Int. Ed.* **2015**, *54*, 2638–2642.

[136] L. Tang, X. Meng, D. Deng, X. Bao, *Adv. Mater.* **2019**, *31*, 1901996.

[137] Q. Fu, X. Bao, *Chin. J. Catal.* **2015**, *36*, 517–519.

[138] D. Deng, K. S. Novoselov, Q. Fu, N. Zheng, Z. Tian, X. Bao, *Nat. Nanotechnol.* **2016**, *11*, 218–230.

[139] Q. Fu, X. Bao, *Chem. Soc. Rev.* **2017**, *46*, 1842–1874.

[140] J. A. Boscoboinik, *J. Phys. Condens. Matter* **2018**, *31*, 063001.

[141] L. Wang, Y. Zhu, J.-Q. Wang, F. Liu, J. Huang, X. Meng, J.-M. Basset, Y. Han, F.-S. Xiao, *Nat. Commun.* **2015**, *6*, 6957.

[142] L. Dong, P. N. Liu, N. Lin, *Acc. Chem. Res.* **2015**, *48*, 2765–2774.

[143] L. Xu, X. Zhou, W. Q. Tian, T. Gao, Y. F. Zhang, S. Lei, Z. F. Liu, *Angew. Chem. Int. Ed.* **2014**, *53*, 9564–9568.

[144] J. Yang, C. Yu, C. Hu, M. Wang, S. Li, H. Huang, K. Bustillo, X. Han, C. Zhao, W. Guo, Z. Zeng, H. Zheng, J. Qiu, *Adv. Funct. Mater.* **2018**, *28*, 1803272.

[145] J. Wang, J. Tang, B. Ding, V. Malgras, Z. Chang, X. Hao, Y. Wang, H. Dou, X. Zhang, Y. Yamauchi, *Nat. Commun.* **2017**, *8*, 15717.

[146] A. M. Jauhar, Z. Ma, M. Xiao, G. Jiang, S. Sy, S. Li, A. Yu, Z. Chen, *J. Power Sources* **2020**, *473*, 228607.

[147] T. K. Slot, F. Yue, H. Xu, E. V. Ramos-Fernandez, A. Sepúlveda-Escribano, Z. Sofer, G. Rothenberg, N. R. Shiju, *2D Mater.* **2020**, *8*, DOI 10.1088/2053-1583/ababef.

[148] Y. Chae, S. Joon Kim, S.-Y. Cho, J. Choi, K. Maleski, B.-J. Lee, H.-T. Jung, Y. Gogotsi, Y. Lee, C. Won Ahn, *Nanoscale* **2019**, *11*, 8387–8393.

[149] V. Natu, J. L. Hart, M. Sokol, H. Chiang, M. L. Taheri, M. W. Barsoum, *Angew. Chem. Int. Ed.* **2019**, *58*, 12655–12660.

[150] B. Ahmed, D. H. Anjum, M. N. Hedhili, Y. Gogotsi, H. N. Alshareef, *Nanoscale* **2016**, *8*, 7580–7587.

[151] M. Cao, F. Wang, L. Wang, W. Wu, W. Lv, J. Zhu, *J Electrochem Soc* **2017**, *164*, A3933.

[152] R. Lotfi, M. Naguib, D. E. Yilmaz, J. Nanda, A. C. T. van Duin, *J. Mater. Chem. A* **2018**, *6*, 12733–12743.

[153] H. Tang, S. Zhuang, Z. Bao, C. Lao, Y. Mei, *ChemElectroChem* **2016**, *3*, 871–876.

[154] M. Naguib, M. Kurtoglu, V. Presser, J. Lu, J. Niu, M. Heon, L. Hultman, Y. Gogotsi, M. W. Barsoum, *Adv. Mater.* **2011**, *23*, 4248–4253.

[155] W. H. K. Ng, E. S. Gnanakumar, E. Batyrev, S. K. Sharma, P. K. Pujari, H. F. Greer, W. Zhou, R. Sakidja, G. Rothenberg, M. W. Barsoum, N. R. Shiju, *Angew. Chem. Int. Ed.* **2018**, *57*, 1485–1490.

[156] M. W. Barsoum, *MAX Phases: Properties of Machinable Ternary Carbides and Nitrides*, Wiley-VCH, **2013**.

[157] Z. Li, L. Yu, C. Milligan, T. Ma, L. Zhou, Y. Cui, Z. Qi, N. Libretto, B. Xu, J. Luo, E. Shi, Z. Wu, H. Xin, W. N. Delgass, J. T. Miller, Y. Wu, *Nat. Commun.* **2018**, *9*, 1–8.

[158] Z. Li, Y. Cui, Z. Wu, C. Milligan, L. Zhou, G. Mitchell, B. Xu, E. Shi, J. T. Miller, F. H. Ribeiro, Y. Wu, *Nat. Catal.* **2018**, *1*, 349–355.

2

A simple and efficient device and method for measuring the kinetics of gas-producing reactions‡

‡ Parts of this work have been published as:

A simple and efficient device and method for measuring the kinetics of gas-producing reactions.

T. K. Slot, N. R. Shiju, G. Rothenberg, *Angew. Chem., Int. Ed.* **2019**, *58*, 17273–17276.
T. K. Slot, N. R. Shiju, G. Rothenberg, *Angew. Chem.* **2019**, *131*, 17433–17436.
DOI: 10.1002/anie.201911005

This work is also featured in a short film, see
https://youtu.be/LLLt6zXl57c

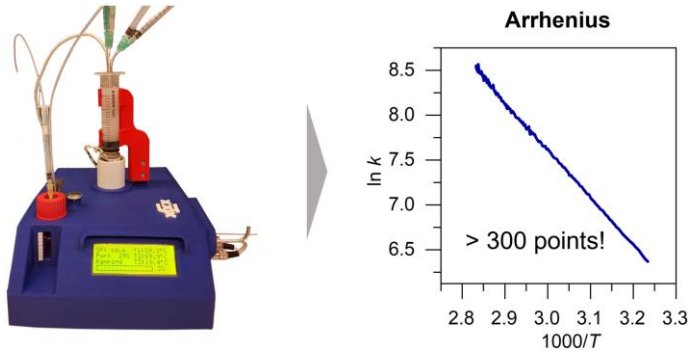

Bursting the bubble: Quick, easy and accurate Arrhenius plots from a single experiment.

Abstract: *We present a new device for quantifying gases or gas mixtures based on the simple principle of bubble counting. With this device we can follow reaction kinetics down to volume step sizes of 8–12 µL. This enables the accurate determination of both time and size of these gas quanta, giving a very detailed kinetic analysis. We demonstrate this method and device using ammonia borane hydrolysis as a model reaction, obtaining Arrhenius plots with over 300 data points from a single experiment. Our device not only saves time and avoids frustration, but also offers more insight into reaction kinetics and mechanistic studies. Moreover, its simplicity and low cost open opportunities for many lab applications.*

Measuring the kinetics of chemical reactions is common in many laboratories. Knowing the reaction kinetics gives us insight into the system as it moves towards equilibrium. It is essential for testing hypotheses, for understanding reaction mechanisms, and for designing and optimising chemical processes.[1–3] Yet despite its importance, the task itself is often mundane, time-consuming, and labour-intensive. This is especially true when determining the temperature-dependence of rate constants, which requires multiple sets of multiple measurements. When dealing with reactions that produce gaseous products, the quantification of gas production at the bench is a hassle. This can be solved using on-line gas chromatography (GC) or mass spectrometry (MS). But since these instruments are expensive, and require long calibration procedures, the most commonly used method today is still the trusted upside-down glass burette.[4–9] This requires only a beaker, a burette and some water. However, the results are less accurate, and the measurements are still time-consuming and labour-intensive.

While studying hydrogen evolution from ammonia borane hydrolysis for MAX-phase supported metal catalysts, we were faced with the task of measuring the temperature dependence of rate constants of a series of catalytic reactions. Rather than slog our way through numerous calibration experiments and repetitions,[10] we developed a simple and efficient bench-top device that automates this analysis. Unlike the upside-down burette, our device measures the development and passage of gas bubbles rather than the displacement of water. As the same device also controls the reaction temperature, it enables a fast and accurate measurement of Arrhenius relations, giving hundreds of data points from a single experiment.

2.1 Theory of bubble formation

Here we present the theoretical and physicochemical foundation for this new device and method. We then show how you can build it and compare its performance to the classic analysis methods. Finally, we show its application in the derivation of Arrhenius relations for the hydrolysis of ammonia borane in the presence of Ru/C catalysts as a model reaction. The detailed design and construction parameters are included in the appendix of this chapter.

When a chemical reaction gives a gaseous product, the number of gas molecules released is directly proportional to the reaction progress. If these molecules are released into a liquid, they will form bubbles. The size and the shape of these bubbles depend on several factors, including the viscosity of the medium, its surface tension, temperature and pressure.[11–13] If the gas is released from a nozzle, we can identify two distinct stages: the formation of the bubble (static stage) and the rising of the bubble (dynamic stage). When a bubble is forming at a gas-liquid interface, the pressure that is needed to extend the bubble is related to the radius of that interface. This is the so-

called *Laplace pressure* (Eq. 2.1).[14] Here, r is the radius of the bubble, γ is the surface tension and Δp is the pressure difference inside/outside the bubble.

$$r = \frac{2\gamma}{\Delta p} \tag{2.1}$$

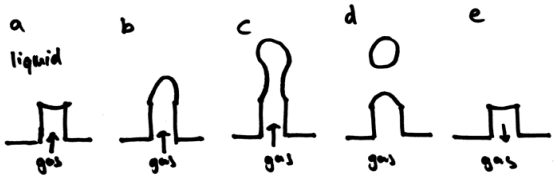

Figure 2.1. The five stages of bubble formation at a gas/liquid interface: (**a**) starting situation, (**b**) expanding of the gas/liquid interface, (**c**) neck formation, (**d**) separation of the free bubble and (**e**) reflow of gas to minimize surface tension.

As the bubble extends, the interface area will increase, and the bubble will fill with gas until its buoyancy force exceeds the surface tension at the nozzle end. When this happens, the bubble will start stretching (Figure 2.1**b/c**). A "neck" then forms, and eventually a division occurs, minimising the surface tension and resulting in a free bubble and a new gas-liquid interface at the nozzle (Figure 2.1**d**). The excess energy of the interface causes some of the gas to flow back, in equilibrium with pressure of the gas in the reactor (Figure 2.1**e**). This completes the cycle, which can then repeat with a new bubble.

When a bubble forms, it quickly accelerates and approaches a terminal velocity, given by the Stokes equation (Eq. 2.2).[15] Here, g is the acceleration due to gravity, d_e is the equivalent bubble diameter (*i.e.*, the diameter of a sphere with same volume as the bubble), μ_l is the dynamic viscosity of the liquid, ρ_f is the density of the liquid and ρ_g the density of the gas.

$$\frac{1}{18}\frac{g{d_e}^2(\rho_f - \rho_g)}{\mu_l} \tag{2.2}$$

Our bubble counter detects the bubbles using a laser beam. Each bubble passes through the beam, scattering/reflecting the photons, and thereby changing the response at the detector. Ideally, we want to measure the bubbles at their terminal velocity, because then we can use the passing velocity as a measure of bubble size. For this, the bubbles must travel straight across the beam. However, this rarely happens. Bubbles deviate from the centre of the cylinder and oscillate or spiral upward.[16] We can control this trajectory by decreasing the cylinder radius. This will force the bubble to the centre as long as there is enough space for liquid to counter flow. If the radius is too small, however, a slow Taylor flow forms, which is unfavourable. We chose a cylinder

diameter of 28 mm which gives enough room for a convectional flow pattern as well as for detecting the bubbles.

2.2 Quantifying gas production by bubble counting

To detect the bubbles and quantify their volume, we designed and built a device comprised of a temperature-controlled reactor and a detection cell (Figure 2.2, see the appendix for a detailed description). The reactor is equipped with additional needle ports for injecting reactants. The detection cell is a glass cylinder filled with liquid and fitted with a gas entry nozzle. This device can run both isothermal experiments as well as slowly ramping up temperature to a fixed set point (0–10 °C min^{-1} ramp rates). A purge gas equalizes the pressure before injection of the reactant. This avoids lag periods before the first bubble appears. For every bubble the device logs three values: the time the bubble crosses the beam, the sample temperature and the beam interruption time.

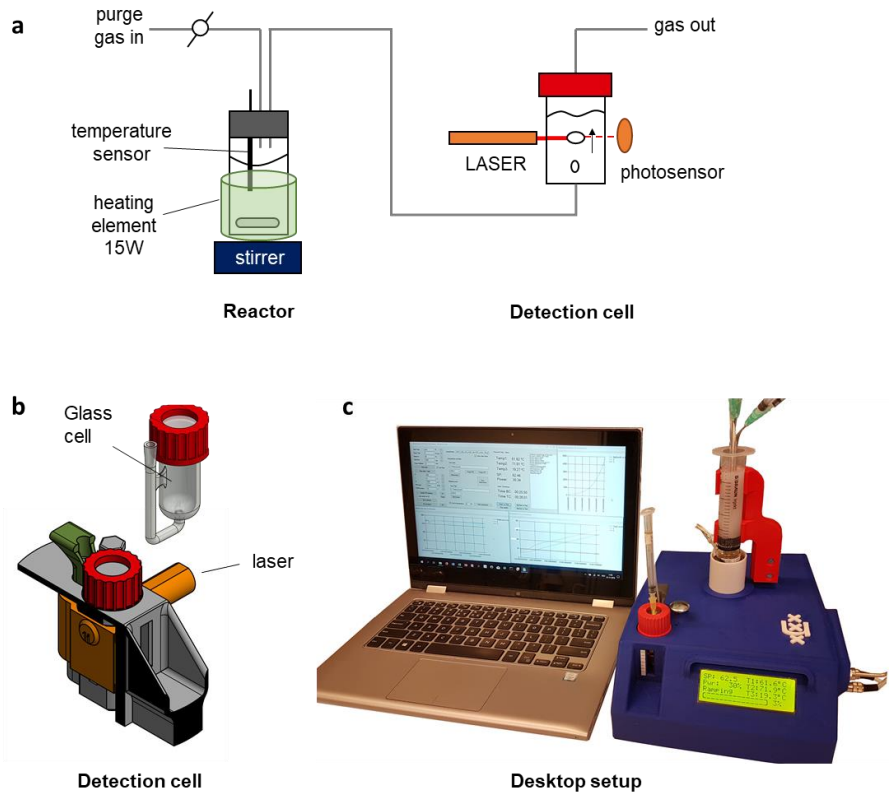

Figure 2.2. The bubble counting device: (**a**) schematic showing the reaction chamber and the detection cell, (**b**) an orthographic projection of the detection cell and its housing, and (**c**) a photo of the system in action.

Bubble formation in liquids depends on the density and the viscosity of both the gas- and liquid phases as well as on the interfacial tension.[17] Ideally, we want the gas bubbles to be as small as possible. Decreasing the nozzle size gives smaller bubbles, but also increases the Laplace pressure (Eq. 2.1). This pressure builds up until a "train" of small bubbles escapes the nozzle. The trade-off between pressure and bubble size forced us to find an optimum size where the bubbles are basically just large enough to escape from the nozzle one by one. Choosing the right solvent here is important. With the radius of the nozzle fixed, we can only influence the bubble volume by changing the surface tension of the liquid. This also changes the viscosity, and with it the upward speed of the bubbles. We chose *n*-hexadecane as our detection liquid, based on its low surface tension (27.6 mN m^{-1}), high boiling point (287 °C), low viscosity (3.45 mPa s) and availability. In general, the liquid should be chosen based on the application. The detection cell can only process a certain number of bubbles per second. This determines the maximum flowrate through the cell. If you need a higher flow rate, you can choose a solvent with high surface tension and correspondingly a larger volume per bubble.

We observed that the bubbles become larger at higher flow rates. To ensure accurate quantification throughout a range of flow rates we used a calibration curve correlating the average bubble volume with flow velocity (see the calibration details plus Figures A2.7 and A2.8 in the appendix). With this calibration, our measurements are accurate up to flow rates of 12 mL min^{-1}. One important advantage over other techniques such as gas chromatography and mass spectrometry is that our method has practically *no lower limit* of detection. The bubble formation can take as much time as needed, allowing us to monitor very slow reactions over the course of several hours/days. Bubble formation is only limited by gas molecules dissolving into the detection liquid and subsequently diffusing through the solution. Our device can detect flow rates as low as 5 μL min^{-1} without any problems. Moreover, changing gases does not influence the bubble volume (Figure A2.6**d**, in Appendix).

$$NH_3BH_3 + 4H_2O \xrightarrow{1\ wt\%\ Ru/C} NH_4^+ + B(OH)_4^- + 3H_2 \qquad (2.3)$$

To test the experimental accuracy of our device, we used the ruthenium-catalysed hydrolysis of ammonia borane to ammonium borate and hydrogen (Eq. 2.3) as a benchmark reaction. This simple reaction proceeds to completion within 30 min at ambient temperature in the presence of catalytic Ru/C, giving no side products.[18–20] Figure 2.3 compares the cumulative bubble volumes for our device and a control experiment under identical conditions using an upside-down burette. Each reaction was repeated in triplicate. In the control reaction, we measured 100 points, which is highly labour-intensive. The automated device measured at the same time no less than 3000 points with high reproducibility.

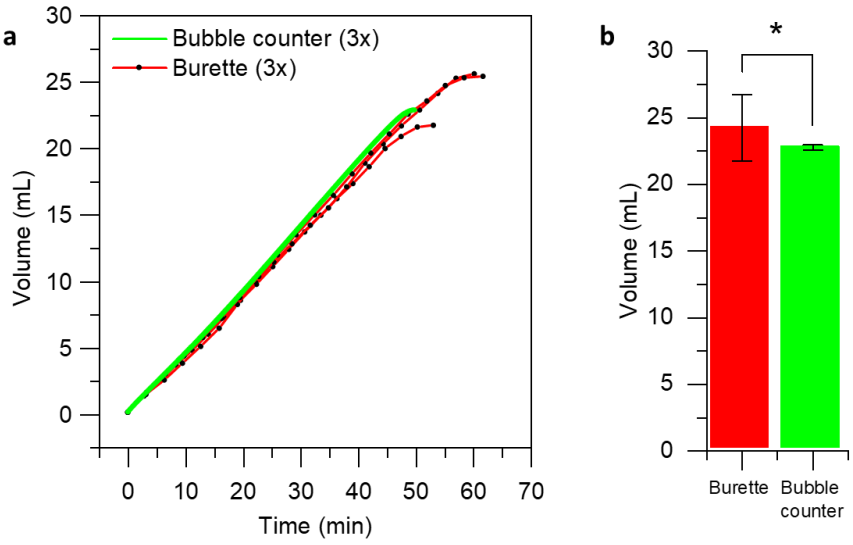

Figure 2.3. (**a**) Total volume versus time for burette method and bubble counter method. Reaction conditions: ammonia borane (0.40 mmol) in water (6.4 mL), 5% Ru/C (2.0 mg) under stirring (1000 rpm) at 23 °C and (**b**) the final volume measured using a burette and the bubble counter with 95% confidence intervals.

2.3 Towards Arrhenius plots

In addition to measuring many data points, our new device can heat the sample under a tightly controlled ramp, enabling the monitoring of reaction kinetics at different temperatures. This means that we can obtain Arrhenius plots with hundreds of data points, allowing accurate determination of activation energies within a few kJ mol^{-1}. Reaction enthalpies or entropies can then be estimated using the Eyring-Polanyi equation.[21–24]

Figure 2.4 demonstrates the power of this new device on the catalytic hydrolysis of ammonia borane (Eq. 2.3). Note that the detailed Arrhenius plot has been produced from *a single experiment* of 30 min. We obtained an activation energy of 79 kJ/mol which is in accordance with the published value of 76 kJ/mol.[25] Repeated experiments gave a confidence interval for activation energy of ± 1.6 kJ/mol. The large number of data points also allows us to study transport phenomena, as well as changes in the rate-determining step. Figure 2.5 shows an example of a 5% Ru/SiO_2 catalyst that shows nonstandard Arrhenius behaviour: At low temperatures, we see a clear induction period where the catalyst is activating. After this activation period, the reaction displays a linear Arrhenius relationship.

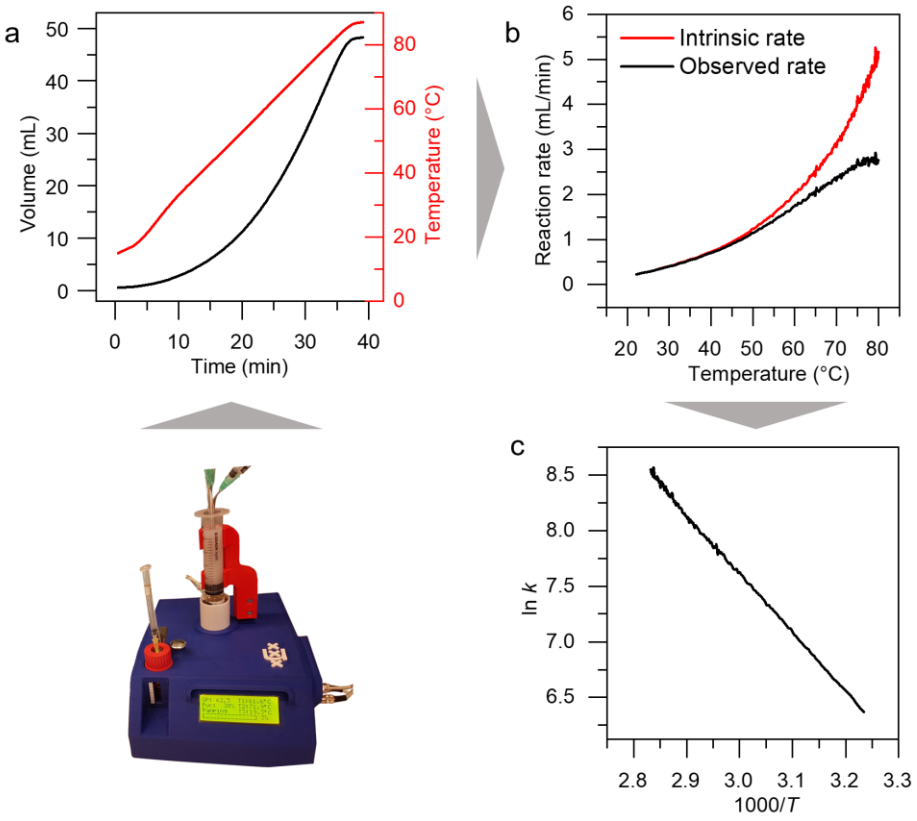

Figure 2.4. Processing of volume data from the hydrolysis of ammonia borane into an Arrhenius plot: (**a**) cumulative volume versus time, (**b**) reaction rate versus temperature, and (**c**) the resulting Arrhenius plot of ln k versus 1000/T with 300 data points, each an average over 10 measurements.

2.4 Conclusions

The new device described in this communication enables the monitoring of chemical reactions giving gaseous products. It is simple, accurate, safe and robust, and allows the quantification of reaction kinetics with high accuracy. Moreover, it can be used for determining temperature/rate relationships and calculating Arrhenius and Eyring parameters quickly and efficiently. The large number of data points per reaction (typically thousands of measurements) enables a thorough statistical analysis and opens opportunities for observing and deriving subtle physicochemical changes that hitherto were not accessible. We hope that the simplicity of this device (it costs < € 250) and its general availability (the CAD files for 3D printing of the parts and all the technical specifications are included in the appendix) will encourage scientists to use it in their labs.

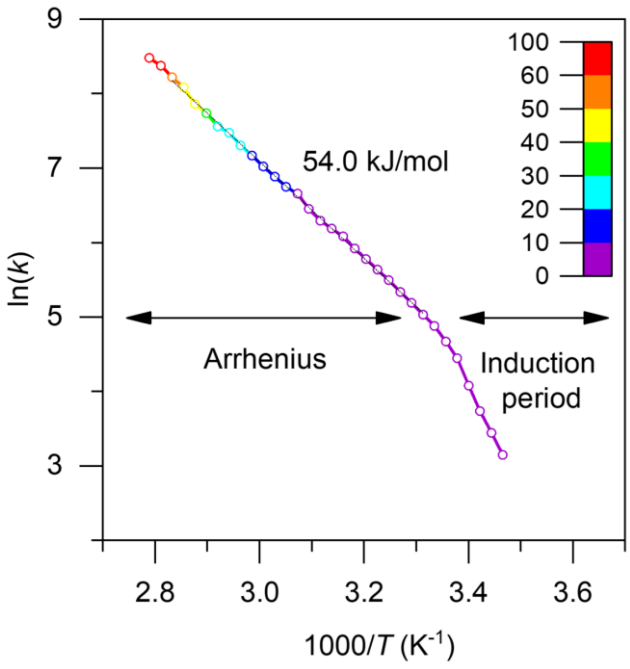

Figure 2.5. Arrhenius plot of the hydrolysis of ammonia borane catalysed by 5% Ru/SiO_2, corrected with a pre-measured reaction order of 0.35. Conversion is represented by a colour scale. For clarity, the graph shows only 30 data points. The actual number of data points in this experiment is 300, each of which is an average of roughly 20 measured bubbles (3000 raw data measurements in total).

2.5 References

[1] J. Shan, F. R. Lucci, J. Liu, M. El-Soda, M. D. Marcinkowski, L. F. Allard, E. C. H. Sykes, M. Flytzani-Stephanopoulos, *Surf. Sci.* **2016**, *650*, 121–129.

[2] J. Tang, L. Zhu, X. Fu, J. Dai, X. Guo, C. Hu, *ACS Catal.* **2017**, 7, 256–266.

[3] H. F. M. Boelens, D. Iron, J. A. Westerhuis, G. Rothenberg, *Chem. – Eur. J.* **2003**, 9, 3876–3881.

[4] Q. Wang, F. Fu, A. Escobar, S. Moya, J. Ruiz, D. Astruc, *ChemCatChem* **2018**, *10*, 2673–2680.

[5] L. Wang, H. Li, W. Zhang, X. Zhao, J. Qiu, A. Li, X. Zheng, Z. Hu, R. Si, J. Zeng, *Angew. Chem. Int. Ed.* **2017**, *56*, 4712–4718.

[6] C.-Y. Peng, L. Kang, S. Cao, Y. Chen, Z.-S. Lin, W.-F. Fu, *Angew. Chem.* **2015**, *127*, 15951–15955.

[7] J. Li, Q.-L. Zhu, Q. Xu, *Catal. Sci. Technol.* **2015**, *5*, 525–530.

[8] M. Hu, H. Wang, Y. Wang, Y. Zhang, J. Wu, B. Xu, D. Gao, J. Bi, G. Fan, *Int. J. Hydrog. Energy* **2017**, *42*, 24142–24149.

[9] A. Bulut, M. Yurderi, İ. E. Ertas, M. Celebi, M. Kaya, M. Zahmakiran, *Appl. Catal. B Environ.* **2016**, *180*, 121–129.

[10] S. C. Cruz, G. Rothenberg, J. A. Westerhuis, A. K. Smilde, *Anal. Chem.* **2005**, 77, 2227–2234.

[11] A. A. Kulkarni, J. B. Joshi, *Ind. Eng. Chem. Res.* **2005**, *44*, 5873–5931.

[12] G. Q. Yang, B. Du, L. S. Fan, *Chem. Eng. Sci.* **2007**, *62*, 2–27.

[13] J. Hua, J. Lou, *J. Comput. Phys.* **2007**, *222*, 769–795.

[14] P.S. marquis de Laplace, *Traité de Mécanique Céleste*, Chez J.B.M. Duprat, **1805**.

[15] G. G. Stokes, J. Larmor, J. W. S. Rayleigh, *Mathematical and Physical Papers*, Cambridge : University Press, **1880**.

[16] A. Weber, H.-J. Bart, A. Klar, *Open J. Fluid Dyn.* **2017**, *07*, 288–309.

[17] M. Huber, D. Dobesch, P. Kunz, M. Hirschler, U. Nieken, *Chem. Eng. Sci.* **2016**, *152*, 151–162.

[18] W. Chen, Z. Wang, X. Duan, G. Qian, D. Chen, X. Zhou, *Chem. Eng. Sci.* **2018**, *192*, 1242–1251.

[19] F. Fu, C. Wang, Q. Wang, A. M. Martinez-Villacorta, A. Escobar, H. Chong, X. Wang, S. Moya, L. Salmon, E. Fouquet, J. Ruiz, D. Astruc, *J. Am. Chem. Soc.* **2018**, *140*, 10034–10042.

[20] X. Feng, Y. Zhao, D. Liu, Y. Mo, Y. Liu, X. Chen, W. Yan, X. Jin, B. Chen, X. Duan, D. Chen, C. Yang, *Int. J. Hydrog. Energy* **2018**, *43*, 17112–17120.

[21] Henry. Eyring, *Chem. Rev.* **1935**, *17*, 65–77.

[22] W. F. K. Wynne-Jones, H. Eyring, *J. Chem. Phys.* **1935**, *3*, 492–502.

[23] M. G. Evans, M. Polanyi, *Trans. Faraday Soc.* **1935**, *31*, 875.

[24] K. J. Laidler, M. C. King, *J. Phys. Chem.* **1983**, *87*, 2657–2664.

[25] S. Basu, A. Brockman, P. Gagare, Y. Zheng, P. V. Ramachandran, W. N. Delgass, J. P. Gore, *J. Power Sources* **2009**, *188*, 238–243.

[26] Ö. Metin, V. Mazumder, S. Özkar, S. Sun, *J. Am. Chem. Soc.* **2010**, *132*, 1468–1469.

2.6 Appendix

2.6.1 Technical description of the bubble counter device

The device consists of four parts: a metal bottom plate, two 3D printed mounting plates that fit on top of each other, and a cover which houses the bubble detection unit (laser and LDR) and the display. The rest of the components are installed on the bottom plate: an Arduino Uno, an Arduino Mega, one stirring motor with magnets, a gas switch valve, a 12V power supply, and the necessary connectors for both power and small signal in/outputs. Gas regulation is achieved by connecting the gas input through a Swagelok regulating needle valve (0-20 mL min^{-1}, part-code: ss-ss2-sl-bu), which is then fed to a 12V solenoid gas switch. The valve is switched by a small common emitter transistor circuit (BD135 or 2N2222) with a 500 Ω resistor between the base and the Arduino control signal (Figure 2.1, bottom right). A "flyback diode" was installed (1N4007) over the solenoid coil for safe demagnetization of the coil. From the gas switch, the gas line is connected to the reactor gas inlet. We took care to avoid creating a large void volume in the gas lines because this adds to the void volume of the reactor, which could delay bubble formation at larger volumes.

Figure A2.1 depicts different CAD projections of the device, showing the locations of the individual components in the bubble counter. The device is assembled on top of an aluminium bottom plate (grey part in Figure A2.1). A 3d-printed mounting plate (olive green in Figure A2.1) rests on top of this, which houses the solenoid gas switch (yellow part, mounted on the bottom plate in Figure A2.1), the needle valve, the electronic connectors, the 12V DC power supply, and the Arduino Uno for temperature control. The second plastic mounting plate mounts a second Arduino Mega (for bubble detection), and a stirrer motor from an IKA Topolino stirring plate (yellow in Figure A2.1). A DIN-5 connector is attached to the back of the device as an optional feature to interface with external devices.

The bubble detector assembly is integrated in the top plate (Figures A2.2 and A2.4). There is a space which fits a plastic detection-cell holder (olive green in Figure A2.4). The detection cell can be any piece of glassware that has (or can hold) an orifice at the bottom (e.g. a Teflon tube) and has a width of about 28 mm. The tubing needs to be resistant to alkanes such as hexadecane or tetradecane. We also developed a custom-built all-glass detection cell (Figure A2.3) which can be used for more corrosive detection liquids.

The laser assembly (orange in Figure A2.4) can be positioned at different heights using a M8 thread. The display (blue in Figure A2.2) is a regular 2004A display equipped with a Hitachi HD44780U display driver. This is connected to the Arduino Uno (managing temperature control) and communicates using the I^2C protocol. On newer models, an Adafruit thermocouple amplifier breakout board with a MAX31855 chip is also mounted

to extend the available sensing temperature range and to automate the calibration of the temperature sensors.

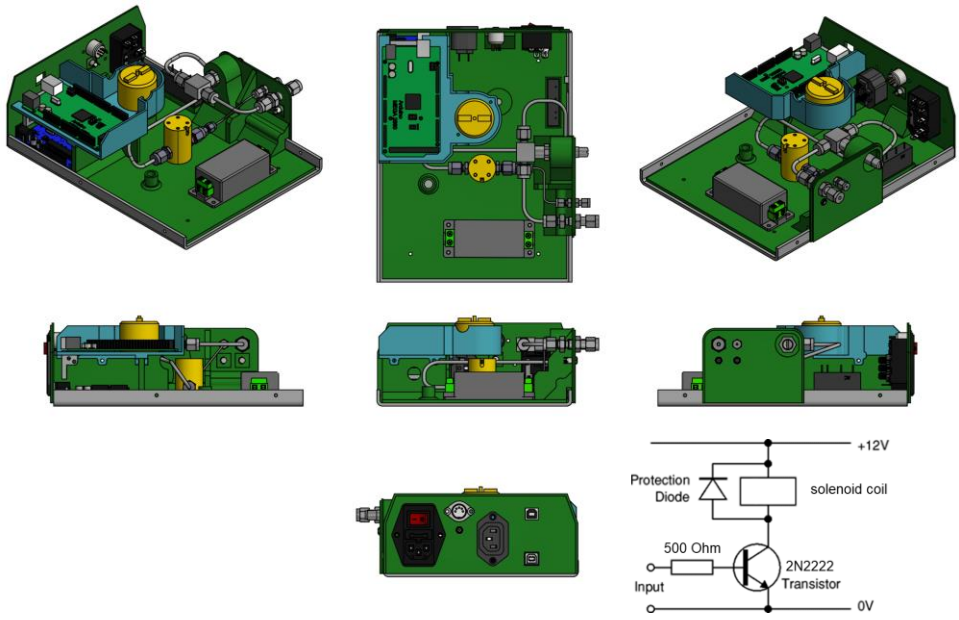

Figure A2.1. CAD views of the back plate assembly and the schematic to control the 12V solenoid coil with a 5V digital signal.

The laser can be attached to the 5V power supply from the Arduino USB port but preferably this is connected to the 12V on-board power supply using a separate voltage regulator. This is to avoid any disturbances in the reference voltage used by the analog-to-digital converters on the Arduino Uno. The laser intensity can be controlled using a current source (e.g. a simple series resistor). The light-dependent resistor (LDR) is positioned 6-8 mm from the glass cell, which is close to the focal length of the glass cylinder. We use simple inexpensive CdS LDRs. The LDR responds to a higher light intensity by lowering its resistance (photoconductivity). The response time of the LDR is enough to detect the bubbles, however, for future devices one could consider to use a silicium-based photosensor such as a SiC photodiode to register the beam interruption time more accurately.

The back of the device features several standard connections: a standard IEC Euronorm C14 power plug with fuse (1A), a female C13 socket functions to deliver power (110V) to the heating element (15W), one 3.5 mm jack plug for the heating element temperature sensor, two USB connections, a thermocouple extension, and a DIN-5 plug to interface with hotplates through the temperature control port.

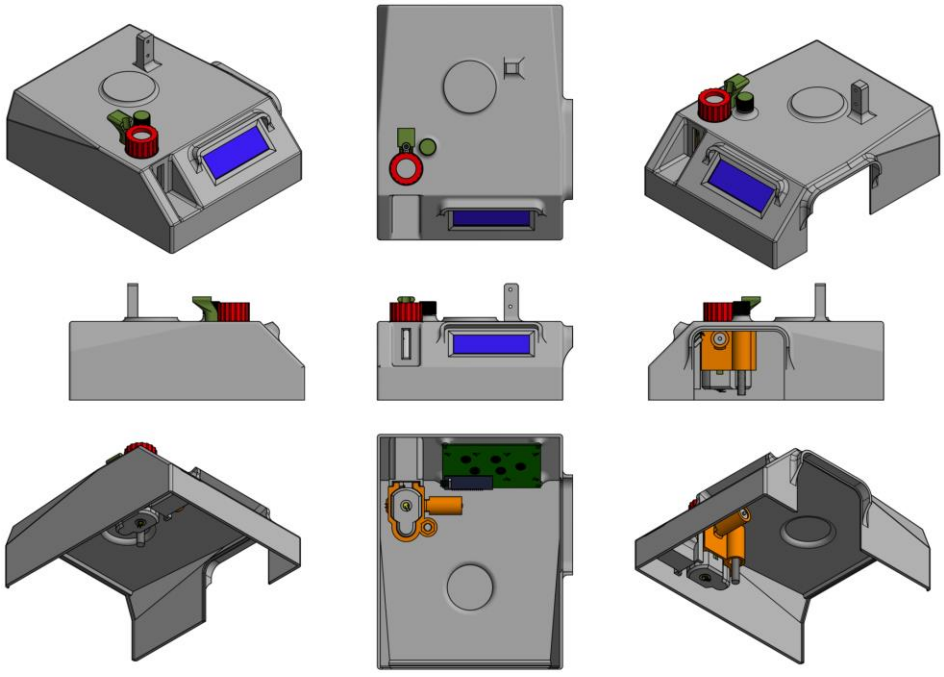

Figure A2.2. CAD views of the cover assembly.

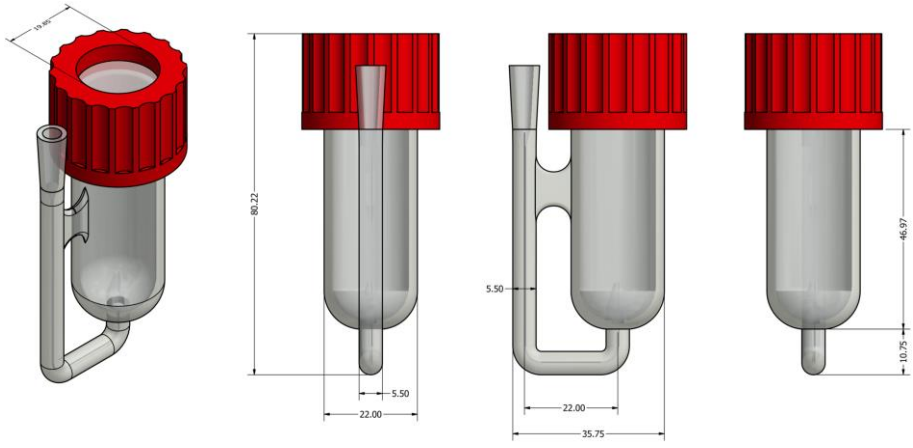

Figure A2.3. CAD views of the all-glass detection cell. Dimensions are in mm.

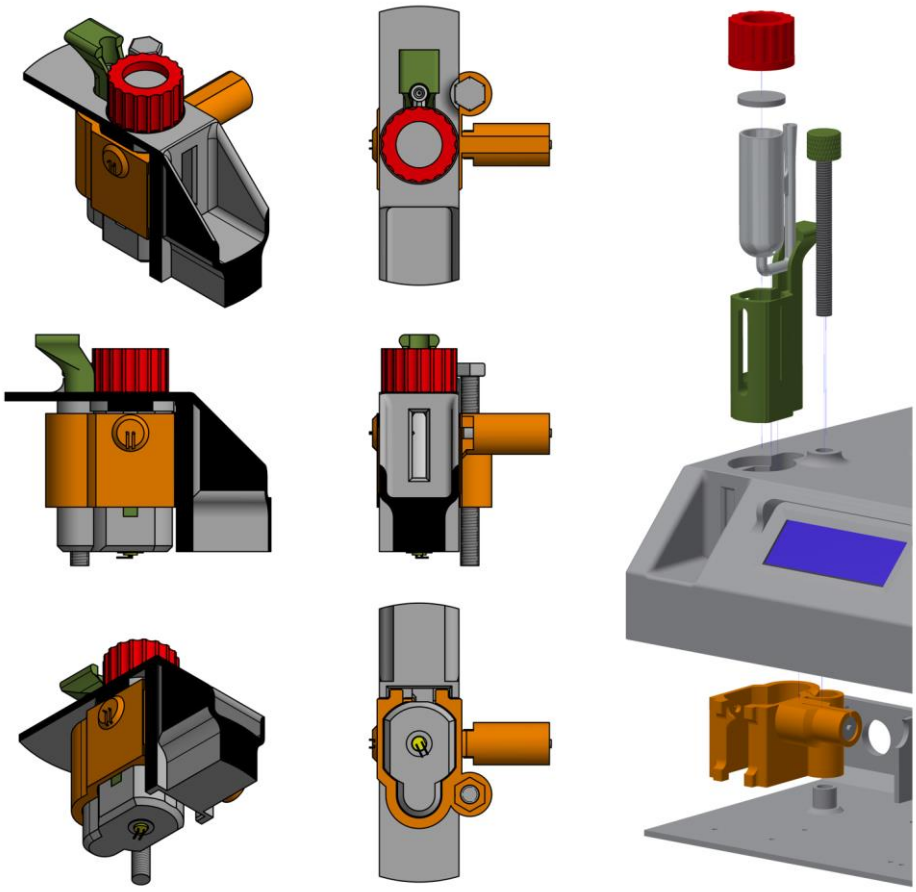

Figure A2.4. CAD views of the detection cell assembly prepared by a cut-out view from the cover assembly. The black regions represent cuts in the cover material. An exploded view of the detection cell is shown on the right.

2.6.2 Reactor head construction

The glass reactor vial is screwed into the so-called "reactor head". A photo of one such reactor head is shown in Figure A2.5**i**, where it is screwed on top of a reactor vial. The function of the reactor head is to create a gastight connector between the reactor and the gas/liquid connections, and to support the reactor above the magnetic stirrer. It can be manufactured from simple disposable materials found on a lab: four 0.8 × 120 mm needles, one 20 mL syringe (BD), one glass Pasteur pipette and a cap to the 10 mL reactor vial. The needles function as ports for inserting or extracting liquids or gasses: two gas ports and one or two capillary syringe ports are available. Video footage of the procedure is available upon request at the author.

The reactor head was homebuilt using the following step-by-step procedure: First, a 10 mL vial cap was drilled (Figure A2.5**a**) to fit a glass Pasteur pipette. This pipette was fused at the tip while making sure the NTC thermosensor fits in the glass pipette before mounting it. Then, 4 holes of 0.8 mm in diameter were drilled next to this central bore. These holes fit the long green needles (120 mm) that function as gas ports (Figure A2.5**a**, inset). It is essential that burrs are removed from the inside of the cap. One way this can be achieved is by pushing the burrs out from inside the cap using the Pasteur pipette. Another way is to use a heated Pasteur pipette to widen a slightly undersized hole. The needles used as gas ports were bent in 100-120° angles. This bend will greatly improve the torsional resistance of the needle, when glued, which avoids leaks (Figure A2.5**b**). The ports for a glass or metal capillary cannot be bent in sharp corners. So for those needles, a very shallow corkscrew bend was applied. All needles plus the closed glass pipette were aligned and fixed in place by a bit of sticky tape above the "nick" of the pipette (Figure A2.5**c**). Then, everything below this nick was rinsed with acetone to remove any dirt and oil residues from touching.

Epoxy resin was mixed (about 5g) and was applied at the top of the cap and the glass pipette, fixing the needles in place (Figure A2.5**d**). The epoxy glue binds the cap to the pipette, seals off any openings and leaves a smooth surface to which the silicone can form a good seal. The glass vial was screwed on the vial before gluing. This helps to calibrate the height of the closed glass pipette. The closed pipette should be positioned 2 mm above the bottom surface of the vial. The rubber seal will add another 2-3 mm of clearance to fit the stirring bar (8 × 3 mm) under the glass tube. The epoxy resin was applied and the glue was left to harden while rolling on the roller bench ensures an even distribution of glue. Any spills were removed with acetone within 2 min of producing them. The epoxy resin hardened to touch in about 30 min.

Sealing

Then, a 20 mL BD syringe was cut axially at the 0.3 mL mark and slid over the cap to form the outside of the reactor head (Figure A2.5**e/f**). Silicone rubber (Resion Resintechnology, the Netherlands, SR1040A, 1kg) with a Shore 40 hardness was used as a sealant. It was prepared (about 15-20 g in total) by mixing two components in a ratio of 1:10 in a wide beaker. The mixture was degassed under vacuum (at room temperature) for 10 min (Figure A2.5**g**). The silicone mixture was then carefully poured into the space between the syringe and the glass pipette, making sure no silicone enters the pipette (Figure A2.5**h**). The silicone hardened overnight and excess silicone was removed using a knife/scissors. Finally, a rubber septum disk (16 × 2 mm) was prepared using a punch and installed to the inside of the cap, around the glass pipette, to yield the final reactor head (Figure A2.5**i**).

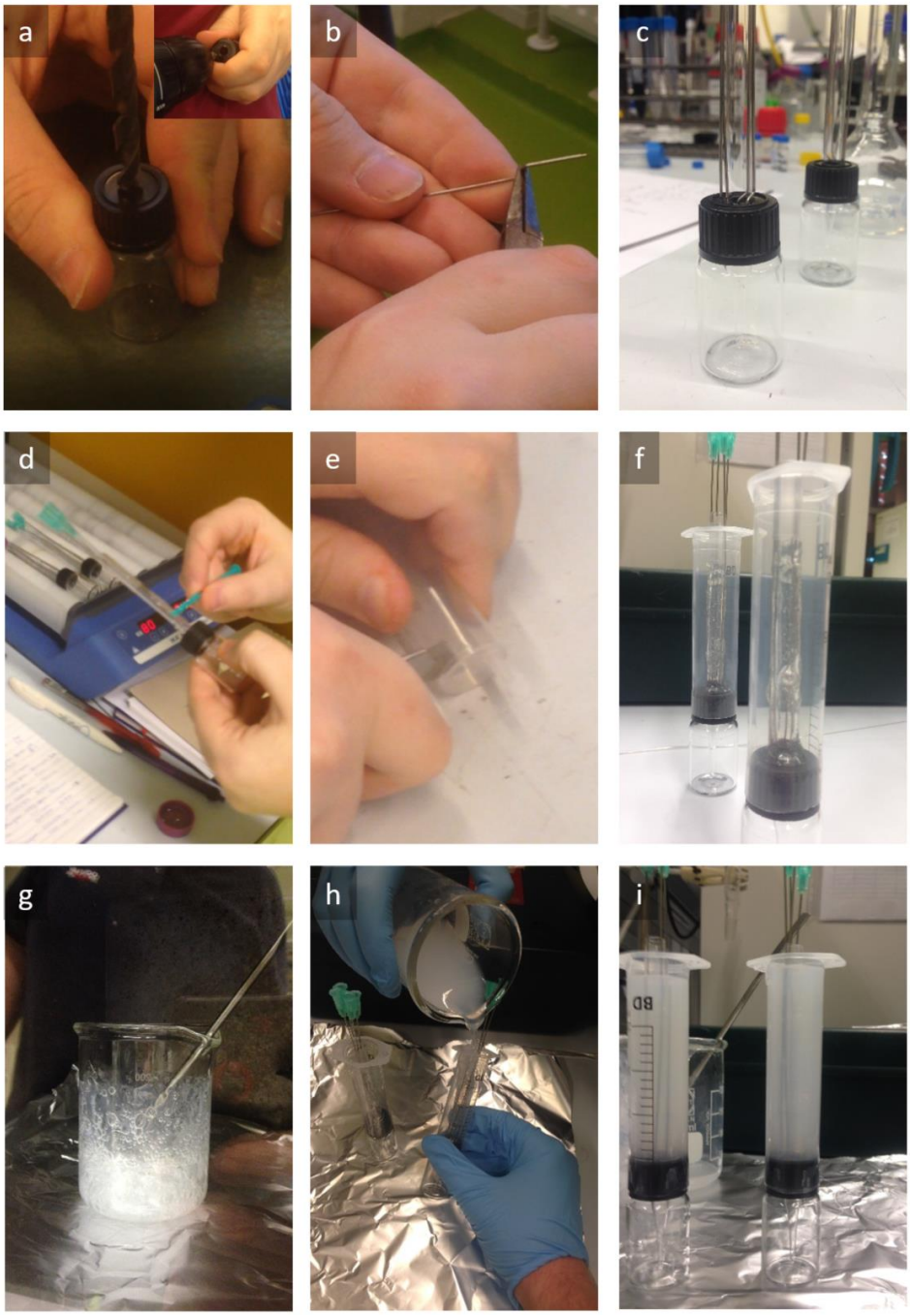

Figure A2.5. Step-by-step procedure for making the reactor head: (**a**) drilling of the cap, (**b**) bending of the needles, (**c**) inserting the closed-off Pasteur pipet and aligning the needles, (**d**) gluing with epoxy resin, (**e**) cutting a 20 mL syringe to form the housing, (**f**) fitting of the housing, (**g**) vacuum degassing of the silicone rubber, (**h**) pouring of silicone, and (**i**) the finished product.

2.6.3 *Experimental details*

General

All chemicals used in this study were purchased from commercial sources (>97% pure) and used as received: ammonia borane (>97%, Sigma Aldrich, 682098, 1g), *n*-hexadecane (Fluka AG, Buchs SG, 138722, 1L), and 5% Ru/C (Alfa Aesar GmbH, 11748, 5g). The device housing and internal parts were printed on a Creality CR-10 3D printer using (poly)lactic acid (PLA, purchased from 123-3D.nl). Design files are available from the authors upon request.

Catalyst preparation

5% Ru/SiO_2 was prepared by wet impregnation: SiO_2 (100 mg, Grace Davison) was combined with a solution of $RuCl_3 \cdot H_2O$ in water and evaporated to dryness on an oil bath (85 °C) under continuous stirring. The resulting sample was dried in an oven at 120 °C for 2 h after which the sample was reduced with 10% H_2/N_2 at 400 °C for 1h (ramp rate: 5 °C min^{-1}).

Sample preparation for catalytic testing

The catalyst, 5% Ru/C (2.5 mg), was suspended in water (6 mL) inside a glass reactor (10 mL), and was ultra-sonicated for 5 s. The reactor was attached to the reactor head which allows gasses and liquids to enter and leave the reactor through several syringe ports. The heating mantle was adjusted so it does not reach above the liquid level inside the reactor. The temperature sensor was inserted in the glass tube, and both the purge gas *inlet* line and the gas *outlet* were attached. The remaining ports were closed off. The reactor was stirred (400 rpm) and allowed to purge with nitrogen at a flow of 2-5 mL min^{-1} for 5 min prior to starting a measurement.

Procedure for isothermal hydrolysis of ammonia borane

Ammonia borane (2 M aq. soln., 0.40 mL) was loaded into a syringe equipped with a glass capillary that reaches into the reactor. The catalyst (2 mg) was suspended in water (6.0 mL) and an 8 × 3 mm stirring bar was added. The capillary was directly inserted into the liquid through one of the syringe ports. All remaining ports were closed. The reactor was then purged using a flowrate of 5 mL min^{-1} for 5 min. During purging, the reactor was heated to the reaction temperature after which the purging was stopped. After 5 seconds, the reactant was injected, resulting in some bubbles forming due to volume displacement. The gas production was then recorded until no more gas was being produced.

Procedure for non-isothermal hydrolysis of ammonia borane

Ammonia borane (2 M aq. soln., 0.40 mL) was loaded into a syringe equipped with a glass capillary that reaches into the reactor. The catalyst (2 mg) was suspended in water (6.0 mL) and an 8 × 3 mm stirring bar was added. The capillary was directly inserted into the liquid through one of the syringe ports. All remaining ports were closed. The reactor was then purged using a flowrate of 5 mL min^{-1} for 5 min. During purging, the reactor was heated to the initial reaction temperature (often room temperature) after which the purging was stopped. After 5 seconds, the reactant was injected, resulting in the formation of some bubbles due to volume displacement. The gas production was then monitored until no more gas was produced. Five seconds later, a ramp of 2 °C min^{-1} was initiated. The sample was heated to 85 °C and held there for 5 min. Then the purge gas was turned on and heating was stopped. The sample was allowed to cool down to room temperature while being purged with gas.

Bubble size calibration

Initially we tried to calculate bubble size from the beam interruption time (BIT). Unfortunately, the BIT was highly dependent on surface tension, viscosity (Figure A2.6**b**), laser height (Figure A2.6**c**) and beam alignment, allowing for large variances in the BIT time. We observed that the flowrate has a large influence on the average bubble volume. The alternative was using the time between bubbles (a measure of flow rate) to estimate bubble size.

We calibrated the bubble counter by extruding 5 mL of air at different flow rates. A syringe pump was equipped with a calibrated glass syringe was used as a gas source. This calibration revealed a linear correlation between bubble volume and flowrate (Figure A2.7**a**). However, when plotted against flow rate in 'bubbles per second', we obtain a better linear relationship with a critical point at a flowrate of 12 mL s^{-1}. (Figure A2.7**b**). We hypothesize that above these flowrates there is more hydrodynamic drag, allowing the bubbles to collect more gas and grow larger. In other words, the convectional flow inside the detection cell cannot keep up in this high-flow regime. Based on this data, we defined an upper detection limit for hexadecane at 12 mL min^{-1}.

One additional reason for choosing the units in bubbles per second is that this can be easily determined from the time between bubbles. The inverse of this time is the flowrate in bubbles s^{-1}. For practical purposes, we opted for a simple linear flow correction (Eq. 2.4) to only include the linear section up to 12 mL min^{-1}. However, if a large range of flowrate is necessary, the whole calibration curve can be used. For all our purposes a limit of 12 mL min^{-1} is more than enough to cover the flow rates in our experiments.

$$V(x) = c_1 x + c_2 = 0.14314x + 7.1341 \qquad (2.4)$$

Here, c_1 and c_2 are constants and x is flow rate in bubbles per second. Volume $V(x)$ is in microliters.

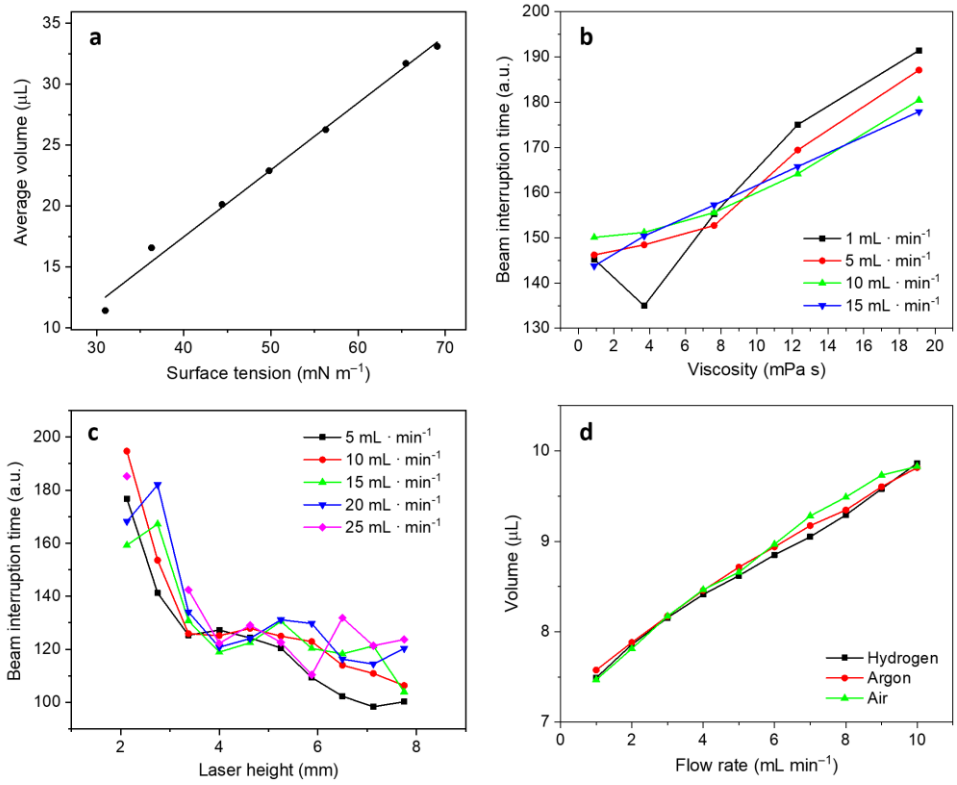

Figure A2.6. (**a**) average bubble volume versus surface tension of a range of ethanol mixtures (0-40%, *v/v*), (**b**), beam interruption time (BIT) versus viscosity, (**c**) beam interruption times (BIT) versus various laser heights, and (**d**) average bubble volume at different flow rates using gasses of different density.

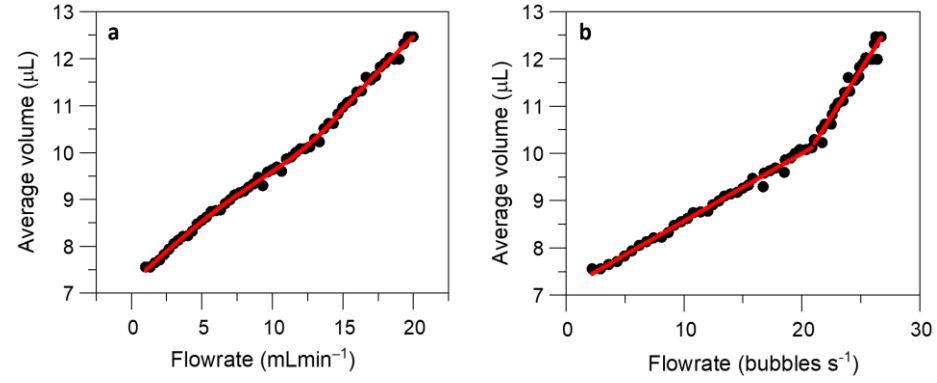

Figure A2.7. (**a**) Average bubble volume versus flowrate (mL min^{-1}) in hexadecane. (**b**) Average bubble volume versus flowrate in bubbles per second.

To verify our flow correction, we carried out additional measurements with known volumes (5 mL) at different flowrates and calculated the final volume using the flow correction (Figure A2.8). This shows that with flowrates up to 12 mL min^{-1} we obtained a final volume within 2% of the specified volume (for flowrates < 5 mL/min this was within 1%). This precision is comparable to mass spectrometry or GC. The instrumental precision of the syringe pump is unknown, so the actual instrument precision might be better.

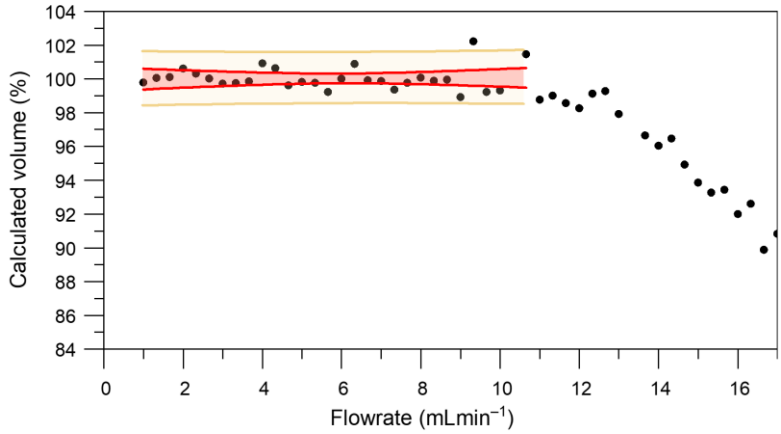

Figure A2.8. Flow-corrected volume (as percentage of the original volume) versus flowrate. The 95% confidence and prediction intervals are represented in red and orange, respectively.

One disadvantage of our system is that the summing of bubbles introduces errors that become larger when larger volumes are being measured (error~ $\sqrt{n}$). To mitigate this effect, a volume meter (or burette) can be connected to the gas outlet to record only the final gas volume to correct the data obtained with the bubble counter. This makes the setup accurate, inexpensive and very versatile.

To investigate the influence of different gas types, we performed experiments with three different gasses: hydrogen, air and argon. The average bubble volume was not influenced significantly between the gasses or binary mixtures of them (Figure A2.6**d**).

Temperature calibration

Temperature data is recorded using a negative temperature coefficient (NTC, Epcos, 100K) temperature sensor, connected as part of a resistor bridge. The voltage (0–5V) is digitized by a 1024-bit analog-to-digital (A/D) converter. The NTC temperature sensors are calibrated against a reference thermocouple (K-type) every half year. The calibration data is stored in the device. We verified that the temperature measured by our device over is accurate within 0.5 °C of the temperature observed using the thermocouple.

Gas expansion and solvent correction

In non-isothermal experiments, the gas above the liquid will expand with increasing temperature and generate extra bubbles. Also, the solvent contributes a vapour pressure that contributes to this effect. For water (7 mL), this accounts for roughly 2 mL of gas over one experiment (Figure A2.9). This volume constitutes about 5-6% of the amount of gas produced in a regular ammonia borane hydrolysis experiment.

Every non-isothermal measurement is corrected using the appropriate solvent blank experiment. The resulting curve is a linear combination of a linear function, representing the ideal gas law, and an exponential function for vapour pressure (Eq. 2.5). Both vapour pressure and gas expansion are dependent on temperature, yet independent of time. This allows for a temperature-based volume subtraction on the data of a non-isothermal measurement.

$$V(T) = V_{gas\ expansion}(T_c) + V_{vapor\ pressure}(T_c) = (c_1 + c_2 T_c) + c_3 e^{-\frac{T_c}{c_4}} \qquad (2.5)$$

Here, V is volume in µL and T_c is temperature in °C. The resulting data was subtracted from the reaction experimental data. All solvent blank corrections are stored in the bubble counter software so it can be easily applied to new measurements. Three types of function formats are available for solvent correction: "linExp", representing the linear-exponential for gas expansion and vapour pressure, "poly9", which represents a polynomial function of 9th degree which can be used for complex shaped curves and "manual", a n-point data subtraction for data that cannot be accurately captured using the other function formats.

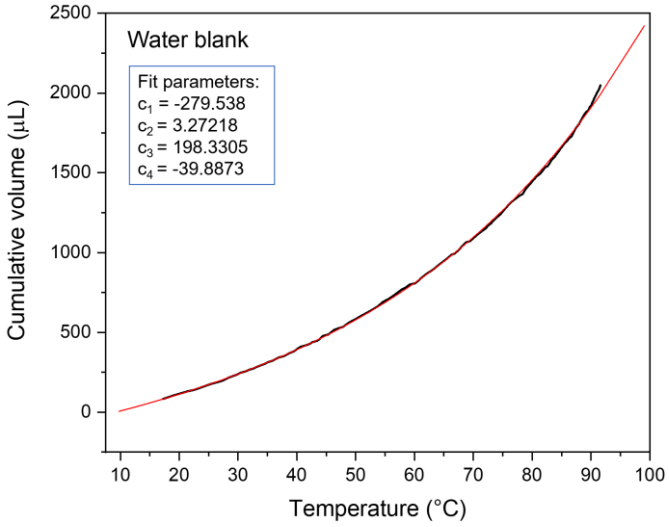

Figure A2.9: Blank measurement for gas expansion and vapour pressure of water and a fitted curve (red curve) and fit parameters using Eq. 2.5.

Calculating intrinsic rate

Ammonia borane conversion is directly related to the amount of hydrogen produced. Hence, we can use the derivative of the volume-time curve as a measure of the reaction rate. At the beginning of the reaction, the substrate concentration remains practically constant, allowing us to treat the observed rates in this area as initial rates. As the reaction progresses, we can calculate the intrinsic reaction rate from the observed rate by using a known reaction order of the reaction with respect to the substrate. (Eq. 2.6) Here, r is the observed reaction rate, k_i is the intrinsic reaction rate, $[S]$ is the substrate concentration and n is the (partial) rate order.

$$r = k_i[S]^n \tag{2.6}$$

For ammonia borane hydrolysis we obtained an order of 0.35 in ammonia borane using Ru/SiO_2 as catalyst.

Purge function

One technical feature that proved necessary for non-isothermal experiments was the addition of a purge function. As the experiment finishes, the reactor cools down and the gas in the reactor contracts. Without relief of this vacuum, this results in a transfer of liquid from the detection cell to the reactor. The purge feature prevents this by switching on the moment the reaction is finished and starts cooling down. Another advantage is that at the reactor and connected detection cell can be purged with a gas (ideally the gas that is being analysed) to equilibrate the concentrations in the detection cell and pre-load the pressure in the reactor, so bubbles are produced the moment gas starts evolving. This eliminates the initial pressurization and thus also a lead time for pushing the gas inside the detection cell. Contrary to the bubble counter device, the upside-down burette method *does* suffer from this pre-pressurization effect, resulting in a lead time that is dependent on the reaction rate of the catalyst.[26]

Bubble detection algorithm

Any sudden interruptions of the laser beam are logged by the bubble counter. The device constantly calculates an average of the background light intensity (measured by the ADC as a voltage). If the intensity of the light drops past a certain threshold, the bubble counter starts a stopwatch to record the time it takes before the light intensity is recovered. This is the beam interruption time (BIT). The moving average of background light intensity protects against false positive bubble detections caused by gradual changes in background light intensity. Bubbles always pass the laser quickly. This means that if the BIT reaches above a certain value, it can't be a bubble. We defined this threshold (safely) at 10000 (1.106 s, based on 9044 Hz counting frequency), which leads to an automatic reset of the background light level when triggered, letting the device return to baseline-monitoring mode. This protects against sudden – yet

persistent – changes to light intensity, causing the machine to wait indefinitely for the light intensity to return to normal. In practice this rarely happens as the laser intensity strongly outweighs the intensity of any outside light sources.

2.6.4 Data processing and calculation

The bubble counter saves data in two files for each experiment: one file listing the time and beam-interruption time (BIT) of the observed bubbles, and one file listing all the temperature data from the PID module. This file includes a log of all experimental actions (such changing any process variables and starting/stopping the ramp or purge gas flow). Every second the temperature data is logged into this file, so generally there is more temperature data than bubble-counting data. This extra data is used to calculate a window average of the temperature at the time a bubble was observed. As discussed earlier, we only use the time data because time between bubbles was a much better predictor of bubble volume compared to BIT.

Data merging & window averaging

The data in both files is merged using an Excel macro (VBA) or a Python script. It calculates a 10 s window average from the data when the bubble was observed. Note that with a constant ramp rate, this will have no negative effect on the accuracy of the temperature average. Window averaging of temperature data reduces noise and improves temperature resolution in the resulting Arrhenius plots.

When all bubbles have been paired with temperature, the data is screened for outliers. Outliers are classified as bubbles with a BIT less than 15 or more than 500, these values can be adjusted in the macro. Small BITs are correlated with microbubbles or rare disturbances before/after a bubble. Overall, less than 0.1% of the bubble data points are rejected.

Flowrate correction

As described before, a linear flow correction is applied to the bubble counting data. This accounts for changes in bubble volume at different flow rates. The volume of the bubble is calculated using Eq. 2.4.

Processing gas-volume data into Arrhenius plots

All ‘extra’ data from bubbles caused by purging and volume displacement after reactant injection are deleted. This leaves only the gas production by the catalytic experiment.

Unless specified otherwise, processing is done as follows: First, the volume data is interpolated to reduce the number of data points. This can be done in two ways, by a window average of the data points, or by interpolating the source data at evenly spaced

points in time. Both methods have advantages and disadvantages. Window averaging has the advantage it averages the same amount of data points for each average, but, data points are not evenly spaced across the temperature axis with the majority of points ending up in the high-temperature region. Equal point spacing indeed gives an even spread of points along the temperature axis, but averages less points in the start of the reaction. For us this is not a problem, since interpolation of a cumulative volume essentially sums up all points in one interval, effectively averaging out any error in individual data points. We normally use a 50 point equal spacing algorithm, unless there is a good reason for grouping the individual data points.

Calculation

A spreadsheet is used to calculate the individual reaction functions. Table A2.1 gives a detailed description how the data is calculated. After interpolation, the volume *vs.* time data is differentiated (col **6**/**7**). Taking the derivative *vs.* temperature is not desirable because the ramp rate may not be constant in the beginning of the experiment (the first 10 °C of heating). Fractional conversion (col **10**) is calculated, based on the expected volume which in turn is based on the added amount of ammonia borane.

Table A2.1: Calculation parameters

Col	Name	Source / Calculation
1	Time (min)	Raw data
2	Beam interruption time (BIT units)	Raw data
3	Volume (µL)	Raw data
4	Volume, blank subtracted (µL)	Raw data
5	Temperature (°C)	Raw data
6	Time Interpol (min)	50 point interpolation from X=**1**,Y =**4**, X data
7	Volume Interpol (µL)	50 point interpolation from X=**1**,Y =**4**, Y data
8	Temperature interpolation (°C)	Interpolation of X=**6** in (X=**1**,Y=**5**), Y data
9	Observed rate (µL/min)	Derivative of (X=**6**, Y=**7**), vs time!
10	Fractional conversion (0..1)	1 – (**7** / maximum expected volume)
11	Intrinsic rate (µL/min)	**9** / ((1-**10**)^n) n = reaction order = 0.15 for ammonia borane hydrolysis
12	Observed rate (M/min)	**9** / constant, depending on stoichiometry of the reaction and molar concentration
13	Intrinsic rate (M/min)	**11** / constant, depending on stoichiometry of the reaction and molar concentration
14	1000/T	1000/(**8** + 273.15)
15	ln (k)	ln(**13**)

3

An experimental approach for controlling confinement effects at catalyst interfaces ‡

‡ Parts of this work have been published as:

An experimental approach for controlling confinement effects at catalyst interfaces.

T. K. Slot, N. Riley, N. R. Shiju, J. W. Medlin, G. Rothenberg,
Chem. Sci. **2020**, *11*, 11024-11029. DOI: 10.1039/D0SC04118A.

This work is also featured in a short film,
see https://youtu.be/gbfuUTw_eQ4

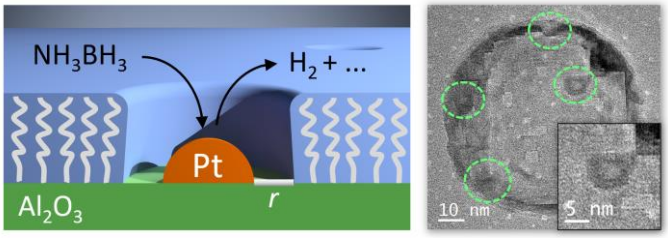

From the top: Designable materials help pinpoint the role of steric confinement in catalysis

Abstract: Catalysts are conventionally designed with a focus on enthalpic effects, manipulating the Arrhenius activation energy. This approach ignores the possibility of designing materials to control the entropic factors that determine the pre-exponential factor. Here we investigate a new method of designing supported Pt catalysts with varying degrees of molecular confinement at the active site. Combining these with fast and precise online measurements, we analyse the kinetics of a model reaction, the platinum-catalysed hydrolysis of ammonia borane. We control the environment around the Pt particles by erecting organophosphonic acid barriers of different heights and at different distances. This is done by first coating the particles with organothiols, then coating the surface with organophosphonic acids, and finally removing the thiols. The result is a set of catalysts with well-defined "empty areas" surrounding the active sites. Generating Arrhenius plots with >300 points each, we then compare the effects of each confinement scenario. We show experimentally that confining the reaction influences mainly the entropy part of the enthalpy/entropy trade-off, leaving the enthalpy unchanged. Furthermore, we find this entropy contribution is only relevant at very small distances, where the "empty space" is of a similar size as the reactant molecule (< 3 Å for ammonia borane). This suggests that confinement effects observed over larger distances must be enthalpic in nature.

3.1 Introduction

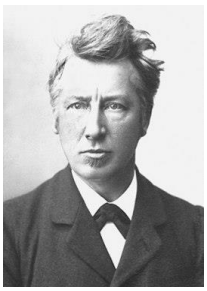

Jacobus van 't Hoff
(1852 -1911)

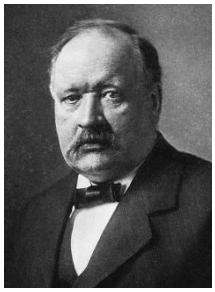

Svante Arrhenius
(1859 -1927)

In 1884, Van 't Hoff realized that an energy term is associated with every chemical transition.[1] Some years later, Arrhenius developed this further, defining the empirical relation between reaction rate and temperature in what is known today as the Arrhenius equation (Eq. 3.1). This empirical relation describes most chemical reactions well.[2] Yet though the equation itself is simple, its chemical meaning is elusive. This is especially true for the nefarious pre-exponential factor. The energy of activation typically corresponds to the barrier needed to cross the transition state threshold along the reaction coordinate. But the pre-exponential factor is somewhat of a theoretical embarrassment. All we know about it is that it comes before an exponent, and that its value is roughly 10^{12}–10^{14} s^{-1}.

$$k = Ae^{\frac{-Ea}{RT}} \tag{3.1}$$

This has not gone unnoticed. In the 1930s, Eyring and Polanyi laid the foundation for what would become transition-state theory.[3,4] They coupled both the activation energy and the pre-exponential factor to relatively simple first principles.[3,4] The Eyring equation assigns the pre-exponential factor as k_BT/h, corresponding to the frequency at which the reactants cross the transition state barrier. These models were developed further at different levels of theory, generally concluding that the predominant factor contributing to the Arrhenius pre-exponential factor is entropy.[5,6]

Yet there is a catch: The models pertain to reactions in the fluid (typically gas) phase, describing collisions between molecules in a homogeneous environment.[7] The situation is different for reactions at surfaces, where the most common mechanism follows the Langmuir-Hinshelwood pathway of reactant adsorption, surface reaction, and product desorption.[8,9] Treating the pre-exponential factor in heterogeneous catalysis as a collision frequency factor is too simplistic. In most heterogeneous catalysts, the active sites take up only a small percentage of the surface. This means that the travel of the reactants across the surface to the active site cannot be ignored.[10] Our goal is to isolate this travel step by sterically confining a reaction that follows the Langmuir-Hinshelwood pathway. By placing barriers at different distances, we hope to understand how much space a heterogeneous reaction needs in relation to the reactant's size.

3.2 Synthesizing confinement

Here, we use a novel synthetic approach to create confinement at different distances from the active site. As our benchmark reaction, we chose the platinum-catalysed hydrolysis of ammonia borane (AB, Eq. 3.2). This reaction produces large amounts of hydrogen gas even in the presence of small amounts of catalyst, whereas the background reaction (using only the γ-alumina support) is negligible. The hydrogen production is easily and accurately monitored by our novel bubble counter.[11] This device can monitor volume step sizes down to 8–12 µL, enabling a very detailed and precise kinetic analysis. Another advantage of this hydrolysis is that its partial reaction order in ammonia borane is very low (typically 0.1–0.2). This small dependence of the reaction rate on the concentration means that we can obtain reliable kinetic and thermodynamic data from a single experiment. The low partial reaction order suggests a complex mechanism. Experimental data illustrates that in such cases, the reaction still obeys the exponential Arrhenius relation. This is because the slowest reaction step(s) dictate the observed activation energy, provided there are no mass transport limitations. Ammonia borane hydrolysis follows a Langmuir-Hinshelwood mechanism, with O–H cleavage as the rate-determining step (the exact surface species is unknown).[12–19]

$$NH_3BH_3 + 4H_2O \xrightarrow[20\text{ - }85°C,\ 45\text{ min}]{Pt/Al_2O_3} NH_4^{\oplus} + B(OH)_4^{\ominus} + 3H_2 \qquad (3.2)$$

To isolate the contribution of the pre-exponential factor in this catalytic system, we prepared a series of supported Pt catalysts in stages (small Pt particles (< 4 nm) were successfully used in other confinement strategies[20,21]). First, a platinum precursor was impregnated on γ-Al_2O_3 using incipient wetness impregnation. This was then dried, calcined and reduced to give metallic Pt nanoparticles on alumina (see Figure 3.1**a** and inset in Figure 3.2). A portion of these catalysts were then coated with a monolayer of alkane thiol (Figure 3.1**b**), which functions as a template for the next step: coating the alumina support surface with organophosphonic acids (Figure 3.1**c**). The organophosphonic acids cover the entire alumina surface with a self-assembled monolayer, forming a hydrophobic coating of alkyl chains.[22–25] Finally, the thiol template was removed by reduction,[26,27] leaving a free zone around the platinum nanoparticle (Figure 3.1**d**).

This approach combines the advantages of both spatial and chemical control around the active site. We can constrain the area around the active site in two dimensions. Further, by using phosphonic acids with organic residues of different lengths, we can obtain coatings of different thicknesses. Similarly, the length of the organic residue on the thiol hypothetically dictates the radius of the resulting "free spaces" (see Figure 3.1**d**).

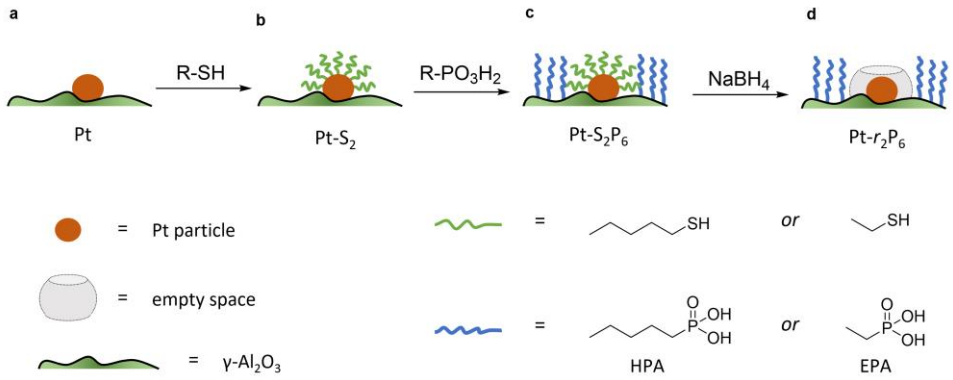

Figure 3.1. Schematic description of our Pt/Al_2O_3 catalysts, showing the stages in creating the confined space surrounding the Pt active sites. (**a**) the plain Pt/Al_2O_3 catalyst (no coating). (**b**) after coating with the organic thiol. (**c**) after coating with the organophosphonic acid. (**d**) after removal of the organic thiol.

The loading of platinum on γ-Al_2O_3 is another important factor.[28–30] On one hand, we want this loading to be as low as possible, because the particle size needs to be small compared to the coating. On the other hand, we must have sufficient Pt on the surface to have enough reactivity for monitoring the reaction. We therefore ran a series of control experiments using catalysts with different Pt loadings to test the influence of the loading on the observed energy of activation (E_a, see Figure 3.2). High loadings result in low E_a values, due to the large particle size and additional mass transfer effects. As the Pt loading decreases, the activation energy increases gradually, starting from 40 kJ mol^{-1} and levelling off towards 65 kJ mol^{-1} as the particles approach their lower size limit. At 0.05 wt% Pt we reach the "sweet spot", where the reaction rate is still high enough to observe and the activation energy remains fairly constant. Repeat experiments gave a standard deviation of only 0.8 kJ mol^{-1} in E_a, confirming the precision of our measurements. Mass-transfer effects are expected to be negligible at low Pt concentration because the particles are farther apart, reducing neighbour interference. This means that the subtle changes in activation energy are likely related to the particle's size and type of exposed facets.[31–33] Furthermore, this low loading ensures the formation of uniform small particles. We did not expect the active sites to be single Pt atoms, as the activation energy still increases when the loading is reduced even further (see point **A** in Figure 3.2).[34] This was confirmed by transmission electron microscopy measurements of the 0.05 wt% $Pt/\gamma Al_2O_3$ catalyst, which showed spherical particles, 2–3 nm in diameter (Figure 3.2, inset).

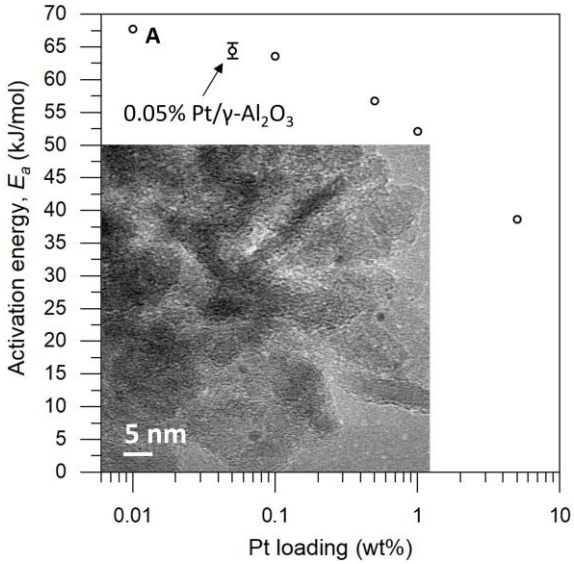

Figure 3.2. Observed activation energy versus Pt loading. Each point is an average of roughly 300 data points. Error bars denote the 95% confidence interval. Inset: transmission electron micrograph of 0.05% Pt/γAl_2O_3. Point "**A**" denotes a catalyst loading of 0.01wt% Pt/γAl_2O_3.

Next, we studied the influence of the PA coating thickness. Batches of 0.05wt% Pt/γAl_2O_3 were coated with methyl-, ethyl-, hexyl-, and octadecyl phosphonic acid (Figure 3.3). With increasing phosphonic acid length, the reaction rate decreases. The PA should be long enough to form a hydrophobic barrier, yet short enough so that it doesn't cover the Pt particle. We selected hexyl phosphonic acid (HPA) as it is sufficiently large compared to the expected Pt particle size, and has a significant influence on the reaction (it reduces the reaction rate ten-fold, see Figure 3.3). Pentane thiol was selected as the thiol. Our hypothesis was that since this thiol is roughly twice the size of ammonia borane, its removal should give ample 'empty space' for the reaction to proceed.

To prove that we can indeed make this empty space around our particle, we tested whether our catalysts would regain their normal catalytic activity after the thiol coating is removed. Figure 3.4 shows the Arrhenius plots for catalysts **a**, **b**, **c** and **d**, when using pentane thiol and hexylphosphonic acid. These plots are highly precise – each Arrhenius curve represents >3000 individual experimental measurements.[11] The turnover frequency (TOF) is calculated by dividing the reaction rate (mmol AB s^{-1}) by the metal loading (mmol Pt; the resulting TOF values and corresponding pre-exponential values are somewhat underestimated because not all Pt is available for reaction). The black curve **a** shows the Arrhenius plot for the plain Pt/Al_2O_3 catalyst. Upon binding of the thiol (**b**, red curve) the catalytic activity drops.[35–39]

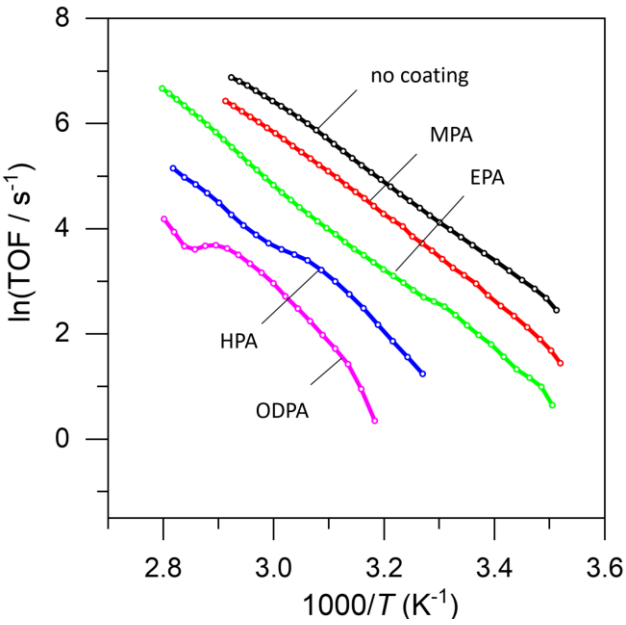

Figure 3.3: Ammonia borane hydrolysis using pristine 0.05 wt% Pt/yAl_2O_3, and coated with methyl phosphonic acid (MPA), ethyl phosphonic acid (EPA), hexyl phosphonic acid (HPA), and octadecyl phosphonic acid (ODPA).

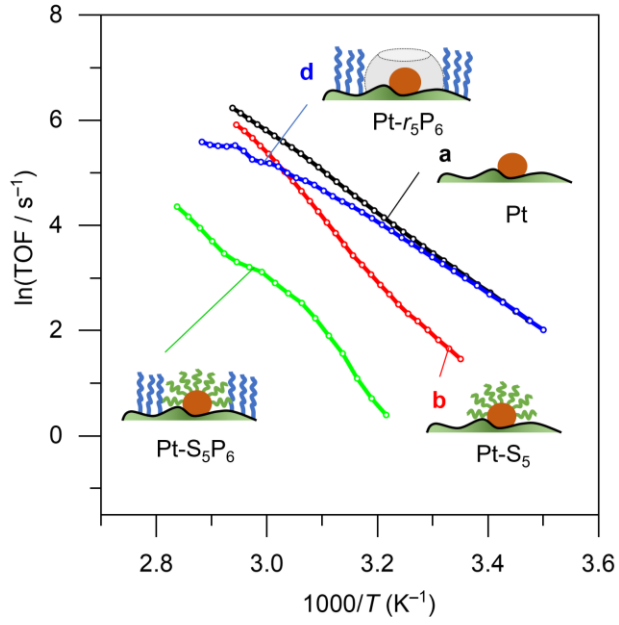

Figure 3.4. Catalytic effect of coating procedure: (**a**) 0.05% Pt/yAl_2O_3, (**b**) pentane thiol coating, (**c**) both pentane thiol coating and phosphonic acid coating and (d) the "free space"-catalyst after removal of the thiol.

At low temperature, the slope of the Arrhenius plot is similar to that of the uncoated catalyst. At higher temperature the slope seems to increase, but this is likely an artefact caused by *in-situ* thiol removal due to the reductive nature of the reaction.[40] Next, the phosphonic acid coating is applied, decreasing the catalytic activity even more (**c**, green curve). The presence of the phosphonic acid groups on the alumina surface was verified by FTIR (see Figure A3.1 in the Appendix). Finally, when we remove the thiol using a mild reduction with sodium borohydride, the catalytic activity returns to the level of the pristine material (**d**, blue curve). This supports our hypothesis of an 'empty space' surrounding the active site. Curiously, at higher temperatures the slope of the Arrhenius plot is slightly reduced compared to the uncoated catalyst (*cf.* curves **d** and **a** in Figure 3.4). This could reflect a change in activation energy, yet we expect no chemical change in the system. A more likely explanation is that the reaction rate is restricted by diffusion limitations around the active site.

3.3 How much "space" does a reaction need?

We then ran a systematic study comparing the effects of short and long thiols and short and long organophosphonic acids. Think of the organophosphonic acid as forming a fence around the space left by the thiol. These binary options result in four different catalyst combinations: {high fence, large space}, {high fence, small space}; {low fence, large space}; and {low fence, small space}. Each of these catalysts requires three synthesis steps, resulting in a total of 13 different catalysts (there are three "duplicates"; for an overview of the synthesis scheme see Figure 3.5).

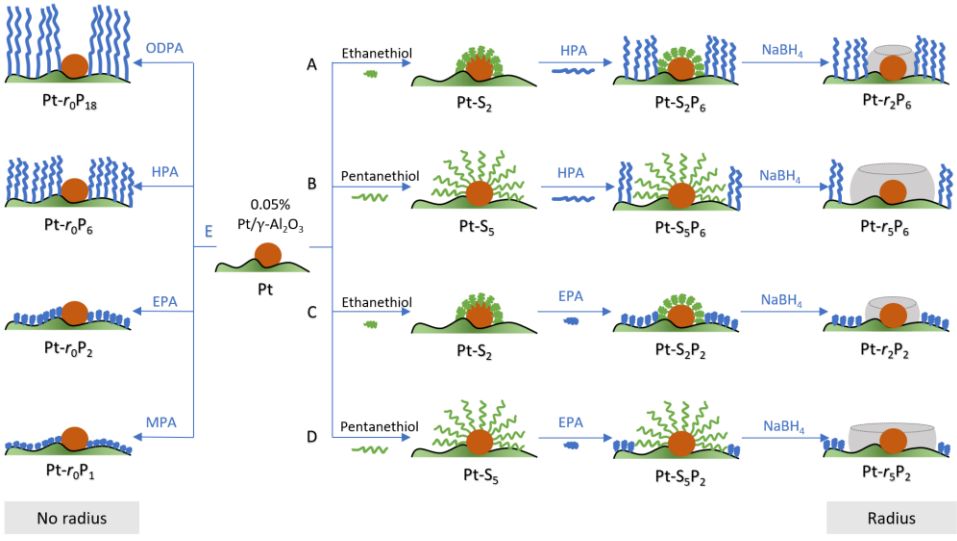

Figure 3.5: Scheme showing an overview of all prepared catalysts.

Our hypothesis was that ammonia borane will experience confinement effects differently in the four different catalyst combinations, and that these would result in different E_a and A values.

Surprisingly, there was no significant difference between the four different "free space" catalysts (*cf.* Figure 3.6, curves **b**, **c**, **d** and **e**). Ammonia borane hydrolysis was *not* hindered by any of these confinement regimes. We concluded that the hydrolysis of ammonia borane needs less than 0.5 nm of free space around the Pt active site. To test this hypothesis, we ran the reaction yet again, this time coating the Pt particles with methane thiol, the smallest thiol. The same synthesis procedure was repeated with both EPA and HPA. Interestingly, this catalyst *did* show a difference between the different "free space" combinations (*cf.* the red curve **c** with the blue and green curves **a** and **b** in Figure 3.7). Curve **d** in Figure 3.7 shows a bend that may reflect a change in activation energy, likely because of AB diffusion through the HPA tails, which become more mobile at higher temperatures.

Based on these experimental results, we can now assign a clearer chemical meaning to the pre-exponential factor for reactions at surfaces. Reactant molecules can adsorb on the surface at any random point (Figure 3.8**b**). They can then travel to the active site, where they may or may not react, depending on their energy and configuration.[41,42] The measured reaction rate is an average of these {adsorption+travel+reaction} combinations, where the direct adsorption can be seen as a pathway with zero travel.

We were able to observe these "free space" structures by transmission electron microscopy. We observed several Pt nanoparticles that are surrounded by a clear area (Figures 3.8**a** and A3.2). These structures are only observable for a few seconds, because the electron beam destroys the organic material.[43–45] The Pt particle size is about 3.9 nm and the free space has a width of about 1.2-1.8 nm. Pentane thiol has a length of about 1.0 nm, so the templating effect by the thiol is about 1.5 times larger than anticipated. Likely, the thiol tails orient incoming phosphonic acid molecules away from the alumina surface when their apolar regions bind together, accounting for the larger radius. Attempts to observe the reaction of ammonia borane hydrolysis in the confined space directly using *in situ* FTIR failed, as we could not differentiate the spectra with and without AB (data not shown). This is likely because the number of Pt-bound molecules is too small in relation to the other species present in the reaction mixture.

To probe the confinement effect even further, we ran additional experiments on the dehydrogenation of ammonia borane under water-free conditions. This reaction produces oligomeric intermediates of increasing size,[46–48] which should show a reduced reaction rate when the products start exceeding the size of the confined space. The Arrhenius plots for these reactions are curved, because of the complex mechanism

and changing rate-determining steps (Figure 3.9). Indeed, the Pt-r_5P_6 catalyst (with a radius of 5) showed a reaction activity that was better than the thiol-coated catalyst at

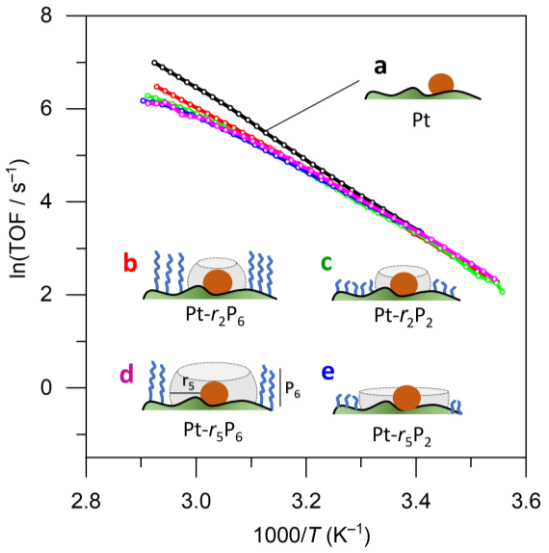

Figure 3.6. Catalytic data for (**a**) 0.05% Pt/γAl_2O_3, and coated catalysts: (**b**) large fence – small radius, (**c**) small fence – small radius, (**d**) large fence – large radius, and (**e**) small fence – large radius. Each data point represents a window average of 10-50 measurements using equal time interpolation (see supporting information for full experimental details).

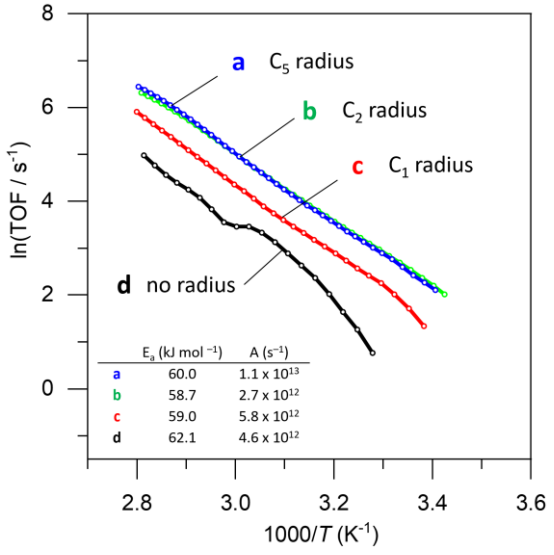

Figure 3.7. Catalytic data for free-space catalysts prepared with (**a**) pentyl-, (**b**) ethyl-, (**c**) methyl- and (**d**) no radius using HPA as surface coating. Each data point represents a window average of 50 measurements. Inset: table with activation energies and pre-exponential factors.

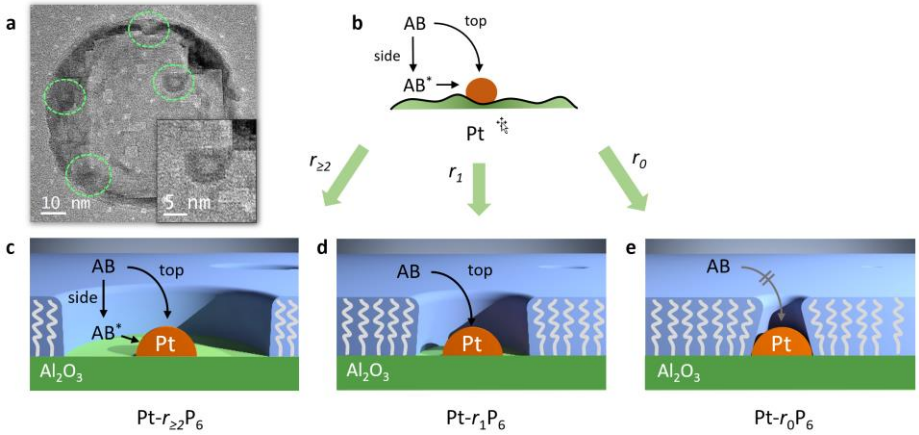

Figure 3.8. Top: (**a**) Transmission electron micrograph of the Pt-r_5P_6 confined space catalyst. (**b**) Schematic drawing of the "side approach" and "top approach" for scenarios with a varying degree of confinement, where * indicates an adsorbed species. Bottom: cross-sectioned 3D representation of (**c**) Pt/Al_2O_3 catalyst with a large free space surrounding the Pt nanoparticles, allowing for top and side NH_3BH_3 approach, (**d**) confined-space Pt/Al_2O_3 catalyst prepared with methane thiol, allowing only the top approach, and (**e**) no-space catalyst where both side and top approach are hindered.

the beginning of the reaction, but later reduced to an activity similar to that of the fully restricted catalyst, likely because of the increasing size of the reacting intermediates. These results provide additional evidence of the confinement effect.

3.4 Confinement and surface travel

Importantly, our experiments allow the direct observation of the effect of confining the active sites on the Arrhenius plot.[49] The reaction rates decrease, yet the slopes (*i.e.*, the activation energies, Figure 3.7, table inset) remain nearly identical in each case. This shows that the confinement only affects the pre-exponential factor, which reduces from $1.1 \cdot 10^{13}\,s^{-1}$ to $0.46 \cdot 10^{13}\,s^{-1}$, corresponding to a decrease in ΔS of $7.3\,J\,K^{-1}$. It doesn't change the chemical environment of the transition state. To the best of our knowledge, this is the first experimental demonstration of this effect for reactions at surfaces. If we associate the energy of activation with the reaction enthalpy, we see that the pre-exponential factor gives an entropy contribution that is closely related to the reactant's approach to the active site. We propose two pathways: "from the top" and "from the side" (see Figure 3.8**b**). In a normal (uncoated) catalyst, both pathways contribute to the catalytic activity. However, when the free space around the active site is too small for the reactant to adsorb, only the "top" pathway is possible. Our experiments allow the quantification of the distance needed for the "side" pathway. In the case of ammonia borane, a gap of roughly 0.75 nm (derived from the size of the Pt-bound EPA molecule) already allows the hydrolysis to proceed at a rate similar to that of a totally

unconstrained catalyst. Considering that the kinetic diameter of ammonia borane is similar to that of ethane (0.44 nm), and that the radius of the free space is about 1.5 times larger, this shows that the remaining gap of <3 Å between the molecule and the "fence" suffices to completely negate the confinement effect.

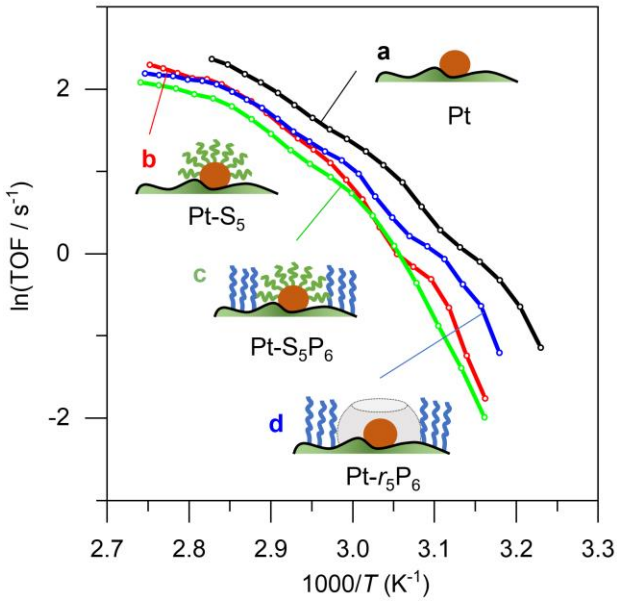

Figure 3.9: Catalytic data for the water-free dehydrogenation of ammonia borane in NMP with (**a**) 0.05% Pt/γAl_2O_3, (**b**) Pt/γAl_2O_3 with pentane thiol coating, (**c**) Pt/γAl_2O_3 with both pentane thiol coating and phosphonic acid coating, and (**d**) the "free space"-catalyst after removal of the thiol. Each data point represents a window average of 10–50 measurements using equal time interpolation (see appendix for more details).

These findings also have more general implications for catalysts that feature confinement.[50–53] Confinement effects observed for enzymes and zeolite cages (which can feature much larger gaps) are typically a trade-off between enthalpy and entropy contributions.[54,55] For example, transition states are enthalpically stabilized in tight zeolite pores, but entropically destabilized. Our experiments separate the two contributions, and show that the entropy contribution to confinement is relevant only at very small distances. This means that confinement effects observed in larger systems have a much larger enthalpy contribution.

3.5 Conclusion

The kinetics of catalytic reactions at surfaces involve four steps: reactant adsorption, surface travel, surface reaction, and product desorption. Using a new method to synthesize heterogeneous catalysts with well-defined "free space" surrounding active

metal nanoparticles at varying degrees of confinement, we created four distinct tiers of confined Pt/Al_2O_3 catalysts. We then ran precise kinetic measurements of the Pt-catalysed hydrolysis of ammonia borane, thereby isolating the contribution of the surface travel step. Our results give important insights regarding the practical ratio between the size of the reactant molecule and the size of the confined space, showing that traditional confinement effects are due to electronic interactions. Moreover, we demonstrate that the surface travel step is primarily reflected in the pre-exponential factor, leaving the activation energy unchanged. Thus, we show experimentally that for reactions at surfaces that follow the Langmuir-Hinshelwood model, the Arrhenius pre-exponential factor describes the travel across the surface, playing an analogous role to that of substrate orientation and collision cross-section in the fluid phase.

3.6 References

[1] J. H. van 't Hoff, *Etudes de Dynamique Chimique*, Amsterdam : F. Muller & Co., **1884**.

[2] L. Xing, Z. Peng, W. Li, K. Wu, *Acc. Chem. Res.* **2019**, *52*, 1048–1058.

[3] H. Eyring, *J. Chem. Phys.* **1935**, *3*, 107–115.

[4] W. F. K. Wynne-Jones, H. Eyring, *J. Chem. Phys.* **1935**, *3*, 492–502.

[5] P. Hänggi, P. Talkner, M. Borkovec, *Rev. Mod. Phys.* **1990**, *62*, 251–341.

[6] A. H. Zewail, *J. Phys. Chem.* **1996**, *100*, 12701–12724.

[7] J. C. Light, J. Ross, K. E. Shuler, in *Kinet. Process. Gases Plasmas* (Ed.: A.R. Hochstim), Academic Press, **1969**, pp. 281–320.

[8] J. K. Nørskov, T. Bligaard, B. Hvolbæk, F. Abild-Pedersen, I. Chorkendorff, C. H. Christensen, *Chem. Soc. Rev.* **2008**, *37*, 2163–2171.

[9] K. J. Laidler, J. H. Meiser, B. C. Sanctuary, *Physical Chemistry*, Houghton Mifflin, **2002**.

[10] L. Fang, B. Albela, B. Yang, Y. Zheng, P. Wu, M. He, L. Bonneviot, *Langmuir* **2018**, *34*, 12713–12722.

[11] T. K. Slot, N. R. Shiju, G. Rothenberg, *Angew. Chem. Int. Ed.* **2019**, *58*, 17273–17276.

[12] W. Chen, D. Li, Z. Wang, G. Qian, Z. Sui, X. Duan, X. Zhou, I. Yeboah, D. Chen, *AIChE J.* **2017**, *63*, 60–65.

[13] K. Feng, J. Zhong, B. Zhao, H. Zhang, L. Xu, X. Sun, S.-T. Lee, *Angew. Chem. Int. Ed.* **2016**, *55*, 11950–11954.

[14] Q. Wang, F. Fu, S. Yang, M. Martinez Moro, M. de los A. Ramirez, S. Moya, L. Salmon, J. Ruiz, D. Astruc, *ACS Catal.* **2019**, *9*, 1110–1119.

[15] F. Fu, C. Wang, Q. Wang, A. M. Martinez-Villacorta, A. Escobar, H. Chong, X. Wang, S. Moya, L. Salmon, E. Fouquet, J. Ruiz, D. Astruc, *J. Am. Chem. Soc.* **2018**, *140*, 10034–10042.

[16] L. Wang, H. Li, W. Zhang, X. Zhao, J. Qiu, A. Li, X. Zheng, Z. Hu, R. Si, J. Zeng, *Angew. Chem. Int. Ed.* **2017**, *56*, 4712–4718.

[17] T. Banu, T. Debnath, T. Ash, A. K. Das, *J. Chem. Phys.* **2015**, *143*, 194305.

[18] L.-L. Long, X.-Y. Liu, J.-J. Chen, J. Jiang, C. Qian, G.-X. Huang, Q. Rong, X. Zhang, H.-Q. Yu, *ACS Appl. Nano Mater.* **2018**, *1*, 6800–6807.

[19] Y. Li, M. Hu, J. Wang, W.-H. Wang, *J. Organomet. Chem.* **2019**, *899*, 120913.

[20] R. Vakili, E. K. Gibson, S. Chansai, S. Xu, N. Al-Janabi, P. P. Wells, C. Hardacre, A. Walton, X. Fan, *ChemCatChem* **2018**, *10*, 4238–4242.

[21] A. M. Lawal, A. Hart, H. Daly, C. Hardacre, J. Wood, *Energy Fuels* **2019**, *33*, 5551–5560.

[22] P. Hao, D. K. Schwartz, J. W. Medlin, *Appl. Catal. Gen.* **2018**, *561*, 1–6.

[23] T. Van Cleve, D. Underhill, M. Veiga Rodrigues, C. Sievers, J. W. Medlin, *Langmuir* **2018**, *34*, 3619–3625.

[24] P. Thissen, M. Valtiner, G. Grundmeier, *Langmuir* **2010**, *26*, 156–164.

[25] C. A. Schoenbaum, D. K. Schwartz, J. W. Medlin, *Acc. Chem. Res.* **2014**, *47*, 1438–1445.

[26] E. W. Elliott, R. D. Glover, J. E. Hutchison, *ACS Nano* **2015**, *9*, 3050–3059.

[27] M. Yuan, S. Zhan, X. Zhou, Y. Liu, L. Feng, Y. Lin, Z. Zhang, J. Hu, *Langmuir* **2008**, *24*, 8707–8710.

[28] L. Bonneviot, G. L. Haller, *J. Catal.* **1991**, *130*, 359–373.

[29] Y. Cao, W. Fu, Z. Sui, X. Duan, D. Chen, X. Zhou, *Ind. Eng. Chem. Res.* **2019**, *58*, 1888–1895.

[30] M. Jobbagy, V. Oestreicher, C. Huck-Iriart, G. Soler-Illia, P. C. Angelomé, *Chem. – Eur. J.*, **2020**, 26, 3157–3165.

[31] I. Chorkendorff, J. W. Niemantsverdriet, *Concepts of Modern Catalysis and Kinetics*, Wiley-VCH, **2017**.

[32] Y. Takasu, T. Akimaru, K. Kasahara, Y. Matsuda, H. Miura, I. Toyoshima, *J. Am. Chem. Soc.* **1982**, *104*, 5249–5250.

[33] W. Chen, J. Ji, X. Feng, X. Duan, G. Qian, P. Li, X. Zhou, D. Chen, W. Yuan, *J. Am. Chem. Soc.* **2014**, *136*, 16736–16739.

[34] F. R. Lucci, J. Liu, M. D. Marcinkowski, M. Yang, L. F. Allard, M. Flytzani-Stephanopoulos, E. C. H. Sykes, *Nat. Commun.* **2015**, *6*, 1–8.

[35] C.-H. Lien, J. W. Medlin, *J. Catal.* **2016**, *339*, 38–46.

[36] K. R. Kahsar, D. K. Schwartz, J. W. Medlin, *J. Am. Chem. Soc.* **2014**, *136*, 520–526.

[37] G. Kumar, T. Van Cleve, J. Park, A. van Duin, J. W. Medlin, M. J. Janik, *Langmuir* **2018**, *34*, 6346–6357.

[38] S. T. Marshall, M. O'Brien, B. Oetter, A. Corpuz, R. M. Richards, D. K. Schwartz, J. W. Medlin, *Nat. Mater.* **2010**, *9*, 853–858.

[39] S. H. Pang, C. A. Schoenbaum, D. K. Schwartz, J. W. Medlin, *Nat. Commun.* **2013**, *4*, 1–6.

[40] K. R. Kahsar, D. K. Schwartz, J. W. Medlin, *J. Mol. Catal. Chem.* **2015**, *396*, 188–195.

[41] Y. Li, W. Cheng, Z.-J. Sui, X.-G. Zhou, D. Chen, W.-K. Yuan, Y.-A. Zhu, *J. Phys. Chem. C* **2019**, *123*, 28275–28283.

[42] J. Liu, C. Zhang, Z. Shen, W. Hua, Y. Tang, W. Shen, Y. Yue, H. Xu, *Catal. Commun.* **2009**, *10*, 1506–1509.

[43] R. F. Egerton, *Ultramicroscopy* **2013**, *127*, 100–108.

[44] Z. J. W. A. Leijten, A. D. A. Keizer, G. de With, H. Friedrich, *J. Phys. Chem. C Nanomater. Interfaces* **2017**, *121*, 10552–10561.

[45] D. T. Grubb, *J. Mater. Sci.* **1974**, *9*, 1715–1736.

[46] W. J. Shaw, J. C. Linehan, N. K. Szymczak, D. J. Heldebrant, C. Yonker, D. M. Camaioni, R. T. Baker, T. Autrey, *Angew. Chem. Int. Ed.* **2008**, *47*, 7493–7496.

[47] X. Zhang, L. Kam, T. J. Williams, *Dalton Trans.* **2016**, *45*, 7672–7677.

[48] W.-W. Zhan, Q.-L. Zhu, Q. Xu, *ACS Catal.* **2016**, *6*, 6892–6905.

[49] L. Luza, A. Gual, J. A. Fernandes, D. Eberhardt, J. Dupont, *Phys. Chem. Chem. Phys.* **2019**, *21*, 16615–16622.

[50] V. Mouarrawis, R. Plessius, J. I. van der Vlugt, J. N. H. Reek, *Front. Chem.* **2018**, *6*, 623.

[51] Q. Fu, X. Bao, *Nat. Catal.* **2019**, *2*, 834–836.

[52] C. Cai, S. Han, W. Liu, K. Sun, L. Qiao, S. Li, X. Zu, *Appl. Catal. B Environ.* **2020**, *260*, 118103.

[53] S. Han, Y. Zhu, C. Cai, J. Zhu, W. Han, L. Chen, X. Zu, H. Yang, M. Gu, *Appl. Phys. Lett.* **2019**, *114*, 113901.

[54] R. Gounder, E. Iglesia, *Acc. Chem. Res.* **2012**, *45*, 229–238.

[55] R. Gounder, E. Iglesia, *Chem. Commun.* **2013**, *49*, 3491–3509.

3.7 Appendix

3.7.1 Additional figures

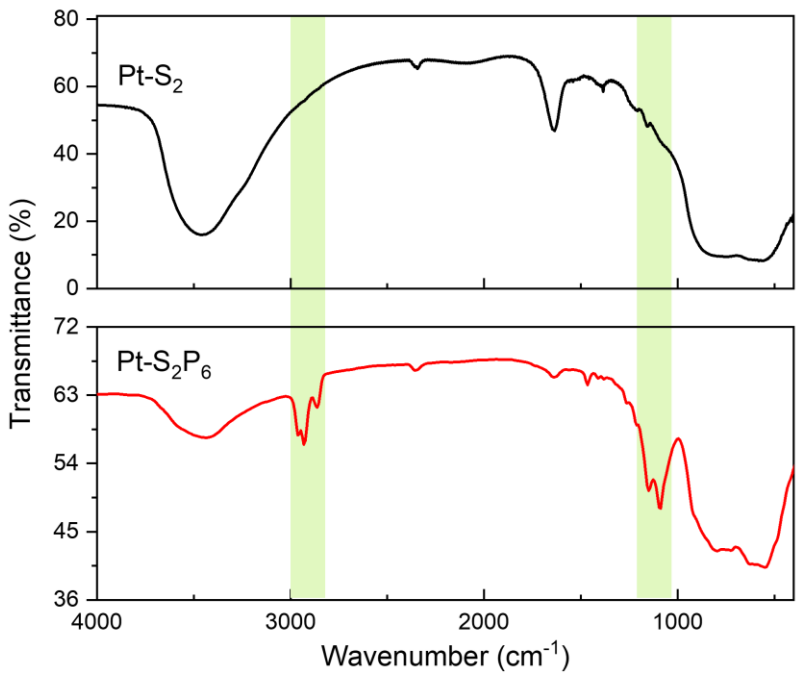

Figure A3.1: FTIR spectrum of Pt-S_2 (ethanethiol-coated) and Pt-S_2P_6 (ethanethiol- and HPA-coated).The signals of surface-bound hexyl phosphonic acid are indicated with green areas.

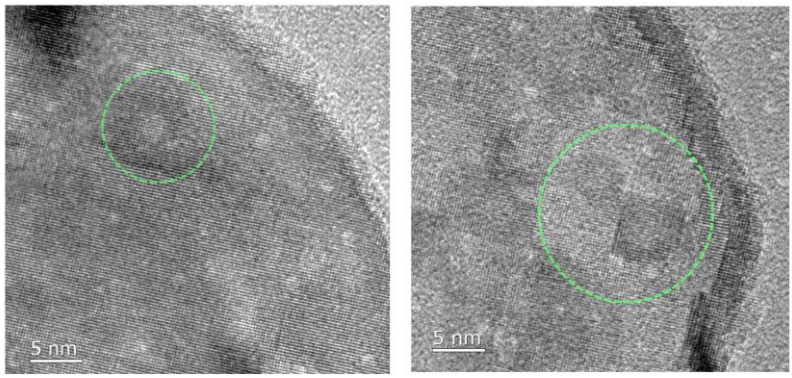

Figure A3.2: Additional HRTEM images of Pt-r_5P_6 (pentanethiol- and HPA-coated) catalyst.

3.7.2 Experimental procedures and methods

All chemicals used in this study were purchased from commercial sources (>97% pure) and used as received. Ammonia borane 97% was obtained from Sigma Aldrich (682098-10G). Reaction kinetics were studied using the homebuilt bubble counter. This system has been described in detail in Chapter 2 of this thesis.

Procedure for isothermal hydrolysis of ammonia borane

Aqueous ammonia borane (0.40 mL, 2 M) was loaded into a syringe (1 mL) equipped with a glass capillary (0.32 mm, 15 cm) that reaches into the reactor below the solvent level. The catalyst (40 mg) was suspended in water (6.0 mL) and a stirring bar (8 × 3 mm) was added. The reactor was closed, and the capillary directly inserted into the liquid through one of the syringe ports. All remaining ports were closed. The reactor was then purged with nitrogen using a flowrate of 5 mL min^{-1} for 5 min. During purging, the reactor was heated to the desired temperature. After the temperature stabilized, the purging was stopped. After 5 seconds, the reactant was injected, resulting in some bubbles forming due to volume displacement. The gas production was then monitored until reaction completion.

Procedure for non-isothermal hydrolysis of ammonia borane

An aqueous solution of ammonia borane (0.40 mL, 2 M) was loaded into a syringe (1 mL) equipped with a glass capillary (0.32 mm, 15 cm) that reaches into the reactor. The catalyst (40 mg) was suspended in water (6.0 mL), cooled to 10 °C and a stirring bar (8 × 3 mm) was added. The reactor was closed, and the capillary directly inserted into the liquid through one of the syringe ports. All remaining ports were closed. The reactor was then purged with nitrogen using a flowrate of 5 mL min^{-1} for 5 min. The temperature was verified to be room temperature (20-25 °C) before the reaction was started. After 5 seconds, the reactant was injected, resulting in some bubbles forming

due to volume displacement. Five seconds later, a ramp of 2 °C min^{-1} was initiated. The sample was heated to 85 °C and held there for 5 min. At the end of the heating program the purge gas (nitrogen) was turned on and heating was stopped.

Procedure for non-isothermal dehydrogenation of ammonia borane

A solution of ammonia borane (0.40 mL, 2 M) in anhydrous *N*-methyl-2-pyrrolidone (NMP) was loaded into a syringe equipped with a glass capillary (0.32 mm, 15 cm) that reaches below the liquid level. The catalyst (40 mg) was suspended in NMP (6.0 mL) and a stirring bar (8 × 3 mm) was added. The reactor was closed, and the capillary directly inserted into the liquid through one of the syringe ports. All remaining ports were closed. The reactor was then purged using a flowrate of 5 mL min^{-1} for 5 min. After 5 seconds, the reactant was injected, resulting in some bubbles forming due to volume displacement. Five seconds later, a ramp of 0.5 °C min^{-1} was initiated. The sample was heated to 140 °C and held there for 5 min. At the end of the heating program the purge gas (nitrogen) was turned on and heating was stopped. The sample was cooled down to room temperature while being purged with nitrogen.

Procedure for Pt impregnation on γ-Al_2O_3

γ-Al_2O_3 extrudate (Ketjen) was grinded and sieved to obtain particles with a diameter of 90 – 53 µm. Grinded γ-Al_2O_3 (1.00 g) was loaded into a glass vial (30 mL) equipped with a vacuum port and a syringe for injecting liquid under vacuum. The goal was to fill 80% of the incipient volume with a Pt solution. An aqueous solution of $Pt(NH_3)_4(NO_3)_2$ (2.6 mg mL^{-1}) was prepared and 3.9 mL was loaded in the syringe. The alumina powder was stirred using a magnetic stirrer (1000 rpm) and vacuum was applied for about 1 minute prior to injection of the liquid. Directly after injection, the vial was agitated manually (with help of the magnetic stirring) to obtain a homogeneous mixture of Pt on alumina. The vacuum was released, leaving a powder that is almost dry to the touch. The alumina was further homogenized using a mortar and pestle and dried overnight at 80 °C in a petri dish, followed by 2h at 120 °C. The next day, the powder was loaded in the tubular furnace and heat-treated under N_2 at 225 °C (5 °C/min ramp), with a 1h holding time. Next, the sample was reduced at 225 °C (5 °C/min ramp) for 2h using a mixture of 10% H_2 in N_2. The catalyst was stored under argon.

Procedure for synthesis of phosphonic acid coated catalysts with no free volume (Pt-R_0P_z)

0.05% Pt/γ-Al_2O_3 (250 mg, 6 µmol Pt) was added to a solution phosphonic acid (40 mM, 40 mL) in THF and stirred overnight. The solution was decanted, and the catalyst annealed at 120 °C for 12 h. The catalyst was washed with THF (3 × 20 mL), then air-dried in a fume hood at room temperature.

Procedure for synthesis of free volume Pt-R_yP_z catalysts

Methanethiol coating (synthesis of Pt-S_1)

Methyl iodide (3.25 mL, 52 mmol) was added to thiourea (3.46 g, 45 mmol) in ethanol (3 mL) and stirred at room temperature. The solvent was removed *in vacuo*, isolating *S*-methylisothiuronium iodide as a white crystalline solid. This solid was dissolved in water (3.6 mL) and heated to 100 °C, evolving methanethiol as a gas. Methanethiol was collected using a cold trap on an ice-water bath, dissolved in ethanol (5 mL), then poured into a suspension of 0.05 wt% Pt/Al_2O_3 (400 mg, 10 µmol Pt) in ethanol (20 mL) and stirred for 24 h. The solution was decanted, and the catalyst washed with ethanol (1 × 20 mL). The catalyst was dried in vacuum oven overnight at 40 °C. At this stage a 100 mg sample of Pt-S_1 was removed for catalytic testing.

Ethanethiol/pentanethiol coating (synthesis of Pt-S_2 and Pt-S_5)

Under a nitrogen atmosphere, 0.05% Pt/γ-Al_2O_3 (500 mg, 13 µmol Pt) was added to 10 mM ethanolic thiol solution (40 mL, 0.4 mmol) and stirred for 24 h. The solution was decanted, and the catalyst washed with ethanol (1 × 20 mL). The catalyst was dried in vacuum oven overnight at 40 °C. At this stage a 100 mg sample of Pt-S_y was removed for testing.

Phosphonic acid coating (synthesis of Pt-S_yP_z)

Under a N_2 environment, Pt-S_y (400 mg, 10 µmol Pt) to a solution phosphonic acid (40 mM, 40 mL) in THF and stirred overnight. The solution was decanted, and the catalyst annealed at 120 °C for 12 h. The catalyst was washed with THF (3 × 20 mL) and air dried in a fumehood overnight. At this stage a 100 mg sample of Pt-S_yP_z was removed for testing.

Removal of thiolate coating (synthesis of Pt-R_yP_z)

Pt-S_yP_z (300 mg, 6 µmol Pt) added to a solution of $NaBH_4$ (0.5 M, 40 mL) in 1:1 EtOH/H_2O and stirred for 10 minutes. The solution was decanted, and the catalyst washed with 1:1 EtOH/H_2O (3 × 20 mL). The catalyst was dried in a vacuum oven at 40 °C overnight.

3.7.3 Data processing and calculation

The data for the Arrhenius plots was obtained from non-isothermal kinetics experiments. Full details for the data preparation can be found in the Appendix of Chapter 2. In short, the bubble counting data (time) was merged with the temperature–time data. Then, a window average was applied to calculate the average temperature at the time of each observed bubble. The volume of each bubble was calculated from the observed flowrate (bubbles s^{-1}). A control experiment using solvent only was subtracted from the volume data, to eliminate any gas production due to gas expansion and/or vapour pressure. The resulting volume–time–temperature data was the basis for the

TOF calculation and the Arrhenius plots. These were calculated using the procedure described in Table 3.1.

Table A3.1: Calculation parameters

Col	Name	Source / Calculation
1	Time (min)	Raw data
2	Beam interruption time (BIT units)	Raw data
3	Volume (µL)	Raw data
4	Volume, blank subtracted (µL)	Raw data
5	Temperature (°C)	Raw data
6	Time Interpol (min)	50 point interpolation from X=**1**,Y =**4**, X data
7	Volume Interpol (µL)	50 point interpolation from X=**1**,Y =**4**, Y data
8	Temperature interpolation (°C)	Interpolation of X=**6** in (X=**1**,Y=**5**), Y data
9	Observed rate (µL/min)	Derivative of (X=**6**, Y=**7**), vs time!
10	Fractional conversion (0–1)	1 – (**7**/maximum expected volume)
11	Intrinsic rate (µL/min)	**9** / ((1-**10**)^{n}) n = reaction order = 0.15 for ammonia borane hydrolysis
12	Observed rate (M/min)	**9** / constant, depending on stoichiometry of the reaction and molar concentration
13	Intrinsic rate (M/min)	**11** / constant, depending on stoichiometry of the reaction and molar concentration
14	1000/T	1000/(**8** + 273.15)
15	ln (k)	ln(**13**)
16	TOF	ln(**11** × 10^{-6} /([equivalents of H_2 per equivalent AB] × [molar volume]) / ((([loading%]/100) × (0.001 × [mass catalyst])) /[molar mass Pt])) = ln(**11** × 10^{-6}/(3 × 22.4) / ((([loading%]/100) × (0.001 × [mass catalyst]))/195.1))

4

Acid catalysis with surface-modified $Ti_3C_2T_x$ MXenes[‡]

[‡] Parts of this work have been accepted for publication as:

Enhancing catalytic epoxide ring-opening selectivity using surface-modified $Ti_3C_2T_x$ MXenes

T. K. Slot, V. Natu, E. V. Ramos-Fernandez, A. Sepúlveda-Escribano, M. Barsoum, G. Rothenberg, and N. Raveendran Shiju, *2D Mater.*, in press.

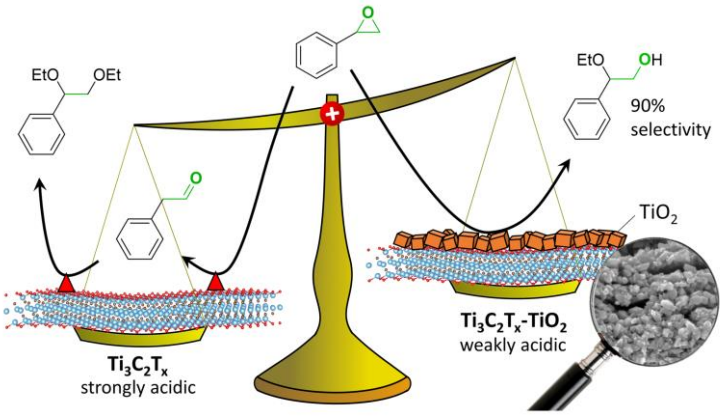

Balancing acidity: Designable materials tune the acidity of MXenes and improve selectivity

Abstract: MXenes are a new family of two-dimensional carbides and/or nitrides. Their 2D surfaces are typically terminated by O, OH and/or F atoms, depending on the delamination conditions. Here we show that $Ti_3C_2T_x$ – the most studied MXene family – is a good acid catalyst, thanks to the surface acid functionalities. We demonstrate this by applying $Ti_3C_2T_x$ in the epoxide ring-opening reaction of styrene oxide and its isomerization in the liquid phase. Interestingly, modifying the MXene surface changes the catalytic activity and selectivity. By oxidizing the surface, we succeeded in controlling the type and number of acid sites and thereby improving the yield of the mono-alkylated product to > 80%. Characterisation studies show that a thin oxide layer, which forms directly on the $Ti_3C_2T_x$ surface, is essential for catalysing the styrene oxide ring-opening. We hypothesize that two kinds of acid sites are responsible for this catalysis: In the MXene, strong acid sites (both Lewis and Brønsted) catalyse both the ring-opening and the isomerization reactions, while in the MXene-TiO_2 composite weaker acid sites catalyse only the ring-opening reaction, increasing the selectivity of the mono-alkylated product.

4.1 Introduction

MXenes are getting increased attention as novel two-dimensional materials. They are prepared by delaminating MAX phases, which are atomically layered solids where M is an early transition state metal, A is a group IIIA/IVA element, and X is carbon or nitrogen.[1] MXenes are denoted by $M_{n+1}X_nT_x$, where T stands for a terminating functional group that depends on the delamination conditions.[2–5] These materials are very versatile. They can be prepared from a variety of MAX phases, and their surface chemistry can be controlled by the conditions of etching and delamination.[6–11] Although stable at high temperatures under inert conditions,[12] they are sensitive to oxidation.[13–17] However, this sensitivity can be controlled by edge-capping the MXene sheets using polyanionic salts.[18]

MXenes have a hierarchical structure, good conductivity and tuneable surface chemistry.[19–22] Because of this, they are widely applied in electrochemistry, batteries, sensors, separation science and electrocatalysis.[23] However, in heterogeneous catalysis, they are less used.[24] MXenes were applied in water–gas shift reaction,[25] dehydrogenation of propane and isobutene,[26] nitrogen fixation,[27] methane dehydro-aromatisation,[28] and oxidation reactions.[29,30] As far as we know, these are the only published thermo-catalytic applications.

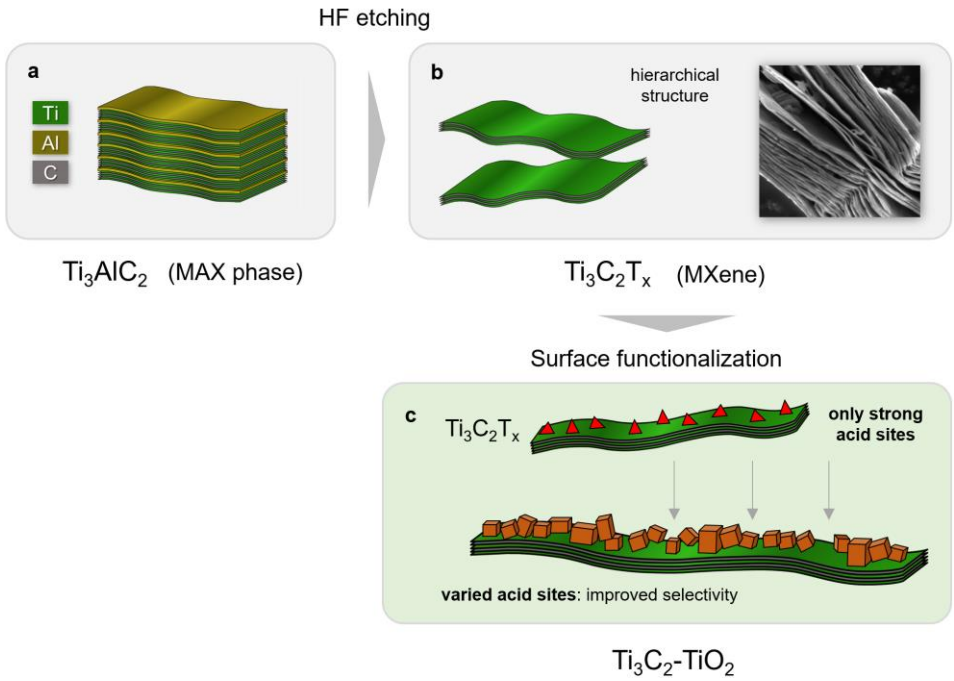

Figure 4.1. Cartoon illustrating the material synthesis from (**a**) MAX phase to (**b**) MXene, followed by (**c**) surface functionalisation, creating MXene-TiO_2 composites.

In this work, we explore the $Ti_3C_2T_x$ MXene and its derivatives as catalysts for acid-catalysed reactions using the styrene oxide ring opening reaction (Eq. 4.1) as a model reaction (Figure 4.1). This is an important route to 1,2-type functional groups, such as β-alkoxy alcohols, which are precursors for a broad range of pharmaceuticals. This reaction is usually acid-catalysed, but can also be catalysed by a base.[31–33] The selectivity to the desired product depends on the catalyst.[34–36] By studying the reaction kinetics and mechanism and we show that the reaction kinetics and selectivity in epoxide ring opening can be controlled by modifying the surface of $Ti_3C_2T_x$.

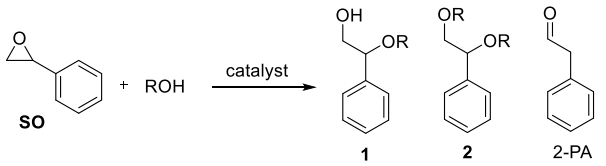

(4.1)

4.2 Experimental

All chemicals were obtained from commercial sources (>97% pure) and used as received. Further details about the instrumentation and methods are included in the Appendix.

MXene ($Ti_3C_2T_x$) Synthesis

The Ti_3AlC_2 powders were synthesized by mixing titanium carbide (TiC) (Alfa Aesar, 99.5%), aluminium (Al) (Alfa Aesar, 99.5%, 325 mesh), and titanium (Alfa Aesar, 99.5%, 325 mesh), powders in a molar ratio of 2:1.05:1, respectively. The mixture was further ball milled at 100 rpm for 24 h to mix the powders. The powders are then transferred to an alumina crucible and heated under flowing argon, Ar, at 1350 °C for 2 h. The heating and cooling rates were set at 5 °C min^{-1}. The resulting loosely sintered blocks were ground using a titanium nitride coated milling bit on a drill press. The milled powders were passed through a 400 mesh (particle size < 38 µm) sieve for further experiments. Ti_3AlC_2 powder (1.0 g) was added to 10 mL of 10% HF solution. The mixture was then stirred for 24 h at room temperature and 300 rpm. The resulting slurry was transferred into a 50 mL centrifuge tube and DI water was added to completely fill the remaining volume. It was then centrifuged at 3500 rpm for 2 min and the resulting clear supernatant was discarded. This washing was repeated several times until the pH of the solution was ≈ 7. After which the bottom sediment was collected and dried under vacuum before further testing. Catalysts were exposed to air for one week prior to use in the reaction, to avoid induction periods at the beginning of the reaction.

Synthesis of MXene-TiO_2 composite

MXene (100 mg) was suspended in 20 mL water in a 75 mL autoclave (without a PTFE liner) and a 30 × 8 mm stirring bar. The autoclave was sealed and quickly heated to 285 °C and kept at this temperature for 30 min while stirring at 800 rpm. Then, the reactor was quenched in water and allowed to cool down to room temperature. The material was washed (5 ×) with water and dried overnight under vacuum at 30 °C.

Catalytic testing

A stock solution of SO was prepared by dissolving styrene oxide (5 mL, 4.36 mmol) and bromobenzene (5 mL) in absolute ethanol to a total volume of 50 mL. The reactions were performed in sealed 20 mL test tubes. Stock solution (5 mL) was added to 5.0 mg catalyst. Tubes were heated in an oil bath and stirred at 600 rpm. Aliquots of 120 µL were taken from the reaction mixture, diluted 10× with ethanol, filtered through a PTFE filter (0.45 µm) and analysed by gas chromatography (He carrier, HP-5 column).

Kinetic studies

Kinetic studies were performed in duplicate in an oven-dried 100 mL three-neck flask equipped with a reflux condenser and a slight N_2 overpressure (<50 mBar). SO stock solution (20 mL) was added to 20 mg catalyst. One neck/opening was equipped with a septum and the rest were stoppered to avoid N_2 flow. During reaction, aliquots of 120 µL were taken from the reaction mixture through the septum, diluted 10 × with ethanol, filtered through a PTFE filter (0.45 µm) and analysed by gas chromatography.

Characterization

Gas chromatography (GC) was performed with a Perkin Elmer Clarus 500, equipped with a flame ionization detector and a 30 m Agilent polysiloxane HP-5 column (0.32 mm ID, 0.25 µm). Helium was used as carrier gas and the column oven was heated from 60 °C to 250 °C with a 25 °C/min heating rate and held at the final temperature for 5 min. Sample solution (1.0 µL) was injected using a split injector with a 1:50 split ratio.

Diffuse reflectance infrared Fourier transform spectroscopy (DRIFTS) was acquired on a FTIR (Nicolet 6700) spectrometer with a HgCdTe (MCT) detector (cooled with liquid N_2). The DRIFTS sample cell (Praying Mantis, Harrick) was fitted with CaF_2 windows and a PID-controlled heater allowing samples to be heated to 700 °C. Samples were preheated in helium to 350 °C for 1 h, and then stepwise cooled till 25 °C while taking background spectra of the preheated sample at every sample temperature. A constant helium flow of 20 mL min^{-1} was maintained throughout the analysis. Spectra of adsorbed pyridine were collected after treating the pre-heated sample in a flow of 1.0-1.4 vol% pyridine in helium for 10 min, followed by evacuation by an oil pump for 30 min. All spectra were measured with resolution of 4 cm^{-1} and accumulation of 64 scans. Confocal Raman spectra were recorded at 532 nm using a Renishaw (Wottonunder-

Edge, United Kingdom) InVia Reflex Raman microscope with a 532 nm frequency-doubled Nd:YAG excitation source in combination with an 1800 lines mm^{-1} grating, and a Peltier-cooled CCD detector (203 K). The instrument included a Leica light microscope with a 50× air objective. The 521 cm^{-1} Raman shift of an internal silicon standard was used to verify the spectral calibration of the system. XPS analysis was carried out in a K-Alpha Spectrometer (Thermo-Scientific). The assignment of the C 1s binding energies was done according to the criteria used by Ganguly *et al*. 284.5 eV for C=C (aromatic double bonds), 285.5 eV for C–OH and sp^3 C–C, 286.5 eV for epoxy, 287.5 for sp^2 C=O (carbonyls, lactones) and 289 eV for carboxylic groups.[37] X-ray diffraction (XRD) measurements were carried out on a Rigaku Miniflex X-ray diffractometer from 4° to 70° using a 2.0° min^{-1} angular velocity.

Scanning Electron Microscope (SEM) images were taken by a FEI Verios 460 using a 5 kV accelerating voltage. HRTEM images were recorded on a FEI Tecnai G2 F20 S-Twin high-resolution transmission electron microscope working at 200 kV (point resolution: 0.24 nm, lattice resolution 0.102 nm, information resolution 0.14 nm). STEM-EDS images were recorded using an EDS detector with energy resolution <127 eV and a resolution of 0.20 nm.

4.3 Results and discussion

First, we prepared $Ti_3C_2T_x$ MXenes by etching Ti_3AlC_2 powders with 10% HF for 24 h under continuous stirring. Rinsing and washing gave a multilayered MXene with –OH, –O and –F as its main surface functional groups. Recent studies suggest that MXenes' sensitivity to oxidation can be used to create materials with new structural and electronic properties.[14,38,39] We envisaged that such treatments could enhance or block certain reaction pathways by altering the surface structure, giving us control over reactivity and selectivity. One such treatment consists of exposing $Ti_3C_2T_x$ to water at hydrothermal conditions above 200 °C. For this, we treated the MXene an autoclave at 285 °C for 30 min. Then, the reactor was quenched in water and the material was washed with water and dried under vacuum at 30 °C for 12 h. This grows small crystals of TiO_2 on the MXene surface, while leaving the bulk of the MXene layers intact. XRD analysis (Figure A4.1) revealed that these crystals have both rutile (27°, 38° and 55°) and anatase (25° and 48°) phases in a ratio 1:2–1:3.[40] These appear as a range of unordered crystals sticking out of the $Ti_3C_2T_x$ basal planes, as shown by scanning electron microscopy (Figure 4.6). Raman spectroscopy showed that the surface consists of anatase titania on both the MXene and the $Ti_3C_2T_x$-TiO_2 composite (Figure A4.2).

We then compared Ti_3AlC_2 MAX phase and its MXene, $Ti_3C_2T_x$, in the catalytic ring opening of styrene oxide by methanol. The MAX phase showed low activity and selectivity to the mono-alkylated product **1** (Table 4.1, entry 2 and 8). Conversely, a

MXene made from this MAX phase showed a high conversion (98%) and a selectivity (90%) to product **1** in 2.5h. This shows that etching out the Al layers increases the catalytic activity. We also ran control reactions using MXenes stored under both argon and air to see the influence of surface oxidation/hydration.[13] The sample stored under argon showed a small induction period (15 min) before product **1** appeared. After this period, the reaction proceeded quickly, whereas the air-exposed sample performed well from the beginning (*cf.* Table 4.1, entries 4/5 and 10/11).

Table 4.1. Catalytic results for the styrene oxide ring opening by methanol.[a]

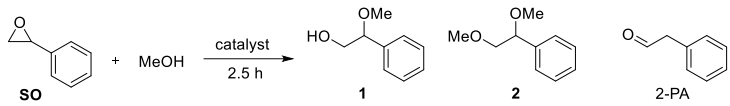

SO 1 2 2-PA

Entry	Catalyst	Conversion (%)	Selectivity 1 (%)	2 (%)	3 (%)
1	No catalyst[c]	1	-	-	-
2	Ti_3AlC_2	15	22	15	63
3	Ti_3AlC_2, H_2O_2 treated	17	41	3	54
4	$Ti_3C_2T_x$, under Ar[c]	75	36	3	51
5	$Ti_3C_2T_x$ air exposed[c]	98	73	18	9
6	Graphene oxide[d]	43	42	53	2
7	No catalyst[c]	7	-	-	-
8	Ti_3AlC_2	25	51	22	27
9	Ti_3AlC_2, H_2O_2 treated	31	70	1	28
10	$Ti_3C_2T_x$, under Ar[c]	98	90	6	4
11	$Ti_3C_2T_x$ air exposed[c]	>99	88	5	5
12	Graphene oxide[d]	94	53	46	10

[a] Reaction conditions: 0.5mL styrene oxide and 5 mg of catalyst in 5 mL methanol in a closed container; stirred for 2.5 h. [b] selectivity towards the single product, based on GC analysis (PhBr, 100 µL internal standard). [c] Average of duplicate experiments. [d] Prepared by Hummer's method.

Subsequently, we tested the pristine and water-treated MXene materials in the styrene oxide ring opening reaction (Figure 4.2). A series of control experiments (data not shown) showed that the reactivity of ethanol was comparable to that of methanol, so we switched to ethanol for safety reasons. Products **1** and **2** were identified and characterized using ^{1}H NMR and 2-dimensional ^{1}H–^{1}H correlation spectroscopy (COSY, see Figs. A4.7 and A4.8). Product **1** is easily distinguished by its characteristic spin splitting in the C$\underline{H}_2$C$\underline{H}$–O$\underline{H}$ system in ^{1}H NMR. Chromatography analysis showed the formation of an intermediate, 2-phenyl acetaldehyde (2-PA). The isomerization of SO to 2-PA over $Ti_3C_2T_x$ is very fast, taking only minutes at 45 °C. (Figure 4.2**a**). The 2-PA is then converted into product **2** following first order kinetics (Figure A4.3).

Interestingly, the kinetics of the reaction in the presence of the structurally altered MXene – the $Ti_3C_2T_x$-TiO_2 composite were totally different compared with the non-treated $Ti_3C_2T_x$ flakes (Figure 4.2**b**). The reaction starts rapidly, and the remainder of the SO was converted to product **1** with a small amount of product **2**. This shows that the surface treatment can limit the conversion of SO into 2-PA, allowing the formation of product **1** in high yields. Since the treatment introduces titania crystals on the surface, the reactivity change may be caused by these crystals. To check this, we ran a control using a commercial titania (Degussa P25, anatase:rutile ratio ~3:1). However, this yielded only 2-PA and no other products (Figure 4.2**c**), showing that TiO_2 is not solely responsible for the reactivity of the treated MXene.

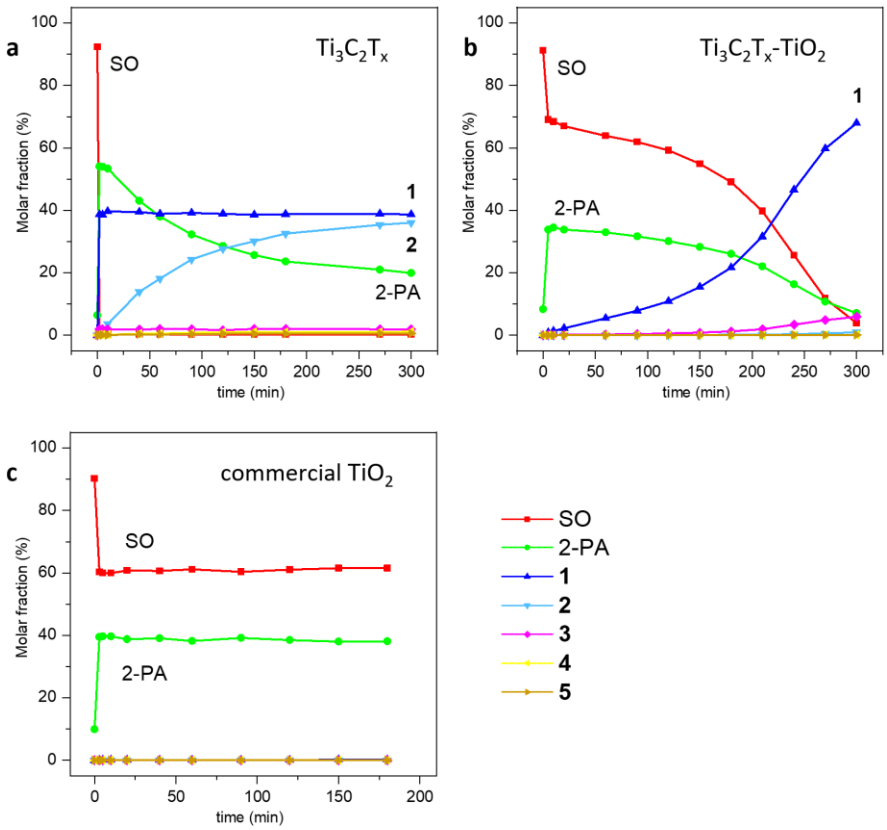

Figure 4.2. Styrene oxide reaction with (**a**) pristine $Ti_3C_2T_x$ MXene, (**b**) water-treated $Ti_3C_2T_x$ MXene with TiO_2 crystals on its surface, and (**c**) a control reaction with TiO_2. Molar fractions of compounds were determined by GC using PhBr as an internal standard. SO = styrene oxide, 2-PA = 2-phenyl acetaldehyde, and **1**–**5** are reaction products. Reaction temperature = 45 °C.

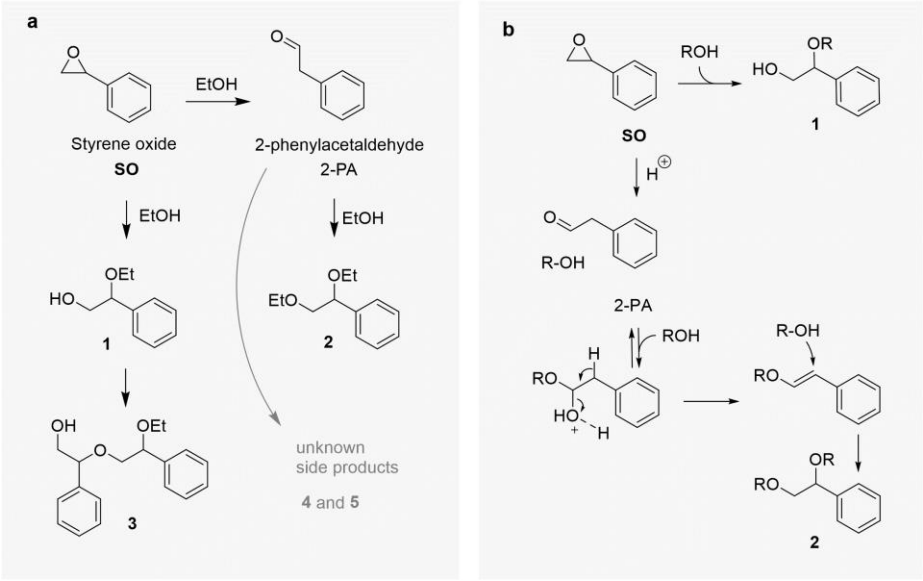

Scheme 1. (**a**) Reaction pathways, products and by-products in the ring opening of styrene oxide catalysed by $Ti_3C_2T_x$ and $Ti_3C_2T_x$-TiO_2 composite. (**b**) Reaction mechanism from 2-PA into products **1** and **2**.

With bulk TiO_2 as catalyst, the concentration of SO decreases steeply. However, the reaction stops within 1–2 min. Control experiments confirmed that SO and 2-PA are not in equilibrium: Neither catalyst yielded any SO when starting from 2-PA as substrate (Figure A4.4). Using 2-PA as starting material we could also verify that 2-PA is the intermediate towards product **2**. Scheme 1**a** gives an overview of the reaction pathways. Regarding the steep drop in SO in the first few minutes of the reaction, we hypothesize that the isomerization of SO initiates polymerization around the stronger acid sites, blocking them from further action. The $Ti_3C_2T_x$-TiO_2 catalyst has fewer strong acid sites, resulting in a smaller concentration drop of styrene oxide. XPS analysis (Figure 4.3, blue curve) of the spent catalyst shows an increase in the signal at 286.3 eV, corresponding to organic CH_x or CO residues at the expense of C–Ti–T_x at 281.9 eV, (Figure 4.3, green curve). This supports our hypothesis of organic residues deposited on the C–Ti–F bonds, which are reactive towards nucleophilic attack. A similar (but less pronounced) increase in CH_x peak intensities was observed for the $Ti_3C_2T_x$-TiO_2 composite after reaction (Figure A4.5, C 1s).

We tested several alcohols as solvent/reactant for the reaction with styrene oxide (Table 4.2). Methanol and ethanol gave good conversions (>99%) and were selective towards product **1**. Isopropyl alcohol gave equal amounts of **1** and **2**, while *t*-BuOH gave mainly product **2**.

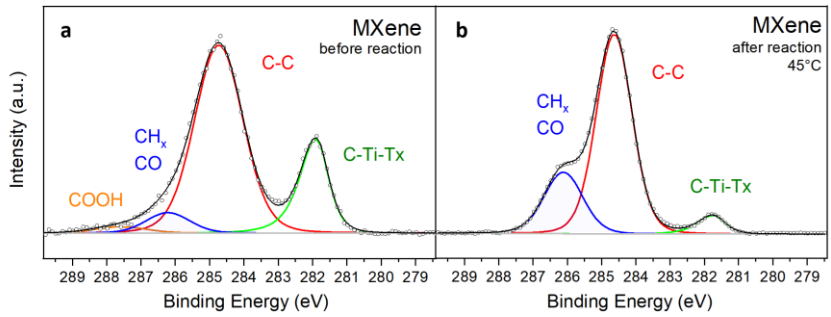

Figure 4.3. XP spectra of the C 1s region of $Ti_3C_2T_x$, (**a**) before and (**b**) after reaction. The peaks are deconvoluted as shown.

This can be explained by a examining the reaction mechanisms of SO and 2-PA with alcohols (Scheme 1b). Bulkier alcohols such as *t*-BuOH react slower towards **1**, because the alcohol attacks a sterically hindered position. Yet isomerization of SO into 2-PA still takes place at a normal rate, consuming the SO before significant amounts of **1** can form. This gives more 2-PA, which converts to product **2** as follows: First, it forms a hemiacetal with one alcohol molecule. This dehydrates, yielding a double bond, which can be attacked at the benzylic carbon. Overall, the reduced rate towards **1**, and the increased concentration of 2-PA, lead to a higher selectivity to product **2** with bulkier alcohols.

Table 4.2. Epoxide ring opening catalysed by $Ti_3C_2T_x$ in different solvents.[a]

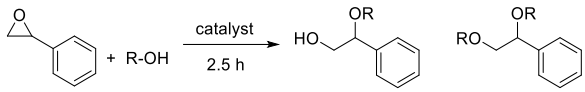

SO 1 2

Entry	Catalyst	Conversion (%)	Selectivity 1 (%)	2 (%)	3 (%)
1	Methanol	>99 (5)	73	18	9
2	Ethanol	>99 (1)	50	46	4
3	Isopropanol	99 (0)	35	35	24
4	*tert*-butanol	79 (0)	4	23	68

[a] Reaction conditions: epoxide (0.874 mmol) and $Ti_3C_2T_x$ (1.0 mg) in 1 mL solvent; stirred at 80 °C for 2.5 h. [b] Conversion of both reactions with and without catalyst (without catalyst in parenthesis). [c] Selectivity towards the single product, based on GC analysis (PhBr as internal standard). [d] An undetermined by-product, <3%, was also observed.

We then tested the catalytic activity of MXene for ethanolysis of other epoxides (Table 4.3). The simple unhindered epoxides (entries 1–5) react readily giving high conversion (>99%) at high selectivity (89%) against a background reaction of <1%

conversion, showing that MXene catalysis has a broad scope for epoxide ring-opening reactions. Sterically hindered epoxides (entries 6 and 7) gave lower conversion, but this was expected as both *i*-Pr and *t*-Bu groups are very bulky. A primary alcohol group improved conversion and selectivity (*cf.* entries 4 and 5), likely because of its electron-withdrawing nature.

The fact that both isomerization and epoxide ring opening are acid-catalysed suggests that both $Ti_3C_2T_x$ and the $Ti_3C_2T_x$-TiO_2 composite have acid sites. We envisage two kinds of acid sites: strong sites (present on MXene) catalysing both the reaction of SO to 2-PA and product **1**, and weaker ones, present on the $Ti_3C_2T_x$-TiO_2 composite, that only catalyse the ring opening of SO to give product **1**. The hydrothermal surface treatment blocks most of the strong acid sites, leaving weaker acid sites to catalyse the reaction.

Table 4.3. Epoxide ring opening of different epoxides by $Ti_3C_2T_x$ in ethanol.[a]

Entry	Catalyst	Conversion[b] (%)	Selectivity[c] (%)	Background conversion[e] (%)
1	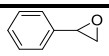	>99	89	1
2		>99	96	0
3		99	95	0
4		79	74	3
5[d]		33	53	3
6		2	76	0
7		6	98	4

[a] Reaction conditions: epoxide (0.874 mmol) and $Ti_3C_2T_x$ (1.0 mg) in 1 mL ethanol; stirred at 80 °C for 2.5 h. [b] Conversion of both reaction with (top) and without catalyst (bottom). [c] Selectivity towards the single product, based on GC analysis (PhBr as internal standard). [d] An undetermined by-product was observed. [e] Background reaction with same conditions, yet leaving out the catalyst.

Characterizing the acid sites is difficult. Ammonia temperature programmed desorption did not show significant desorption. Pyridine diffuse reflectance infrared Fourier transform spectroscopy (DRIFTS) reveals the presence of both Lewis and Brønsted acid sites on $Ti_3C_2T_x$ (Figure 4.4**c**). The bands at 1450, 1588, 1612 cm^{-1} are commonly assigned to Lewis acid sites, the one at 1545 cm^{-1} to Brønsted acid sites and the one at 1486 cm^{-1} to a combination of Lewis and Brønsted acid sites.[41–44] The broad signal at 1425 cm^{-1} is assigned to H–bonded pyridine. Because of the low signal we

could not quantify the ratio of Lewis/Brønsted sites. Similarly, the signal-to-noise ratio of pyridine DRIFTS of the $Ti_3C_2T_x$-TiO_2 composites was too low to assign the type of acid sites. This shows that the $Ti_3C_2T_x$-TiO_2 composite has fewer acid sites than $Ti_3C_2T_x$. The latter's surfaces are functionalized by −OH, −O and −F.[38] X-ray photoelectron spectroscopy (XPS) revealed a small amount of moderately acidic carboxylic groups had formed after hydrothermal treatment (C 1s, Figure 4.5). Additionally, a lot of TiO_2 had formed on the surface at the expense of C−Ti−T_x groups (Ti 2p, O 1s, and C 1s, Figure 4.5). Our hypothesis is that the fluorinated MXene surface is responsible for the stronger acid sites (Figure 4.4**a**). Lewis acidity is derived from Ti^+ sites and Brønsted acidity is caused by surface −OH groups adjacent to −F groups. The −F groups withdraw electron density from the −OH groups making them even more acidic. In the $Ti_3C_2T_x$-TiO_2 composite, most of the surface is covered with TiO_2 crystals with known Lewis and Brønsted acidity (Figure 4.4**b**).[45] The Ti 2p spectrum after reaction (Figure A4.6) showed a decrease in Ti−C contributions and an increase in Ti−O contributions. This suggests the surface is being slowly oxidized into TiO_2 during the reaction. Similarly, the O 1s showed an increase in signals at 531.5 eV and 532.8 eV, corresponding to C−Ti−O_x and $Ti(OH)_x$, moieties, respectively. TEM analysis (Figure 4.6**b**) revealed a thin layer (< 5 nm) of amorphous titania forming at the surface during the reaction. The F 1s spectrum did not show any new contributions, albeit that the total F signal decreased after reaction (Figure A4.6).

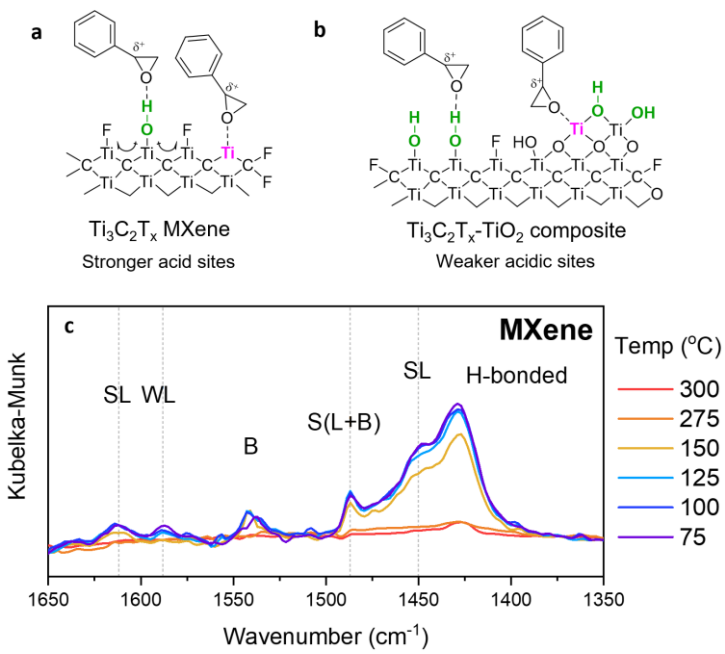

Figure 4.4. Illustration of types of acid sites on $Ti_3C_2T_x$ (top) showing (**a**) stronger sites close to F-groups, and (**b**) weaker sites from O–Ti bonds. (**c**) Pyridine DRIFTS for the $Ti_3C_2T_x$ sample. S: strong, W: weak, L: Lewis acid, B: Brønsted acid. For example: WL = weak Lewis acid.

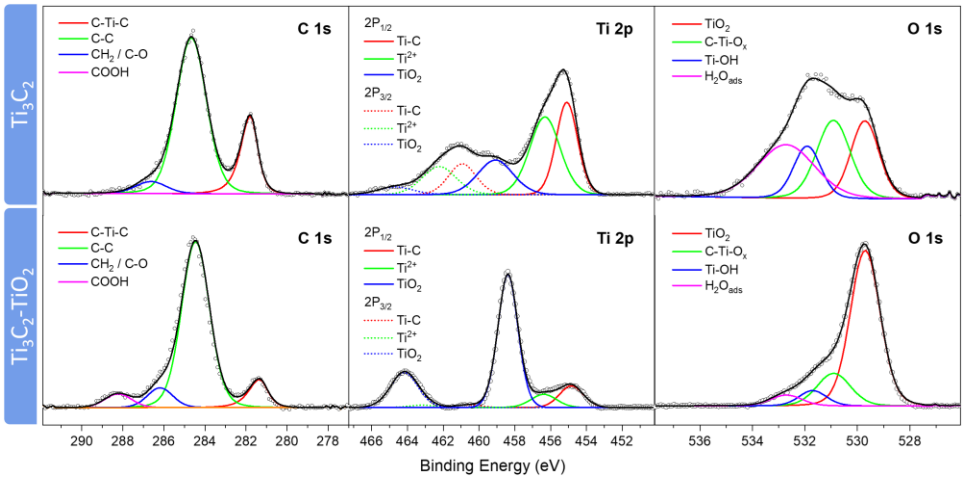

Figure 4.5. Normalized XPS spectra of $Ti_3C_2T_x$ (top) and $Ti_3C_2T_x$-TiO_2 composite (bottom). Intensity is in arbitrary units.

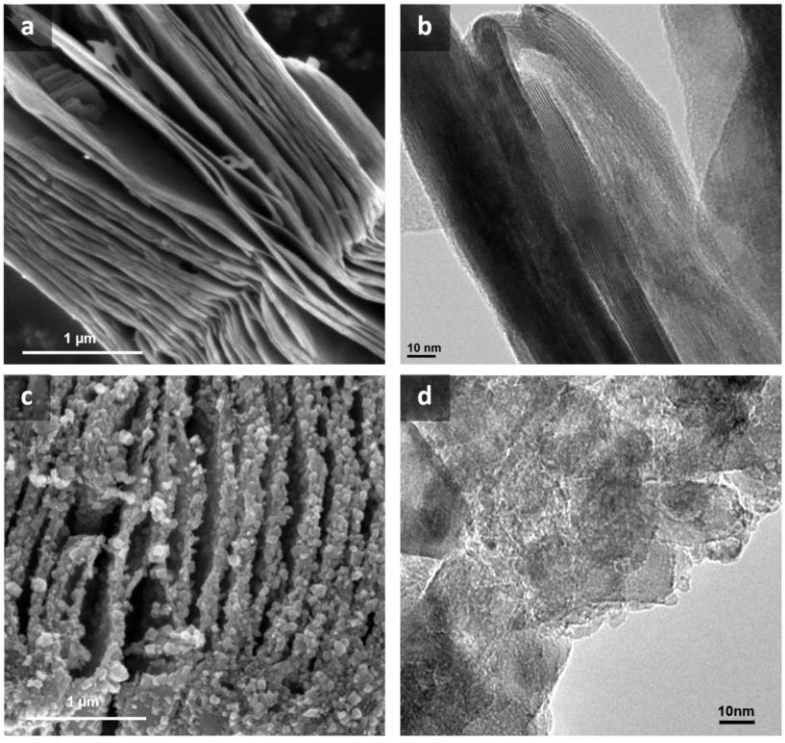

Figure 4.6. (**a**) SEM micrograph of $Ti_3C_2T_x$ multilayers, (**b**) TEM micrograph of the spent $Ti_3C_2T_x$ catalyst after reaction with SO. (**c**) SEM micrograph of $Ti_3C_2T_x$-TiO_2 composite showing TiO_2 particles at the multilayer edges. (**d**) TEM of the spent $Ti_3C_2T_x$-TiO_2 composite catalyst.

Similar changes occurred during reaction of the MXene composite, though less pronounced (Figure A4.5). The C 1s spectrum showed an increase in alkyl contributions and a decrease of fluorine contributions. O 1s showed an increase in Ti^{2+}–O and hydrated $Ti(OH)_x$ contributions. $Ti(OH)_x$ groups are the major contributors to the Lewis/Brønsted acidity.[46,47] The increase in reactivity after 150 min (Figure 4.2**b**) is likely related to this increase.

4.4 Conclusion

$Ti_3C_2T_x$ flakes can be used as acid catalysts for isomerization and ring opening of SO. These two reactions compete on the $Ti_3C_2T_x$ surfaces, likely because of the strong acid sites, promoted by the F-groups. The presence of small TiO_2 crystals at the $Ti_3C_2T_x$ flake edges produced by a hydrothermal treatment in H_2O_2, containing both Brønsted and Lewis acid sites, is responsible for the acid catalysis. The hydrothermal treatment creates a TiO_2 layer that blocks most of the strong acid sites responsible for the isomerization reaction. This alters the reaction kinetics, increasing the selectivity of the main product **1** up to 90%. This opens doors to apply MXene or MXene composites in other acid-catalysed reactions as well. Overall, the availability of several different types of MXenes and their derivatives offers a new opportunity for controlling selectivity and activity in catalysis.

4.5 References

[1] M. W. Barsoum, *MAX Phases: Properties of Machinable Ternary Carbides and Nitrides*, Wiley-VCH, **2013**.

[2] M. Naguib, V. N. Mochalin, M. W. Barsoum, Y. Gogotsi, *Adv. Mater.* **2014**, *26*, 992–1005.

[3] M. Ronda-Lloret, V. S. Marakatti, W. G. Sloof, J. J. Delgado, A. Sepúlveda-Escribano, E. V. Ramos-Fernandez, G. Rothenberg, N. R. Shiju, *ChemSusChem*, **2020**, 13, 6401–6408.

[4] J. L. Hart, K. Hantanasirisakul, A. C. Lang, B. Anasori, D. Pinto, Y. Pivak, J. T. van Omme, S. J. May, Y. Gogotsi, M. L. Taheri, *Nat. Commun.* **2019**, *10*, 522.

[5] G. Gao, A. P. O'Mullane, A. Du, *ACS Catal.* **2017**, 7, 494–500.

[6] Per. O. Å. Persson, J. Rosen, *Curr. Opin. Solid State Mater. Sci.* **2019**, *23*, 100774.

[7] K. D. Fredrickson, B. Anasori, Z. W. Seh, Y. Gogotsi, A. Vojvodic, *J. Phys. Chem. C* **2016**, *120*, 28432–28440.

[8] A. D. Handoko, K. D. Fredrickson, B. Anasori, K. W. Convey, L. R. Johnson, Y. Gogotsi, A. Vojvodic, Z. Wei. Seh, *ACS Appl. Energy Mater.* **2018**, *1*, 173–180.

[9] O. Mashtalir, M. Naguib, V. N. Mochalin, Y. Dall'Agnese, M. Heon, M. W. Barsoum, Y. Gogotsi, *Nat. Commun.* **2013**, *4*, 1716.

[10] A. Qian, J. Y. Seo, H. Shi, J. Y. Lee, C.-H. Chung, *ChemSusChem* **2018**, *11*, 3719–3723.

[11] B. Anasori, M. R. Lukatskaya, Y. Gogotsi, *Nat. Rev. Mater.* **2017**, *2*, 1–17.

[12] M. Seredych, C. E. Shuck, D. Pinto, M. Alhabeb, E. Precetti, G. Deysher, B. Anasori, N. Kurra, Y. Gogotsi, *Chem. Mater.* **2019**, *31*, 3324–3332.

[13] Y. Chae, S. Joon Kim, S.-Y. Cho, J. Choi, K. Maleski, B.-J. Lee, H.-T. Jung, Y. Gogotsi, Y. Lee, C. Won Ahn, *Nanoscale* **2019**, *11*, 8387–8393.

[14] H. Tang, S. Zhuang, Z. Bao, C. Lao, Y. Mei, *ChemElectroChem* **2016**, *3*, 871–876.

[15] M. Cao, F. Wang, L. Wang, W. Wu, W. Lv, J. Zhu, *J Electrochem Soc* **2017**, *164*, A3933.

[16] R. Lotfi, M. Naguib, D. E. Yilmaz, J. Nanda, A. C. T. van Duin, *J. Mater. Chem. A* **2018**, *6*, 12733–12743.

[17] T. K. Slot, F. Yue, H. Xu, E. V. Ramos-Fernandez, A. Sepúlveda-Escribano, Z. Sofer, G. Rothenberg, N. R. Shiju, *2D Mater.* **2020**, *8*, 015001.

[18] V. Natu, J. L. Hart, M. Sokol, H. Chiang, M. L. Taheri, M. W. Barsoum, *Angew. Chem. Int. Ed.* **2019**, *58*, 12655–12660.

[19] D. Wang, F. Li, R. Lian, J. Xu, D. Kan, Y. Liu, G. Chen, Y. Gogotsi, Yingjin. Wei, *ACS Nano* **2019**, *13*, 11078–11086.

[20] T. A. Le, Q. V. Bui, N. Q. Tran, Y. Cho, Y. Hong, Y. Kawazoe, Hyoyoung. Lee, *ACS Sustain. Chem. Eng.* **2019**, 7, 16879–16888.

[21] B. Huang, N. Li, W.-J. Ong, Naigen. Zhou, *J. Mater. Chem. Mater. Energy Sustain.* **2019**, 7, 27620–27631.

[22] J. Zhang, Y. Zhao, X. Guo, C. Chen, C.-L. Dong, R.-S. Liu, C.-P. Han, Y. Li, Y. Gogotsi, G. Wang, *Nat. Catal.* **2018**, *1*, 985–992.

[23] Y. Gogotsi, B. Anasori, *ACS Nano* **2019**, *13*, 8491–8494.

[24] Z. Li, Y. Wu, *Small* **2019**, *15*, 1804736.

[25] E. B. Deeva, A. Kurlov, P. M. Abdala, D. Lebedev, S. M. Kim, C. P. Gordon, A. Tsoukalou, A. Fedorov, C. R. Müller, *Chem. Mater.* **2019**, *31*, 4505–4513.

[26] Z. Li, L. Yu, C. Milligan, T. Ma, L. Zhou, Y. Cui, Z. Qi, N. Libretto, B. Xu, J. Luo, E. Shi, Z. Wu, H. Xin, W. N. Delgass, J. T. Miller, Y. Wu, *Nat. Commun.* **2018**, *9*, 1–8.

[27] J. D. Gouveia, Á. Morales-García, F. Viñes, J. R. B. Gomes, F. Illas, *ACS Catal.* **2020**, *10*, 5049–5056.

[28] R. Thakur, M. Hoffman, A. VahidMohammadi, J. Smith, M. Chi, B. Tatarchuk, M. Beidaghi, C. A. Carrero, *ChemCatChem* **2020**, 12, 3639–3643.

[29] M. Ding, W. Chen, H. Xu, Z. Shen, T. Lin, K. Hu, C. hui Lu, Z. Xie, *J. Hazard. Mater.* **2020**, *382*, 121064.

[30] M. Ding, W. Chen, H. Xu, Z. Shen, T. Lin, K. Hu, Q. Kong, G. Yang, Z. Xie, *Chem. Eng. J.* **2019**, *378*, 122177.

[31] Z. Xue, J. Jiang, M.-G. Ma, M.-F. Li, T. Mu, *ACS Sustain. Chem. Eng.* **2017**, *5*, 2623–2631.

[32] A. Santiago-Portillo, S. Navalón, P. Concepción, M. Álvaro, H. García, *ChemCatChem* **2017**, *9*, 2506–2511.

[33] E. V. Beletskiy, X. Hou, Z. Shen, J. R. Gallagher, J. T. Miller, Y. Wu, T. Li, M. C. Kung, H. H. Kung, *J. Am. Chem. Soc.* **2016**, *138*, 4294–4297.

[34] M. Mirza-Aghayan, M. Alizadeh, M. Molaee Tavana, R. Boukherroub, *Tetrahedron Lett.* **2014**, *55*, 6694–6697.

[35] A. Das, N. Anbu, M. Sk, A. Dhakshinamoorthy, S. Biswas, *ChemCatChem* **2020**, *12*, 1789–1798.

[36] P. Dutta, P. Kalita, P. K. Baruah, *ChemistrySelect* **2016**, *1*, 1650–1657.

[37] G. Ramos-Fernandez, M. Muñoz, J. C. García-Quesada, I. Rodriguez-Pastor, I. Martin-Gullon, *Polym. Compos.* **2018**, *39*, 2116–2124.

[38] B. Ahmed, D. H. Anjum, M. N. Hedhili, Y. Gogotsi, H. N. Alshareef, *Nanoscale* **2016**, *8*, 7580–7587.

[39] H. Zou, B. He, P. Kuang, J. Yu, Ke. Fan, *ACS Appl. Mater. Interfaces* **2018**, *10*, 22311–22319.

[40] C. Hernandez-Mejia, E. S. Gnanakumar, A. Olivos-Suarez, J. Gascon, H. F. Greer, W. Zhou, G. Rothenberg, N. R. Shiju, *Catal. Sci. Technol.* **2016**, *6*, 577–582.

[41] J. Lu, K. M. Kosuda, R. P. Van Duyne, P. C. Stair, *J. Phys. Chem. C* **2009**, *113*, 12412–12418.

[42] C. A. Teles, P. M. de Souza, R. C. Rabelo-Neto, M. B. Griffin, C. Mukarakate, K. A. Orton, D. E. Resasco, F. B. Noronha, *Appl. Catal. B Environ.* **2018**, *238*, 38–50.

[43] Y. H. Wang, W. G. Gao, H. Wang, Y. E. Zheng, W. Na, K. Z. Li, *RSC Adv.* **2017**, 7, 8709–8717.

[44] A. I. Osman, J. K. Abu-Dahrieh, A. Abdelkader, N. M. Hassan, F. Laffir, M. McLaren, D. Rooney, *J. Phys. Chem. C* **2017**, *121*, 25018–25032.

[45] E. V. Ramos-Fernandez, N. J. Geels, N. R. Shiju, G. Rothenberg, *Green Chem.* **2014**, *16*, 3358–3363.

[46] L. E. Oi, M.-Y. Choo, H. V. Lee, H. C. Ong, S. B. A. Hamid, J. C. Juan, *RSC Adv.* **2016**, *6*, 108741–108754.

[47] J. L. Ropero-Vega, A. Aldana-Pérez, R. Gómez, M. E. Niño-Gómez, *Appl. Catal. Gen.* **2010**, *379*, 24–29.

4.6 Appendix

4.6.1 Experimental details

Calculation of molar fractions

Styrene oxide, 2-phenyl acetaldehyde and products **1** and **2** were obtained in >95% purity and identified using NMR. For each compound a series of calibration solutions was prepared using bromobenzene as internal standard. The respective relative response factors of the reactants (in reference to styrene oxide) were determined and used to calculate molar fractions, selectivities and yields. For other known compounds, the relative response factors were estimated using existing methods.[1] For unknown compounds we used the response factor of product **1**. GC signals were integrated and divided by the bromobenzene areas. The resulting fractions were corrected with the relative response factors to calculate molar quantities.

4.6.2 Additional figures

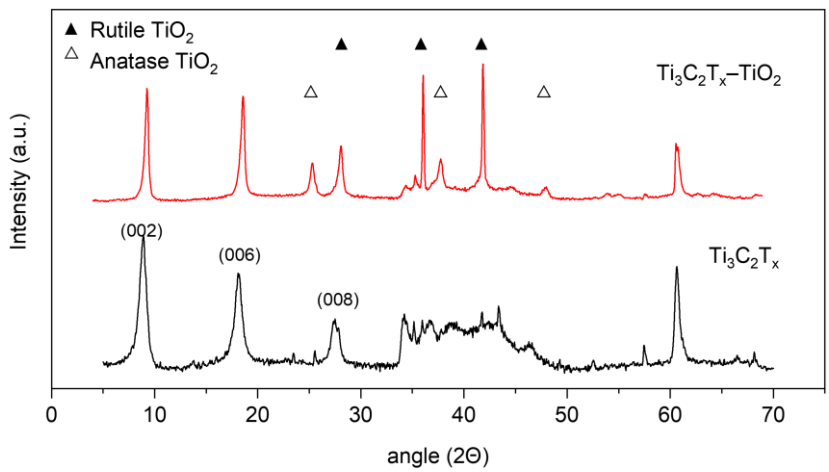

Figure A4.1. XRD data of $Ti_3C_2T_x$ (bottom) and $Ti_3C_2T_x$-TiO_2 composite (top).

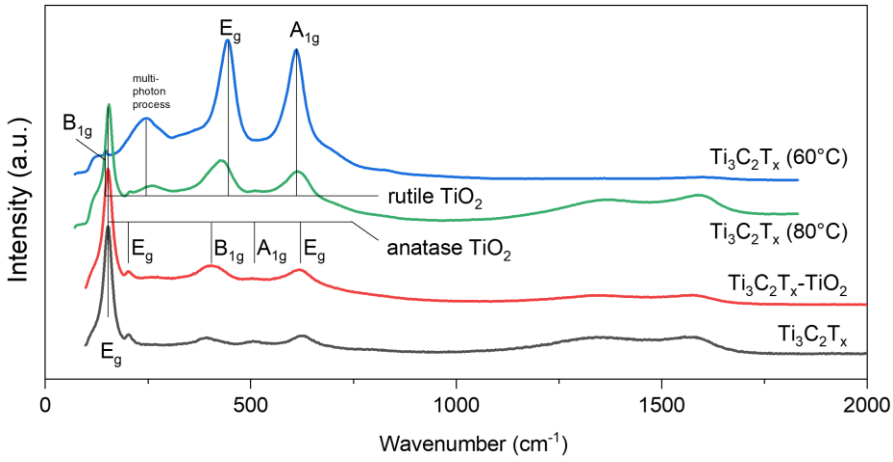

Figure A4.2. Normalized Raman spectra of $Ti_3C_2T_x$ (black), $Ti_3C_2T_x$-TiO_2 (red), and $Ti_3C_2T_x$ MXene after reaction with SO for 5h at 60 °C (blue) and 80 °C (green).

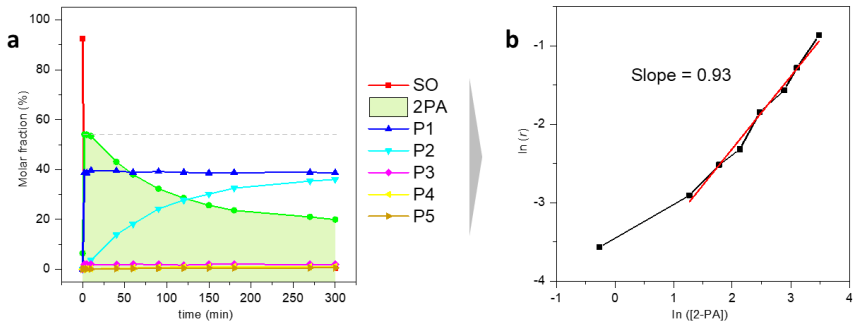

Figure A4.3. (**a**) Reaction of styrene oxide with MXene at 45 °C in ethanol, and (**b**) a replot of ln (rate) of 2-PA conversion versus ln concentration. The grey line in figure a represents the maximum attained concentration of 2-PA.

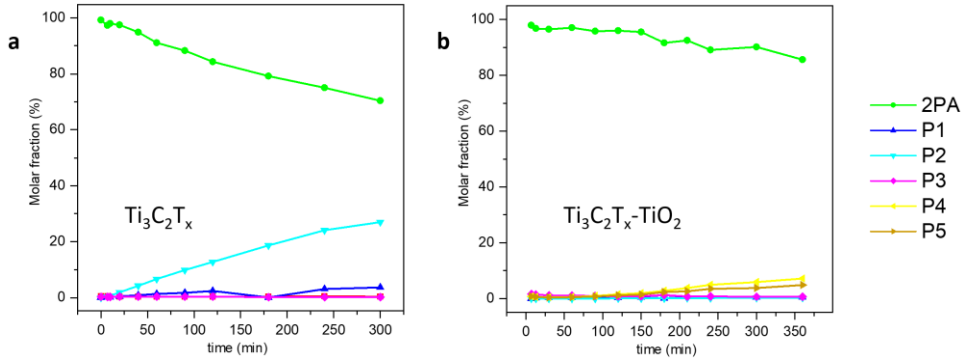

Figure A4.4. Reaction of 2-phenyl acetaldehyde with (**a**) Ti_3C_2Tx MXene and (**b**) Ti_3C_2Tx-TiO_2 composite in ethanol at 45 °C.

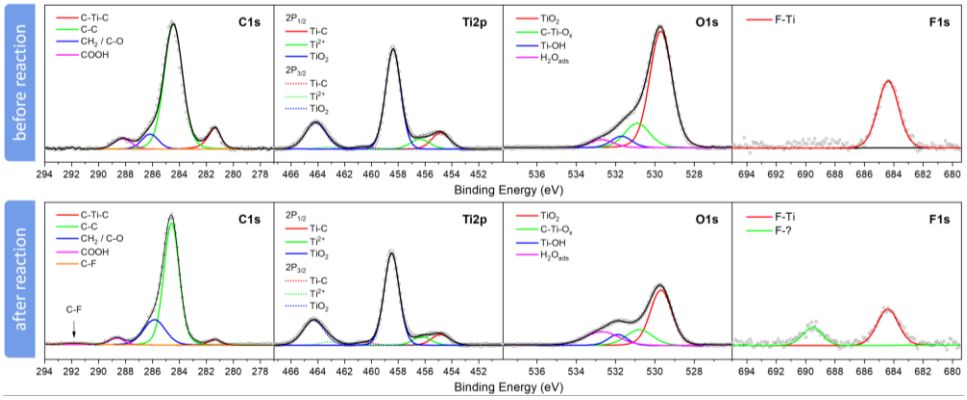

Figure A4.5. Normalized X-ray photoelectron spectra of Ti_3C_2-TiO_2 composite before reaction (top) and after reaction at 45 °C (bottom). Intensity is in arbitrary units.

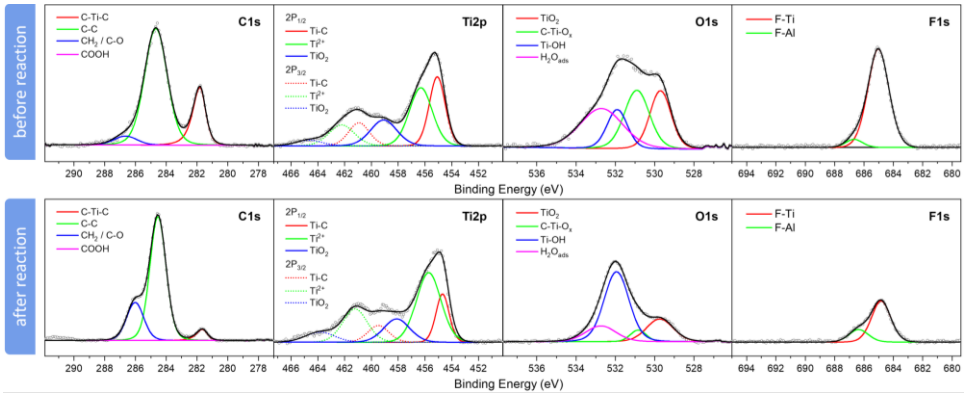

Figure A4.6. Normalized X-ray photoelectron spectra of $Ti_3C_2T_x$ MXene before reaction (top) and after reaction at 45 °C (bottom). Intensity is in arbitrary units.

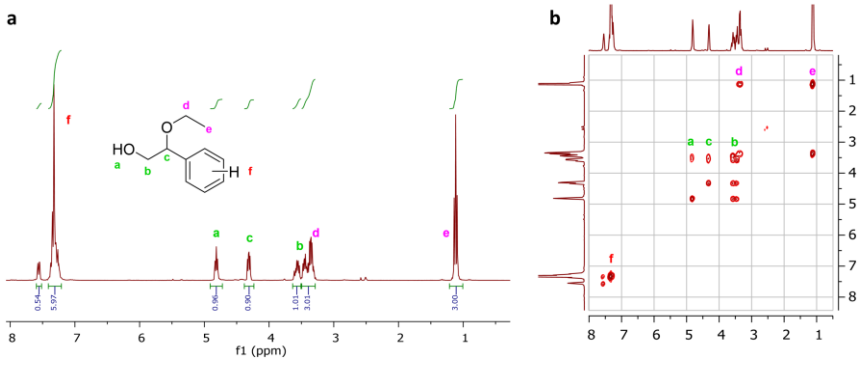

Figure A4.7. (**a**) ^{1}H NMR spectrum of product 1, obtained from the reaction of styrene oxide with MXene-TiO_2 composite at 45 °C in ethanol and (**b**) ^{1}H COSY correlation spectrum for product **1**. The ^{1}H spectrum **a** contains an unknown aromatic impurity at 7.6 ppm without any cross-signals in COSY.

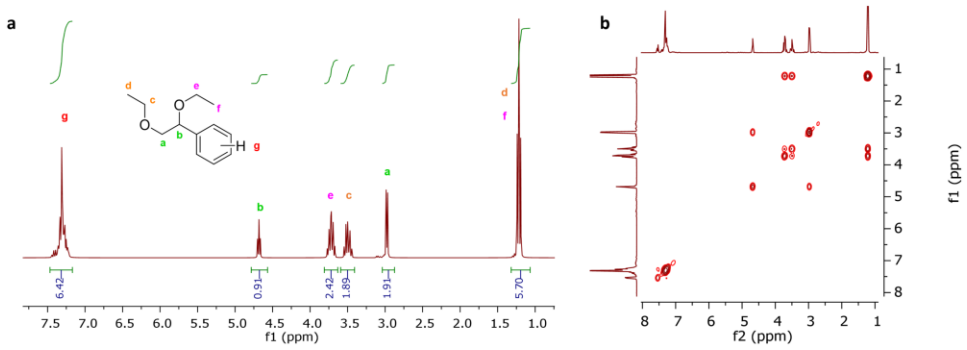

Figure A4.8. (**a**) ^{1}H NMR spectrum of product **2**, obtained from the reaction of styrene oxide catalysed by MXene-TiO_2 composite at 45 °C in ethanol and (**b**) ^{1}H COSY correlation spectrum for product **2**. The ^{1}H spectrum contains a minor amount of 2-PA as an impurity, which mainly contributes to the aromatic signal.

NMR data for figures A4.7 and A4.8

Product **1**: ^{1}H NMR (300 MHz, Chloroform-*d*) δ 7.47 – 7.16 (m, 5H), 4.46 (dd, *J* = 8.3, 3.9 Hz, 1H), 3.70 (td, *J* = 8.4, 2.9 Hz, 2H), 3.58 – 3.33 (m, 2H), 2.80 (s, 1H), 1.25 (t, *J* = 7.0 Hz, 3H). ^{1}H NMR (300 MHz, DMSO-d_6) δ 7.43 – 7.04 (m, 5H), 4.81 (d, *J* = 5.9 Hz, 1H), 4.31 (dd, *J* = 7.2, 4.5 Hz, 1H), 3.63 – 3.39 (m, 2H), 3.34 (dq, *J* = 7.0, 3.7 Hz, 2H), 1.10 (dt, *J* = 7.0, 2.5 Hz, 3H).

Product **2**: ^{1}H NMR (300 MHz, Chloroform-*d*) δ 7.48 – 7.17 (m, 5H), 4.68 (t, *J* = 5.6 Hz, 1H), 3.72 (dq, *J* = 9.3, 7.1 Hz, 2H), 3.50 (dq, *J* = 9.3, 7.0 Hz, 2H), 2.98 (d, *J* = 5.7 Hz, 2H), 1.22 (t, *J* = 7.1 Hz, 6H).

4.6.3 References

[1] J. de Saint Laumer, S. Leocata, E. Tissot, L. Baroux, D. M. Kampf, P. Merle, A. Boschung, M. Seyfried, A. Chaintreau, *J. Sep. Sci.* **2015**, *38*, 3209–3217.

[2] G. Ramos-Fernandez, M. Muñoz, J. C. García-Quesada, I. Rodriguez-Pastor, I. Martin-Gullon, *Polym. Compos.* **2018**, *39*, 2116–2124.

[3] A. Ganguly, S. Sharma, P. Papakonstantinou, J. Hamilton, *J. Phys. Chem. C* **2011**, *115*, 17009–17019.

5

Surface oxidation of MXene enhancing the catalytic activity of Pt nanoparticles ‡

‡ Parts of this work have been published as:

Surface oxidation of $Ti_3C_2T_x$ enhances the catalytic activity of supported platinum nanoparticles in ammonia borane hydrolysis

T. K. Slot, F. Yue, H. Xu, E. V. Ramos-Fernandez, A. Sepúlveda-Escribano, Z. Sofer, G. Rothenberg and N. Raveendran Shiju.

2D Mater. **2021**, 8, 015001. DOI: 10.1088/2053-1583/ababef

This work is also featured in a short animation, see https://youtu.be/T6ooXNkuC9Q

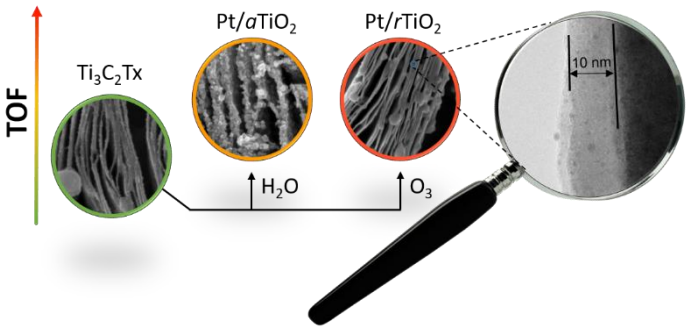

Ozone therapy: a new route to oxygen-deficient rutile TiO_2, boosting the activity of Pt nanoparticles in ammonia borane hydrolysis.

5

Abstract: MXenes, first discovered in 2011, are two-dimensional transition metal carbides or nitrides. Because of their interesting electrical and optical properties, they are studied for applications in batteries, supercapacitors and electrocatalysis. However, MXenes are rarely used in heterogeneous catalysis and, to our knowledge, there are no reports on the use of oxidized MXenes in catalysis. Here, we used $Ti_3C_2T_x$-derived materials as supports for platinum nanoparticles and studied their effectiveness for the hydrolysis of ammonia borane, which is a promising hydrogen carrier. Hydrogen can be released from ammonia borane through catalytic hydrolysis. Most heterogeneous catalysts reported for this purpose contain a noble metal supported on a metal oxide support. The interaction between the metal and the support is important in determining the catalytic performance. Our results show that the electronic environment of platinum can be modified by oxidising the surface of MXene, thus providing a new way of developing active catalysts. Oxidising agents, such as water and ozone can be used for this purpose. This electronic modification enhances the catalytic activity of platinum for ammonia borane hydrolysis, which is relevant for other reactions related to energy production/storage.

5.1 Introduction

MXenes are novel two-dimensional transition metal carbides, nitrides or carbonitrides.[1] Their structure is defined as $M_{n+1}X_nT_x$, where M is an early transition metal, X is carbon and/or nitrogen, and T stands for a terminating functional group.[2] They are produced by extracting the 'A' layers from MAX phases, which are layered ternary transition metal carbides.[2–5] MXenes have been studied extensively in the past few years, especially for electrocatalysis.[6–13] Their thermo-catalytic applications, however, are less known. Li *et al.* recently showed that MXenes are promising supports for nanoparticle-based catalysts and they can change the nature of the active sites, making them highly selective towards C–H activation.[14,15] Here, we use a different approach: we reasoned that oxidizing the surface of MXenes can influence the metal supported on it, thereby modulating the catalytic activity when compared to the metal supported on pristine MXene. Taking ammonia borane hydrolysis as a probe reaction, we show that this oxidation approach enhances the catalytic activity of supported metal particles. Usually, the oxidation leads to particles of anatase (TiO_2) along the edges of the flakes and the basal planes.[16–18] Reaction conditions such as temperature and solvent choice can control the structure of the resulting titania ranging from simple layers to complex nanostructures.[17,19] Here we used, for the first time, controlled oxidation with ozone, which resulted mainly in *rutile* titania on a partially exfoliated $Ti_3C_2T_x$ MXene surface. Impregnating this surface with a platinum salt gave stable sub-nanometre platinum particles that were highly active as ammonia borane hydrolysis catalysts.

Ammonia borane hydrolysis is an emerging method for on-demand hydrogen generation. While hydrogen is acknowledged as the fuel of the future,[20–23] its current storage and transportation methods have serious drawbacks. Hydrogen storage should be safe, easy, reversible, and should have a high gravimetric/volumetric capacity. This makes chemical hydrogen storage a promising option.[24–26] Recently, ammonia borane (NH_3BH_3) attracted considerable attention because of its high hydrogen density, stability and relative ease of hydrolysis.[27–33] Here, we show how modifications on the MXene surface can influence the reactivity of Pt particles towards H_2 generation from ammonia borane. (Eq. 5.1)

$$NH_3BH_3 + 4H_2O \xrightarrow[\substack{20\text{ - }85°C,\\ 45\text{ min}}]{Pt/Ti_3C_2T_x} NH_4^{\oplus} + B(OH)_4^{\ominus} + 3H_2 \qquad (5.1)$$

5.2 Results and discussion

First, we studied the ozone oxidation of $Ti_3C_2T_x$ MXene. We suspended $Ti_3C_2T_x$ in chloroform and then bubbled ozone at controlled conditions (see experimental section for details). For comparison, we also used two other oxidative treatments:

hydrothermal treatment at 200 °C, and treatment with H_2O_2 (see Figure 5.1). These oxidative treatments changed the surface of MXene significantly (*cf.* SEM images in Figure 5.1). We then impregnated all three samples with platinum using the double-solvent method (water in hexanes).[34] The samples were dried at 80 °C, heat-treated at 250 °C in nitrogen and finally reduced at 250 °C using 10% hydrogen in nitrogen. The final Pt loading was 1 wt%.

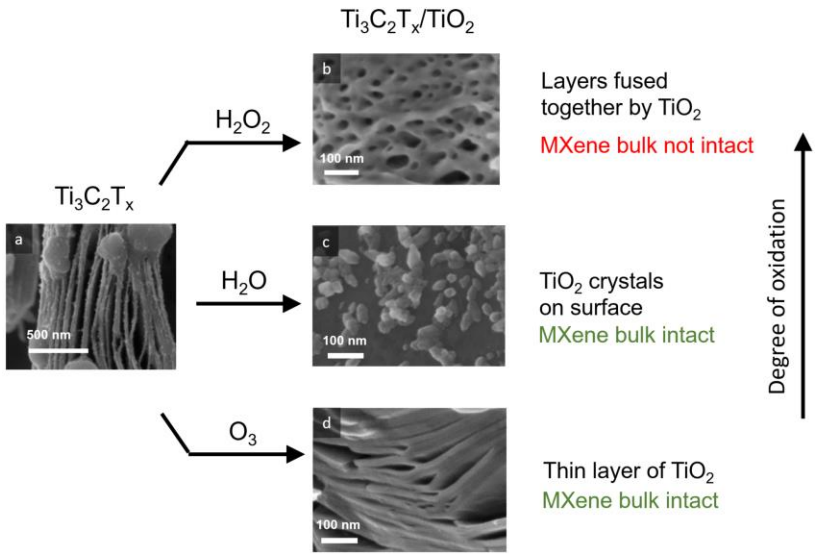

Figure 5.1. Synthesis routes to the $Ti_3C_2T_x$-TiO_2 composites with corresponding SEM images: (**a**) pristine $Ti_3C_2T_x$, (**b**) H_2O_2 treated $Ti_3C_2T_x$, (**c**) water-treated $Ti_3C_2T_x$, and (**d**) ozone-treated $Ti_3C_2T_x$.

We then tested these catalysts in ammonia borane hydrolysis.[35–44] The progress of this reaction can be easily monitored by measuring the volume of H_2 produced, using our new gas quantification setup.[45] This device precisely records gas production with time, gathering thousands of data points for a single reaction. Additionally, ammonia borane hydrolysis has a very low concentration dependence on ammonia borane (partial reaction order n=0.1–0.2), allowing us to gather turnover frequency (TOF) data with respect to temperature as well. All TOFs were calculated assuming the total weight of Pt is available for catalysis (in practice, the TOF values per available Pt atom would be somewhat higher, considering the small size of the clusters, 0.6-1.6 nm).

Control reactions showed that the catalytic activity of pristine or oxidized MXenes without platinum was negligible. Platinum supported on untreated MXene (Pt/MXene) gave a turnover frequency of 40 min^{-1}. Supporting Pt on ozone-treated MXene (Pt/MXene-O_3) increased the TOF seven-fold to 250–300 min^{-1} (see Figure 5.2**a**). This shows that the surface treatment influences the reactivity significantly. Pt supported on water-treated MXene (Pt/MXene-H_2O) also gave a high TOF (Figure 5.2**a**). The apparent activation energy (E_a) calculated from Arrhenius plots is 69 kJ mol^{-1} for

Pt/MXene-O_3. The peroxide treated MXene did not show any improvement compared to the milder oxidation methods. The apparent activation energy of Pt/MXene-H_2O is higher (99 kJ mol^{-1}), suggesting these samples have different rate-determining steps (in the case of a single reaction step) or a have a different environment around the active site.

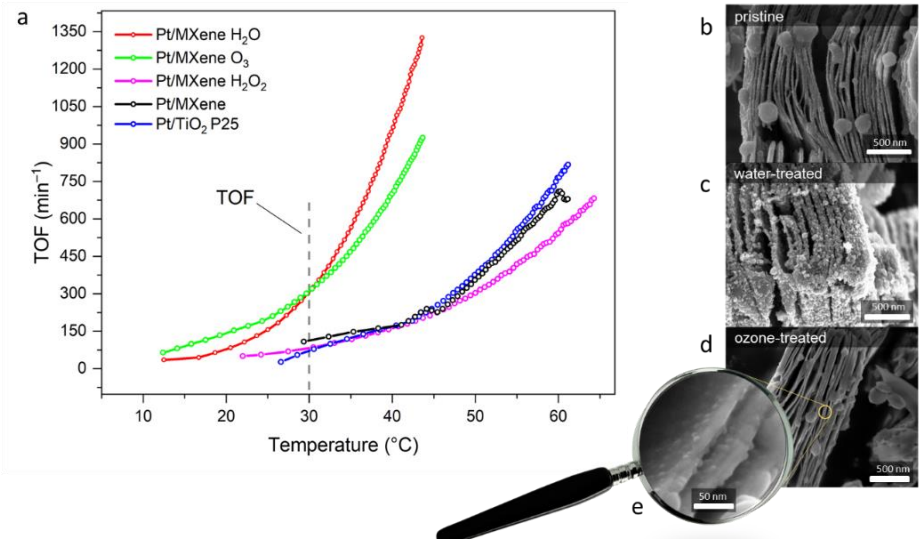

Figure 5.2. (**a**) Turnover frequency (TOF) versus temperature for the hydrolysis of ammonia borane of several MXene-TiO_2 composites. Data is shown for conversion between 0 and 20%. Scanning electron micrographs of Pt-loaded catalysts of (**b**) pristine $Ti_3C_2T_x$, (**c**) water-treated $Ti_3C_2T_x$, and (**d**) ozone-treated $Ti_3C_2T_x$ and (**e**) at higher magnification.

We then studied the structure of the modified catalysts using several characterization techniques. An overview of the catalyst properties is shown in Table 5.1. Interestingly, scanning electron microscopy (SEM) showed no major structural changes after ozone exposure of $Ti_3C_2T_x$ MXene (*cf.* Figs. 5.2**b** to 5.2**d**). In contrast, we saw major changes on the surface of MXene when treated hydrothermally or with H_2O_2 (Figure 5.1**b**), proving that the surface structure changes depend on the treatment method. Oxidation of $Ti_3C_2T_x$ MXene with water gave crystalline structures on the surface.[18,46,47] X-ray diffraction (XRD) shows these structures mainly consist of anatase titania (Figure 5.3). Peroxide treatment completely converted the MXene bulk into amorphous titania and, consequently, did not show any improved reactivity. This suggests that a MXene lattice core is required for reactivity enhancement. XRD shows that each oxidation method gives different titania phase compositions (Figure 5.3). Ozone treatment results in rutile and amorphous phases. Hydrothermal treatment gives both rutile and anatase, while hydrogen peroxide produces an amorphous material, comparable with bulk TiO_2. The exact reasons for these differences are unclear. We think this is related to the oxidant strength and/or solvent type. Transmission electron micrographs (TEM)

revealed an oxidised surface layer of around 10–15 nm thickness for the ozone treated samples (Figure 5.6**d**). XRD further revealed that ozone treatment generated a crystalline phase corresponding to rutile titania (Figure 5.3). This is interesting, as rutile TiO_2 usually forms at higher temperatures while our ozone experiments were run at ambient temperature. Other oxidation treatments predominantly led to the formation of anatase titania.[16,46] As far as we know, this is the first report showing that oxidation with ozone forms rutile titania on MXene surfaces.

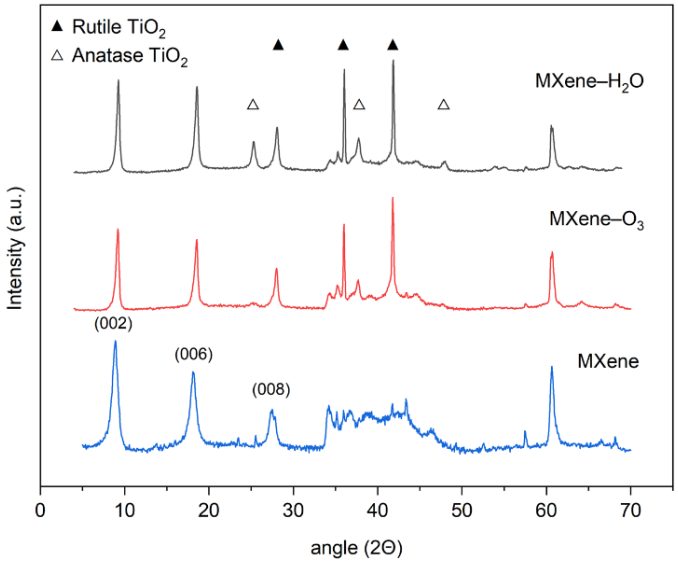

Figure 5.3. X-ray diffractograms of pristine MXene (blue), ozone-treated MXene (red), and water-treated MXene (black).

Table 5.1. Overview of physical and catalytic parameters for the MXene composite catalysts

Material	**TOF[a] 30 °C (min^{-1})**	**E_a[b] ($kJ\ mol^{-1}$)**	**Pt particle size[c] (nm)**	**SSA ($m^2\ g^{-1}$)**
Pt/MXene	39	60	1.6	23
Pt/MXene-O_3	265	69	0.6	30
Pt/MXene-H_2O	272	99	1.5	10
Pt/TiO_2-anatase	38	64	-	5

[a] Calculated from H_2 production using reaction order of 0.15 in ammonia borane. [b] Apparent activation energy obtained from triplicate run data up to 20% conversion of ammonia borane. [c] Calculated from HAADF-TEM data statistical analysis observing >100 particles.

Raman spectroscopy on our oxidised MXenes showed the characteristic TiO_2 bands as well as the D/G band corresponding to graphitic layers (see Figure 5.4). For the ozone-treated sample, we observed strong rutile TiO_2 signals at 430 cm^{-1} (E_g) and 607 cm^{-1} (A_{1g}), confirming the presence of rutile titania at the surface.[48–50] The water-treated sample showed strong anatase TiO_2 signals at 152 and 204 cm^{-1} (E_g) while the remaining signals at 408, 506 and 621 cm^{-1} overlap with those of MXene.

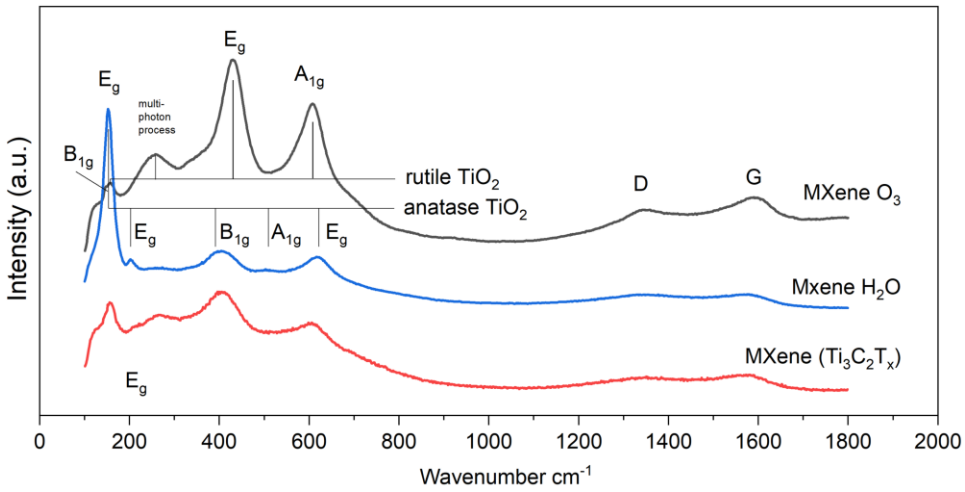

Figure 5.4. Raman spectra for ozone-treated MXene, water-treated MXene and pristine MXene

The N_2 adsorption measurements for pristine and ozone-treated MXene gave BET surface areas of 23 and 30 $m^2 g^{-1}$, respectively (Figure 5.5). A MXene-TiO_2 composite was reported to have a surface area of 32 $m^2 g^{-1}$ in previous work.[51] Literature estimates range from 8 to 30 m^2 g^{-1} for multilayer $Ti_3C_2T_x$, depending on the degree of delamination.[51–53]

Electron microscopy studies of Pt/MXene-O_3 and Pt/MXene-H_2O showed a uniform distribution of Pt particles (see Figure 5.6). For Pt/MXene-O_3, the Pt particles are also well dispersed within the space between the MXene layers as shown by SEM (Figure 5.2**e**). However, particle size distribution studies showed a major difference (Figure 5.6**e**-**f**). A relatively uniform size distribution with an average particle size around 1.5–1.6 nm was observed for Pt/MXene and Pt/MXene-H_2O. However, the Pt particles on Pt/MXene-O_3 were smaller, with an average size of 0.6 nm. Thus, the characterization data show that our unique ozone treatment method gives a surface enriched with rutile titania and the Pt nanoparticles deposited on this surface remain small in size. In previous work, we observed the retention of small particle size when Ru was deposited on bulk rutile titania. However, in that case a lattice matching was possible between the rutile RuO_2 intermediate and rutile TiO_2.[54] Such matching is not expected here, so the

small particle size cannot be explained by this reason. Ozone is very reactive, and there is no water to facilitate crystallisation, as in the case of the MXene-H_2O material.

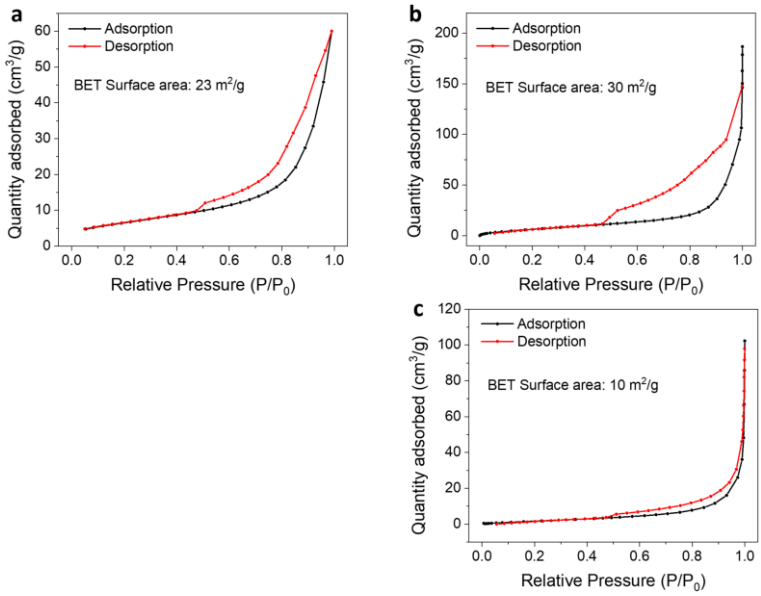

Figure 5.5. N_2 adsorption-desorption isotherms (-196 °C) for (**a**) pristine MXene, (**b**) ozone-treated MXene, and (**c**) water-treated MXene.

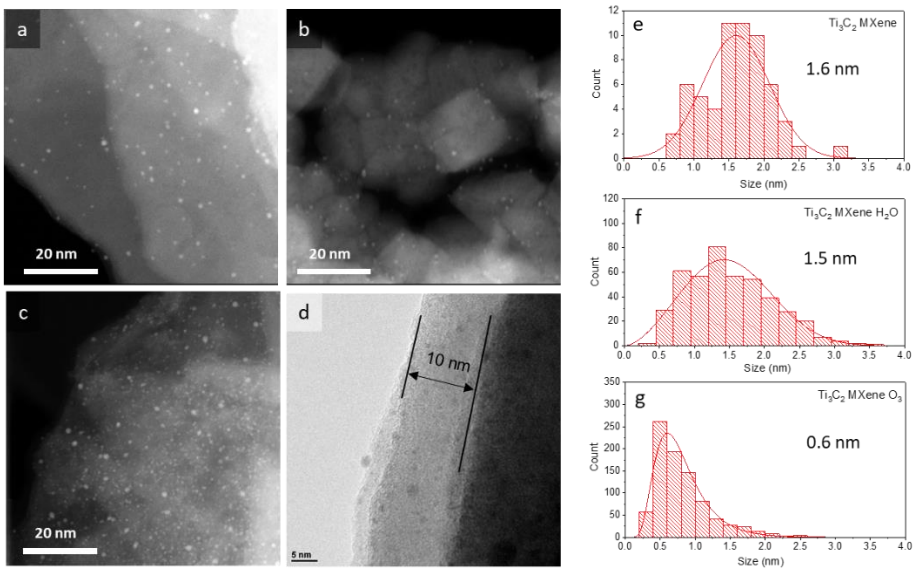

Figure 5.6. HAADF-STEM images of 1wt% loaded (**a**) Pt/MXene, (**b**) Pt/MXene-H_2O, (**c**) Pt/MXene-O_3 catalysts, (**d**) TEM micrograph of 1% platinum-loaded Pt/MXene-O_3 catalysts, and (**e-g**) statistical analysis of Pt particle size obtained from HAADF-STEM micrographs (a-c), respectively.

We expect that ozone treatment forms a rough amorphous/rutile surface, with many defect sites, possibly even oxygen vacancies. The rough surface likely hinders the aggregation of Pt atoms during particle formation, allowing the structure to retain a small Pt particle size. Chen *et al.* studied the relation between catalytic activity of Pt and its particle size on carbon nanotubes, suggesting an optimal Pt particle size of 1.8nm.[55] For smaller particles, they observed a decreasing TOF. However, their support does not interact with the Pt particles. We *do* observe very good activity at small sizes, especially for the ozone-treated catalyst. This suggests that the high TOF is the result of an electronic interaction between the Pt particles and the oxidised MXene support. The ozone-treated and water-treated catalysts are equally active, even though their particle sizes differ. This shows that particle-size effects are less important here.

TEM data shows that platinum particles are deposited on the surface titania layer, apparently with no direct contact with the bulk MXene (Figure 5.6**d**). To compare the activity of this material with bulk titania, we prepared and tested a Pt/TiO_2 catalyst, using a commercial bulk titania (Degussa P25, anatase:rutile ~3:1) as the support. However, this catalyst was less active than the oxidized MXene catalysts (Figure 5.2**a**). This suggests that the electronic nature of Pt is modified on oxidized $Ti_3C_2T_x$ MXene, enhancing its catalytic activity. Though the Pt nanoparticles are supported on the titania layer, the underlying bulk MXene has an influence, making it different from Pt/bulk titania catalysts.

To gain further insight, we studied the electronic structure of the Pt/MXene catalysts with XPS. Pt 4f XPS spectra and their deconvolution show that the binding energy shifts upward by 0.4 eV (Figure 5.7**a**) for Pt/MXene-O_3 and Pt/MXene-H_2O. This indicates that Pt is in a higher oxidation state when it is deposited on oxidised MXene. This shift is even more pronounced than what was previously reported for $Pt/Ti_3C_2T_x$.[14] This shift also correlates with the high catalytic activity of Pt/MXene–O_3 and Pt/MXene–H_2O (Figure 5.2**a**). If the electron transfer is from the TiO_2 to the supported particle, a shift towards lower binding energy is expected. We may assume that the reverse occurs in this case, making the Pt nanoparticles more electron deficient. XPS confirmed that the surfaces of all of the oxidised MXene samples contain TiO_2, and that the titania surface is electron-deficient compared to bulk titania (Figure 5.7**b**/**c**). We hypothesize that for both Pt/MXene–O_3 and Pt/MXene–H_2O the shift of the Pt 4f signal stems from the interaction of Pt with this electron-deficient titania layer, withdrawing charge from interacting Pt particles.

At high temperatures (>500 °C), $Ti_3C_2T_x$ MXene can even form Pt-Ti intermetallic phases, which modifies the catalytic activity.[14] We did not observe intermetallic phases (our treatment temperature was 250 °C); thus, this can be ruled out as the cause of enhanced catalytic activity. The ammonia part in ammonia borane is electron-rich and may interact strongly with the small Pt particles on the oxidised MXene, enhancing the rate of the reaction.

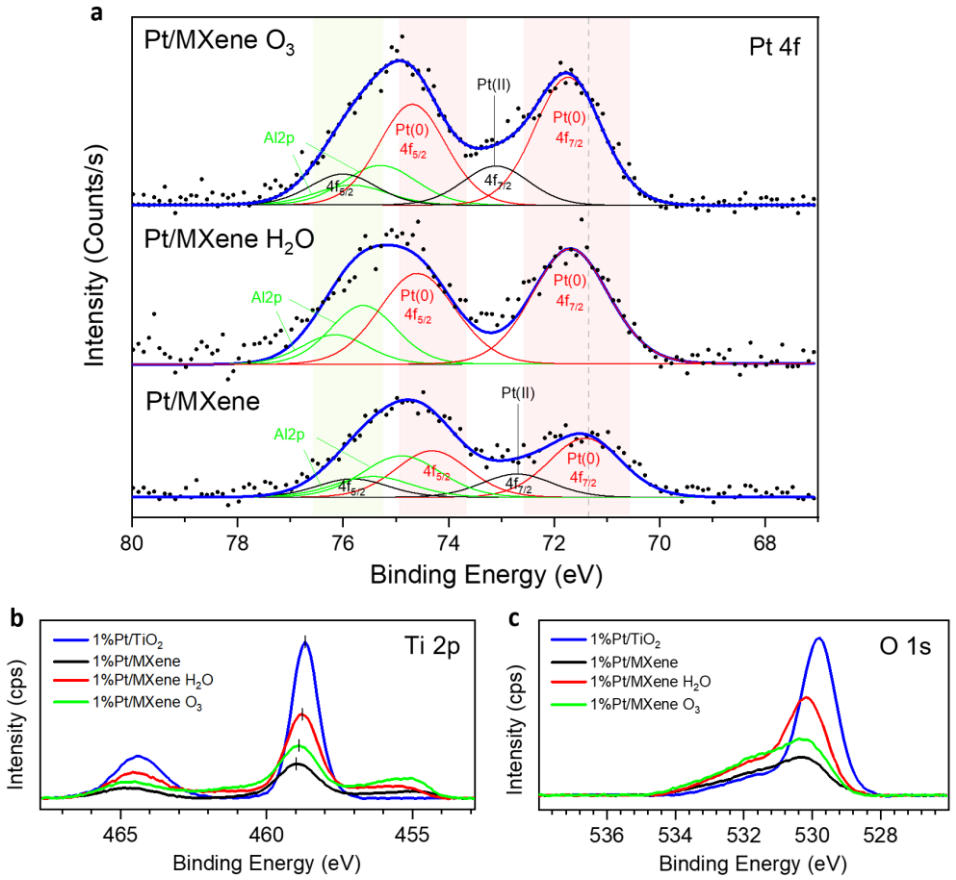

Figure 5.7. XPS spectra of (**a**) Pt 4f region (with deconvolution) of 1wt% platinum-loaded MXene-TiO_2 composites compared to Pt/MXene, (**b**) Ti 2p, and (**c**) O 1s regions of the 1wt% platinum-loaded MXene-TiO_2 composites compared to MXene.

The mechanism of ammonia borane hydrolysis is still unclear. According to Chen *et al.*, ammonia borane hydrolysis is expected to proceed through a Langmuir-Hinshelwood mechanism with O–H bond cleavage by Pt-bound NH_3BH_2* as rate-determining step (where * indicates a free surface site).[56] Other authors agree that O–H cleavage must be the rate determining step, however, there is no consensus regarding the reacting borane species.[57–64] Increased NH_4^+ concentrations did not influence our hydrolysis reaction much, suggesting B–N bond dissociation is not a critical step for our catalyst and might even not happen at all. It is widely known that ammonia borane hydrolysis depends on the pH of the solution, increasing reaction rate in presence of both acid and base.[59,61,65,66] When NaOH was added to the reaction mixture, we observed a 30% increase in reaction rate, suggesting that OH^- plays a role in the reaction. Both water and aqueous base dissociate reversibly on Pt surface according to Eqs. 5.2 and 5.3.[67]

Electron-deficient Pt therefore increases the surface concentration of OH*, hence directly impacting the rate-determining step. Electron-deficient Pt also enables dissociation of B–H bonds, improving the reaction rate for the Pt/MXene-H_2O and Pt/MXene-O_3 catalysts.

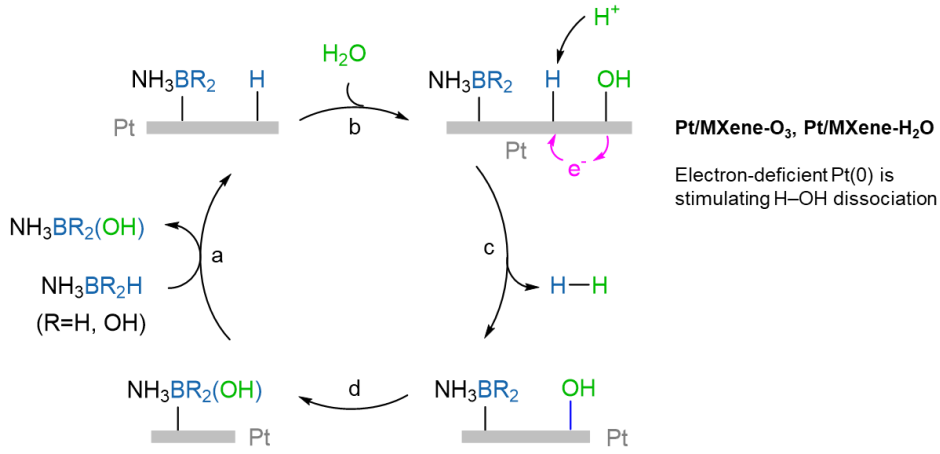

Figure 5.8. Suggested mechanism for Pt-catalysed ammonia borane hydrolysis: (a) binding and dissociation of the B–H bond on the Pt surface, (b) water adsorption and dissociation, (c) hydrogen formation, and (d) the rate-determining step: combining OH* with NH_3BR_2.

$$H_2O + * \rightleftharpoons OH^* + H^+ + e^- \quad (5.2)$$

$$OH^- + * \rightleftharpoons OH^* + e^- \quad (5.3)$$

Based on this information, we suggest a variation on the mechanisms proposed by Chen *et al.* focussing on O–H bond cleavage and subsequent reaction with NH_3BH_2* (Figure 5.8). Ammonia borane adsorbs on the Pt surface and one B–H bond dissociates, forming NH_3BH_2* and H* (Figure 5.8**a**). Water adsorbs to the surface and dissociates into OH*, H^+ and e^-(Figure 5.8**b**). This H^+/e^- pair reacts with H* to form hydrogen (Figure 5.8**c**). Then, the OH* intermediate combines with NH_3BH_2*, forming $NH_3BH_2(OH)$* (Figure 5.8**d**) which then desorbs. The remaining B–H bonds react analogously. The electron deficient Pt plays a key role in this process.

5.3 Conclusions

We show for the first time that room temperature ozone treatment is an effective method for modifying the surface of MXenes. The simple controlled treatment with ozone at room temperature yields a mildly oxidised surface, which is less oxidised compared to hydrothermal or H_2O_2 treatments. Importantly, the oxidation with ozone

creates a thin surface layer of predominantly rutile titania. Conventional heating methods require a high temperature to produce rutile titania. Depositing platinum on this layer results in highly dispersed nanoparticles with an average size less than 1 nm, yet with a more electron-deficient state than that of Pt on non-treated MXene. This means that the electronic environment of a supported metal nanoparticle can be modified by surface oxidation of the MXene. Overall, this electronic modification enhances the catalytic activity of platinum nanoparticles for ammonia borane hydrolysis, giving a faster and more efficient hydrogen production in ammonia borane hydrolysis. Considering the growing number of MXene compositions reported, the scope of study for their further derivatisation and application is very broad.

5.4 Experimental Section

MXene ($Ti_3C_2T_x$) Synthesis

All chemicals were obtained from commercial sources and were used as received. Ti_3AlC_2 was obtained from Carbon-Ukraine and had a purity > 95%, verified by X-ray diffraction (XRD). Ti_3AlC_2 was etched with HF (40 wt%) for 7 days under continuous stirring at room temperature. Afterwards, the mixture was repeatedly centrifuged and washed with deionized water until the pH of the supernatant was neutral. The powder obtained after this procedure was dried under vacuum. The resulting material is denoted as $Ti_3C_2T_x$.

Synthesis of MXene composites

Ozone treatment (MXene-O_3). $Ti_3C_2T_x$ (100 mg) was suspended in chloroform (10 mL) and stirred at 1000 rpm. Ozone was bubbled through the suspension at a rate of 25 mL min^{-1} for 1 h at 22 °C. The mixture was centrifuged (3000 × *g*) and washed twice with chloroform. The product was dried under vacuum at 30 °C for 16 h.

Hydrothermal treatment of MXene (MXene-H_2O). $Ti_3C_2T_x$ (100 mg) and water (25 mL) were added to a 75 mL autoclave. The mixture was stirred (600 rpm) and heated to 285 °C within 20 min and held at this temperature for 30 min. The autoclave was air-cooled to 25 °C within 15 minutes. The resulting MXene-TiO_2 composite was washed with H_2O five times, and with ethanol once, then dried under vacuum at 30 °C for 16 h.

Hydrogen peroxide treatment of MXene (MXene-H_2O_2). $Ti_3C_2T_x$ (50 mg) and ethanol (25 mL) were added to a 100 mL round-bottom flask. The mixture was stirred and heated to 70 °C, after which 30% H_2O_2 (1.0 mL) was slowly added. The mixture was stirred at 70 °C for 2.5 h. The remaining solid material was washed five times with H_2O and once with ethanol, then dried under vacuum at 30 °C for 16 h.

Platinum impregnation procedure

The impregnation procedure has been adapted from the double-solvent method.[34] Support material (100 mg) was loaded into a 2 mL vial with 1 mL of *n*-hexane. Tetra–amine platinum nitrate (50.1 mg) was dissolved in water (1.00 mL) and 40 μL of this solution was added to the suspension under stirring (2000 rpm). The mixture was stirred for 16 h. The *n*-hexane was decanted, and the residue was dried in air for 3 h. The impregnated material was further dried at 80 °C for 3 h, 120 °C for 2 h and then heat-treated in nitrogen at 250 °C for 1h. Finally, the samples were reduced at 250 °C for 1h in a 250 mL min^{-1} stream of 10 % (*v* v^{-1}) hydrogen in nitrogen.

Catalytic testing

A 10 mL glass reactor was filled with catalyst (2.0 mg) and water (8 mL). The reactor was mounted in the bubble counter setup.[45] The reactor was then cooled to 20 °C on an ice bath after purging with H_2 for 5 min. An aqueous solution of ammonia borane (2 M, 400 μL) was injected into the reactor through a glass capillary directly into the solution. The sample was stirred continuously at 600 rpm with a 8 × 3 mm stirring bar. The sample was heated at a rate of 2 °C min^{-1} to 85 °C and held there until no more gas was evolving from the reaction. Hydrogen production was monitored throughout the experiment by counting bubbles forming in a hexadecane medium. A blank experiment with only water (8 mL) was also performed to record the gas volume increase due to gas expansion and increasing vapour pressure of the solvent. This blank was subtracted from all experiments.

Characterization

All chemicals were obtained from commercial sources (>97% pure) and used as received. Gas chromatography (GC) was performed with a Perkin Elmer Clarus 500, equipped with a flame ionization detector and a 30 m Agilent polysiloxane HP-5 column (0.32 mm ID, 0.25 μm). Helium was used as carrier gas and the column oven was heated from 60 °C to 250 °C with a 25 °C/min heating rate and held at the final temperature for 5 min. Sample solution (1.0 μL) was injected using a split injector with a 1:50 split ratio. N_2 adsorption isotherms were recorded on a Thermo Scientific Surfer instrument at -196 °C. All samples were completely degassed under a high vacuum (<10^{-4} torr) at 200 °C for 6 h prior to each measurement.

Confocal Raman spectra were recorded at 532 nm using a Renishaw (Wottonunder-Edge, United Kingdom) InVia Reflex Raman microscope with a 532 nm frequency-doubled Nd:YAG excitation source in combination with a 1800 lines mm^{-1} grating, and a Peltier-cooled CCD detector (203 K). The instrument included a Leica light microscope with a 50 × air objective. The 521 cm^{-1} Raman shift of an internal silicon standard was used to verify the spectral calibration of the system. XPS analysis was carried out in a K-Alpha Spectrometer (Thermo-Scientific). The assignment of the C 1s

binding energies was executed according to the criteria used by Ganguly *et al.* 284.3 eV for C=C (aromatic double bonds), 285.4 eV for C–OH and sp^3 C–C, 286.5 eV for epoxy, 287.5 for sp^2 C=O (carbonyls, lactones) and 289 eV for carboxylic groups.[68] X-ray diffraction (XRD) measurements were carried out on a Rigaku Miniflex X-ray diffractometer from 4° to 70° using a 2.0° min^{-1} angular velocity.

Scanning Electron Microscope (SEM) images were taken by a FEI Verios 460 using a 5 kV accelerating voltage. High resolution transmission electron microscopy (HRTEM) images were recorded on a FEI Tecnai G2 F20 S-Twin high-resolution transmission electron microscope working at 200 kV (point resolution: 0.24 nm, lattice resolution 0.102 nm, information resolution 0.14 nm). STEM-EDS images were recorded using an EDS detector with energy resolution <127 eV and a resolution of 0.20 nm.

5.5 References

[1] M. Naguib, M. Kurtoglu, V. Presser, J. Lu, J. Niu, M. Heon, L. Hultman, Y. Gogotsi, M. W. Barsoum, *Adv. Mater.* **2011**, *23*, 4248–4253.

[2] M. Naguib, V. N. Mochalin, M. W. Barsoum, Y. Gogotsi, *Adv. Mater.* **2014**, *26*, 992–1005.

[3] W. H. K. Ng, E. S. Gnanakumar, E. Batyrev, S. K. Sharma, P. K. Pujari, H. F. Greer, W. Zhou, R. Sakidja, G. Rothenberg, M. W. Barsoum, N. R. Shiju, *Angew. Chem. Int. Ed.* **2018**, *57*, 1485–1490.

[4] M. W. Barsoum, *MAX Phases: Properties of Machinable Ternary Carbides and Nitrides*, Wiley-VCH, **2013**.

[5] J. L. Hart, K. Hantanasirisakul, A. C. Lang, B. Anasori, D. Pinto, Y. Pivak, J. T. van Omme, S. J. May, Y. Gogotsi, M. L. Taheri, *Nat. Commun.* **2019**, *10*, 522.

[6] J. Halim, I. Persson, E. J. Moon, P. Kühne, V. Darakchieva, P. O. Å. Persson, P. Eklund, J. Rosen, M. W. Barsoum, *J. Phys. Condens. Matter* **2019**, *31*, 165301.

[7] A. Miranda, J. Halim, M. W. Barsoum, A. Lorke, *Appl. Phys. Lett.* **2016**, *108*, 033102.

[8] S. Zhou, X. Yang, W. Pei, N. Liu, Jijun. Zhao, *Nanoscale* **2018**, *10*, 10876–10883.

[9] Y. Jiang, T. Sun, X. Xie, W. Jiang, J. Li, B. Tian, Chenliang. Su, *ChemSusChem* **2019**, *12*, 1368–1373.

[10] J. Zhang, Y. Zhao, X. Guo, C. Chen, C.-L. Dong, R.-S. Liu, C.-P. Han, Y. Li, Y. Gogotsi, G. Wang, *Nat. Catal.* **2018**, *1*, 985–992.

[11] C. (John) Zhang, L. McKeon, M. P. Kremer, S.-H. Park, O. Ronan, A. Seral-Ascaso, S. Barwich, C. Ó. Coileáin, N. McEvoy, H. C. Nerl, B. Anasori, J. N. Coleman, Y. Gogotsi, V. Nicolosi, *Nat. Commun.* **2019**, *10*, 1795.

[12] Y. Wang, C. Ma, W. Ma, W. Fan, Y. Sun, H. Yin, X. Shi, X. Liu, Y. Ding, *2D Mater.* **2019**, *6*, 045025.

[13] X. Li, M. Li, Q. Yang, H. Li, H. Xu, Z. Chai, K. Chen, Z. Liu, Z. Tang, L. Ma, Z. Huang, B. Dong, X. Yin, Q. Huang, C. Zhi, *ACS Nano* **2020**, *14*, 541–551.

[14] Z. Li, L. Yu, C. Milligan, T. Ma, L. Zhou, Y. Cui, Z. Qi, N. Libretto, B. Xu, J. Luo, E. Shi, Z. Wu, H. Xin, W. N. Delgass, J. T. Miller, Y. Wu, *Nat. Commun.* **2018**, *9*, 1–8.

[15] Z. Li, Y. Cui, Z. Wu, C. Milligan, L. Zhou, G. Mitchell, B. Xu, E. Shi, J. T. Miller, F. H. Ribeiro, Y. Wu, *Nat. Catal.* **2018**, *1*, 349–355.

[16] B. Ahmed, D. H. Anjum, M. N. Hedhili, Y. Gogotsi, H. N. Alshareef, *Nanoscale* **2016**, *8*, 7580–7587.

[17] G. Zou, J. Guo, Q. Peng, A. Zhou, Q. Zhang, B. Liu, *J. Mater. Chem. A* **2015**, *4*, 489–499.

[18] M. Cao, F. Wang, L. Wang, W. Wu, W. Lv, J. Zhu, *J Electrochem Soc* **2017**, *164*, A3933.

[19] H. Tang, S. Zhuang, Z. Bao, C. Lao, Y. Mei, *ChemElectroChem* **2016**, *3*, 871–876.

[20] E. M. Leitao, T. Jurca, I. Manners, *Nat. Chem.* **2013**, *5*, 817–829.

[21] U. Eberle, M. Felderhoff, F. Schüth, *Angew. Chem. Int. Ed.* **2009**, *48*, 6608–6630.

[22] P. Verma, K. Yuan, Y. Kuwahara, K. Mori, H. Yamashita, *Appl. Catal. B Environ.* **2018**, *223*, 10–15.

[23] H. Cheng, T. Kamegawa, K. Mori, H. Yamashita, *Angew. Chem. Int. Ed.* **2014**, *53*, 2910–2914.

[24] S. Akbayrak, S. Özkar, *Int. J. Hydrog. Energy* **2018**, *43*, 18592–18606.

[25] C. W. Hamilton, R. Tom Baker, A. Staubitz, I. Manners, *Chem. Soc. Rev.* **2009**, *38*, 279–293.

[26] W. Grochala, P. P. Edwards, *Chem. Rev.* **2004**, *104*, 1283–1316.

[27] R. Kumar, A. Karkamkar, M. Bowden, T. Autrey, *Chem. Soc. Rev.* **2019**, *48*, 5350–5380.

[28] J. Liao, D. Lu, G. Diao, X. Zhang, M. Zhao, H. Li, *ACS Sustain. Chem. Eng.* **2018**, *6*, 5843–5851.

[29] D. Lu, J. Liao, H. Li, S. Ji, B. G. Pollet, *ACS Sustain. Chem. Eng.* **2019**, 7, 16474–16482.

[30] J. Liao, Y. Feng, W. Lin, X. Su, S. Ji, L. Li, W. Zhang, B. G. Pollet, H. Li, *Int. J. Hydrog. Energy* **2020**, *45*, 8168–8176.

[31] H. Liu, C. Xu, R. Lu, Q. Wang, J. Wu, Y. Wang, Y. Zhang, T. Sun, G. Fan, *Int. J. Hydrog. Energy* **2019**, *44*, 16548–16556.

[32] S. Akbayrak, Y. Tonbul, S. Özkar, *ACS Sustain. Chem. Eng.* **2020**, *8*, 4216–4224.

[33] H. Wang, C. Xu, Q. Chen, M. Ming, Y. Wang, T. Sun, Y. Zhang, D. Gao, J. Bi, G. Fan, *ACS Sustain. Chem. Eng.* **2019**, 7, 1178–1184.

[34] A. Aijaz, A. Karkamkar, Y. J. Choi, N. Tsumori, E. Rönnebro, T. Autrey, H. Shioyama, Q. Xu, *J. Am. Chem. Soc.* **2012**, *134*, 13926–13929.

[35] G. Fan, X. Li, Y. Ma, Y. Zhang, J. Wu, B. Xu, T. Sun, D. Gao, J. Bi, *New J. Chem.* **2017**, *41*, 2793–2799.

[36] X. Ren, H. Lv, S. Yang, Y. Wang, J. Li, R. Wei, D. Xu, B. Liu, *J. Phys. Chem. Lett.* **2019**, *10*, 7374–7382.

[37] S. Wang, D. Zhang, Y. Ma, H. Zhang, J. Gao, Y. Nie, X. Sun, *ACS Appl. Mater. Interfaces* **2014**, *6*, 12429–12435.

[38] Z. Li, T. He, D. Matsumura, S. Miao, A. Wu, L. Liu, G. Wu, P. Chen, *ACS Catal.* **2017**, 7, 6762–6769.

[39] W. Chen, X. Duan, G. Qian, D. Chen, X. Zhou, *ChemSusChem* **2015**, *8*, 2927–2931.

[40] Q. Zhou, L. Qi, H. Yang, C. Xu, *J. Colloid Interface Sci.* **2018**, *513*, 258–265.

[41] D. Xu, Z. Cui, J. Yang, M. Yuan, X. Cui, X. Zhang, Z. Dong, *Int. J. Hydrog. Energy* **2017**, *42*, 27034–27042.

[42] L.-L. Fu, D.-F. Zhang, Z. Yang, T.-W. Chen, J. Zhai, *ACS Sustain. Chem. Eng.* **2020**, *8*, 3734–3742.

[43] B. Zhao, K. Feng, Y. Wang, X. Lv, H. Zheng, Y. Ma, W. Yan, X. Sun, J. Zhong, *Catal. Sci. Technol.* **2017**, 7, 5135–5142.

[44] J. Zhang, W. Chen, H. Ge, C. Chen, W. Yan, Z. Gao, J. Gan, B. Zhang, X. Duan, Y. Qin, *Appl. Catal. B Environ.* **2018**, *235*, 256–263.

[45] T. K. Slot, N. R. Shiju, G. Rothenberg, *Angew. Chem. Int. Ed.* **2019**, *58*, 17273–17276.

[46] H. Tang, S. Zhuang, Z. Bao, C. Lao, Y. Mei, *ChemElectroChem* **2016**, *3*, 871–876.

[47] B.-J. Hsieh, M.-C. Tsai, C.-J. Pan, W.-N. Su, J. Rick, H.-L. Chou, J.-F. Lee, B.-J. Hwang, *Electrochimica Acta* **2017**, *224*, 452–459.

[48] S. Rico-Francés, E. O. Jardim, T. A. Wezendonk, F. Kapteijn, J. Gascon, A. Sepúlveda-Escribano, E. V. Ramos-Fernandez, *Appl. Catal. B Environ.* **2016**, *180*, 169–178.

[49] L. Kernazhitsky, V. Shymanovska, T. Gavrilko, V. Naumov, L. Fedorenko, V. Kshnyakin, J. Baran, *Ukr. J. Phys.* **2014**, *59*, 246–253.

[50] S. Challagulla, K. Tarafder, R. Ganesan, S. Roy, *Sci. Rep.* **2017**, 7, 8783.

[51] J. Zhu, Y. Tang, C. Yang, F. Wang, M. Cao, *J. Electrochem. Soc.* **2016**, *163*, A785.

[52] Y. Dall'Agnese, P. Rozier, P.-L. Taberna, Y. Gogotsi, P. Simon, *J. Power Sources* **2016**, *306*, 510–515.

[53] B. Wang, A. Zhou, F. Liu, J. Cao, L. Wang, Q. Hu, *J. Adv. Ceram.* **2018**, *7*, 237–245.

[54] C. Hernandez-Mejia, E. S. Gnanakumar, A. Olivos-Suarez, J. Gascon, H. F. Greer, W. Zhou, G. Rothenberg, N. R. Shiju, *Catal. Sci. Technol.* **2016**, *6*, 577–582.

[55] W. Chen, J. Ji, X. Feng, X. Duan, G. Qian, P. Li, X. Zhou, D. Chen, W. Yuan, *J. Am. Chem. Soc.* **2014**, *136*, 16736–16739.

[56] W. Chen, D. Li, Z. Wang, G. Qian, Z. Sui, X. Duan, X. Zhou, I. Yeboah, D. Chen, *AIChE J.* **2017**, *63*, 60–65.

[57] K. Feng, J. Zhong, B. Zhao, H. Zhang, L. Xu, X. Sun, S.-T. Lee, *Angew. Chem. Int. Ed.* **2016**, *55*, 11950–11954.

[58] Q. Wang, F. Fu, S. Yang, M. Martinez Moro, M. de los A. Ramirez, S. Moya, L. Salmon, J. Ruiz, D. Astruc, *ACS Catal.* **2019**, *9*, 1110–1119.

[59] F. Fu, C. Wang, Q. Wang, A. M. Martinez-Villacorta, A. Escobar, H. Chong, X. Wang, S. Moya, L. Salmon, E. Fouquet, J. Ruiz, D. Astruc, *J. Am. Chem. Soc.* **2018**, *140*, 10034–10042.

[60] H. Wu, Q. Luo, R. Zhang, W. Zhang, J. Yang, *Chin. J. Chem. Phys.* **2018**, *31*, 641–648.

[61] L. Wang, H. Li, W. Zhang, X. Zhao, J. Qiu, A. Li, X. Zheng, Z. Hu, R. Si, J. Zeng, *Angew. Chem. Int. Ed.* **2017**, *56*, 4712–4718.

[62] T. Banu, T. Debnath, T. Ash, A. K. Das, *J. Chem. Phys.* **2015**, *143*, 194305.

[63] L.-L. Long, X.-Y. Liu, J.-J. Chen, J. Jiang, C. Qian, G.-X. Huang, Q. Rong, X. Zhang, H.-Q. Yu, *ACS Appl. Nano Mater.* **2018**, *1*, 6800–6807.

[64] Y. Li, M. Hu, J. Wang, W.-H. Wang, *J. Organomet. Chem.* **2019**, *899*, 120913.

[65] Q. Yao, K. Yang, X. Hong, X. Chen, Z.-H. Lu, *Catal. Sci. Technol.* **2018**, *8*, 870–877.

[66] L. D'Ulivo, R. Spiniello, M. Onor, B. Campanella, Z. Mester, A. D'Ulivo, *Anal. Chim. Acta* **2018**, *998*, 28–36.

[67] M. J. T. C. van der Niet, N. Garcia-Araez, J. Hernández, J. M. Feliu, M. T. M. Koper, *Catal. Today* **2013**, *202*, 105–113.

[68] G. Ramos-Fernandez, M. Muñoz, J. C. García-Quesada, I. Rodriguez-Pastor, I. Martin-Gullon, *Polym. Compos.* **2018**, *39*, 2116–2124.

6

Ruthenium–tin on disordered MAX phase boosting 4-nitroaniline reduction ‡

‡ Parts of this work have been submitted as:

Ruthenium on alkali-exfoliated $Ti_3(Al_{0.8}Sn_{0.2})C_2$ MAX phase catalyzing reduction of 4-nitroaniline with ammonia borane

T. K. Slot, P. Oulego, Z. Sofer, G. Rothenberg and N. Raveendran Shiju.

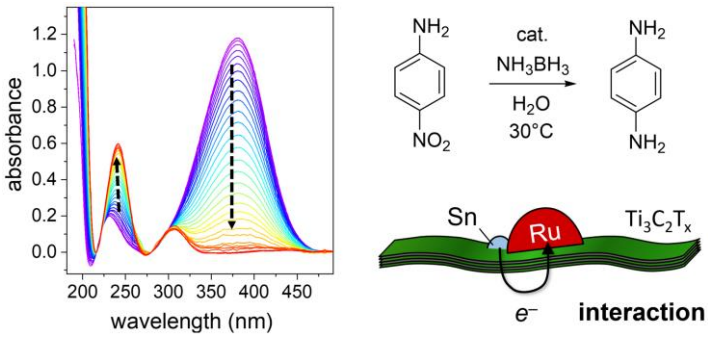

Ru–Sn synergy: Tin boosting reduction and stabilizing Ru on disordered MAX phase catalysts

Abstract: MAX phases are gaining increased interest in catalysis, typically for high-temperature applications. They can also be delaminated into 2D-structures, so-called MXenes, enabling better accessibility and the tuning of active site surroundings. Here, we present an analogous yet different approach, using an alkaline treatment to prepare a $Ti_3(Al_{0.8}Sn_{0.2})C_2$ MAX phase derivative, with an open, disordered structure. This new material, which is missing most of the larger interlayer spacing, is a good support for ruthenium particles (1.6 nm diameter). Ru on disordered MAX phase catalyzes both ammonia borane hydrolysis (TOF = 580 min^{-1}) and the reduction of 4-nitroaniline (TOF = 13 min^{-1}). Using the former as a benchmark reaction, we show that the open disordered structure of the support promotes catalytic activity. The boost in reactivity is related to a metal–support interaction, improving the activity of metallic ruthenium. We also show here, for the first time, that supported Ru is a good catalyst for reducing nitroaniline with ammonia borane. Overall, our results reveal that disordered MAX-derivatives are promising as catalyst supports, owing to their potential for tuning the electronic properties at the metal active sites.

6.1 Introduction

Heterogeneous catalysis occurs at active sites, but in many cases the support itself also plays an important role. This is especially true for MAX phases, a novel class of laminar materials with the formula $M_{n+1}AX_n$, where M is an early transition metal, A is an element in group 13 or 14, and X is either carbon or nitrogen.[1] They are stable at extreme conditions, making them very useful for high-temperature reactions, such as *n*-butane dehydrogenation.[2] For low-temperature reactions, we want to open up the MAX phase structure, improving accessibility. One way to do this is by extracting the 'A' layers, resulting in layered transition metal carbides or nitrides, so-called MXenes.[2–4] These are noted as $M_{n+1}X_nT_x$, where T stands for a terminating functional group that depends on the delamination conditions.[3,5,6] The chemistry of MAX phases and MXenes was studied extensively in the past few years, especially for electrocatalysis,[5,7–11] yet their thermo-catalytic applications are less known.[12]

MAX phases can be delaminated into MXenes thanks to the weaker M–A bonds. Most of the delamination methods use HF or fluorides.[13–18] The resulting fluor-based MXenes are sensitive to oxidation.[19–22] Recently, less hazardous delamination methods were developed using alkaline treatment.[23] The literature describes a variety of treatments, ranging from low NaOH concentrations all the way to molten NaOH.[24–27] Such etching dissolves the aluminum between the titanium carbide layers, causing delamination. Zhang *et al.* reported etching and exfoliation of Ti_3AlC_2 in alkaline conditions, obtaining delaminated MAX phases, also known as $Ti_3C_2T_x$ MXenes.[23] They found that successful exfoliation depends on temperature and NaOH concentration, producing MXenes rich in oxide or hydroxyl terminal groups.

Partially delaminated MXenes (obtained by HF treatment) can be delaminated further using bases such as NaOH, KOH and LiOH.[23,28–32] This treatment gives a composite material with needle-like titanate structures on top of the MXene layer.[33] The exact composition of these structures is unknown. For example, treating $Ti_3C_2T_x$ MXene with sodium hydroxide gives $NaTi_{1.5}O_{8.3}$,[33] $Na_2Ti_3O_7$,[29,33] and $NaTi_8O_{13}/NaTiO_2$.[30] Sodium titanates (NTOs) are useful as anode materials in electrocatalysis,[30,34] but in delamination they are unwanted impurities.

Here we study the potential of an alkaline-etched MAX phase, $Ti_3(Al_{0.8}Sn_{0.2})C_2$, as a support for metal nanoparticles.[35] Taking ammonia borane hydrolysis and the reduction of 4-nitroaniline as test reactions, we show that this disordered MAX phase enhances the activity and stability of supported ruthenium nanoparticles. Its structure is more open, enabling a better electronic interaction with ruthenium, thereby boosting catalytic activity. Our results show how the surface-particle interactions of Ru on NaOH-treated MAX phase influences both the hydrogen generation and reduction reactions. To the best of our knowledge, this is also the first report of a Ru-catalyzed hydrogenation of 4-nitroaniline with ammonia borane (AB).

6.2 Results and discussion

First, we synthesized the $Ti_3(Al_{0.8}Sn_{0.2})C_2$ MAX phase (herein TASC) by heating Ti, Al and, Sn and TiC in a 1:1:0.2:1.9 ratio (see experimental section for details). We then opened this structure by NaOH treatment at 200, 275 and 350 °C for 20 h. The material was then impregnated with ruthenium particles using the double solvent method.[36] The catalysts were then tested in ammonia borane hydrolysis (Eq. 6.1) using our bubble counter to monitor hydrogen production.[37] We know that the reactivity for H_2 generation and reduction reactions often go hand in hand, making ammonia borane hydrolysis a convenient way to screen catalysts for both reactions.[38,39]

$$NH_3BH_3 + 4H_2O \xrightarrow[20\text{ - }85°C,\ 45\text{ min}]{\text{Ru/TASC-NaOH}} NH_4^{\oplus} + B(OH)_4^{\ominus} + 3H_2 \qquad (6.1)$$

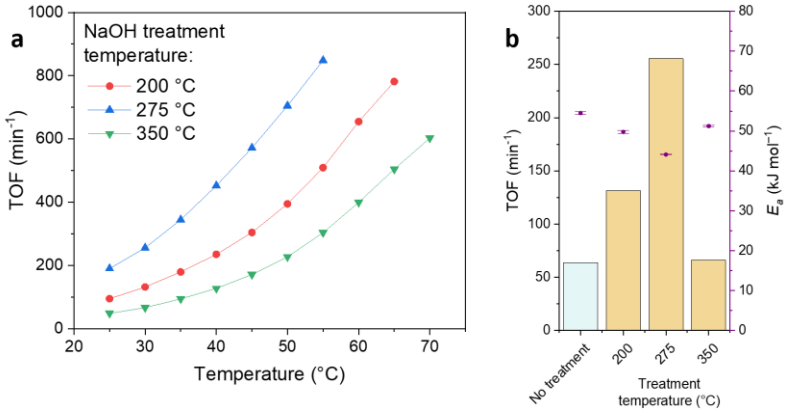

Figure 6.1. (**a**) Catalytic data for 1 wt% Ru catalysts prepared from the NaOH-treated materials at different temperatures. Each point is a window average of at least 20 measurements. (**b**) Bar graph of TOF at 30 °C with the apparent activation energy (E_a) for each material. Error bars represent the standard deviation in E_a, as derived from a linear fit of each Arrhenius plot based on 3000 measured data points.

Turnover frequency (TOF) values were calculated by the rate of gas formation (mol_{H_2}/mol_{Ru}), assuming all impregnated Ru is available for catalysis (in practice, the TOF values per available Ru atom could be higher). All NaOH treatments of the TASC enhanced the activity of the ruthenium when compared to Ru on untreated TASC (64 min^{-1}, Figure 6.1). The materials before impregnation were inactive. Treatment at 275 °C gave the highest TOF (200 min^{-1}), a four-fold improvement over the untreated sample. This temperature is slightly above those used by Li *et al.*[23]

This improved activity prompted us to further study the structure of the materials. During treatments at temperatures 200 °C, 275 °C and 350 °C, the volume of the material increased by 2×, 3–4× and 10×, respectively. Using scanning electron microscopy (SEM) we identified ribbon-like structures emerging from the basal plane of the MAX phase (*cf.* Figures 6.2**a**/**c**). At 200 °C, small crystalline structures appear (Figure 6.2**b**), which can be attributed to NaOH crystals. At 275 °C, long nanoribbons appear with a thickness of 15–50 nm and an average width of 180 nm (50–400 nm, see Figure 6.2**c**). We expect these ribbons to be either MXene or some form of titanate or aluminate.[30,33] X-ray diffraction (XRD) showed no other crystalline phase besides the MAX phase, nor a broad background that could be attributed to amorphous material. At 275 °C, the MAX signals at 9° and 18° related to the interlayer ordering of 002 and 004 disappeared while the other MAX signals remained. This indicates that the ordering in these directions is lost by interlayer separation. The XRD data suggests that the material contains a disordered MAX bulk phase with partially exfoliated MXene ribbons on its surface.

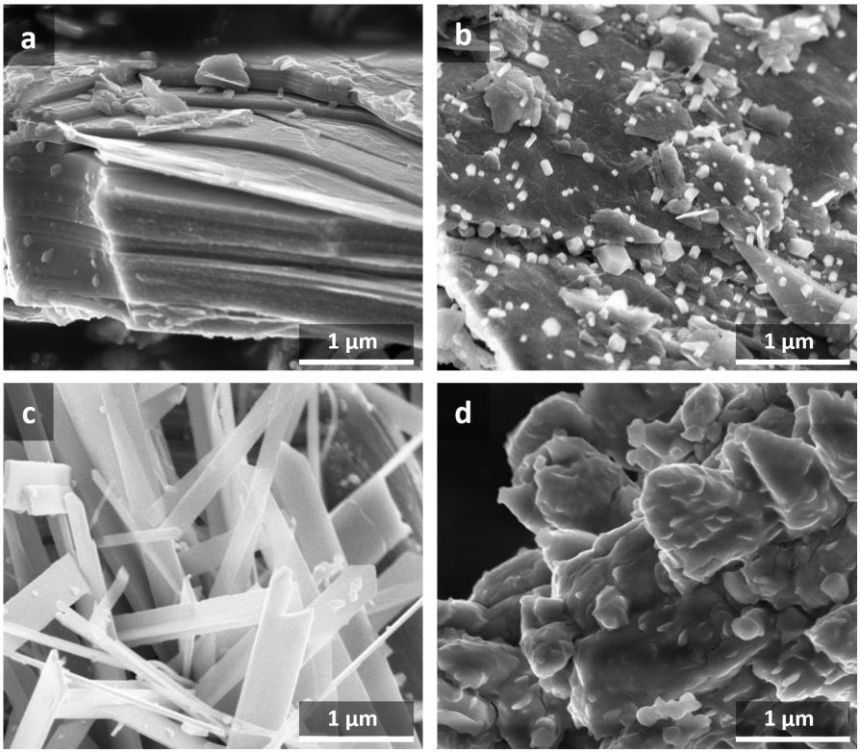

Figure 6.2. Scanning electron micrographs of (**a**) pristine TASC MAX phase, TASC MAX phase after NaOH treatment at temperatures: (**b**) 200 °C, (**c**) 275 °C, and (**d**) 350° for 20 h.

The NaOH reacts with the Al layers of the MAX phase, starting with the exposed Al at the sides, then moving inwards. During this reaction, $Al(OH)_4^-$ and hydrogen gas form.

We hypothesize that the combination of aluminum hydration on an atomic level and gas evolution on a macroscopic level push the MAX layers apart, snapping off the MXene ribbons in the process. The NaOH treatment leaves more tin exposed on the surface (*cf.* entries 1 and 2, Table A6.2), and tin does not catalyze ammonia borane hydrolysis (see the line marked "no cat" in Figure 6.3**a**). X-ray photoelectron spectroscopy (XPS) elemental mapping confirmed the loss of aluminum (only 0.1 at% remains on the surface) and showed very low levels of sodium (1.7 at%) on the surface after treatment. This means that these structures are not sodium titanate nor any other titanate/aluminate. Zhang *et al.* suggests NaOH treatment requires > 20 M concentrations to suppress any NTO formation.[23] We did not observe NTO formation at 4 M concentrations. Low NaOH concentrations have the advantage that less sodium is retained by the material (1.7 at%, see Table A6.2, compared to 6.3 at%[23]). Using SEM-EDS elemental mapping, we learned that the surface of the needles contains Ti, C, and O, suggesting a MXene or oxidized MXene structure.

Under hydrothermal conditions, the $Ti_3C_2T_x$ MXene can form crystalline TiO_2 structures.[20,40–42] However, the XRD shows neither anatase nor rutile titania. This is because our method does not introduce any electron-withdrawing fluor groups. These make the titanium atoms vulnerable to nucleophilic attack and thus TiO_2 formation. Additionally, the alkaline environment halts the decomposition of NTO structures into TiO_2 and water, which typically occurs under acidic conditions. FTIR spectra (data not shown) show the presence of −OH and −O groups. We therefore assume the MXene surface is covered mainly with oxygen functionalities. Raman spectroscopy shows two new signals at 201 and 273 cm^{-1} compared to pristine TASC (Figure A6.2). In the samples treated at 275 and 350 °C the D and G bands at 1350 and 1575 cm^{-1} (characteristic for graphitic layers) are absent. The sample treated at 350 °C shows two faint signals at 781 and 868 cm^{-1} that correspond to titanate structures.[26] This, combined with the absence of any TASC signals in XRD, implies that most of the TASC has converted into amorphous titanate(s). Throughout the different treatment temperatures, the signals from MAX phase at 391 and 626 cm^{-1} (corresponding to titanium oxycarbides, TiO_xC_y) remain present. This suggests there is no significant change in the surface groups and the structures connecting them.[43] Signals from anatase and rutile TiO_2 appear at similar locations, although, their most characteristic signals for anatase E_g at 145 cm^{-1} and E_g/A_{1g} at 640/611 cm^{-1} are absent.[44–46] The signal at 137 cm^{-1} cannot be attributed to TiO_2 and is likely caused by an oxycarbide species. From XPS quantification we derived the Ti:O:C element ratios as 1:3:1 (Table A6.2, entry 1), excluding adsorbed water in the calculation. This supports our hypothesis that the surface is covered with oxycarbide species.

Table 6.1. Overview of chemical composition of the surface by XPS analysis and total Ru content by ICP-MS.[a]

Entry	Method	ICP-MS[a]	X-ray Photoelectron spectroscopy[b]							
		Ru[a] (wt%)	Ru 3d[c] (at%) 5.9	Sn 3d (at%)	C 1s[d] (at%)	O 1s (at%)	Ti 2p[e] (at%)	Al 2s (at%)	F 1s (at%)	Na 1s (at%)
1	Ru/TASC-NaOH	0.355[f]	5.9	0.57	14	65	13	0.0	-	1.7
2	Ru/TASC	0.38[f]	3.2	0.34	10	61	9.1	15	-	1.1
3	Ru/MXene	0.42	2.6	-	34	37	12	4.1	10	0.5
4	Ru/TiO_2 anatase	0.39	3.2	-	23	49	24	-	-	1.3

[a] Triplicate experiments, standard deviation < 0.01 wt%. [b] Deconvoluted from C 1s signal. [b] Based on region scans using the deconvoluted adventitious carbon (284.8 eV) signal as internal standard. [c] Partially overlapping with C 1s. [d] All C 1s signals excluding adventitious carbon. [e] Overlapping with Ru 3p signal. [f] Based on quadruple experiments.

We compared the NaOH-treated materials to five other support materials that are similar in structure or composition: TASC MAX phase, anatase TiO_2, MXene prepared using HF, oxidized MXene and alumina (Figure 6.3**a**/**c**). The NaOH-treated materials showed superior performance in the hydrolysis of ammonia borane, giving turnover frequencies of 315 and 582 min^{-1} for the samples containing 1 wt% and 0.4 wt% Ru, respectively. In earlier work, we demonstrated that NaOH itself enhances the hydrolysis of ammonia borane by about 30%.[47] Our materials were rinsed extensively with deionized water after synthesis, to avoid NaOH carry-over. A series of control experiments with added NaOH showed that the TOFs increased by 5–25%, eliminating NaOH carry-over as explanation for the observed TOF increase.

Because of the large TOF difference between the sample prepared with 0.4% Ru and 1% Ru, we decided to study the effect of Ru loading on the catalytic activity. We impregnated the NaOH-treated material with 0.08, 0.16, 0.32, 0.40, 0.48, 0.64, 0.80, 1.2 and 1.6 wt% ruthenium. We observed an optimum at around 0.4 wt%, where the highest turnover frequencies were observed (Figure 6.3**b**). Our bubble counting device can generate Arrhenius plots with hundreds of data points. This allows us to detect small differences (<1 kJ/mol) in apparent activation energy.[37] The best performing catalyst had an apparent activation energy of 43 kJ/mol and contained 0.4 wt% ruthenium. This activation energy differs from that of Ru/TASC and commercial Ru/Al_2O_3 (Figure 6.3**c**). The activation energy decreases for ruthenium concentrations larger than 1wt%. This may reflect a Ru-Sn interaction, likely due to the low surface

area (3.2 m^2g^{-1}) of the TASC-NaOH material, which leads to a low dispersion of ruthenium at higher concentrations.[23]

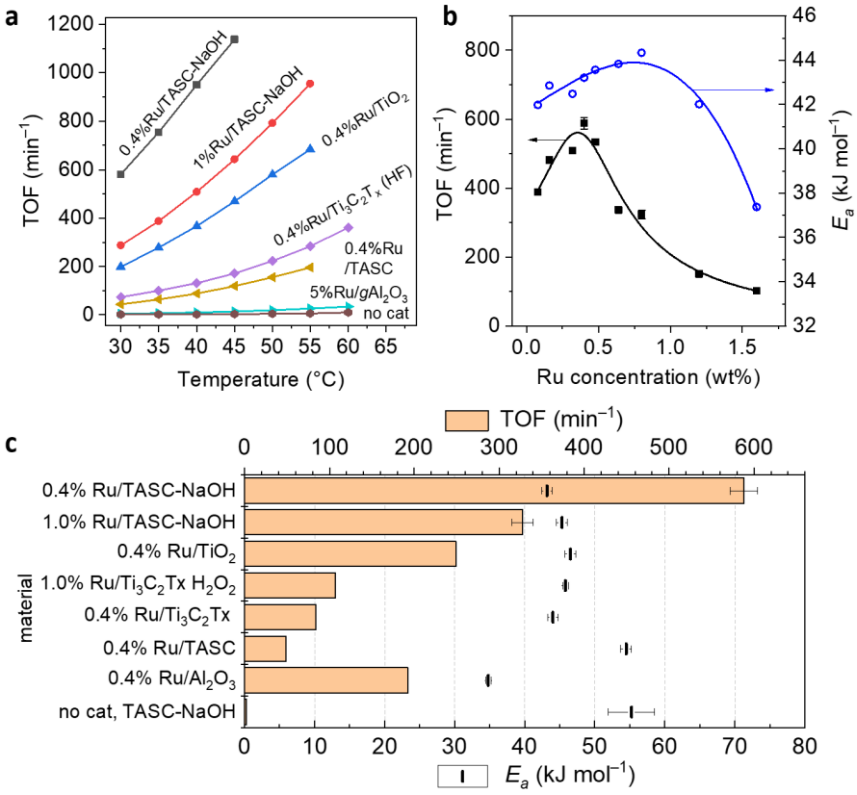

Figure 6.3. Catalytic data for (**a**) TOF at different temperatures, (**b**) TOF for various concentrations of Ru/TASC-NaOH catalysts versus TOF (left axis), and apparent activation energy (E_a, right axis). (**c**) TOF values (30 °C) for various ruthenium-impregnated materials in the hydrolysis of ammonia borane. Error bars depict standard deviation.

Transmission electron microscopy and scanning transmission electron microscopy using high-angle annular dark-field (STEM-HAADF) imaging revealed that the Ru particles are well dispersed on the needle-like structures with an average size of 1.6 nm (Figure 6.4**b/c**, the Ru particle size distribution for Ru/TASC-NaOH is included in Figure A6.9). The particles are close together, yet still equidistant. We think this is because of the contribution of the Sn at the surface of the needle-like structures of the TASC-NaOH, which helps to anchor and grow the Ru nanoparticles.

Our catalyst screening gave three catalysts with 0.4 wt% Ru that were most active: Ru/TASC-NaOH, Ru/TASC and Ru/TiO_2. Though TASC-NaOH has a more open structure than TASC, its surface area (3.2 m^2 g^{-1}) is still much lower than the TiO_2 catalyst (226 m^2 g^{-1}, Figure A6.7). Yet Ru/TASC-NaOH and Ru/TASC are more active than

Ru/TiO_2 (Figure 6.3**a**). We then tested the catalysts in the reduction of 4-nitroaniline using ammonia borane as the reductant (Figure 6.5). Without ruthenium there was no reaction. The three best catalysts for AB hydrolysis also performed well in the hydrogenation of 4-nitroaniline, giving a TOF value of 13 min^{-1} for the Ru/TASC-NaOH catalyst. This was the best catalyst, followed by Ru/TASC and Ru/TiO_2 (Figure 6.5**c**).

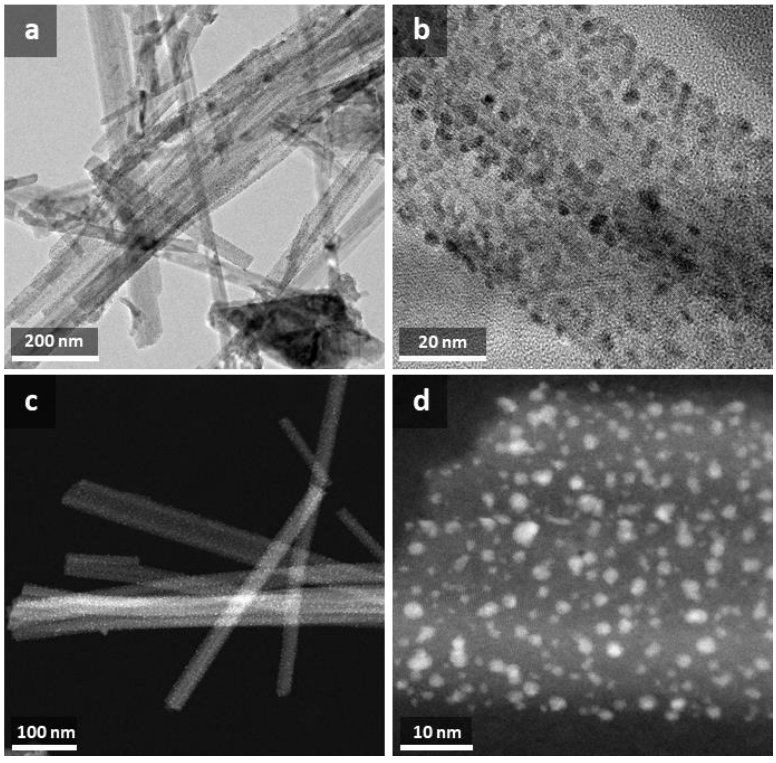

Figure 6.4. (**a**/**b**) Transmission electron micrographs of Ru/TASC-NaOH and (**c**/**d**) STEM-HAADF images of the same catalyst.

Commercial Ru/C and $Ru/Ti_3C_2T_x$ (which was exfoliated using the common HF method) showed almost zero to no reactivity. To compare our TOF values to literature results, we also ran experiments at 25 °C; Ru/TASC-NaOH, Ru/TASC and Ru/TiO_2 gave TOF values of 7.1, 6.6, and 3.9 min^{-1}, respectively. Literature TOF values range from 1.25 min^{-1} to 97 min^{-1} (Table A6.2). Our catalyst performs well, and often better than most noble metal catalysts. We mainly used a reaction temperature of 45 °C in further experiments because this reduced the amount of scattering by bubbles in our UV/Vis analysis setup. Ru/TASC-NaOH remained stable for 6 reaction cycles, however Ru/TASC showed slight degradation after 6 cycles (Figure A6.10). Probably, some of the Ru particles are lost because of poor adhesion to the MAX phase support.

The fact that the catalysts perform well in both reactions was unexpected, because a catalyst that performs well in H_2 generation (from AB) would leave less AB for reaction with 4-nitroaniline. As such, the mechanisms of both reactions may be similar. Hydrogenation of 4-nitroaniline using boranes generally follow either a tandem reduction pathway,[48–53] or a transfer hydrogenation pathway.[54–57] A tandem hydrogenation first produces hydrogen, which is then used as reductant in an ensuing reaction.[38,50,58] Transfer hydrogenation starts with B–H bond cleavage, to give an [M]–H active species. This species rapidly reduces nitro arenes into the corresponding N-aryl hydroxylamines, which are reduced further into aryl amines using NH_3BH_3.[59] Ammonia borane hydrolysis is believed to proceed through a Langmuir-Hinshelwood type mechanism with O–H bond cleavage as the rate-determining step.[60,61] However, the exact reactive species is unknown.[62–69] Ammonia borane likely first adsorbs on the metal surface after which one B–H bond dissociates, forming NH_3BH_2* and H* (analogous to the previous mechanism).

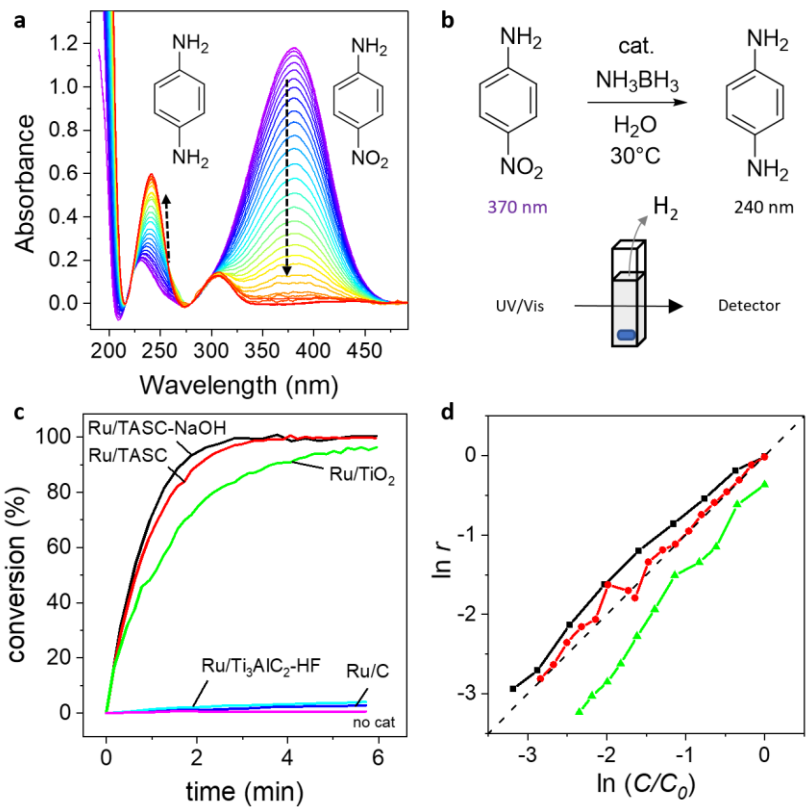

Figure 6.5. (**a**) Background-corrected UV/Vis spectra of Ru/TASC (7s interval). (**b**) Reaction equation for the reduction of 4-nitroaniline. (**c**) Reduction of 4-nitroaniline by ammonia borane by various ruthenium-impregnated catalysts. (**d**) log/log plot of rate vs concentration corresponding to the samples in panel **c**; the dashed line represents a first-order reaction.

Then, water adsorbs and dissociates into OH*, and a H^+/e^- pair. This H^+/e^- pair combines with H* to form hydrogen, and the OH* intermediate combines with NH_3BH_2*, forming $NH_3BH_2(OH)$*, which then desorbs. The remaining B–H bonds react in a similar way. To check whether H_2 was an important intermediate in the reaction, we ran a control reaction using a H_2 as the sole reductant. After a 30 min induction period, the 4-nitroaniline slowly started converting at a rate of 0.077 h^{-1}, about 20.000 times slower than the reaction using ammonia borane as the reductant. Thus, hydrogen is not the main intermediate in this reaction.

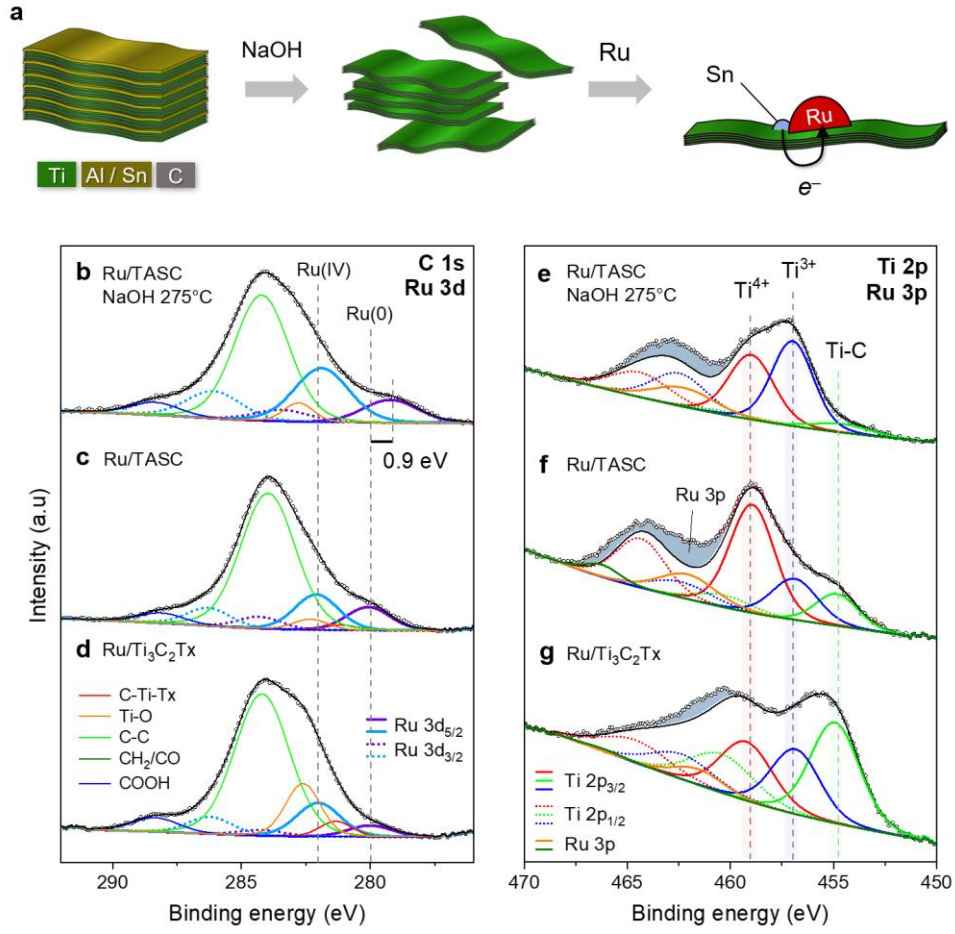

Figure 6.6. (**a**) Cartoon of the TASC synthesis and the interaction between Ru and Sn. C 1s XPS spectra of (**b**) Ru/NaOH-treated TASC MAX phase, (**c**) Ru/TASC MAX phase and (**d**) Ru/$Ti_3C_2T_x$ MXene. Ti 2p XPS spectra of (**e**) Ru/NaOH-treated TASC MAX phase, (**f**) Ru/TASC MAX phase and (**g**) Ru/$Ti_3C_2T_x$ MXene. The blue-grey area in **e**–**g** represents the Ru 3p signal.

To study the ruthenium nanoparticles, we used X-ray photoelectron spectroscopy (Figure A6.3–S6). Unfortunately, the Ru 3d signal was convoluted with the C 1s signal

so we had to establish some guidelines before we could properly deconvolve the signals (Figure 6.6**b**-**d**). From control experiments on oxidized MAX phase and MXene (Figure A6.8) we observe a large signal at 284.8 (C–C) and a separate signal at 288 eV (COOH) with no large signals in between. Additionally, there were no large or distinct signals below 283 eV. Note that for HF-exfoliated MXene we *do* observe these signals corresponding to C–Ti–F group, but these groups are absent when using NaOH treatment. This means the signals observed below 283 eV can only come from Ru $3d_{5/2}$. These signals are commonly found in the range 279.5 – 282.5 eV, depending on the oxidation state of ruthenium.[70,71] We also detected a signal at 286.4 eV, which fits to Ru $3d_{3/2}$ signals with a spin-orbit splitting of 4.2 eV.[72,73] All samples show two distinct Ru signals: Ru(0) at 279.8 eV and Ru(IV) at 282.3 eV. This suggests that some of the Ru is in non-metallic form.

A control experiment of ammonia borane hydrolysis using RuO_2 was inactive, showing that the Ru(IV) species is not important for catalysis. Surprisingly, for the most active catalyst, NaOH-treated MAX phase, the Ru(0) signal is shifted 0.9 eV down to lower binding energy compared to Ru(0) on TASC MAX phase or $Ti_3C_2T_x$-HF. This shift, which indicates a higher electron density, correlates with the high activity in ammonia borane hydrolysis.

Previously, we showed that electron-deficient Pt improves the activity of the metal for ammonia borane hydrolysis.[40] There, the MXene formed a thin titania layer on the MXene surface, shifting the Pt to a higher binding energy. Here, an opposite shift occurs. There are three differences that set the Ru results apart from the Pt ones. Firstly, there is a lot of Sn at the surface that can interact with the Ru. Secondly, the support material is different. NaOH treatment does not leave any F groups on the MXene surface, which could react to form TiO_2. This means the Ru metal is in direct contact with the MXene, facilitating electron transfer. And finally, Ru is less electron-rich than Pt, so donating electrons to it could speed up the reaction.

Characterizing the electronic structure of the Ti is complicated by the overlap between the Ti 2p and Ru 3d signals. However, these signals can be extracted using a similar approach as with Ru 3d and C 1s. Ru 3p signals are much broader than Ti 2p and there are no Ru signals below 461 eV.[73–75] This means that the Ti 2p signals up to 459 eV can be quantitatively assigned. We observed Ti–C at 454.9 eV, Ti^{3+} at 457.1 eV and Ti^{4+} at 459.0 eV in all three samples (Figure 6.6**e**–**g**). After taking into consideration the spin-orbit splitting of 5.5 eV and a peak broadening of about 1.1–1.3 (Full Width at Half Maximum, FWHM) due to the Coster-Kronig effect,[76] we could extrapolate the Ti $2p_{1/2}$ peaks and estimate the broad Ru 3p signals (grey area in Figure 6.6**e**-**g**).

XPS shows an increase in Ti^{3+} level in the NaOH-treated sample, making it the predominant titanium species on the surface. This comes at the expense of the Ti–C species. Such high levels of Ti^{3+} may cause a downshift in Ru(0) on the NaOH-treated

MXene. Ti^{3+} species are commonly associated with defects within TiO_2.[77] There is a correlation between TOF and Ti^{3+} concentration for the samples in the order TASC > $Ti_3C_2T_x$ > NaOH-treated TASC. However, the Ti^{3+} alone is not responsible for the catalytic effect, as no reaction occurs without ruthenium. Instead, we think the electron rich Ru(0) is influenced by tin. Trace amounts of Sn (0.3–0.6 at%) are present on the surface of our TASC catalysts (Table A6.2, entries 1/2). Ru and Sn can form alloys or interact with one another (Figure 6.6**a**) .[78–81] Tin can modify the selectivity of Ru in hydrogenation reactions.[80,82–85] It also stabilizes supported metals.[86] Our TASC-NaOH catalyst contains twice the amount of Sn on the surface compared to pristine TASC. At low Ru concentrations, this may form an alloy after reduction at 350 °C.[87] When Sn and Ru are close, the Sn can donate electron-density to the Ru(0), explaining the downshifts by 0.9 eV in XPS. The Ru nanoparticles are also close to one another, possibly enhancing this effect even further. This also explains why the signal corresponding to RuO_x is not shifted as much as Ru(0); this species is electron-deficient and non-conductive, making an interaction with Ti–C or the neighboring Ru(0) difficult.

6.3 Conclusion

We successfully synthesized a disordered MAX phase, TASC, with ribbon-like structures using a method relying on low concentrations of NaOH whilst avoiding side-reactions producing NTOs. The surface of this material contains Sn and Ti^{3+}, both of which can interact with ruthenium, decreasing the electron binding energy of the metallic Ru atom. This shift in binding energy is likely responsible for the high activity in ammonia borane hydrolysis giving a TOF of 580 min^{-1} at a loading of only 0.4 wt% ruthenium. This electronic interaction can be a useful tool for catalyst design, allowing one to tune the activity and electronic properties of metal nanoparticles by using the right (functionalized) MXene as a support.

6.4 References

[1] M. Naguib, M. Kurtoglu, V. Presser, J. Lu, J. Niu, M. Heon, L. Hultman, Y. Gogotsi, M. W. Barsoum, *Adv. Mater.* **2011**, *23*, 4248–4253.

[2] W. H. K. Ng, E. S. Gnanakumar, E. Batyrev, S. K. Sharma, P. K. Pujari, H. F. Greer, W. Zhou, R. Sakidja, G. Rothenberg, M. W. Barsoum, N. R. Shiju, *Angew. Chem. Int. Ed.* **2018**, *57*, 1485–1490.

[3] M. Naguib, V. N. Mochalin, M. W. Barsoum, Y. Gogotsi, *Adv. Mater.* **2014**, *26*, 992–1005.

[4] M. W. Barsoum, *MAX Phases: Properties of Machinable Ternary Carbides and Nitrides*, Wiley-VCH, **2013**.

[5] J. L. Hart, K. Hantanasirisakul, A. C. Lang, B. Anasori, D. Pinto, Y. Pivak, J. T. van Omme, S. J. May, Y. Gogotsi, M. L. Taheri, *Nat. Commun.* **2019**, *10*, 522.

[6] G. Gao, A. P. O'Mullane, A. Du, *ACS Catal.* **2017**, *7*, 494–500.

[7] J. Halim, I. Persson, E. J. Moon, P. Kühne, V. Darakchieva, P. O. Å. Persson, P. Eklund, J. Rosen, M. W. Barsoum, *J. Phys. Condens. Matter* **2019**, *31*, 165301.

[8] A. Miranda, J. Halim, M. W. Barsoum, A. Lorke, *Appl. Phys. Lett.* **2016**, *108*, 033102.

[9] S. Zhou, X. Yang, W. Pei, N. Liu, Jijun. Zhao, *Nanoscale* **2018**, *10*, 10876–10883.

[10] Y. Jiang, T. Sun, X. Xie, W. Jiang, J. Li, B. Tian, Chenliang. Su, *ChemSusChem* **2019**, *12*, 1368–1373.

[11] J. Zhang, Y. Zhao, X. Guo, C. Chen, C.-L. Dong, R.-S. Liu, C.-P. Han, Y. Li, Y. Gogotsi, G. Wang, *Nat. Catal.* **2018**, *1*, 985–992.

[12] Z. Li, L. Yu, C. Milligan, T. Ma, L. Zhou, Y. Cui, Z. Qi, N. Libretto, B. Xu, J. Luo, E. Shi, Z. Wu, H. Xin, W. N. Delgass, J. T. Miller, Y. Wu, *Nat. Commun.* **2018**, *9*, 1–8.

[13] A. Feng, Y. Yu, Y. Wang, F. Jiang, Y. Yu, L. Mi, L. Song, *Mater. Des.* **2017**, *114*, 161–166.

[14] M. Naguib, R. R. Unocic, B. L. Armstrong, J. Nanda, *Dalton Trans.* **2015**, *44*, 9353–9358.

[15] G. Lv, J. Wang, Z. Shi, L. Fan, *Mater. Lett.* **2018**, *219*, 45–50.

[16] O. Mashtalir, M. Naguib, V. N. Mochalin, Y. Dall'Agnese, M. Heon, M. W. Barsoum, Y. Gogotsi, *Nat. Commun.* **2013**, *4*, 1716.

[17] A. Qian, J. Y. Seo, H. Shi, J. Y. Lee, C.-H. Chung, *ChemSusChem* **2018**, *11*, 3719–3723.

[18] S. Elumalai, M. Yoshimura, M. Ogawa, *Chem. – Asian J.* **2020**, *15*, 1044–1051.

[19] Y. Chae, S. Joon Kim, S.-Y. Cho, J. Choi, K. Maleski, B.-J. Lee, H.-T. Jung, Y. Gogotsi, Y. Lee, C. Won Ahn, *Nanoscale* **2019**, *11*, 8387–8393.

[20] H. Tang, S. Zhuang, Z. Bao, C. Lao, Y. Mei, *ChemElectroChem* **2016**, *3*, 871–876.

[21] M. Cao, F. Wang, L. Wang, W. Wu, W. Lv, J. Zhu, *J Electrochem Soc* **2017**, *164*, A3933.

[22] R. Lotfi, M. Naguib, D. E. Yilmaz, J. Nanda, A. C. T. van Duin, *J. Mater. Chem. A* **2018**, *6*, 12733–12743.

[23] T. Li, L. Yao, Q. Liu, J. Gu, R. Luo, J. Li, X. Yan, W. Wang, P. Liu, B. Chen, W. Zhang, W. Abbas, R. Naz, D. Zhang, *Angew. Chem. Int. Ed.* **2018**, *57*, 6115–6119.

[24] P. Gu, S. Zhang, C. Zhang, X. Wang, A. Khan, T. Wen, B. Hu, A. Alsaedi, T. Hayat, X. Wang, *Dalton Trans.* **2019**, *48*, 2100–2107.

[25] X. Xie, Y. Xue, L. Li, S. Chen, Y. Nie, W. Ding, Z. Wei, *Nanoscale* **2014**, *6*, 11035–11040.

[26] D. Sun, A. Zhou, Z. Li, L. Wang, *J. Adv. Ceram.* **2013**, *2*, 313–317.

[27] D. Li, Y. Liang, X. Liu, Y. Zhou, *J. Eur. Ceram. Soc.* **2010**, *30*, 3227–3234.

[28] J. Xuan, Z. Wang, Y. Chen, D. Liang, L. Cheng, X. Yang, Z. Liu, R. Ma, T. Sasaki, F. Geng, *Angew. Chem. Int. Ed.* **2016**, *55*, 14569–14574.

[29] C. Zeng, F. Xie, X. Yang, M. Jaroniec, L. Zhang, S.-Z. Qiao, *Angew. Chem.* **2018**, *130*, 8676–8680.

[30] X. Sun, K. Tan, Y. Liu, J. Zhang, L. Hou, C. Yuan, *Chin. Chem. Lett.* **2020**, 31, 2254–2258.

[31] Z. Wei, Z. Peigen, T. Wubian, Q. Xia, Z. Yamei, S. ZhengMing, *Mater. Chem. Phys.* **2018**, *206*, 270–276.

[32] B. Yang, Y. She, C. Zhang, S. Kang, J. Zhou, W. Hu, *Nanomaterials* **2020**, *10*, 345.

[33] Y. Dong, Z.-S. Wu, S. Zheng, X. Wang, J. Qin, S. Wang, X. Shi, X. Bao, *ACS Nano* **2017**, *11*, 4792–4800.

[34] Q. Xu, J. Xu, H. Jia, Q. Tian, P. Liu, S. Chen, Y. Cai, X. Lu, X. Duan, L. Lu, *J. Electroanal. Chem.* **2020**, *860*, 113869.

[35] Z. Li, Y. Cui, Z. Wu, C. Milligan, L. Zhou, G. Mitchell, B. Xu, E. Shi, J. T. Miller, F. H. Ribeiro, Y. Wu, *Nat. Catal.* **2018**, *1*, 349–355.

[36] A. Aijaz, A. Karkamkar, Y. J. Choi, N. Tsumori, E. Rönnebro, T. Autrey, H. Shioyama, Q. Xu, *J. Am. Chem. Soc.* **2012**, *134*, 13926–13929.

[37] T. K. Slot, N. R. Shiju, G. Rothenberg, *Angew. Chem. Int. Ed.* **2019**, *58*, 17273–17276.

[38] M. Muzzio, H. Lin, K. Wei, X. Guo, C. Yu, T. Yom, Z. Xi, Z. Yin, S. Sun, *ACS Sustain. Chem. Eng.* **2020**, *8*, 2814–2821.

[39] Y.-H. Zhou, Q. Yang, Y.-Z. Chen, H.-L. Jiang, *Chem. Commun.* **2017**, *53*, 12361–12364.

[40] T. K. Slot, F. Yue, H. Xu, E. V. Ramos-Fernandez, A. Sepúlveda-Escribano, Z. Sofer, G. Rothenberg, N. R. Shiju, *2D Mater.* **2020**, *8*, 015001.

[41] V. Natu, J. L. Hart, M. Sokol, H. Chiang, M. L. Taheri, M. W. Barsoum, *Angew. Chem. Int. Ed.* **2019**, *58*, 12655–12660.

[42] R. Zheng, C. Shu, Z. Hou, A. Hu, P. Hei, T. Yang, J. Li, R. Liang, J. Long, *ACS Appl. Mater. Interfaces* **2019**, *11*, 46696–46704.

[43] C. Magnus, D. Cooper, J. Sharp, W. M. Rainforth, *Wear* **2019**, *438–439*, 203013.

[44] S. Rico-Francés, E. O. Jardim, T. A. Wezendonk, F. Kapteijn, J. Gascon, A. Sepúlveda-Escribano, E. V. Ramos-Fernandez, *Appl. Catal. B Environ.* **2016**, *180*, 169–178.

[45] T. Mazza, E. Barborini, P. Piseri, P. Milani, D. Cattaneo, A. Li Bassi, C. E. Bottani, C. Ducati, *Phys. Rev. B* **2007**, *75*, 045416.

[46] Y. Zhang, W. Wu, K. Zhang, C. Liu, A. Yu, M. Peng, J. Zhai, *Phys. Chem. Chem. Phys.* **2016**, *18*, 32178–32184.

[47] F. Fu, C. Wang, Q. Wang, A. M. Martinez-Villacorta, A. Escobar, H. Chong, X. Wang, S. Moya, L. Salmon, E. Fouquet, J. Ruiz, D. Astruc, *J. Am. Chem. Soc.* **2018**, *140*, 10034–10042.

[48] S. Ghosh, B. R. Jagirdar, *Dalton Trans.* **2018**, *47*, 17401–17411.

[49] J. Du, J. Chen, H. Xia, Y. Zhao, F. Wang, H. Liu, W. Zhou, B. Wang, *ChemCatChem* **2020**, *12*, 2426–2430.

[50] Q. Yang, Y.-Z. Chen, Z. U. Wang, Q. Xu, H.-L. Jiang, *Chem. Commun.* **2015**, *51*, 10419–10422.

[51] J. Du, J. Hou, B. Li, R. Qin, C. Xu, H. Liu, *J. Alloys Compd.* **2020**, *815*, 152372.

[52] X. Li, L. Song, D. Gao, B. Kang, H. Zhao, C. Li, X. Hu, G. Chen, *Chem. – Eur. J.* **2020**, *26*, 4419–4424.

[53] Q. Sun, N. Wang, T. Zhang, R. Bai, A. Mayoral, P. Zhang, Q. Zhang, O. Terasaki, J. Yu, *Angew. Chem. Int. Ed.* **2019**, *58*, 18570–18576.

[54] Ö. Metin, A. Mendoza-Garcia, D. Dalmızrak, M. S. Gültekin, S. Sun, *Catal. Sci. Technol.* **2016**, *6*, 6137–6143.

[55] K. Ganjehyan, B. Nişancı, M. Sevim, A. Daştan, Ö. Metin, *Appl. Organomet. Chem.* **2019**, *33*, e4863.

[56] X. Liu, L. Zhang, J. Wang, N. Shang, S. Gao, C. Wang, Y. Gao, *Appl. Organomet. Chem.* **2020**, *34*, e5438.

[57] L. Zhang, J. Wang, N. Shang, S. Gao, Y. Gao, C. Wang, *Appl. Surf. Sci.* **2019**, *491*, 544–552.

[58] S. N. H. MD Dostagir, M. K. Awasthi, A. Kumar, K. Gupta, S. Behrens, A. Shrotri, S. K. Singh, *ACS Sustain. Chem. Eng.* **2019**, *7*, 9352–9359.

[59] D. Andreou, D. Iordanidou, I. Tamiolakis, G. S. Armatas, I. N. Lykakis, *Nanomaterials* **2016**, *6*, 54.

[60] W. Chen, D. Li, Z. Wang, G. Qian, Z. Sui, X. Duan, X. Zhou, I. Yeboah, D. Chen, *AIChE J.* **2017**, *63*, 60–65.

[61] T. K. Slot, N. Riley, N. R. Shiju, J. W. Medlin, G. Rothenberg, *Chem. Sci.* **2020**, *11*, 11024–11029.

[62] K. Feng, J. Zhong, B. Zhao, H. Zhang, L. Xu, X. Sun, S.-T. Lee, *Angew. Chem. Int. Ed.* **2016**, *55*, 11950–11954.

[63] Q. Wang, F. Fu, S. Yang, M. Martinez Moro, M. de los A. Ramirez, S. Moya, L. Salmon, J. Ruiz, D. Astruc, *ACS Catal.* **2019**, *9*, 1110–1119.

[64] F. Fu, C. Wang, Q. Wang, A. M. Martinez-Villacorta, A. Escobar, H. Chong, X. Wang, S. Moya, L. Salmon, E. Fouquet, J. Ruiz, D. Astruc, *J. Am. Chem. Soc.* **2018**, *140*, 10034–10042.

[65] H. Wu, Q. Luo, R. Zhang, W. Zhang, J. Yang, *Chin. J. Chem. Phys.* **2018**, *31*, 641–648.

[66] L. Wang, H. Li, W. Zhang, X. Zhao, J. Qiu, A. Li, X. Zheng, Z. Hu, R. Si, J. Zeng, *Angew. Chem. Int. Ed.* **2017**, *56*, 4712–4718.

[67] T. Banu, T. Debnath, T. Ash, A. K. Das, *J. Chem. Phys.* **2015**, *143*, 194305.

[68] L.-L. Long, X.-Y. Liu, J.-J. Chen, J. Jiang, C. Qian, G.-X. Huang, Q. Rong, X. Zhang, H.-Q. Yu, *ACS Appl. Nano Mater.* **2018**, *1*, 6800–6807.

[69] Y. Li, M. Hu, J. Wang, W.-H. Wang, *J. Organomet. Chem.* **2019**, *899*, 120913.

[70] D. J. Morgan, *Surf. Interface Anal.* **2015**, *47*, 1072–1079.

[71] J. Balcerzak, W. Redzynia, J. Tyczkowski, *Appl. Surf. Sci.* **2017**, *426*, 852–855.

[72] L.-Å. Näslund, Á. S. Ingason, S. Holmin, J. Rosen, *J. Phys. Chem. C* **2014**, *118*, 15315–15323.

[73] P. Paunović, D. S. Gogovska, O. Popovski, A. Stoyanova, E. Slavcheva, E. Lefterova, P. Iliev, A. T. Dimitrov, S. H. Jordanov, *Int. J. Hydrog. Energy* **2011**, *36*, 9405–9414.

[74] J. Wojciechowska, E. Gitzhofer, J. Grams, A. Ruppert, N. Keller, *Materials* **2018**, *11*, 2329.

[75] H. Cheng, W. Lin, X. Li, C. Zhang, F. Zhao, *Catalysts* **2014**, *4*, 276–288.

[76] M. Ohno, *J. Electron Spectrosc. Relat. Phenom.* **2004**, *136*, 221–228.

[77] M. J. Jackman, A. G. Thomas, C. Muryn, *J. Phys. Chem. C* **2015**, *119*, 13682–13690.

[78] M. J. Mendes, O. A. A. Santos, E. Jordão, A. M. Silva, *Appl. Catal. Gen.* **2001**, *217*, 253–262.

[79] L. Perring, P. Feschotte, F. Bussy, J. C. Gachon, *J. Alloys Compd.* **1996**, *245*, 157–163.

[80] E. Bonnefille, F. Novio, T. Gutmann, R. Poteau, P. Lecante, J.-C. Jumas, K. Philippot, B. Chaudret, *Nanoscale* **2014**, *6*, 9806–9816.

[81] L. Stievano, S. Calogero, F. E. Wagner, S. Galvagno, C. Milone, *J. Phys. Chem. B* **1999**, *103*, 9545–9556.

[82] K. Y. Cheah, T. S. Tang, F. Mizukami, S. Niwa, M. Toba, Y. M. Choo, *J. Am. Oil Chem. Soc.* **1992**, *69*, 410–416.

[83] M. Toba, S. Tanaka, S. Niwa, F. Mizukami, Z. Koppány, L. Guczi, K.-Y. Cheah, T.-S. Tang, *Appl. Catal. Gen.* **1999**, *189*, 243–250.

[84] V. M. Deshpande, K. Ramnarayan, C. S. Narasimhan, *J. Catal.* **1990**, *121*, 174–182.

[85] K. Tahara, E. Nagahara, Y. Itoi, S. Nishiyama, S. Tsuruya, M. Masai, *J. Mol. Catal. Chem.* **1996**, *110*, L5–L6.

[86] Y. Hara, K. Endou, *Appl. Catal. Gen.* **2003**, *239*, 181–195.

[87] V. A. Mazzieri, M. R. Sad, C. R. Vera, C. L. Pieck, R. Grau, *Quím. Nova* **2010**, *33*, 269–272.

6.5 Appendix

6.5.1 Experimental details

TOF calculation

Turnover frequency (TOF) was calculated based on the following literature-reported reaction parameters: turnover number (or inverse of the molar ratio $mol_{catalyst}$:$mol_{substrate}$), yield and time, or: selectivity, conversion, and time. The reaction must reach a yield > 80%. If yield was not reported, it was calculated from conversion and selectivity by yield = selectivity × conversion. The TOF is calculated using Eq. 6.2.

$$\mathrm{TOF} = \frac{n_{substrate} \times converion \times selectivity}{n_{catalyst} \times time} = \frac{n_{substrate} \times yield}{n_{catalyst} \times time} \qquad (6.2)$$

Here, TOF is turnover frequency (min^{-1}), $n_{substrate}$ is molar amount of substrate (mmol), $n_{catalyst}$ is molar amount of catalyst, assuming all metal is available for reaction (mmol), *conversion* (%), s*electivity* (%) and *yield* (%), and time (min) is the reaction time to complete the reaction to a yield of at least 80%.

Procedure for MXene ($Ti_3C_2T_x$-HF) Synthesis

Ti_3AlC_2 was obtained from Carbon-Ukraine and had a purity > 95% (verified by XRD). Ti_3AlC_3 was etched with HF (40 wt%) for 7 days under continuous stirring at room temperature. The mixture was repeatedly centrifuged and washed with deionized water until the pH of the supernatant was neutral. The powder obtained after this procedure was dried under vacuum. This material is denoted as $Ti_3C_2T_x$.

TASC MAX phase synthesis

Titanium, aluminum, and tin were obtained from General Research Institute for Nonferrous Metals, Beijing, China. TiC was obtained from Zhuzhou Haokun Hard Materials Co., Ltd, Hunan, China. A mixture of titanium (48 μm, 99.5 wt% purity), aluminum (75 μm, 99.5 wt% purity), tin (75 μm, 99.5 wt% purity) and TiC (48 μm, 99.5 wt% purity) powder (in the atomic ratio 1:1:0.2:1.9) was mixed using a stainless steel milling ball for 24h. The powder mixture was heated at 1450 °C for 15 min in Ar. Once the mixture was cooled down to room temperature, the resulting Ti_3AlC_2 was crushed and milled into the required powder size (Mesh 400). This resulted in a D(50) particle size of 9.53 μm. This material has the composition $Ti_3(Al_{0.8}Sn_{0.2})C_2$ and is denoted as TASC. No Sn evaporation was observed during synthesis.

Procedure for TASC-NaOH Synthesis

TASC (1.0 g) was loaded in a 75 mL autoclave and 4 M NaOH solution (25 mL) was added. The autoclave was immediately sealed after addition of the base solution. The mixture was stirred and heated at 200 °C, 275 °C, or 350 °C for 20 hours. The autoclave was cooled to room temperature. The remaining solid material was collected, centrifuged (3500 × *g*) washed with H_2O (10x) and ethanol (2x), then dried under vacuum at 30 °C.

Procedure for Ru impregnation (double solvent method)

The impregnation procedure has been adapted from the double-solvent method.[1] Support material (100 mg) was loaded into a 2 mL vial with 1 mL of hexanes. Ruthenium chloride·xH_2O (30.3 mg, 41.5% Ru metal content) was dissolved in water (1 mL) and 40 μL of this solution was added to the material suspension and stirred overnight. The materials were decanted and dried to air for 3h. The impregnated materials were further dried 3 h at 80 °C, 2 h at 120 °C, and then heat-treated in nitrogen at 350 °C for 1 h. The resulting samples were then reduced at 350 °C for 1 h in a 250 mL/min stream of 10% (*v*/*v*) hydrogen in nitrogen.

General procedure for isothermal hydrolysis of ammonia borane

Aqueous ammonia borane (0.40 mL, 2 M) was loaded into a syringe (1 mL) equipped with a glass capillary (0.32 mm, 15 cm) that reaches into the reactor below the liquid level. The catalyst (5.0 mg) was suspended in water (8.0 mL) and a stirring bar (8 × 3 mm) was added. The reactor was closed, and mounted in the bubble counter setup.[2] The capillary was directly inserted into the liquid through one of the syringe ports. All remaining ports were closed. The reactor was then purged with nitrogen using a flow rate of 5 mL min^{-1} for 5 min while the sample was continuously stirred at 600 rpm. During purging, the reactor was heated to the desired temperature. After the temperature stabilized, the purging was stopped. The reactant was injected (within 5 seconds of stopping the purge gasflow), resulting in some volume displacement. The gas production was then monitored until the reaction was completed.

General procedure for non-isothermal hydrolysis of ammonia borane

A 10 mL reactor was loaded with catalyst (2.0 mg), water (8 mL), and an 8 × 3 mm stirrer bar. The reactor was then cooled to around 20 °C on an ice bath after purging with H_2 for 5 min. An aqueous solution of ammonia borane (2 M, 400 μL) was injected into the reactor through a glass capillary directly into the solution and the sample was stirred continuously at 600 rpm. The sample was heated at a ramp rate of 2 °C min^{-1} to 85 °C and held there until no more gas was evolving from the reaction, or until the hold-time reached 120 minutes. Hydrogen production was monitored throughout the experiment by counting bubbles, forming in a hexadecane medium. A blank experiment with only water (8 mL) was also performed to record the gas volume with temperature. Gas is produced due to gas expansion and increasing vapor pressure of the solvent. This blank was subtracted from all experiments. (See details in section "Blank experiment correction")

Procedure for isothermal reduction of 4-nitroaniline (*p*NA)

A standard quartz UV/Vis cuvette (l = 1 cm) was loaded with catalyst (0.20 mg), water (2 mL) and a small stirrer bar. An aqueous solution of ammonia borane (1 M, 10 μL) was added to the cuvette and the reaction mixture was stirred (1000 rpm) for 5 min. Then, an aqueous solution of 4-nitroaniline (5 mM, 50 μL) was added, marking the start of the reaction. The reaction mixture was stirred constantly (1000 rpm) while taking UV/Vis spectra from 700-190 nm at regular intervals (3–15 s). The spectra were processed using a Python script. First, a spike removal filter was applied to remove any spikes due to bubbles passing the beam. Then, for all spectra a difference spectrum was calculated using an average of the last 3 spectra recorded before the addition of *p*NA. All subsequent spectra contained a maximum for the *p*NA at 390 nm, which is converted into the product, forming at 240 nm. Then, a scatter-correction was applied by fitting a baseline to the linear section between 490-650 nm and subtracting this

from the data. This successfully corrected some of the recorded reactions where the solution in the cuvette became somewhat turbid. The relative intensities at both wavelengths are tabulated versus time and used for calculating conversion. For one sample (Ru/TiO_2) we had to correct the data for a reduction in absorption due to bubbles or excessive scattering. To do this, we assume that the amount of reactants + products remains constant, meaning – in theory – the total absorbance should remain constant (Eq. 6.3). We verified with GC that this reaction indeed produces one product. We observed that this total absorbance indeed remained approximately constant and did not deviate more than 15% in the first minute after *p*NA addition. For all other catalysts, this A_{tot} did not deviate more than 5%.

$$A_{tot} = \frac{A_{240\,nm}}{\varepsilon_{product}} + \frac{A_{390\,nm}}{\varepsilon_{reactant}} \tag{6.3}$$

Then we use this total absorbance value A_{tot} to normalize existing values (of the Ru/TiO_2 sample) by dividing the recorded absorbance values at each wavelength by A_{tot} for a given spectrum. Then, these absorbance values were converted into concentrations of reactant and product using the Lambert-Beer law.

Bubble counter data acquisition

A detailed description of the bubble detection device is available elsewhere.[2]

Processing of bubble counter data (by included software)

The data obtained from the bubble counter are saved in two files: one file listing the time and size the beam-interruption time (BIT) and one file listing all the temperature control data from the PID module. The data in both files are merged to obtain the BIT, time of detection and temperature for each bubble. A window average (5 seconds) is applied to the temperature ramp data, reducing noise in the obtained Arrhenius plots.

As described before,[2] a linear flow correction is applied to the bubble counting data. This is to account for changes in bubble volume. The volume of the bubble is calculated with Eq. 6.4.

$$V(x) = c_1 x + c_2 = 0.14314x + 7.1341 \tag{6.4}$$

Here, c_1 and c_2 are constants and x is flow rate in bubbles per second. Volume $V(x)$ is in microliters.

Blank experiment correction

This correction is only performed for non-isothermal experiments. The reason this is necessary is because the gas above the liquid will expand with increasing temperature and generate extra bubbles. Also the liquid contributes a vapor pressure that accounts for a total of roughly 3 mL of gas over the course of one experiment. Relative to the total volume this is never more than 10% of the gas production of the entire experiment.

To correct for void volume expansion and vapor pressure, a blank experiment with only solvent is ran with exactly the same parameters. The resulting data is then subtracted from the reaction experimental data (see Appendix 2 on p. 41 for more information). These blanks are stored in the bubble counter software so it can be easily applied to new data.

Processing of volume data into Arrhenius plots

All data from bubbles caused by purging and/or volume displacement after reactant injection are deleted. This leaves only the gas production by the catalytic experiment. First, the volume data is interpolated to reduce the number of points. This can be done in two ways, by a window average of the data points, or by interpolating evenly spaced points in time from the source data. Both methods have advantages and disadvantages. Window averaging has the advantage it always averages the same number of data points, but the data points are not evenly spaced across the temperature axis. This means that the majority of points will end up in the high temperature region. Equal point spacing indeed gives a good spread of points, but averages fewer points in the lower temperature range and more in the later part of the reaction. Unless specified otherwise, we applied a 50 point equal-spacing interpolation. After interpolation, we take the derivative of the volume data versus time. Then the fractional conversion is calculated, based on the expected volume which in turn is based on the known amount of ammonia borane which was added to the reactor. Then the intrinsic rate of the catalyst is calculated assuming a pre-measured reaction order of 0.15. This value is an average obtained after multiple isothermal runs of ammonia borane hydrolysis. This data is then used to derive Arrhenius plots and TOF calculations.

6.5.2 Materials and Instrumentation

All chemicals were obtained from commercial sources (>97% pure) and used as received.

Gas chromatography (GC) was performed with a Perkin Elmer Clarus 500, equipped with a flame ionization detector and a 30 m Agilent polysiloxane HP-5 column (0.32 mm ID, 0.25 µm). He was used as carrier gas and the column oven was heated from 60 °C to 250 °C with a 25 °C/min heating rate and held at the final temperature for 5 min. Sample solution (1.0 µL) was injected using a split injector with a 1:50 split ratio.

N_2 adsorption-desorption isotherms were recorded on a BELsorp-MAX II (BEL, Japan) at 77 K. The TiO_2 control sample was measured using a Thermo Scientific Surfer instrument at 77 K. All samples were completely degassed under a high vacuum ($<10^{-4}$ torr) at 200 °C for 6 h before each measurement.

Confocal Raman spectra were recorded at 532 nm using a Renishaw (Wottonunder-Edge, United Kingdom) InVia Reflex Raman microscope with a 532 nm frequency-

doubled Nd:YAG excitation source in combination with an 1800 lines mm^{-1} grating, and a Peltier-cooled CCD detector (203 K). The instrument included a Leica light microscope with a 50× air objective. The 521 cm^{-1} Raman shift of an internal silicon standard was used to verify the spectral calibration of the system.

The X-ray photoelectron spectroscopy (XPS) measurements were performed on a SPECS spectrometer equipped with a Phoibos 100 MCD analyzer and a monochromatized X-ray Al Kα (1486.6 eV). High resolution spectra were taken with an energy pass of 30 eV and an energy step of 0.1 eV. Binding energies (BE), referenced to the C 1s line at 284.8 eV, have an accuracy of ± 0.1 eV. The assignment of the C 1s binding energies was done according to the criteria used by Ganguly *et al.* 284.5 eV for C=C (aromatic double bonds), 285.5 eV for C–OH and sp^3 C–C, 286.5 eV for epoxy, 287.5 for sp^2 C=O (carbonyls, lactones) and 289 eV for carboxylic groups.[3]

X-ray diffraction (XRD) measurements were carried out on a Rigaku Miniflex X-ray diffractometer from 4° to 70° using a 2.0° min^{-1} angular velocity.

Scanning Electron Microscope (SEM) images were taken by a FEI Verios 460 using a 5 kV accelerating voltage. HRTEM samples were dispersed in ethanol, sonicated for 2 min and sprayed on a carbon-coated copper grids and then allowed to air-dry. High resolution transmission electron microscopy (HRTEM) were carried out using a Tecnai F30 microscope operated at an accelerating voltage of 300 kV, equipped with a field emission gun (FEG) and an ultra-high-resolution pole-piece that provided a point-to-point resolution of 0.19 nm. STEM-EDS images were recorded using an EDS detector with energy resolution <127 eV and a resolution of 0.20 nm. Scanning transmission electron microscopy (STEM) micrographs were recorded using a High Angular Annular Dark Field detector (HAADF) in a probe-corrected FEI Titan 60-300 operated at 300 kV and equipped with a high brightness X-FEG and Cs CETCOR corrector for the condenser system to provide sub-angstrom probe size. A few additional HRTEM micrographs were recorded on a FEI Tecnai G2 high-resolution transmission electron microscope working at 200 kV, equipped with a FEG.

UV/Vis measurements were recorded on a Varian Cary 50 Bio spectrophotometer, equipped with a variable-speed stirrer module, using quartz cuvettes (l = 1 cm).

The Ru content was determined by ICP mass spectrometry with dynamic reaction cell (ICP-DRC-MS) after microwave digestion, using an Agilent 7700x spectrometer. Rhodium (^{103}Rh) was used as internal standard. All samples were digested by acid assisted microwave irradiation using Ethos One de Milestone SK-10 microwave unit. 3 mL of aqua regia (3 HCl: 1 HNO_3 mixture) were added to 15 mg of each of the samples in closed Teflon vessels with micro-inserts. The microwave program consisted of subjecting the samples to a power of 500 W for two steps of 15 min and 10 min at 180 °C. A summary of the instrumental parameters for ICP-MS is shown in table A6.1.

Table A6.1. Instrumental parameters for ICP-MS.

Inductively Coupled Plasma		Mass Spectrometer		Dynamic reaction cell	
RF power (W)	1550	Sampling cone	Nickel	He flow rate (mL min^{-1})	4.3
Carrier gas (L/min)	1.07	Skimmer cone	Nickel		
Plasma gas (L/min)	15	Peak pattern	3 points		
Auxiliary gas (L/min)	0	Replicates	3		
Sample depth (mm)	10	Sweeps/replicate	100		
Solution uptake rate (mL/min)	0.1	Integration time	0.2 s		
Nebulizer	Micromist	Analytical masses	^{101}Ru		

6.5.3 Additional tables and figures

Table A6.2. Overview of catalytic activity of several catalysts developed for the reduction of 4-nitroaniline (*p*NA) using ammonia borane.

Entry	Catalyst	Temperature (K)	TOF[a] (mol *p*NA/mol cat, min^{-1})	Reference
1	$Ag_{0.64}$-$Au_{0.36}$@CeO_2	298	1.25	[4]
2	Pt/CeO_2-rGO	298	1.44	[5]
3	CoN@PCN	303	2.5	[6]
4	Ag/MTA	298	4.2[b]	[7]
5	$Au_{66}Pd_{34}$/C	298	4.8	[8]
6	Ru/TASC-NaOH	298	7.1	this work
7	$Cu_{0.8}Ni_{0.2}$-CeO_2/rGO	298	8.1	[9]
8	Ru/TASC-NaOH	318	13	this work
9	NP-Cu@Cu_2O	303	13	[10]
10	Pd@MIL-101	298	97	[11]

[a] Calculated using equation 6.2 in this appendix. [b] $NaBH_4$ was used as reductant instead of ammonia borane.

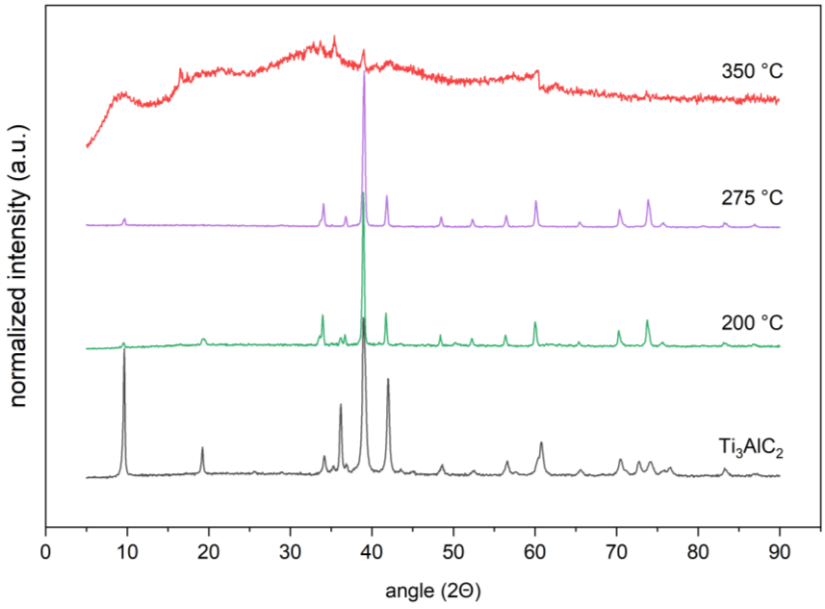

Figure A6.1. X-ray diffractograms of pristine TASC MAX phase before and after NaOH treatment.

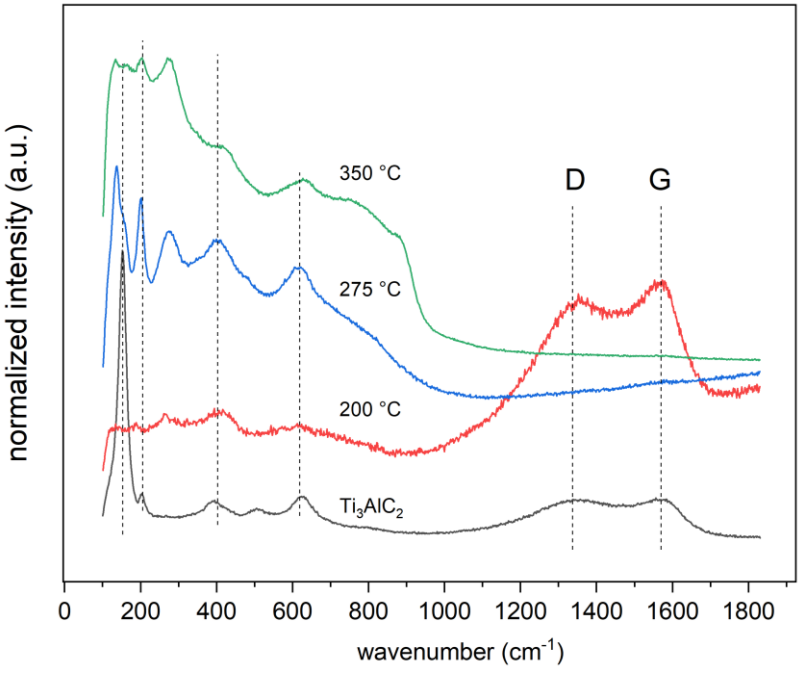

Figure A6.2. Raman spectra of TASC MAX phase before and after NaOH treatment at different treatment temperatures.

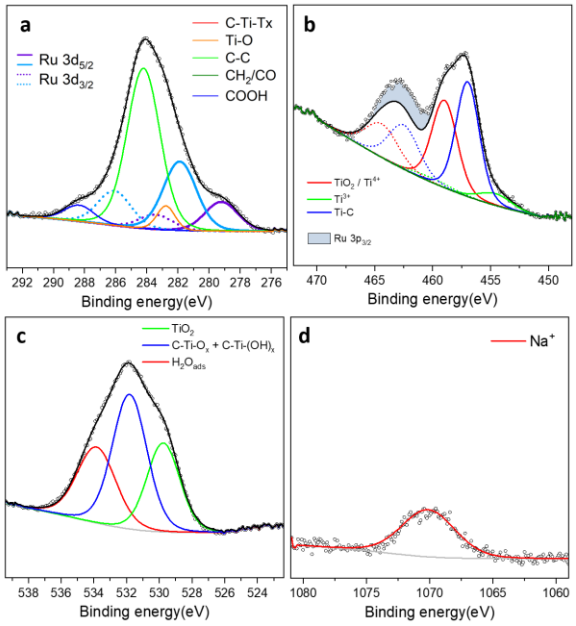

Figure A6.3. Normalized XPS spectra of 0.4 wt% Ru/NaOH-treated TASC presenting (**a**) C 1s/Ru 3d, (**b**) Ti 2p/Ru 3p, (**c**) O 1s, and (**d**) Na 1s.

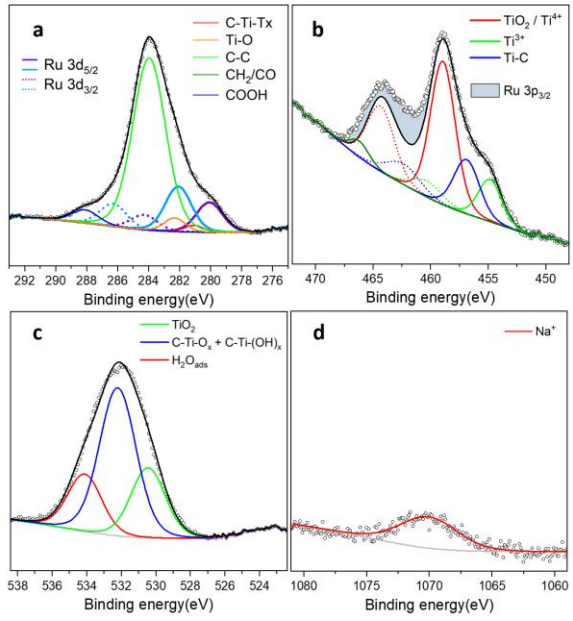

Figure A6.4. Normalized XPS spectra of 0.4 wt% Ru/ TASC presenting (**a**) C 1s/Ru 3d, (**b**) Ti 2p/Ru 3p, (**c**) O 1s, and (**d**) Na 1s.

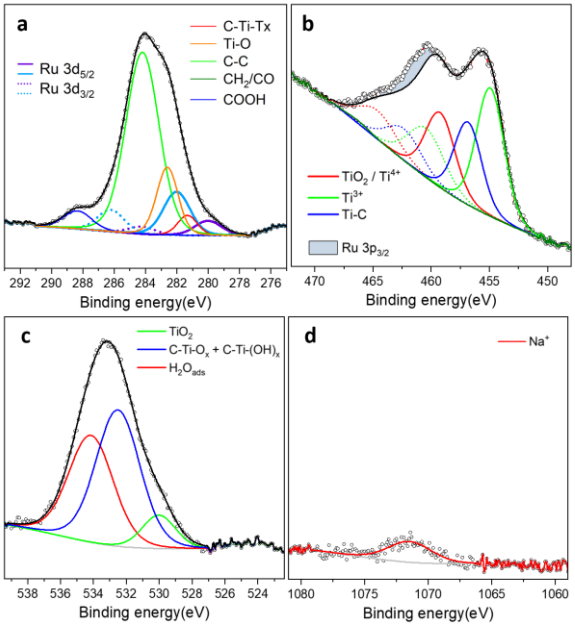

Figure A6.5. Normalized XPS spectra of 0.4 wt% Ru/$Ti_3C_2T_x$ (HF method) presenting (**a**) C 1s/Ru 3d, (**b**) Ti 2p/Ru 3p, (**c**) O 1s, and (**d**) Na 1s.

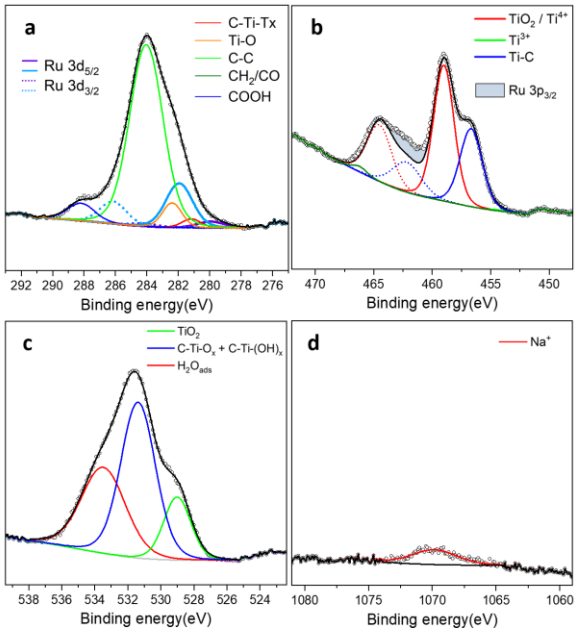

Figure A6.6. Normalized XPS spectra of 0.4 wt% Ru/TiO_2 anatase presenting (**a**) C 1s/Ru 3d, (**b**) Ti 2p/Ru 3p, (**c**) O 1s, and (**d**) Na 1s.

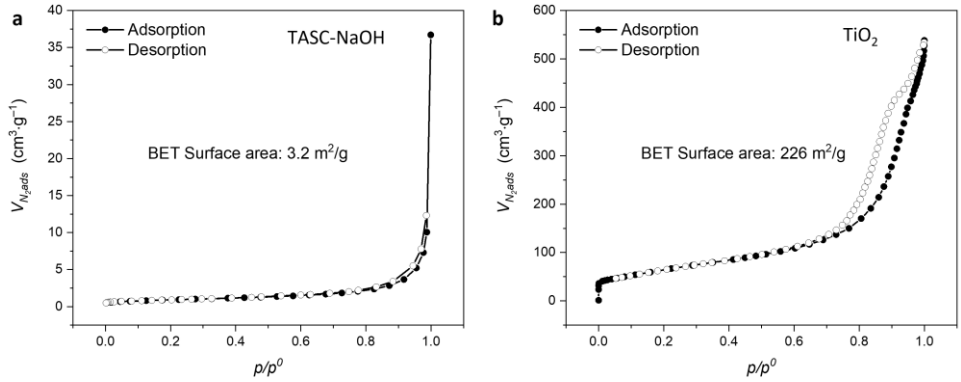

Figure A6.7. N_2 adsorption isotherms (77 K) for (a) TASC-NaOH and (b) TiO_2.

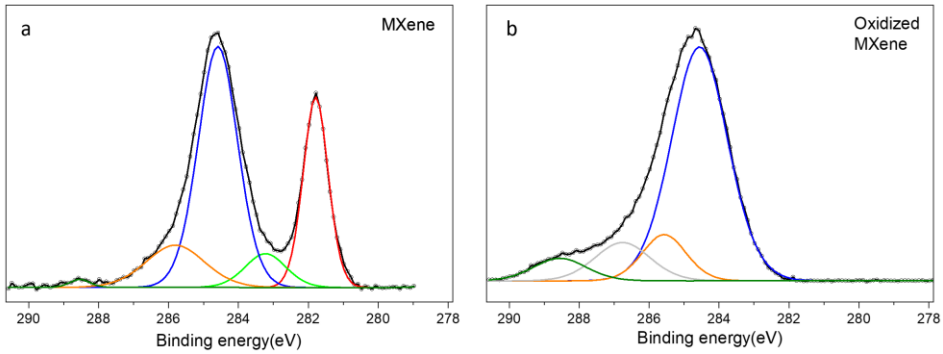

Figure A6.8. XPS spectra of (a) pristine MXene and (b) oxidized MXene.

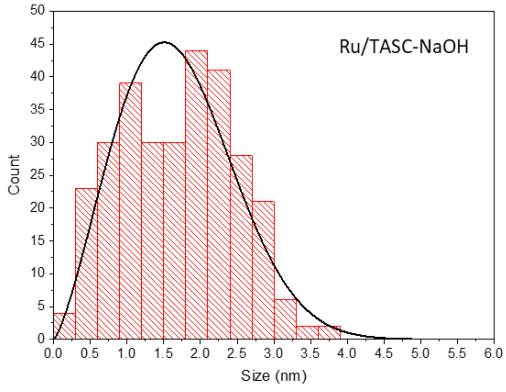

Figure A6.9. Particle size distribution of 0.4 wt% Ru/TASC-NaOH, from TEM micrographs.

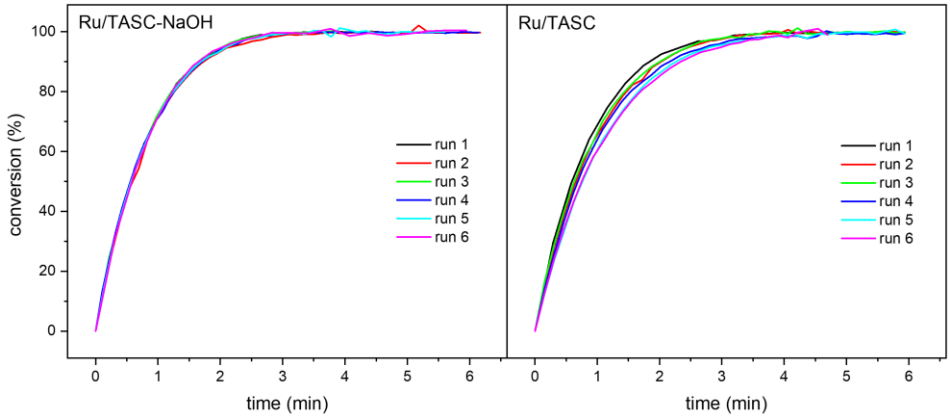

Figure A6.10. Recycle data for Ru/TASC-NaOH and Ru/TASC catalysts in the reduction of 4-nitroaniline.

6.5.4 References

[1] A. Aijaz, A. Karkamkar, Y. J. Choi, N. Tsumori, E. Rönnebro, T. Autrey, H. Shioyama, Q. Xu, *J. Am. Chem. Soc.* **2012**, *134*, 13926–13929.

[2] T. K. Slot, N. R. Shiju, G. Rothenberg, *Angew. Chem. Int. Ed.* **2019**, *58*, 17273–17276.

[3] G. Ramos-Fernandez, M. Muñoz, J. C. García-Quesada, I. Rodriguez-Pastor, I. Martin-Gullon, *Polym. Compos.* **2018**, *39*, 2116–2124.

[4] D. Liu, W. Li, X. Feng, Y. Zhang, *Chem. Sci.* **2015**, *6*, 7015–7019.

[5] X. Wang, D. Liu, S. Song, H. Zhang, *J. Am. Chem. Soc.* **2013**, *135*, 15864–15872.

[6] L. Zhang, J. Wang, N. Shang, S. Gao, Y. Gao, C. Wang, *Appl. Surf. Sci.* **2019**, *491*, 544–552.

[7] D. Andreou, D. Iordanidou, I. Tamiolakis, G. S. Armatas, I. N. Lykakis, *Nanomaterials* **2016**, *6*, 54.

[8] M. Muzzio, H. Lin, K. Wei, X. Guo, C. Yu, T. Yom, Z. Xi, Z. Yin, S. Sun, *ACS Sustain. Chem. Eng.* **2020**, *8*, 2814–2821.

[9] Y.-H. Zhou, S. Wang, Y. Wan, J. Liang, Y. Chen, S. Luo, C. Yong, *J. Alloys Compd.* **2017**, *728*, 902–909.

[10] J. Du, J. Hou, B. Li, R. Qin, C. Xu, H. Liu, *J. Alloys Compd.* **2020**, *815*, 152372.

[11] Q. Yang, Y.-Z. Chen, Z. U. Wang, Q. Xu, H.-L. Jiang, *Chem. Commun.* **2015**, *51*, 10419–10422.

Summary

Enzymes are remarkably active and selective catalysts and excellent examples where confinement contributes to catalytic efficiency. Their elaborate protein structures allow enzymes to bind substrates, guide them into the active site(s), and stabilize the transition state, enabling very complex reaction pathways. Translating enzyme properties like confinement to heterogeneous catalysts might help to create better catalysts. In this thesis we studied the effect of confinement on heterogeneous catalytic reactions using an experimental approach. We took two routes: one where we actively create confinement by adding a barrier at different distances from the active site, and one where we utilize surface modification of novel two-dimensional materials to create confinement in the interlayer spacing. These two-dimensional materials were also studied for their intrinsic catalytic activity and as a support for metallic nanoparticles.

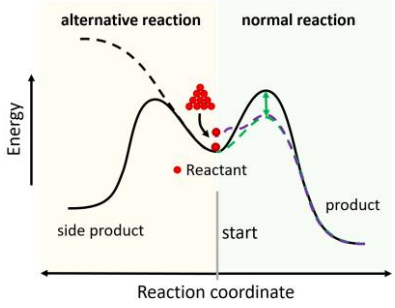

Confinement comes in different shapes and sizes. In **Chapter 1** we studied the most prominent cases of confinement reported in literature and developed a framework to explain the observed confinement effects. We hypothesize that these effects can be captured by three phenomena: (1) decreasing the activation energy, (2) increasing the local concentration of reactants (increasing the reaction rate), and (3) steric effects such as pre-organisation and restricting access to alternative reaction pathways. These effects can be described by a simple energy–reaction-coordinate diagram. Stabilizing the transition state reduces the enthalpy term of the Gibbs free energy ($\Delta G^{\ddagger}$), and pre-organisation (and confinement) influences the entropy term of $\Delta G^{\ddagger}$ energy barrier. Changes in local concentration influence neither. From this perspective, we expect confinement effects to mainly influence entropy of the transition-state Gibbs free energy.

Changes in the Gibbs free energy can be conveniently studied by Arrhenius or Eyring analysis of experimental kinetic data. These analyses separate the enthalpy and entropic contributions to the reaction barrier. We expect confinement effects to influence the entropy contribution, which impacts the pre-exponential factor of these models. Such analyses require us to obtain detailed kinetic data of chemical reactions. In **Chapter 2**, we developed a novel device and method to quantify gas production using the principle of bubble counting. The device is simple, accurate, and robust, allowing the quantification of reaction kinetics with high precision. Using this 'bubble counter' we can determine temperature/rate relationships and calculate Arrhenius and Eyring parameters quickly and efficiently. The large number of data

points enables a thorough statistical analysis and allows us to observe subtle physicochemical changes (such as induction effects or changes in the rate-determining step) that hitherto were inaccessible.

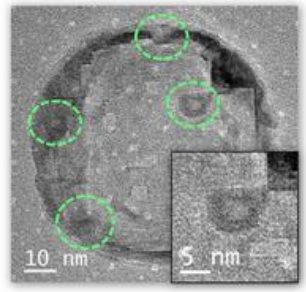

In **Chapter 3**, we applied this method to study confinement effects around Pt nanoparticles (on an alumina support) with various degrees of molecular confinement at the active site. We devised a three-step synthesis strategy to confine the nanoparticles by constructing a physical barrier ("fence") at a controlled distance from the Pt nanoparticles. This was done by first coating the Pt nanoparticles with organothiols (to "block out" a region around the particles), followed by a surface coating of organophosphonic acids. Finally, the thiols were removed, opening up the space around the Pt active site. We then measured their catalytic activity in the hydrolysis of ammonia borane using the fast and precise online measurements provided by our bubble counter. We found that confining the reaction mainly influences the entropy part of the enthalpy/entropy trade-off, leaving the enthalpy unchanged. We further found that this entropy contribution is only relevant at *very* small distances, where the "empty space" is of a similar size as the reactant molecule (< 3 Å for ammonia borane). This suggests that confinement effects observed over larger distances must be enthalpic in nature and involve electronic interactions to stabilize the transition state.

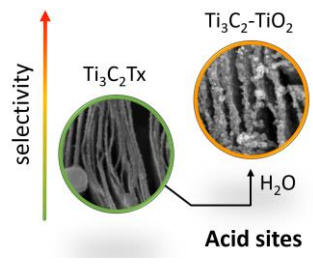

In **Chapter 4**, we start our investigation on novel two-dimensional MXene materials for catalysis. We show that etching and delamination of Ti_3AlC_2 MAX phase creates a partially-opened multilayer MXene material with different types of acid functionalities. These catalysts also feature some inter-layer confinement, but the size of the gap between the layers is very difficult to control. Our results show that both MXene and MXene-TiO_2 composite materials can catalyse the ring opening and isomerisation of styrene oxide. We discovered that these catalysts contains both Lewis and Brønsted acidic sites. Post-modification of the MXene effectively changes the type and concentration of surface acidic sites, improving the yield of the mono-alkylated product up to > 80%. We hypothesize that our catalysts contains two types of acid sites: In the MXene samples, strong acid sites (both Lewis and Brønsted) catalyse both the ring opening and the isomerization reactions, while in the MXene-TiO_2 composite weaker acid sites catalyse only the ring-opening reaction, increasing the selectivity the mono-alkylated product. This chapter shows how $Ti_3C_2T_x$ MXene can be applied as an acid catalyst and how the acidic strength can be tuned by modifying the MXene surface.

In **Chapter 5**, we explored the use of MXene as a *support* for metallic nanoparticles. It turned out to be challenging to place the particles exclusively in the confined inter-layer space within the MXene. So instead, we used wet impregnation to load the MXene with platinum nanoparticles on all available MXene surfaces. We found that $Ti_3C_2T_x$ (T_x is –F, –O or =O) MXene and especially oxidized $Ti_3C_2T_x$ MXene have a unique interaction with the Pt nanoparticles, influencing their electronic structure and subsequently their reactivity in the hydrolysis of ammonia borane. By leveraging the oxidation sensitivity of the Ti–F bonds in $Ti_3C_2T_x$, it was possible to grow a thin oxide layer (10 nm) on the surface of the MXene. This layer was different from the bulk oxides (rutile/anatase TiO_2) and the ultra-thin oxide layer present on pristine MXene and helped stabilizing the fine Pt nanoparticles under reaction conditions. Finally, we show that by controlling the oxide layer we can control the interaction of the support surface with the Pt nanoparticles, creating efficient catalysts for on-demand hydrogen generation. This strategy offers new tools for catalyst design and helps us to create better catalysts for energy applications.

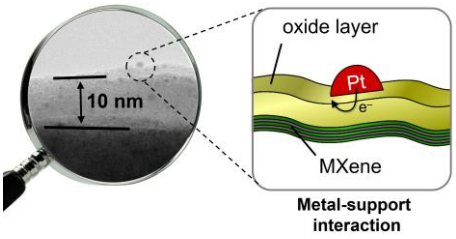

To avoid the oxidation sensitivity of MXene, we investigated fluorine-free delamination methods. In **Chapter 6**, we applied alkaline etching to a MAX phase where aluminium is partially substituted by tin. We found that alkaline solutions can dissolve the Al interlayers at relatively low concentrations, whilst avoiding side-reactions producing sodium titanates. This creates ribbons of MXene and a bulk MAX phase with disordered interlayer spacing. Unfortunately, the layers are either separated completely or not at all, so we couldn't control the interlayer spacing using this method. Nevertheless, we found this material was a good support for ruthenium nanoparticles, giving good results in the catalytic reduction of 4-nitroanline. After alkaline etching, the surface of the disordered MAX phase contains Sn and Ti^{3+}, both of which can interact with ruthenium to form metal-support interactions. We show that ruthenium impregnated on NaOH-treated materials outperform regular Ti_3AlC_2 MAX phase and MXene in both catalytic activity and stability, owing to the interaction of Ru with Sn.

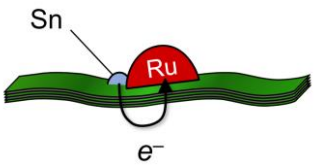

Overall, this thesis shows the importance of confinement effects in catalysis and provides a framework for analysing these effects. We developed a novel device that allows for highly precise kinetics measurements of several gas-producing model reactions. We gained important insights about the role of the pre-exponential factor in surface catalysis and the range over which confinement effects are important. Finally,

the thesis establishes MXenes and MAX phases as a new type of catalytic materials and supports in heterogeneous catalysis. The oxidation sensitivity of MXene provides a new tool for influencing the reactivity of these materials and by tuning the electronic structure at the active sites.

Samenvatting

Enzymen zijn zeer actieve en selectieve katalysatoren, en een prachtig voorbeeld waar opsluiting ('confinement') van het molecuul bijdraagt aan katalytische efficiëntie. Door de uitgebreide eiwitstructuren kunnen enzymen moleculen binden, deze naar de actieve site(s) geleiden, en vervolgens de overgangstoestand stabiliseren, waardoor zeer complexe reactiepaden door het reactant bewandeld kunnen worden. Het overzetten van enzymeigenschappen (zoals opsluiting) naar heterogene katalysatoren kan hun werking mogelijk aanzienlijk verbeteren. In dit proefschrift bestuderen we het effect van opsluiting op heterogene katalytische reacties met een experimentele benadering. Hiertoe gebruiken we twee verschillende methodes: één waarbij we actief opsluiting creëren door op een katalysator een barrière te plaatsen op verschillende afstanden van de katalytische site, en één waarbij we gebruikmaken van oppervlaktemodificatie om nieuwe tweedimensionale materialen te modificeren en zodoende opsluiting te creëren tussen de lagen. Deze nieuwe materialen hebben we ook bestudeerd als katalysator en als dragermateriaal voor katalytisch actieve metallische nanodeeltjes.

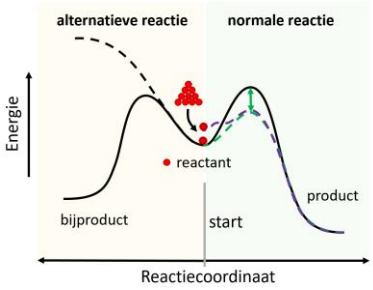

Opsluiting van katalytische reacties is op vele manieren waargenomen. In **hoofdstuk 1** hebben we de meest prominente gevallen van opsluiting in de literatuur bestudeerd en een structuur ontwikkeld om de waargenomen opsluitingseffecten te verklaren. Onze hypothese is dat deze effecten kunnen worden verklaard door drie fenomenen: (1) het verlagen van de activeringsenergie, (2) het verhogen van de lokale concentratie van reactanten (wat het verhogen van de reactiesnelheid als gevolg heeft), en (3) sterische effecten zoals pre-organisatie wat de toegang tot alternatieve reactiepaden kan ontzeggen. Deze effecten kunnen worden beschreven door een eenvoudig energie-reactiecoördinaat diagram. Het stabiliseren van de overgangstoestand verlaagt het enthalpiedeel van de Gibbs-vrije energie barrière ($\Delta G^{\ddagger}$), en pre-organisatie (en dus ook opsluiting) beïnvloedt het entropie deel van deze barrière. Veranderingen in de lokale concentratie hebben geen invloed op de entropie of enthalpie. Hierdoor verwachten we dat opsluitingseffecten voornamelijk de entropie van de Gibbs-vrije energie in overgangstoestand zullen beïnvloeden.

Veranderingen in de Gibbs vrije energie kunnen gemakkelijk worden bestudeerd met Arrhenius- of Eyring-analyses van experimentele kinetische data. Deze analyses scheiden de bijdragen van enthalpie en entropie op de reactiebarrière. We verwachten dat opsluitingseffecten de entropiebijdrage zullen beïnvloeden, wat uiteindelijk de pre-exponentiële factor van deze modellen zal beïnvloeden. Dergelijke analyses vereisen zeer

gedetailleerde kinetische gegevens van de reactie die we bestuderen. In **hoofdstuk 2** hebben we een nieuw apparaat ontwikkeld om gasproductie vanuit een chemische reactie te kwantificeren door het tellen van bellen. Het apparaat is eenvoudig, nauwkeurig en robuust, waardoor de reactiekinetiek met hoge precisie kan worden vastgesteld. Met behulp van deze 'bellenteller' kunnen we temperatuur-reactiesnelheid-relaties bepalen en kunnen we Arrhenius- en Eyring-parameters snel en efficiënt berekenen. Het grote aantal datapunten maakt een grondige statistische analyse mogelijk en stelt ons in staat om subtiele fysisch-chemische veranderingen (zoals inductie-effecten of veranderingen in de snelheidsbepalende stap van de reactie) waar te nemen, iets wat tot nu toe niet goed mogelijk was.

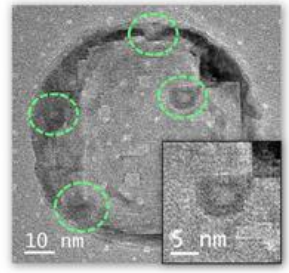

In **hoofdstuk 3** hebben we dit apparaat toegepast om opsluitingseffecten te bestuderen bij Pt-nanodeeltjes op een aluminiumoxide dragermateriaal waarbij de mate van moleculaire opsluiting werd gevarieerd. We bedachten een drietraps synthesestrategie om de nanodeeltjes op te sluiten door een fysieke barrière (een "hek") te construeren op een gecontroleerde afstand van de Pt-nanodeeltjes. Dit werd gedaan door de Pt-nanodeeltjes eerst te bedekken met organothiolen (om een gebied rond de deeltjes "af te zetten" of "te blokkeren"), gevolgd door een oppervlaktecoating van een organofosfonzuur. Ten slotte werden de thiolen verwijderd, waardoor de ruimte rond de actieve Pt-site werd geopend. Vervolgens hebben we de katalytische activiteit van deze katalysatoren vastgesteld met de hydrolyse van ammoniakboraan, welke werd gemeten met behulp van onze bellenteller. We ontdekten dat het opsluiten van de reactie voornamelijk het entropiegedeelte van de enthalpie/entropie-wisselwerking beïnvloedt, waarbij de enthalpie ongewijzigd blijft. We ontdekten verder dat deze entropiebijdrage alleen relevant is op zeer kleine afstanden, waar de "lege ruimte" een vergelijkbare grootte heeft als het reactant (<3 Å voor ammoniakboraan). Dit suggereert dat opsluitingseffecten, welke over grotere afstanden worden waargenomen, enthalpisch van aard zijn en dus elektronische interacties moeten omvatten waarmee de overgangstoestand gestabiliseerd wordt.

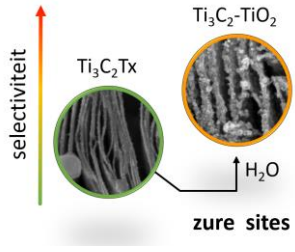

In **hoofdstuk 4** onderzoeken we het nieuwe tweedimensionale materiaal, MXene, voor gebruik in de katalyse. We laten zien dat etsen en delamineren van de Ti_3AlC_2 MAX-fase een halfopen meerlaags MXene materiaal creëert met verschillende soorten zuurfunctionaliteiten. Deze katalysatoren vertonen ook een geringe mate van opsluiting tussen de lagen, maar de laagafstand is erg moeilijk te beïnvloeden. Onze resultaten tonen aan dat zowel MXene als MXene-titania composieten de ringopening en isomerisatie van styreenoxide

kunnen katalyseren. We ontdekten dat deze katalysatoren zowel Lewis- als Brønsted-zure sites bevatten. Postmodificatie van de MXene verandert het type en de concentratie van de zure sites aan het oppervlak, waardoor de opbrengst van het mono-gealkyleerde product tot > 80% kon worden verbeterd. Onze hypothese is dat onze katalysatoren twee soorten zure sites bevatten: de MXene-materialen bevatten sterk-zuurplaatsen (zowel Lewis als Brønsted) welke zowel de ringopening als de isomerisatiereactie katalyseren, terwijl de MXene-titania-composiet zwakkere zuurplaatsen bevat die alleen de ringopening katalyseren, waardoor de selectiviteit van het mono-gealkyleerde product toeneemt. Dit hoofdstuk laat zien hoe $Ti_3C_2T_x$ MXene kan worden toegepast als zure katalysator en hoe de zuursterkte kan worden aangepast door het MXene-oppervlak te modificeren.

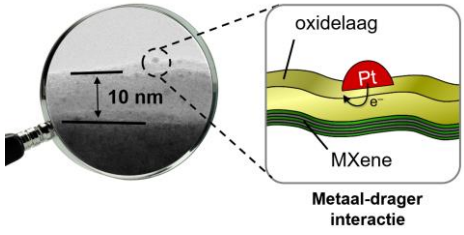

In **hoofdstuk 5** hebben we MXene gebruikt als dragermateriaal voor metallische nanodeeltjes. Het bleek een uitdaging te zijn om de deeltjes uitsluitend tussen de MXene lagen te plaatsen. Dus in plaats daarvan hebben we de deeltjes op het volledige beschikbare MXene oppervlak geïmpregneerd. We ontdekten dat $Ti_3C_2T_x$ (T_x is −F, −O of = O) MXene en vooral de geoxideerde vorm hiervan een unieke interactie heeft met de Pt-nanodeeltjes, waardoor hun elektronische structuur (en vervolgens hun reactiviteit) wordt beïnvloed. Door gebruik te maken van de oxidatiegevoeligheid van de Ti-F-bindingen in $Ti_3C_2T_x$, was het mogelijk om een dunne oxidelaag (10 nm) op het oppervlak van de MXene te laten groeien. Deze laag was anders dan de bulkoxiden (rutiel / anatase TiO_2) en de kleine oxidelaag zoals deze aanwezig is op het ongerepte MXene. Deze oxidelaag hielp bij het stabiliseren van de kleine Pt-nanodeeltjes onder reactieomstandigheden. Ten slotte laten we zien dat we door het beïnvloeden van de oxidelaag de interactie van het drageroppervlak met de Pt-nanodeeltjes kunnen regelen, waardoor efficiënte katalysatoren worden gecreëerd voor het genereren van waterstof vanuit ammoniakboraan. Deze strategie biedt een nieuw gereedschap voor katalysatorontwerp en helpt ons om betere katalysatoren voor energietoepassingen te creëren.

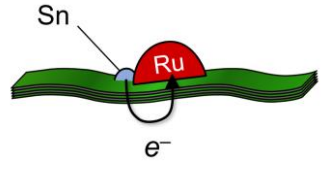

Om de oxidatiegevoeligheid van MXene te vermijden, hebben we een fluorvrije methode van delamineren (alkalische etsen) onderzocht. In **hoofdstuk 6** hebben we dit toegepast op een MAX-fase waar aluminium voor ongeveer 20% is vervangen door tin. We ontdekten dat alkalische oplossingen de Al-tussenlagen bij relatief lage concentraties kunnen oplossen, terwijl nevenreacties zoals vorming van natriumtitnanaat konden worden vermeden. Hierdoor ontstaan een soort

linten van MXene en een bulk MAX-fase met een ongeordende tussenlaagafstand. Helaas zijn de lagen óf volledig óf helemaal niet gescheiden, dus we konden de laagafstand met deze methode niet sturen. Desalniettemin ontdekten we dat dit materiaal een goede drager is voor ruthenium nanodeeltjes, welke de reductie van 4-nitroanline katalyseert. Na het etsen bevat het oppervlak van de ongeordende MAX-fase zowel Sn en Ti^{3+}, welke beide een interactie kunnen aangaan met de ruthenium deeltjes (een zogenaamde metaal-dragerinteractie). We laten zien dat het ruthenium geïmpregneerd op NaOH-behandelde materialen beter presteert dan de reguliere Ti_3AlC_2 MAX-fase en MXene op zowel katalytische activiteit als stabiliteit. Dit is dankzij de interactie van Ru met Sn.

Dit proefschrift laat het belang zien van opsluitingseffecten in de katalyse en biedt handvaten voor het analyseren van deze effecten. We hebben een nieuw apparaat ontwikkeld dat zeer nauwkeurige kinetische metingen van gas-producerende reacties mogelijk maakt. We hebben belangrijke inzichten verworven over de rol van de pre-exponentiële factor in heterogene katalyse en de afstanden waarbinnen opsluitingseffecten een belangrijke factor zijn. Ten slotte vestigt dit proefschrift MXenes en MAX-fasen als nieuwe typen katalytische- en dragermaterialen binnen de heterogene katalyse. Verder laten we zien dat de oxidatiegevoeligheid van MXene gebruikt kan worden als een nieuw instrument om de reactiviteit van deze materialen te sturen en om de elektronische structuur van katalytische sites te beïnvloeden.

Publications

Part of this thesis

Chapter 1: T.K. Slot, N.R. Shiju and G. Rothenberg, Principles of confinement in heterogeneous catalysis. *Manuscript in preparation*

Chapter 2: T.K. Slot, N.R. Shiju, G. Rothenberg, A Simple and Efficient Device and Method for Measuring the Kinetics of Gas-Producing Reactions, *Angew. Chem. Int. Ed.* **2019**, *58*, 17273–17276; *Angew. Chem.* **2019**, *131*, 17433–17436.

Click the link to watch a 1-minute video.

Chapter 3: T.K. Slot, N. Riley, N. Raveendran Shiju, J. Will Medlin, G. Rothenberg, An experimental approach for controlling confinement effects at catalyst interfaces, *Chem. Sci.* **2020**, *11*, 11024–11029,

Click the link to watch a 1-minute animation.

Chapter 4: T.K. Slot, V. Natu, E.V. Ramos-Fernandez, A. Sepúlveda-Escribano, M. Barsoum, G. Rothenberg, and N. Raveendran Shiju, Enhancing catalytic epoxide ring-opening selectivity using surface-modified $Ti_3C_2T_x$ MXenes, *2D mater., in press.*

Chapter 5: T.K. Slot, F. Yue, H. Xu, E.V. Ramos-Fernandez, A. Sepúlveda-Escribano, Z. Sofer, G. Rothenberg, N.R. Shiju, Surface oxidation of $Ti_3C_2T_x$ enhances the catalytic activity of supported platinum nanoparticles in ammonia borane hydrolysis, *2D Mater.* **2020**, *8*, 015001

Click the link to watch a 1-minute animation.

Chapter 6: T.K. Slot, P. Oulego, Z. Sofer, G. Rothenberg and N. Raveendran Shiju, Ruthenium on alkali-exfoliated $Ti_3(Al_{0.8}Sn_{0.2})C_2$ MAX phase catalyzing reduction of 4-nitroaniline with ammonia borane., s*ubmitted.*

Other publications

1. W. Zhang, P. Oulego, T.K. Slot, G. Rothenberg, N.R. Shiju, Selective Aerobic Oxidation of Lactate to Pyruvate Catalyzed by Vanadium-Nitrogen-Doped Carbon Nanosheets, *ChemCatChem* **2019**, *11*, 3381–3387.

2. W. Böhmer, T. Knaus, A. Volkov, T.K. Slot, N.R. Shiju, K. Engelmark Cassimjee, F.G. Mutti, Highly efficient production of chiral amines in batch and continuous flow by immobilized ω-transaminases on controlled porosity glass metal-ion affinity carrier, *J. Biotechnol.* **2019**, *291*, 52–60.

3. T.K. Slot, D. Eisenberg, G. Rothenberg, Cooperative Surface-Particle Catalysis: The Role of the "Active Doughnut" in Catalytic Oxidation, *ChemCatChem* **2018**, *10*, 2119–2124.

4. D. Eisenberg, T.K. Slot, G. Rothenberg, Understanding Oxygen Activation on Metal- and Nitrogen-Codoped Carbon Catalysts, *ACS Catal.* **2018**, *8*, 8618–8629.

5. I.M. Denekamp, M. Antens, T.K. Slot, G. Rothenberg, Selective Catalytic Oxidation of Cyclohexene with Molecular Oxygen: Radical Versus Nonradical Pathways, *ChemCatChem* **2018**, *10*, 1035–1041.

6. J. Biemolt, I.M. Denekamp, T.K. Slot, G. Rothenberg, D. Eisenberg, Boosting the Supercapacitance of Nitrogen-Doped Carbon by Tuning Surface Functionalities, *ChemSusChem* **2017**, *10*, 4018–4024.

7. T.K. Slot, D. Eisenberg, D. van Noordenne, P. Jungbacker, G. Rothenberg, Cooperative Catalysis for Selective Alcohol Oxidation with Molecular Oxygen, *Chem. Eur. J.* **2016**, *22*, 12307–12311.

8. J. van Ameijde, T.K. Slot, R.M.J. Liskamp, Towards the synthesis of sulfonamide-based RNA mimetics, *Tetrahedron Asymmetry,* **2010**, *21*, 469–475.

9. P.M. van Hasselt, G.E.P.J. Janssens, T.K. Slot, M. van der Ham, T.C. Minderhoud, M. Talelli, L.M. Akkermans, C.J.F. Rijcken, C.F. van Nostrum, The influence of bile acids on the oral bioavailability of vitamin K encapsulated in polymeric micelles, *J. Control. Release,* **2009**, *133*, 161–168.

Contributions to this thesis

Overview of co-authors' contributions to the individual thesis chapters.

Chapter 1

Introduction

T. K. Slot	Developed the hypotheses, surveyed the literature and wrote the manuscript.
G. Rothenberg	Reviewed the manuscript and made suggestions for improvements.
N. R. Shiju	Reviewed the manuscript and made suggestions for improvements.

Chapter 2

A simple and efficient device and method for measuring the kinetics of gas-producing reactions

T. K. Slot	Conceived the idea, designed and built all prototype/devices (incl. CAD drawings), 3D-printed all parts, designed the electronics, and programmed the microcontrollers. Developed the software for the PC. Developed the data processing algorithms. Performed all experiments, including calibration and validation experiments. Wrote the manuscript.
G. Rothenberg	Reviewed the manuscript and made suggestions for improvements.
N. R. Shiju	Reviewed the manuscript and made suggestions for improvements.

Chapter 3

An experimental approach for controlling confinement effects at catalyst interfaces

T. K. Slot	Co-developed the synthesis strategy, designed the experiments. Performed the characterization experiments (TEM, FTIR) and ran the preliminary studies. Supervised the experiments done by N. Riley. Analysed and interpreted the data. Wrote the manuscript.

	Conducted part of the synthesis and kinetic experiments (50%).
N. Riley	Conducted part of the synthesis and kinetic experiments (50%).
G. Rothenberg	Co-developed the synthesis strategy. Reviewed the manuscript and made suggestions for improvements.
N. R. Shiju	Reviewed the manuscript and made suggestions for improvements.
J. W. Medlin	Reviewed the manuscript and made suggestions for improvements.

Chapter 4

Acid catalysis with surface-modified Ti_3C_2Tx MXenes

T. K. Slot	Designed the experiments and developed the hypotheses. Synthesized the catalytic composite materials. Ran all catalytic experiments. Performed all characterization experiments (incl. XRD, NMR, SEM, DRIFTS, and FTIR) except for TEM and XPS. Analysed and interpreted the data (incl. XPS analysis) and wrote the manuscript.
V. Natu	Synthesized the MXene precursor.
E.V. Ramos-Fernandez	Conducted XPS measurements and TEM experiments.
A. Sepúlveda-Escribano	Reviewed the manuscript and made suggestions for improvements.
M. Barsoum	Reviewed the manuscript and made suggestions for improvements.
G. Rothenberg	Reviewed the manuscript and made suggestions for improvements.
N. R. Shiju	Reviewed the manuscript and made suggestions for improvements.

Chapter 5

Surface oxidation of MXene enhancing the catalytic activity of Pt nanoparticles

T. K. Slot	Developed the hypotheses and designed the experiments. Synthesis of the composite materials and catalysts. Ran the catalytic experiments. Performed all characterization experiments (incl. XRD, Raman, SEM, and TEM studies) except the HAADF-TEM and XPS measurements. Analysed

	and interpreted the experimental data (incl. XPS analysis) and wrote the manuscript.
F. Yue	Conducted HAADF-TEM experiments.
H. Xu	Reviewed the manuscript and made suggestions for improvements.
E.V. Ramos-Fernandez	Conducted XPS measurements.
A. Sepúlveda-Escribano	Reviewed the manuscript and made suggestions for improvements.
Z. Sofer	Synthesized MXene material using HF. Reviewed the manuscript and made suggestions for improvement.
G. Rothenberg	Reviewed the manuscript and made suggestions for improvements.
N. R. Shiju	Reviewed the manuscript and made suggestions for improvements.

Chapter 6

Ruthenium–tin on disordered MAX phase boosting 4-nitroaniline reduction

T. K. Slot	Developed the hypotheses and designed the experiments. Synthesis of the catalysts. Ran all catalytic experiments. Performed all characterization (incl. XRD, Raman, UV/Vis, FTIR and SEM-EDS) except the TEM and XPS measurements. Created software for UV/Vis data analysis. Analysed and interpreted the data (incl. XPS analysis) and wrote the manuscript.
P. Oulego	ICP-MS measurements, XPS and TEM measurements. Reviewed the manuscript and made suggestions for improvement.
Z. Sofer	Synthesized MXene material using HF. Reviewed the manuscript and made suggestions for improvement.
G. Rothenberg	Reviewed the manuscript and made suggestions for improvements.
N. R. Shiju	Reviewed the manuscript and made suggestions for improvements.

Acknowledgements

About five years ago, I came to the University of Amsterdam to pursue a master's degree in chemistry. After a bit of a heavy period, this seemed like the right place for a fresh start. Little did I know that this decision would start such a wonderful chapter in my life. Now, I am finishing with a PhD! And I could *not* have done this without the support of *you*: my thesis advisors, colleagues, students, family and friends that helped me and stood by me. Thank you all!

First of all I would like to thank my promotors **Gadi Rothenberg** and **Shiju Raveendran**. Your support and advice was essential to this project's success. I cannot wish for a better team. Your guidance, knowledge and ideas have led me through the jungle of confinement chemistry and your trust, inspiration and kindness made every day a pleasure to come in.

My adventure started when I registered for a course in heterogeneous catalysis. This was the first time I met **Gadi**. I was impressed with how you could make the principles of heterogeneous catalysis understood using little more than commons sense and a blackboard. By this time I had already finished a research project in the synthetic organic chemistry group, and was a little over a dozen credits short from graduation. Yet, you roused me from the benches and gave me a project. Why do courses, when you can have fun in the lab, right? I liked it so much that this project grew into my new official master project. One of your big strengths is to take people with you in whatever you do and make them part of it. For example, we always worked on manuscripts *together*, which is a student's goldmine! Explaining seemingly small differences, like when to use 'show' and when 'demonstrate', but also learning your language of hums and nods while you read, and hoping you wouldn't spot the "pompous It" I accidentally left two paragraphs down, it was a true feast. But most importantly, you *care* about the person behind the scientist. Whenever I was stuck (or thought I was stuck) you always managed to pull me right out and make a big mountain seem like nothing more than a hill with a view, *to enjoy* of course! How many rounds we must have strolled around the building, under the guise of getting some water or tea, while you shared your advice and wisdom. Gadi, I lack the words to express my gratitude for all the things you have done and shared, but please know that it made all the difference. Thank you.

Shiju, your approach to science has been a real inspiration. I think the first time I met you was when I was just starting my master project with David and Gadi. I am not sure if you remember, but you were giving me a hard time for operating in the lab without finishing the safety test first. Luckily all that was forgiven when you accepted me as your PhD student. You taught me the importance of applications and making sure to have meaningful and useful results before continuing with characterization, even when I had such burning questions about the mechanisms or the catalyst's surface. Whenever an idea or experiment failed, you always have another idea to try, making you the *never-ending fountain of ideas*. Also on a personal level, you also gave valuable advice. I cannot begin to count all the times we called, on many occasions in the evening

or during the weekend. Thank you for your trust, your confidence and for giving me the freedom to run my own projects. But what impressed me most is your personality and modesty. Thank you for everything you did and all your help these past four years.

Next, I want to take the opportunity to thank the members of my promotion committee, prof. dr. **Petra de Jongh**, prof. dr. **Laurent Bonneviot**, prof. dr. **Hualong Xu**, prof. dr. **Evert-Jan Meijer**, prof. dr. **Hong Zhang** and dr. **Francesco Mutti**. Thank you for your time, reading my thesis and participating in my defence.

During my master's project, I worked under the supervision of **David Eisenberg.** David, it was so refreshing having you as my supervisor. You once said: I trust you to do what is right. This trust opened a way for me to really make my own decisions and feel proud and confident about their results. I admire your boundless positivism. You are one of the most knowledgeable, driven (in a purely positive way) and inspirational supervisors I have had, full of ideas, making it such a joy to learn from you. I also remember the Chanukah celebration with the HCSC group at your place, lighting the "oil molecule"-menorah that we designed and 3D printed *… and melted*. I am sure I will come and visit you soon in Israel.

Next, I want to thank my colleagues of the HCSC, CatEng and FunMat groups. I have been so fortunate to work besides you all. Maybe it's a good place to kick off with my fellow PhD 'ceremoniates', **Maria** and **Ilse**. All three of us are defending our theses within the span of one week in April after finishing our PhDs on time. That is something to be proud of!

Maria. You are my most direct colleague, working on MAX phases and MXenes – like me – with Shiju. I could not wish for a better PhD-companion, to bounce ideas around or to just have a chat! I even tried to learn Spanish for a short while, but that was not the greatest success on my part 😉. *¡Espero que mi español pobre, como esta frase, te hace reír mucho!* Thanks for explaining all the "bad" Spanish I picked up from movies: all the bad words, Mexican words and 'Duolingo' Spanish. :) Thank you for all the tea breaks, your help, fun activities, parties, diners and barbecues! I wish you all the best with your new postdoc position. I know you and Pete will conquer the world.

Ilse. Thank you for your analytical expertise and for proofreading so many of my papers and parts of this thesis. Thanks for keeping up the group spirit and organizing so many get-togethers. I cannot think of a single activity where you did not either coordinate or actively participate (but actually still coordinate, 😉). For sure, you are the best narrator for "*Weerwolven*". I always felt I could talk with you about almost anything. Fondly, I think back of our time at Schiermonnikoog, attending the CAIA course (and … uhm… yes, the rear break calliper did turn out to be stuck, ooops … my bad). Defending your thesis well within your 4 years, is an achievement I can only envy. Thank you for

being my paranymph! I wish you all the best, and I hope that somehow you will be able to find your way to Australia during these COVID times.

Andreea. You are the fiery colleague that any office should have. I fondly think back of all the conversations and discussions we had. Your spontaneous ideas often made my day. I remember us playing ball between the growing mushrooms outside of the E building (not the best idea). Or parties and barbecues at your place (very good ideas) and you visiting me with Maria which was a lot of fun. Thank you for all the coffee breaks, fun and drinks. You were not afraid to look for collaborations, even when our bosses preferred us to stay out of each other's territories. I'll just say: we made some great hairy MXene-MOFs! 😉 All the best with your postdoc.

To the reader, it may seem that I only have female colleagues, but nothing is farther from the truth. **Jasper**, I want to thank you for the numerous discussions we had about catalysis and electrocatalysis. You were always ready to help and your vast knowledge of organic chemistry came in very handy when we were figuring out what was happening with our styrene oxide ring opening reaction. **Eric**. You definitely brought some *Deutsche Gründlichkeit* into our group. Thank you for all the discussions and the useful tips and trick on drawing nice graphics. It was also very exciting for me to have your project as one of the first applications of the bubble counter for your high-temperature experiments. Many thank for the pumpkins! They were delicious.

Pieter, thank you for taking over the responsibilities of the bubble counters. I guess you are now the *de facto* champion of the bubble counters! I value our conversations and your sharp comments about how we could improve the measurements. It contributed a lot to making the macros even better. Also many thanks for proofreading parts of my thesis. I am sure you will do a fabulous PhD!

Sheetal and **Ihsan**. I think a little over a year ago, you both joined Shiju's team. I really enjoyed all the couch discussions and lunch stories about your previous postdoc experiences. Sheetal, thank you for collaborating and for sharing *so many lunches*. I think I am not alone when I say we truly enjoyed each lunch you prepared. Ihsan, you are a very respectful guy and I want to thank you for all the collaborative work. Thanks for staying in touch during the busy days of getting this thesis ready, and for helping me with so many things in the lab when I had trouble reaching the SP. Thank you for inviting me to a wonderful Indonesian dinner.

Layla, our "firecracker" from Italy (100% meant as a compliment!). Thank you for all the conversations, especially during the last three months while we shared the fume hood in E0.36. Thanks for the virtual Italian cooking lesson you arranged with Gadi and other colleagues at Christmas. I can honestly say this was the first time I used pre-soaked dried mushrooms in a dish.

There is one crucial part of the HCSC operation that cannot be overlooked. And that is the team that is making the lab into the great, smoothly operating workplace that I grew accustomed to: **Norbert**, **Paul** and **Marjo**. Norbert, you are *the* force that keeps the lab operational. Thank you for all the lunch and coffee conversations, all the fun talks in between conference presentations and – of course – all your help! I'm sure it is not always easy to help everybody, yet you always found time to help me with my project needs, everything from advice, to buying parts for the bubble counters to last-minute adsorption measurements, you did it all. Thank you!

Paul, the electronics wizard from the lab. We both share an interest in electronics and I always have much admiration for the devices you designed and built. I enjoyed asking you loads of extra questions, like how to communicate with mass flow controllers or what are the requirements of a lab-safe device. Thanks for all your help! I remember your workbench was always filling up with stirring plates that were dropped off with notes like "not working" or "not stirring": burnt wiring, PCBs drenched in oil, you have seen it all. Yet you always look ahead positively.

Marjo. Tuesday was always a particularly nice day. It usually meant you were in. As the walking encyclopaedia of the group's history, you always had nice stories to share at the coffee table. What I enjoyed even more were all the little practical things that you shared with me throughout the years. I gladly looked over your shoulder as you fixed oil pumps or explained how and when to clean a Penning gauge. Thank you for all the help with my questions about adsorption measurements. I wish you a great and well-deserved retirement.

Ed. Thank you for the numerous GCMS measurements you took for me and my students and for all the discussions on how to interpret the spectra. I want to thank **Jan Meine** and **Andreas** for their support with the NMR equipment. Jan, you are the wizard of NMR and I am sure you are missed by many. I hope you enjoy your well-earned retirement. **Dorette**, thank you for all the nice conversations and help with the glove box, chemicals and other things. I should not forget the *Alperol Spritz*, of course. I forgot how we got to this subject, but when you learned I never had one, you brought me one as a gift, such a nice surprise! **Taasje and Simon**, you both have a truly *gezellige* vibe: Thanks for all your help with lab access and pulling chemicals from the bunker.

I thank professor **Hualong Xu** of Fudan University for hosting me for almost three months in Shanghai. Going to China was the greatest experience from my PhD period. Even though I was far away from home, you (and your group!) made me feel like I was at right at home. I want to thank all your students, in particularly **Wenjie**, **Wang Sheng**, **Junjie** and **Kevin** (sorry, I don't remember all the names): thank you for all your support. **Sun Chao** and **Huang Zhen,** the unmistakable masters of machine! It was a pleasure to work with both of you and I still hope to welcome you in the NL one day. Special thanks to **Junjie** for organizing the trip to his hometown in Zhejiang province, **Fang Yue** for

arranging the HAADF-TEM measurements, **Qin Feng** you for taking care of all the visa and registration paperwork and of course professor **Wei Shen**, for all the great discussions!

I had the pleasure of working with scientists from many other countries as well. I want to thank **Paula Oulego** (Spain), for all her help with XPS, TEM, N_2 adsorption and ICP-MS measurements and the discussion of the data. I want to thank **Enrique Ramos-Fernandez** (Spain) for the XPS measurements, TEM measurements, and all the insightful discussions. Furthermore, I'd like to thank **Varun Natu** and **Michel Barsoum** (USA) from Drexel University and **Zdenek Sofer** (Czech Republic) from University of Chemistry and Technology Prague for supplying MXene and MAX phase materials and for discussions. I want to thank **Maurits Boeije**, **Wilbert Vrijburg** and **Bernardus Zijlstra** at VSparticle for the nice collaboration on making catalysts with your new spark-ablation technology.

I want to thank **Eitan Oksenberg** (AMOLF) for training me on the TEM and helping me with the specialized measurements of our Pt/Al_2O_3 catalysts, which were so easily damaged by the electron beam.

Teaching was an important part of my duties as a PhD student. It was a pleasure to teach in the *Molecuul en Leven* practical labs. I was part of many teaching duos. In particular, I want to thank **Bob**, **Kevin** and **Marianne** for their passion and collaborative spirit during the course. I also want to tank **Stefania** for arranging the teaching duties and letting me do the experiments I liked best.

Ning, **Stefania**, **Klaas-Jan**, and **Amanda**. Thank you for the discussions during the group meetings. **Vitaly**, we briefly shared a fume hood while you worked on the Niacin project. It was a lot of fun to have you around and learn from you and about life in Israel. **Kamila**, you were always really interested in how everybody was doing, dissecting their life choices (and plans!) with interest and vigour. Somehow you always end up asking me questions required me to think and take a deep look inside. Thanks for all your advice. **Sang-Ho,** thank you for all the discussions and being my friend. You were a great colleague to have. I wish you all the best at KAUST, and I hope you and your wife are doing great. **Edwin**, you have left a long time ago, but I still remember some nice discussions and ideas on the big matters of life. I could always find you in your "secret" hideaway in the GC room. I'm afraid to tell you that nowadays your space is occupied by a UV/Vis spectrophotometer.

We also had a strong Chinese delegation present in our group. **Yuan**, you are the very nice and the more 'quiet' type of PhD student. It was not until I went to China that I discovered that you were a true heavyweight in haggling. Wow! Thank you for all your help while I was in Shanghai. **Wei**! I think you did more experiments than anybody else in the group, and you always had a smile on your face. Thank you for all the discussions

and collaborations. It was so much fun to be your paranymph at your PhD defence. Thank you for all the good times. **Yiwen**, thank you for the discussions.

I want to thank **Johan** for all the insightful discussions. I envy your understanding of physics and modelling. It was such fun to work on the DataFish project. **Connor**, I am very happy you found a place with Amanda to pursue a PhD. **Lennard**, thank you for your enthusiasm and sharing with me your knowledge on 2D correlation spectroscopy. Why didn't you do a PhD?! I am still puzzled. **Vikash**, thank you for all the work you did and for the ideas you brought into our discussions. I also want to thank **Erik, Roelof** and **Koen** for all the ideas and good company.

During the last years, I had help from many master students. **Nathan**, because of your work were able to solve a really tough question about confinement (see Chapter 3). You were a great student with a truly remarkable personality. It was a pleasure to have you in the lab. Your views of the world made lunches so entertaining and inspiring. You are the only student I know that had a quote book written about him by fellow students, so I guess I'm not the only one who thinks so. **Murray**, you were here for your master project to work on a truly tough project about cover-confinement. I have not seen a student with more experimental output than what you did. Your perseverance to crack this nut was amazing, but unfortunately the ideas we had were not working like we imagined. *Freddy is still going strong!* **Clara,** your project was partly with a company, ChainCraft, and partly at the UvA. Especially with me on the other side of the globe (in China), you took charge of your project and delivered a great thesis. Thank you for all your work and, of course, the Lebanese sweets you brought! **Michelle**, you did some great exploratory work on MXenes and peroxide oxidation. It was because of your work that we knew exactly how far we could go before our MXene structure would fuse into one big mess of titania. **Martijn**, you are one of a kind: the Korean-speaking Dutch master student and pallbearer. Thank you for your work on cyclohexene oxidation. **David**, thank you for your work on cyclohexene oxidation and teaching me a few Hebrew words.

I supervised many bachelor students that supported me with day-to-day experiments or ran their own projects to do exploratory work. **Sem**, thanks to your experiments on the rheometer we could figure out precisely how we needed to change the constitution of the graphene oxide pastes to 3D print them. **Peter**, you did a great job exploring graphene-supported core-shell catalysts for oxidation reactions, **Dylan**, your exploratory work really helped to lay a solid foundation for the 3D printing project of Sem. **Kevin**, your work on graphene synthesis was very useful to figure out how to synthesize the highest quality graphene oxide. I want to thank my other students, **Yuman**, **Akshay**, **Jeen**, **Joost**, **Bastiaan**, **Juliaan**, **Nawand**, **Duane** and **Maarten**. Your contributions have often been vital to determine my research strategy. I want to thank each and all of you, as well as any of you who I might have forgotten to mention. In that case I apologise!

Fran, Martijn and **Connor**, I wish you all the best for your PhD the coming years. I hope that within four yours you will be where I am today. Fran, take care of our little bubble counters! If you every need any help, just give a shout!

Jan van Maarseveen, bedankt voor jouw kennis en kunde om het raadsel van de styreenoxide ring opening te kraken. **Marissa**. Jouw lach maakte me van binnen altijd enorm vrolijk. Ik denk met veel plezier terug aan alle keren dat ik op de 2e verdieping langskwam om even te buurten. Je had altijd even tijd voor een praatje. En nu de powervrouw van SusPhos, Wow! **Martin** en **Bas**, bedankt voor al jullie hulp met het vriesdrogen. **Hans**, bedankt voor alle praatjes die we afgelopen jaren hebben gemaakt. **Dieuwertje**, jij hebt een speciaal plekje. Je hebt over de jaren ook best wat dingen op je bordje gekregen. Het was enorm fijn om hier met jou over te kunnen praten. Ik denk nog met veel plezier terug aan het Rachmaninoff concert. Ik wens je alle goeds.

I want to thank all colleagues from HomKat for all the discussions, and fun times after work, in particularly **Klaas**, **Tijmen**, **Tessel**, **Wojciech**, **Lotte**, **Roel**, **Arnout**, **Pim**, **Lukas**, **Zohar**, **Didjay and Marianne**. I fondly think back of our time at the CAIA course at Schiermonnikoog (the course on catalysis from that nobody can escape … *literally*). Marianne, it was a lot of fun to teach the practical labs with you. I hope you are happy in your new job and I wish you all the best!

I want to thank **Marcel**, **Stefanie** and **Renate** for all the help with the official business, packages and samples, and emptying the mailbox during corona times.

Graag wil ik ook mijn vrienden **Wessel** en **Daniel** bedanken. We kennen elkaar sinds het 1e jaar organisch scheikundepracticum in Utrecht. Bedankt voor de goede vriendschap, voor alle belletjes en bezoekjes en natuurlijk voor jullie kennis en het *stevig* proeflezen van mijn thesis. Zonder jullie had mijn thesis er waarschijnlijk nu heel anders uit gezien.

Nico, hartstikke bedankt voor jouw bijdrage bij de controle van de tekst.

Jochum, **Joost**, **Joris**, en **Rene**. Bedankt voor alle gezellige kaartavonden. Ook al komt het er nu niet altijd meer van. 😉

Johan Zutt, bedankt dat je mijn interesse in de scheikunde zo hebt weten te voeden op de middelbare school. Buiten lestijd groene kaliummanganaat K_2MnO_4 in de smelt maken… ik weet het nog goed!

Ben en **Cora**, bedankt voor jullie gezelligheid, warmte, en dat we na pap en mams overlijden bij jullie gezinnetje mochten aansluiten. Dat heeft voor mij een enorm groot verschil gemaakt.

Mam en **pap**. Ik ben jullie ongelofelijk dankbaar voor al jullie onvoorwaardelijke liefde en steun. Jullie hebben me altijd vrij gelaten om zelf een pad te kiezen en jullie hebben mij daar altijd onvoorwaardelijk bij gesteund. Zo kon ik spelenderwijs mijn interesses

verkennen. Ik vermoed dat dat ook tot enige frustraties zal hebben geleid toen er zo af en toe wat explodeerde in het tuinhuisje. Toch zijn het juist *die* ervaringen, die het pad naar vandaag hebben geleid. Ik had zo graag gewild dat jullie bij deze dag zouden kunnen zijn, al was het maar om te zien dat het *"toch nog is goedgekomen"* 😉. Stiekem hoop ik dat jullie deze dag meekrijgen, en dat jullie – op een afstandje – trots zullen zijn. Deze is voor jullie!

Lieve **Floor,** we hebben samen veel overwonnen. Ik ben ontzettend dankbaar voor alle liefde en steun die je mij de afgelopen jaren hebt gegeven. Maar ook ver daarvoor! Ik denk met veel plezier terug aan alle "experimenten" waarmee wij van jongs af aan mee in de weer waren. Van het bouwen van parachutes (die veel te ver wegvlogen) tot een enorme (2 m hoge) iglo in de achtertuin toen het eindelijk weer eens fatsoenlijk sneeuwde, alles altijd samen. Ik ben dan ook echt ontzettend blij dat jij er vandaag bij bent als paranimf. Ik kan me geen lievere en betere zus wensen. ♡♡♡

– Thierry Slot, December 2020, Amsterdam

Thierry Slot was born in Alkmaar, The Netherlands, in 1986. He earned two BSc degrees (Pharmacy and Chemistry, *cum laude*) from Utrecht University, before moving to Amsterdam to join the master program 'Molecular Design, Synthesis and Catalysis' at the Free University and the University of Amsterdam. After completing his research project under the supervision of Dr. David Eisenberg and Prof. Gadi Rothenberg, he graduated *cum laude* in 2016.

In 2016, he started his PhD with Prof. Rothenberg and Dr. Shiju Raveendran as part of the NWO TOP-PUNT project *Catalysis in Confined Spaces*. For four years, he toiled to unravel the mysteries of confinement chemistry by altering the surface structure of various catalytic materials, the results of which are summarised in this book. During this time, he also spent three months at Fudan University in Shanghai at the group of Prof. Hualong Xu. He has published 12 peer-reviewed papers and invented a new device for studying the kinetics of gas-producing reactions. The project combined four of his passions: chemistry, material design, electronics and 3D printing.

ISBN 978-94-6416-483-1